Specialized Track Bridge Structure for Light Rail Construction on Floating Bridges

Travis E. Thonstad

A thesis
submitted in partial fulfillment of the
requirements for the degree of

Master of Science in Engineering

University of Washington
2013

Committee:
John F. Stanton
Marc O. Eberhard
Michael R. Motley

Program Authorized to Offer Degree:
Department of Civil and Environmental Engineering

University of Washington

Abstract

Specialized Track Bridge Structure for Light Rail Construction on Floating Bridges

Travis E. Thonstad

Chair of the Supervisory Committee:

Professor John F. Stanton

Civil and Environmental Engineering

Sound Transit's East Link Light Rail project carries light rail transit (LRT) to east King County Washington over the existing Homer M. Hadley Memorial Bridge. Although there are examples of similar projects on cable-stayed and suspension bridges, there is no precedent for LRT on floating bridges. The design of a specialized track bridge structure is required to allow light rail vehicles to travel across the bridge's four expansion joints.

The Curved Element SUpported RAil (CESURA) concept employs a novel method to overcome the motions at the interfaces between the fixed and floating portions of the bridge. This system passively adjusts vertical and horizontal alignments

to allow the rails to undergo the movements intrinsic to the nature of the floating structure.

Because of the complexities of the CESURA system, the non-standard components that comprise its major elements, and the unknown interactions between these parts, extensive experimental research data was needed to validate and calibrate computer models which will be used to produce the final design.

A full-scale test of a part of the system was conducted in the University of Washington's Structural Engineering Laboratory. The tested system consisted of approximately one quarter of the CESURA system. The constructed specimen was subjected to exaggerated geometric configurations compared with those that would arise during normal operation, and it was tested under both vertical and horizontal forces.

The specimen behaved largely as anticipated and revealed no major shortcomings. The behavior of the system was found to be largely independent of the imposed geometric configuration. Both the re-centering capabilities and geometric design of the system were also investigated by examining the effect of specific elements of the current design.

The system was found to be highly sensitive to the construction process. Component tolerances should be adjusted to facilitate their precise location within the system. Specific fabrication methods should be adjusted to prevent the undesirable construction sequence that was necessary in the component testing. Instrumentation of the full-scale

prototype test, to be conducted at the Transportation Technology Center, Inc. (TTCI) facility in Pueblo, Colorado in 2013, should be planned carefully to avoid the issues encountered during the testing program.

This thesis is dedicated to my grandmother, Avis Thonstad,

whose love and support will be greatly missed.

Acknowledgements

This work was funded by Parsons Brinckerhoff, and the author would first like to thank John Harrison, Tom Cooper, and Behrooz Emam for their guidance and patience during the necessarily iterative construction process in the laboratory. The author would also like to thank Bryan Williams from Jacobs Engineering for his tremendous efforts to procure rail fasteners in small quantities and John Sleavin at Sound Transit for his continued support throughout the research project. The author would sincerely like to thank Andy Foan, the inventor of the CESURA system who made this project possible, and for his explanations of the mechanics of the system.

It is with immense gratitude that the author acknowledges the support and guidance of his committee chair, Professor John F. Stanton who has been a font of knowledge and expertise throughout this research project.

The author would like to thank his review committee members, Professors Marc O. Eberhard and Michael R. Motley for sharing their knowledge and providing valuable feedback; the employees of Sound Transit and Amstead RPS for lending rail components for use in the experiment; Bryan Germann and the employees at Direct Measurements Incorporated for their training on the DPS system; Vongsant “Vince” Chaijaroen for his expertise throughout the experimental phase of the project, and Lucas Whitesell, Jake Gruber, Scott Tetzlaff, Kevin Tsuchida, Kevin Martin, Travis Corigliano, and Spencer Livermore for their help with construction and testing.

Finally, the author would like to thank his friends and colleagues Max Stephens, Olafur Haraldsson, Bo-Shiuan Wang, Hung Viet Tran, Mohammad Malakoutian, and Trent Tinney for their advice and assistance throughout the research project; Johnathan Wiegand for sharing his spectacular MATLAB routines; his parents Ralph and Jeri Thonstad for stressing the importance of education and hard work; and his fiancé Sarah Coddington for her immeasurable patience, support, and understanding throughout this research project.

Table of Contents

List of figures

Chapter 1

Chapter 2

Chapter 3

Chapter 4

List of tables

Chapter 2

Chapter 5

Chapter 6

Chapter 1 Introduction

1.1 East Link Project Overview

Sound Transit's East Link Light Rail project carries light rail transit (LRT) to east King County Washington, servicing downtown Bellevue and Redmond, extending the current Central Link network that connects downtown Seattle to the SeaTac Airport. The planned East Link service map is shown in Figure 1-1, including the current Central Link route and the extension underway to connect the Central Link to the University of Washington. The chosen route traverses Lake Washington over the existing Homer M. Hadley Memorial Bridge, a pontoon bridge that currently carries westbound traffic and reversible high-occupancy vehicle (HOV) traffic lanes for Interstate 90.

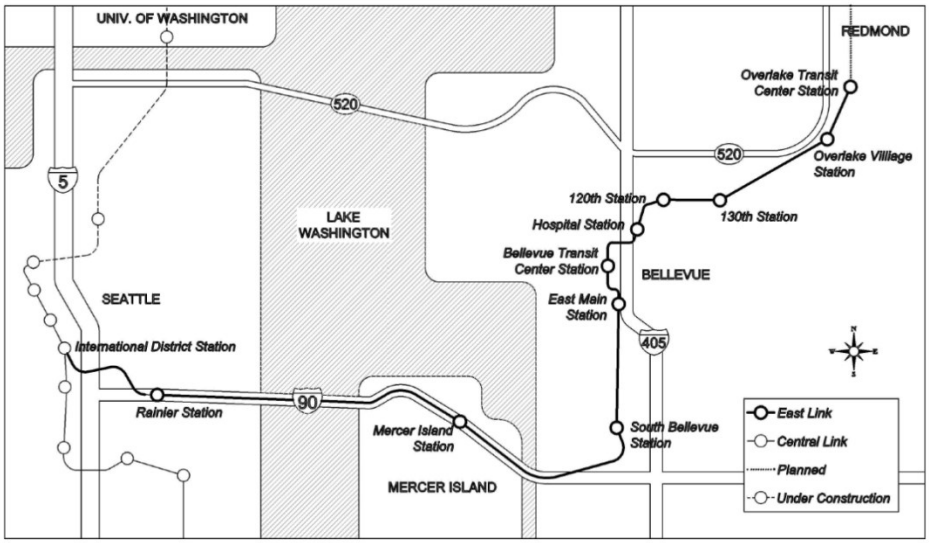

Figure 1-1: Current Central Link and proposed East Link light rail service routes.

In 2008, a study was conducted by an Independent Review Committee to evaluate the feasibility and impact of LRT on I-90. Although there are examples of similar projects on cable-stayed and suspension bridges, there is no precedent for LRT on floating bridges (Parsons Brinckerhoff, 2006). The results of the examination of previous reports and test results showed that issues arising from the dynamic motions of the pontoon structure could be mitigated. In particular, the report identified the need for special track bridge structures to allow light rail vehicles (LRV's) to travel across the bridge's four expansion joints. Parsons Brinckerhoff (PB) was engaged to develop preliminary designs and conduct prototype testing of this track bridge. The University of Washington was engaged to conduct component tests. Further testing of a complete system at the Transportation Technology Center, Inc. (TTCI) facility in Pueblo, Colorado is planned for 2013.

The Homer M. Hadley Memorial Bridge can be thought of consisting of five spans: two fixed portions that extend a short distance beyond the east and west banks of Lake Washington, one floating portion, and two transition spans that act like pin ended members traversing the gap between the fixed and floating portions of the bridge. Figure 1-2 shows a schematic diagram of the bridge with the floating and transition span lengths.

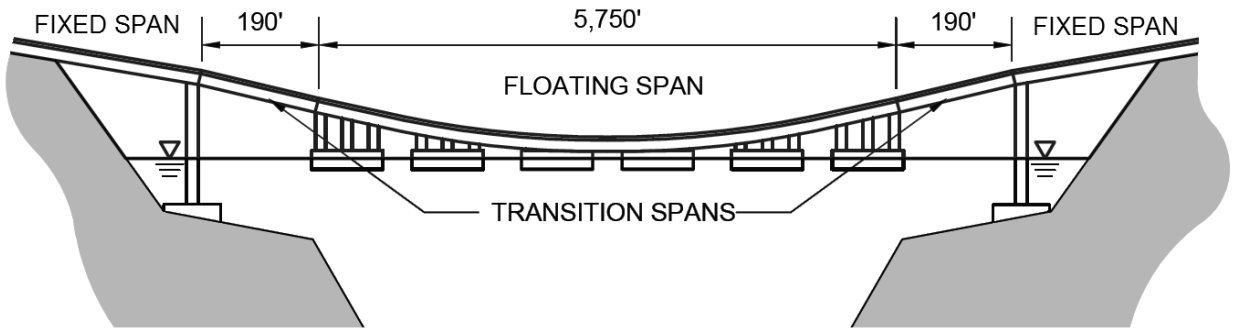

Figure 1-2: Schematic diagram of the Homer M. Hadley Memorial bridge.

The transition spans must accommodate displacements and rotations caused by both the inertial forces of the light rail vehicle (LRV) and the conditions on Lake Washington. These motions are small enough not to affect that vehicle traffic, but they are problematic for the LRV because they produce sharp changes in the vertical and horizontal alignments of the track and undesirable stresses in the rails.

1.2 Component Motions

Four major component motions; surge, pitch, yaw, and roll must be accommodated for at the interface between adjacent spans of the bridge. These motions are described in the following paragraphs and are summarized in Figure 1-3.

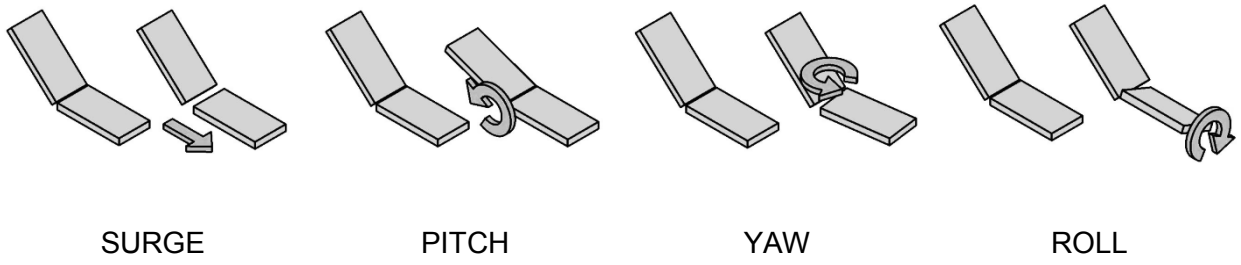

Figure 1-3: Four component motions at the interface between the transition and floating spans (highly exaggerated).

1.2.1 Surge

Surge causes adjacent spans to move longitudinally, in the direction of traffic, with respect to one another. It is caused by environmental factors, such as wind and lake conditions as well as temperature effects. For vehicular traffic, this motion is accommodated at standard expansion joints. For LRT, the lengthening of the rail is accounted for by standard rail expansion joints at either end of the track bridge. The continuous welded rails (CWR) that will be present in the track bridge structure itself will be able to slide longitudinally in their rail fasteners.

1.2.2 Pitch

Pitch is a rotation about a horizontal axis transverse to the longitudinal axis of the bridge and is caused by a variation in lake level, which is controlled by the Hiram M. Chittenden Locks near the Ballard neighborhood in north Seattle. The change in water level is about two feet per year, with the highest levels recorded in the spring and the lowest recorded in the winter. A small component of pitch is also caused by the

weight of the LRT as it crosses onto the floating span and causes it to float lower in the water. This rotation creates a change in vertical slope at the expansion joint that must be accommodated by the track bridge.

This sharp change in rail trajectory is problematic. One possible approach would be to allow the rails to bend over a long distance, reducing the local stresses and local deformations of the rail, but this choice would leave the rails unsupported over this same distance, and unable to carry the weight of the LRT. The second option is to keep the rails fully supported at regular intervals, but this solution concentrates the change in slope at the interface between spans and causes high stresses and displacements demand. The optimal solution would marry these two possibilities, providing a transition from one slope to the other that is both continuously supported and spreads the deformation over a long length of rail.

1.2.3 Yaw

Yaw is defined as the rotation of the track bridge about a vertical axis, and is caused lateral movement of the floating bridge. It results from the stretch of the anchoring cables that are meant to restrain the movement of the floating pontoons as they respond to wind and other loading. This rotation creates a change in horizontal alignment that must also be accounted for by the track bridge. Similar to the pitch movement, yaw creates a hinge type rotation at the interface between the transition and the fixed/ floating portion of the bridge.

1.2.4 Roll

Roll, or rotation about the longitudinal axis, is caused by environmental conditions, wind and lake conditions, as well as the inertia of the LRV vehicle as it traverses the joint. The inertial and wave forces cause a rotation of the floating span about a longitudinal axis, parallel to the direction of traffic. In a report submitted in 2006, the design and consulting firm KPFF found that weighted trucks carrying the equivalent of the LRV axle loads caused a displacement at the leading pontoon corner of over seven inches (KPFF, 2005). Unlike pitch and yaw, roll produces a twist in the track, which must transition from one transverse slope to another, because one end of the track bridge is fixed against rotation and the other end must follow the rotation of the floating span. Of the component motions roll causes the most difficulties because of the higher mode of the deformed configuration. This dynamic effect along with the roll caused by lake conditions must be accommodated at this transition in addition to the effects of surge, roll, and yaw.

1.3 Design Alternatives

Traditionally, horizontal and vertical curvatures in railroads are relatively constant, and designers strive to limit misalignments at deck abutments. The objective of these constraints is to provide track geometries that are largely predictable, and provide safe operating conditions. There are, therefore, few track bridges that experience conditions comparable to those in I-90, on which to base new designs.

Several solutions were explored by the designers before the selection of the system under investigation. Presented subsequently are two systems already in service that possess many of the same capabilities that are required for this application and the alternative solution that was considered before the final system selection.

1.3.1 Vancouver SkyBridge

The SkyTrain system in Vancouver, B.C., Canada encounters a similar problem as it traverses the cable-stayed bridge (SkyBridge) crossing the Fraser River. Temperature and LRV inertial forces cause surge and pitch at the span abutments, although about one-third the magnitude of those required in the East Link design. Figure 1-4 shows a photograph of the solution that was developed.

Figure 1-4: SkyBridge expansion joint picturing cylindrical elastomeric springs (Parsons Brinckerhoff, 2006).

The joint that was employed in this application consists of ten tie plates, spanning the bridge expansion joint, each connected to the decking surfaces through two elastomeric spring (Parsons Brinckerhoff, 2006). These specialized springs allow the rails to bend over the 14 foot transition section while still providing the vertical support needed to maintain ride quality. This system was, however, not designed or tested for the considerable yaw rotations and horizontal displacements that are expected on the I-90 floating bridge.

1.3.2 Tagus River Bridge

The Tagus River Bridge in Lisbon, Portugal was retrofitted for LRV traffic in 1999. This suspension bridge has the unique feature of a continuous under truss over the suspended spans. Thermal expansion and train live loads cause large deflections at the bridge abutments; the design longitudinal movement of 60 inches was accommodated by implementing a sliding box girder straddling the expansion joint (Rao, 2000). In addition to expansion, live loads cause a sharp change in grade at the bridge ends, which is dispersed over the length of the sliding girder by fasteners connected to ties though neoprene shims (Rao, 2000). This solution, although a viable alternative, was also untested for the significant roll and yaw movements present on the I-90 bridge.

1.3.3 Three bar alternative

Early designs for the East Link expansion joint included a three beam alternative that is shown in Figure 1-5. This concept consists of three wide flange beams on either side of the rails, connected near the center of the expansion joint by two pivots. Steel ties spanning between the beams, perpendicular to the direction of LRV travel, supported the rails. Specialized fasteners, similar to those used in the SkyBridge and Tagus River designs, allow vertical displacements and strong axis bending of the rail cross section.

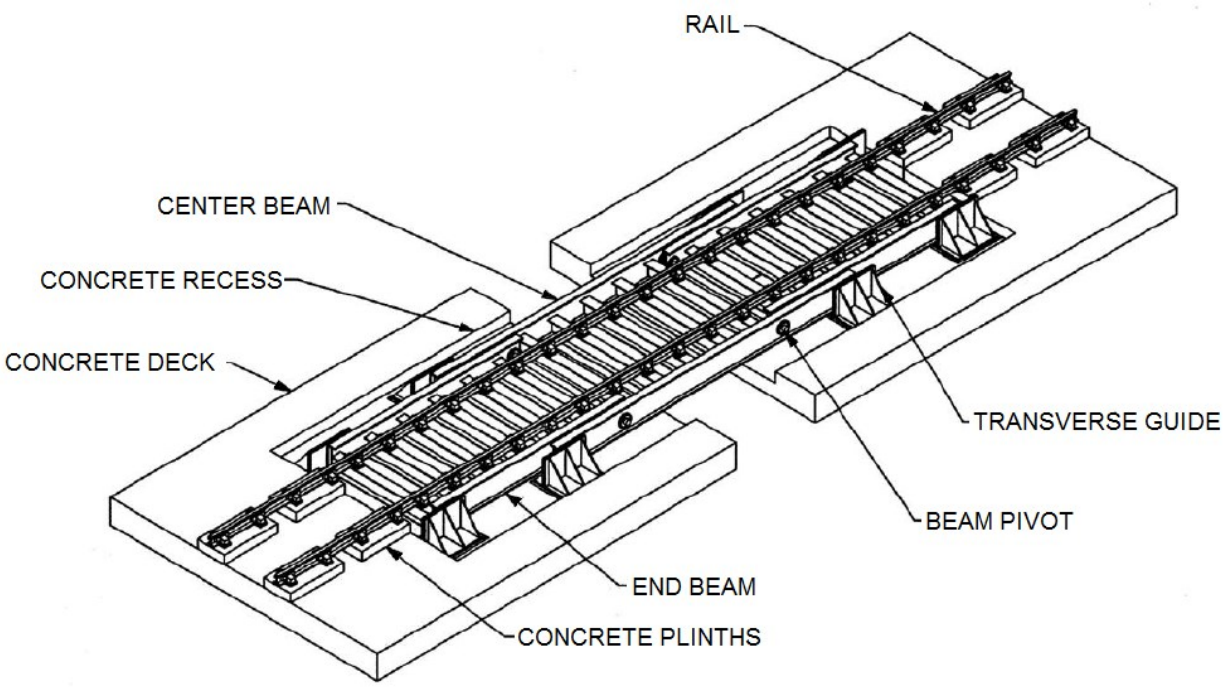

Figure 1-5: Schematic view of the three bar design alternative considered for the East Link light rail expansion

With this configuration, yaw rotations are transferred to the system by the transverse guides causing bending of the beams in a horizontal plane, producing a

smooth horizontal alignment. Under a pitch rotation, the center beam is sloped at half the rotation of the transition span. By bisecting the concentrated rotation and providing displacement and rotation capacity in the fasteners, the resulting system could accommodate the rotation capacity required for the East Link expansion track bridge structure.

1.3.4 CESURA system

The system that is the focus of this research employs a novel method to overcome the motions at the interfaces between the transition span and the fixed and floating spans. The Curved Element SUpported RAil (CESURA) concept, pictured in Figure 1-6, is a passively adjusting system that bends the rails to provide a smooth, continuously supported transition between incoming and outgoing rail trajectories. This system has the capability to traverse the interface between the fixed or floating span and the transition span and adjust the vertical and horizontal alignments to allow the rails to undergo the surge, pitch, yaw, and roll movement intrinsic to the nature of the Homer M. Hadley pontoon bridge.

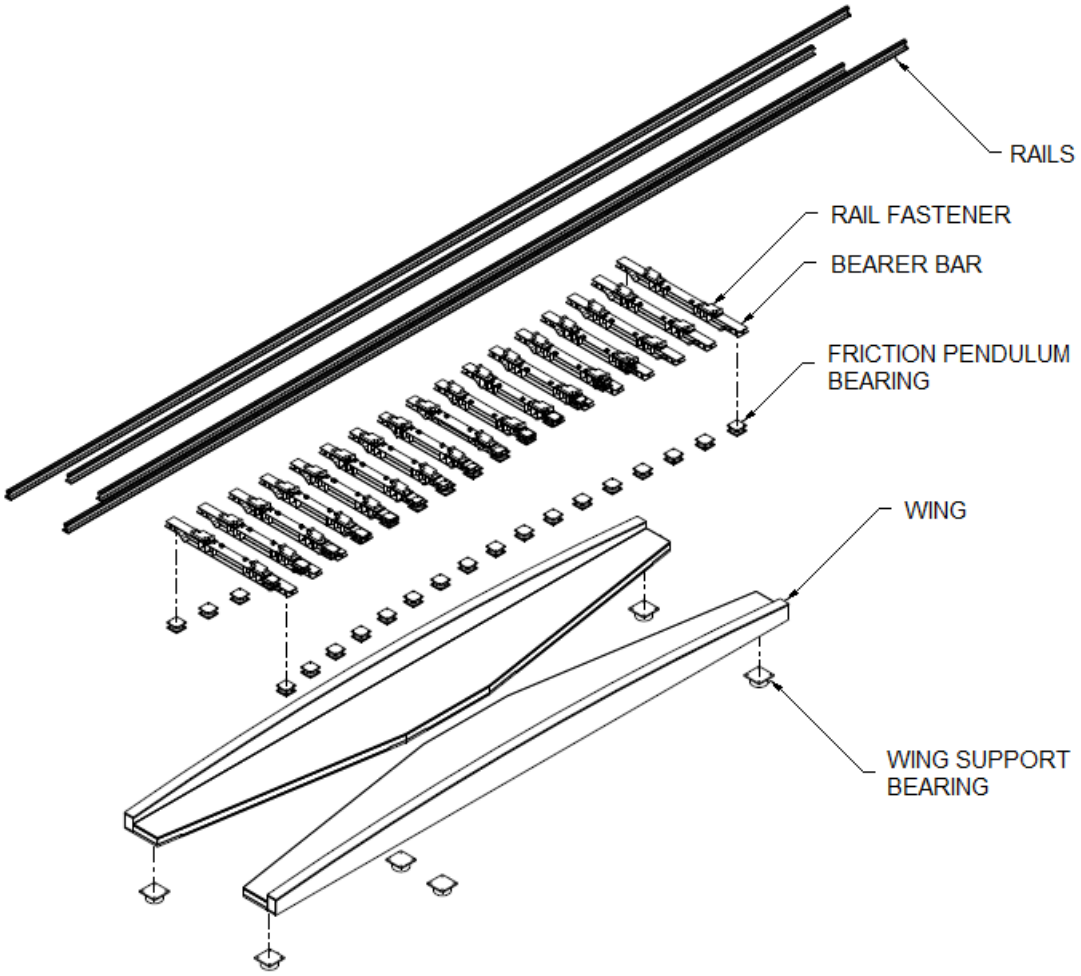

Figure 1-6: Exploded view of the CESURA system.

The CESURA system is comprised of three major component classes: two box girders, or "wings", 34 friction pendulum bearings that provide rotation and transverse sliding capacity, and 17 transverse steel ties, or "bearer bars". The rails are connected to the ties using special fasteners that provide acoustic isolation. The two wings are supported on bearings by the bridge deck at three locations and are oriented longitudinally to the direction of the rails. Attached to each wing are 17 friction

pendulum system (FPS) bearings that are arranged in a semi-circular curve, or "yoke" on the wing's top surface. These bearings, traditionally used for seismic isolation, were chosen because of their large displacement capacity and re-centering capabilities. Specialty bearings were designed for this application, and are discussed further in Section 2.5.1. The bearer bars span transversely between the wings, and are attached at either end to the top surface of the friction pendulum bearings.

Each wing is supported at three locations, two on either the fixed or floating portion of the bridge and one on the transition span. The arrangement is shown in Figure 1-6. These supports are oriented to form two triangles, each with one leg positioned parallel to the rails. The third vertex of each of these triangles is offset from the rails' longitudinal axis and positioned so that the support arrangement resembles a bow-tie. With this configuration, as the bridge joint undergoes relative rotations and translations, the box girders undergo both changes in longitudinal slope and transverse rotation. In such a manner, a cresting vertical curve requires the wings to rotate outwards, away from one another, while a sagging vertical curve requires the wings to rotate inwards, toward one another. This feature is important, as it is this movement that drives the kinematics of the system and the passive adjustment of the rail supports.

The wings rotate about the axis defined by their two fixed supports. As the box girder twists inward or outward, the friction pendulum bearings must undergo a vertical motion proportional to the distance from their centers to the wings axis of rotation. By setting the friction pendulum bearings on a curve that forms part of a circle

on the wing's surface, the vertical change experienced by each of the bearings varies from one end of the CESURA system to the other, and creates an elliptical vertical curve whose minor axis is dictated by the wing's rotation. With the proper choice of the yoke radius and the distances between the wing's supports, the ellipse provides a smooth transition from one trajectory to the other, without large inconsistencies in slope at either end of the track bridge.

1.4 CESURA Kinematics

The system's kinematics are described in detail in Section 6.1. Figure 1-7 shows an idealized, version of one side of the CESURA system subjected to a pitch motion. The motion and subsequent geometry of the system produced by the pitch motion is the easiest to visualize and illustrates how the configuration of the system affects the resulting vertical alignment of the rails.

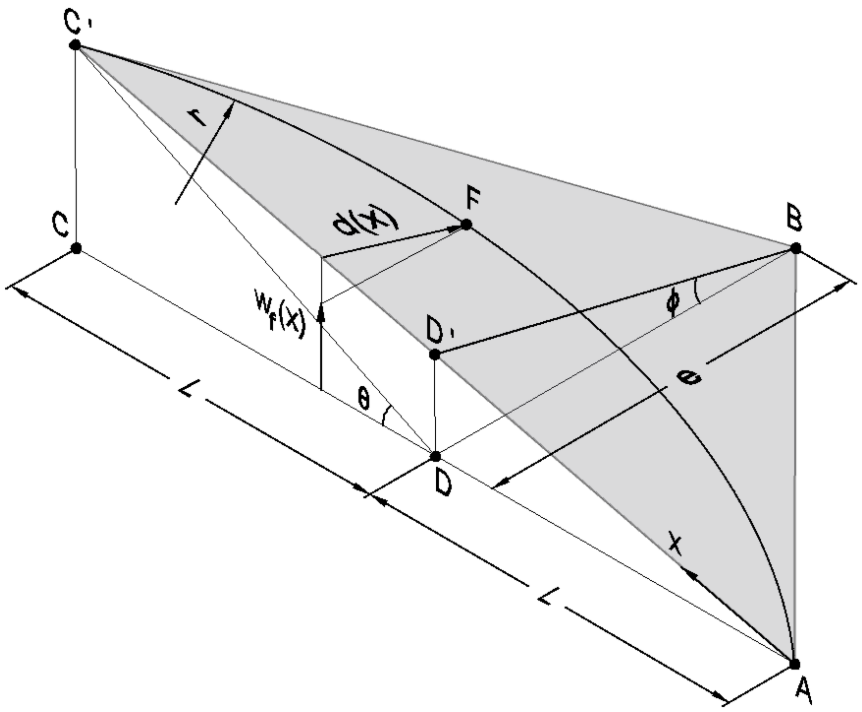

Figure 1-7: Idealized CESURA wing geometry subjected to a pitch rotation

Points *A, B* and *C* represent the location of the wing's supports on the bridge surface in the reference condition. For convenience, plane ABC may be thought of as horizontal. Points *D* and *B* are both positioned directly over the joint that joins the transition span to the fixed or floating portions of the bridge. In this picture, the lines *AC* and *DB* are perpendicular. Points *C'* and *D'* are points on the wings surface after the joint has undergone a pitch rotation, about the axis *DB*, of magnitude θ. In this configuration, rails would run along a path parallel to the line *AC*. Assuming that the pitch angle, θ, is small, the length *CC'* and *DD'* are given by

$$\mathrm{CC'} = \mathrm{L}\theta \qquad \mathrm{DD'} = \frac{\mathrm{L}\theta}{2} \tag{1-1}$$

The twist angle of the wing, ϕ, is then

$$\phi = \frac{DD'}{e} = \frac{L\theta}{2e} \tag{1-2}$$

Assuming that the bearings yoke is given by a circle with radius, *r*, and that *x* is defined to be the distance from point *A* along the line *AC'*, then the offset distance, *d*, as a function of *x* is given by,

$$d(x) = \sqrt{r^2 - L^2 - x^2 + 2Lx} - \sqrt{r^2 - L^2} \tag{1-3}$$

Defining $w_f(x)$ to be the vertical displacement due to a pitch rotation of an arbitrary point, *F*, along the path defined by *d*, it can be shown that:

$$w_f(x) = \frac{\theta x}{2} - \frac{L\theta}{2e}\left(\sqrt{r^2 - L^2 - x^2 + 2Lx} - \sqrt{r^2 - L^2}\right) \tag{1-4}$$

Which is an elliptical arc joining the two trajectories. The slope of this vertical curve at the boundary $x = 2L$, should match the slope of the transition span, θ.

$$w_f'(2L) = \theta = \frac{\theta}{2} - \frac{L\theta(-2(2L)+2L)}{2e\sqrt{r^2-L^2-(2L)^2+2L(2L)}} \tag{1-5}$$

This implies that in order to have continuous slopes at the end of the CESURA system, the relationship between the bearing eccentricity, the length of the system, and the FPS bearing's yoke radius must be

$$\left(\frac{r}{L}\right)^2 = \left(\frac{L}{e}\right)^2 + 1 \tag{1-6}$$

Figure 1-8 shows one half of one wing of the CESURA system, with supports at points A and B. Equation 1-6 can be expressed succinctly by the parameter α, defined as the angle between the longitudinal axis AD and the bearings rotational axis AB.

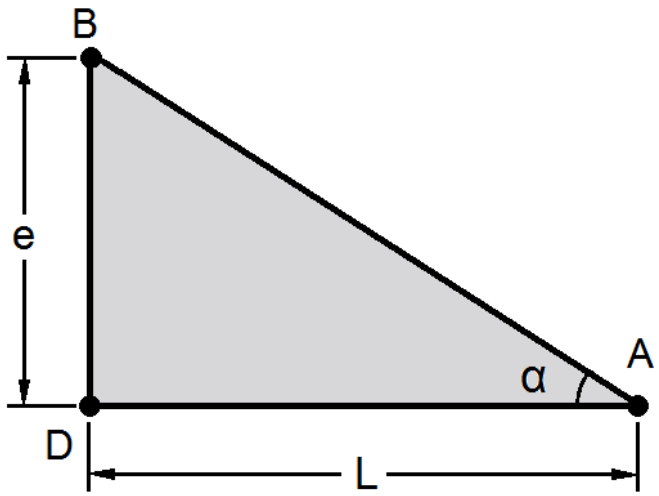

Figure 1-8: Idealized CESURA wing bearing support diagram.

In order to have continuous slopes at the end of the CESURA system, the relationship between the radius of the bearing yoke, the length of the system, and the parameter α is given by Equation 1-7.

$$\sin\alpha = L/R \tag{1-7}$$

As long as the middle bearing lies along the line defined by the angle α, the amount of twist that the wing experiences for a given amount of pitch is constant. Although this procedure allows the development of a geometric design strategy,

departures from this idealized geometry add complexities that must be accounted for in order to produce smooth transitions between track bridge and bridge deck.

The foregoing discussion outlines the major movements that the track bridge must undergo. However, these give rise to many smaller displacements, the determination of which is not simple. For example, the rigid body twisting rotation of the wings under pitch motions causes the bearings at each end of a bearer bar to approach one another or move apart. Thus the bearing must accommodate a translation as well as a rotation. Furthermore, some rotation capacity about the transverse axis is desirable to accommodate the rotation induced by rail bending as the LRT vehicle travels across the track bridge. Yaw of the track bridge also imposes some rotation demands on the bearings about their vertical axes. Last, these motions may be predicted assuming that the components other than the rails act as rigid bodies. Inevitable deformations of the components lead to further local displacement and rotation demands at the points of articulation in the system.

The integrity of the track is a primary concern. Therefore Friction Pendulum (FPS) Bearings were chosen to support the bearer bars, because they have a re-centering feature that would bring the track geometry back to its original condition after any loading, such as the passage of an LRT vehicle over the track bridge or wave action on the floating span. Friction Pendulum Bearings were conceived for seismic isolation, and unavoidably include some friction. While that feature is useful for seismic applications because it dissipates energy, it is counter-productive in the track bridge because it

might inhibit re-centering. The effectiveness of the re-centering feature is a primary consideration to be investigated experimentally.

1.5 Objectives

Because of the complexities of the CESURA system, the non-standard components that comprise its major elements, and the unknown interactions between these parts, extensive experimental research data is needed to validate and calibrate computer models which will be used to produce the final design. The objective of the research, presented subsequently, is to assess the validity and effectiveness of specific components of the system, investigate the effects of specific design choices on the behavior of the track bridge, identify construction issues, and develop and test instrumentation strategies to be used in the full scale prototype test.

Chapter 2 Experimental Setup

2.1 Overview

To generate experimental data to be used for model validation, a full-scale test of a part of the system was conducted. The specimen was constructed using design drawings provided by Parsons Brinckerhoff. The tested system consisted of one end of the CESURA system: four bearer bars, eight friction pendulum bearings and four sections of rail. The specimen was subjected to the component motions (pitch, roll, and yaw) and was tested under two separate loading regimes: a cyclic vertical LRV axle load, and a constant vertical LRV axle load with a cyclic horizontal LRV design wind load. The system was also tested in the neutral condition to determine the system's stiffness, which consisted of a constant vertical LRV axle load with a monotonically increasing horizontal force. The specimen was heavily instrumented to capture local stresses, both normal and shear, global displacements, and local rotations. Many of the instruments duplicated one another to assess the validity and effectiveness of specific instrumentation strategies.

The observed and measured responses of the system were then analyzed to develop insights and recommendations for the most efficient design of the system and the most effective instrumentation strategy.

2.2 Test Matrix

The test matrix was generated to address the following:

- System behavior under vertical loading
- System behavior under horizontal loading, specifically the re-centering capabilities of the system, including the effects of the friction pendulum bearings and the frame action from the bearer bar-rail interaction
- The influence of different wing orientations, corresponding to the component motions of the floating bridge, on the response of the system
- The transverse stiffness of the system
- The possible ratcheting effect if horizontal loading was cycled in only one direction.

The major variable in the geometric testing program was wing orientation. In the reference condition, the test loading was applied with the location of the pseudo-axle located first halfway between the second and third bearer bars and then directly over bearer bar 03. In all other geometric tests the pseudo-axle was always over the third bearer bar. Stiffness tests were conducted in both the neutral (flat) condition with all four rails attached, and in the reference (sloped) condition with only the running rails attached. In the yaw configuration, the horizontal load was applied cyclically about a zero force condition as well as cyclically about a mean positive and negative force (i.e. zero to positive max or zero to negative max).

Table 2-1: Experimental Test Matrix

Test	*Description*	*Axle Location*	*Slope (%)*	*Rotation (deg)*		*Yaw (in)*
				Left	Right	
Friction Tests						
FRK01	PTFE Friction test	BB04	0%	0	0	0
FRK02	PTFE Friction tests	BB04	4%	0	0	0
Stiffness Tests						
STF01	Horizontal stiffness tests	BB04	0%	0	0	0
STF02	No Guard rail test	BB04	4%	0	0	0
Geometric Tests						
REF01	Reference condition test	BB02-BB03	4%	0	0	0
REF02	Reference condition test	BB03	4%	0	0	0
PIT01	Pitch test (Sag Vertical Curve)	BB03	4%	-3	+3	0
PIT02	Pitch test (Crest Vertical Curve)	BB03	4%	+3	-3	0
ROL01	Roll Test	BB03	4%	+3	+3	0
REF03	Reference condition test	BB03	4%	0	0	0
YAW01	Yaw Test	BB03	4%	0	0	1

For an additional description of the testing procedure, the identification of the different wing configurations, and the method by which each geometric condition was achieved in the laboratory refer to Appendix C, which contains the final report submitted to Parsons Brinckerhoff.

For the friction and stiffness tests, the loading protocol consisted of manually adjusting the vertical force until the design LRV load was reached. In the stiffness and friction tests conducted in the neutral position, vertical loads were applied under displacement control. In the stiffness and friction tests conducted in the reference position, tests were conducted under load control.

The vertical forces on the specimen were determined by the MTS load cell output and the configuration of the loading system. The loading beam was statically determinate, so knowledge of the MTS load allowed the vertical force on the pseudo-axle to be computed using statics. Horizontal forces were applied to the specimen through a hydraulic center-hole ram connected to an electrically powered pump. Initially, small displacement pulses were applied to specimen to remove any residual static friction forces. Displacements were then applied to the specimen by manually controlling pump pressure, keeping the velocity of the specimen as constant as possible.

In the friction tests, the instantaneous friction coefficient was then computed from the constant vertical load and the applied horizontal load. In the stiffness tests, the displacement of the specimen was monitored at the point of application of the transverse force, and the transverse stiffness could be observed by tracking the load-displacement behavior of the system.

For each geometric configuration, two loading protocols were used. The vertical loading protocol consisted of sinusoidal cycles of vertical load, oscillating about a mean axle load of approximately 16 kips, and varying from approximately 4 kips to the maximum design LRV axle load of 28 kips at a frequency of 0.5 Hz. These tests were conducted under load control. In order to prevent uplift of the axle, the minimum load was maintained above zero vertical force. The lower value of these cycles varied from test to test because of the configuration of the testing apparatus. In configurations

where the vertical loading protocol was conducted after the horizontal loading protocol, cycles were continued until the transverse position of the bearer bars stabilized.

For the horizontal load, sinusoidal loading at a frequency of 0.5 Hz was applied to system through the pseudo-axle assembly. The horizontal cycles were conducted under either load or displacement control. For configurations where load control was used, the cycles were symmetric about the zero force condition. For configurations where displacement control was used, the cycles were symmetric about the zero displacement condition. In either case, the amplitude of the input signal was manually adjusted until the desired LRV design wind load of 3 kips was achieved. Friction forces inevitably existed in the testing apparatus, and their magnitude was established by special tests at the start of the program. In all subsequent tests, the load applied by the actuator was increased by the value of the previously-measured friction force so that the CESURA system experienced the full design load. In tests where load control was used, cycles were continued until the transverse position as read by the MTS LVDT had stabilized. In tests where displacement control was used at least 20 cycles were recorded.

In the yaw configuration, two additional horizontal loading protocols were used. Each consisted of a “one sided” time history. The vertical load was applied manually under force control up to an axle load of 28 kips. Haversine cycles of horizontal load were then applied to the specimen ranging from zero to the design horizontal load plus rig friction forces at a frequency of 0.5 Hz. The goal was to investigate whether the

displacement response would stabilize, or continue increasing without bound. The tests were conducted in both the MTS actuators tensile and compressive directions. These tests were conducted under force control.

2.3 Test Configuration

The test configuration was designed to act as a pin-ended cantilever in a horizontal plane, with transverse restraint provided by the geometry of the friction pendulum bearings and the frame action caused by the interaction between the rails and bearer bars. Care was taken to produce an experimental apparatus that was adjustable, in order to provide the most versatility should different testing regimes and wing geometries be required. The major components of the CESURA system were replicated at full scale, and were constructed to the prescribed tolerances. Stability and safety of the resulting system was of paramount concern given the unknown interactions and behavior of the proposed system.

The design of the testing apparatus and the construction of the specimen and testing apparatus are described in detail. Figure 2-1 shows an overview of the constructed apparatus.

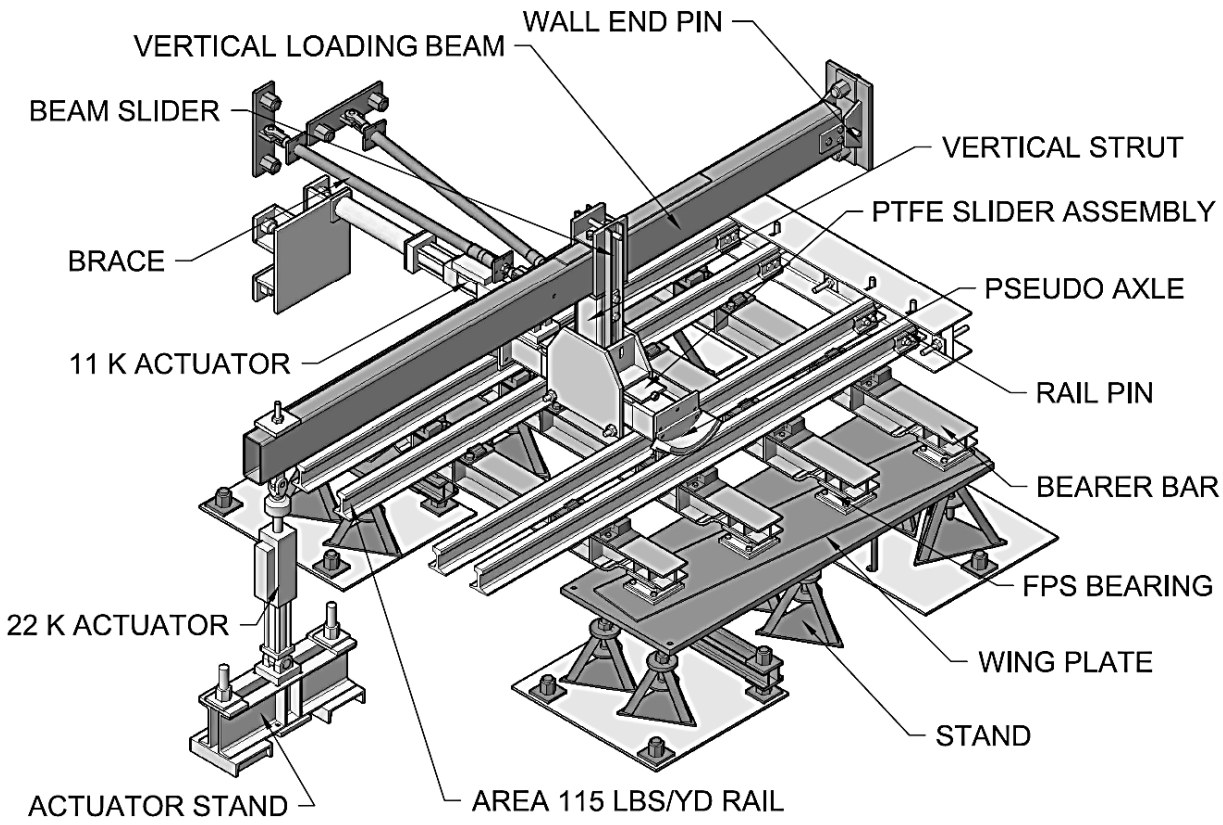

Figure 2-1: Orthographic View of Testing Apparatus

For additional descriptions of each of the components of the test specimen and test apparatus refer to Appendix C. For the dimensions and geometry of each of the fabricated components refer to Appendix B for detailed design drawings.

2.4 Test Apparatus Design

The test apparatus consisted of four major components; a vertical loading system, a wing plate assembly, a pseudo axle assembly, and a horizontal loading system.

2.4.1 Vertical loading system

The vertical loading system, shown in Figure 2-2, consisted of an HSS section spanning from the strong wall to the vertical MTS actuator, a wall pin that connected this HSS section to the strong wall, a sliding assembly that allowed for the longitudinal movement of the pseudo axle assembly and a wall brace.

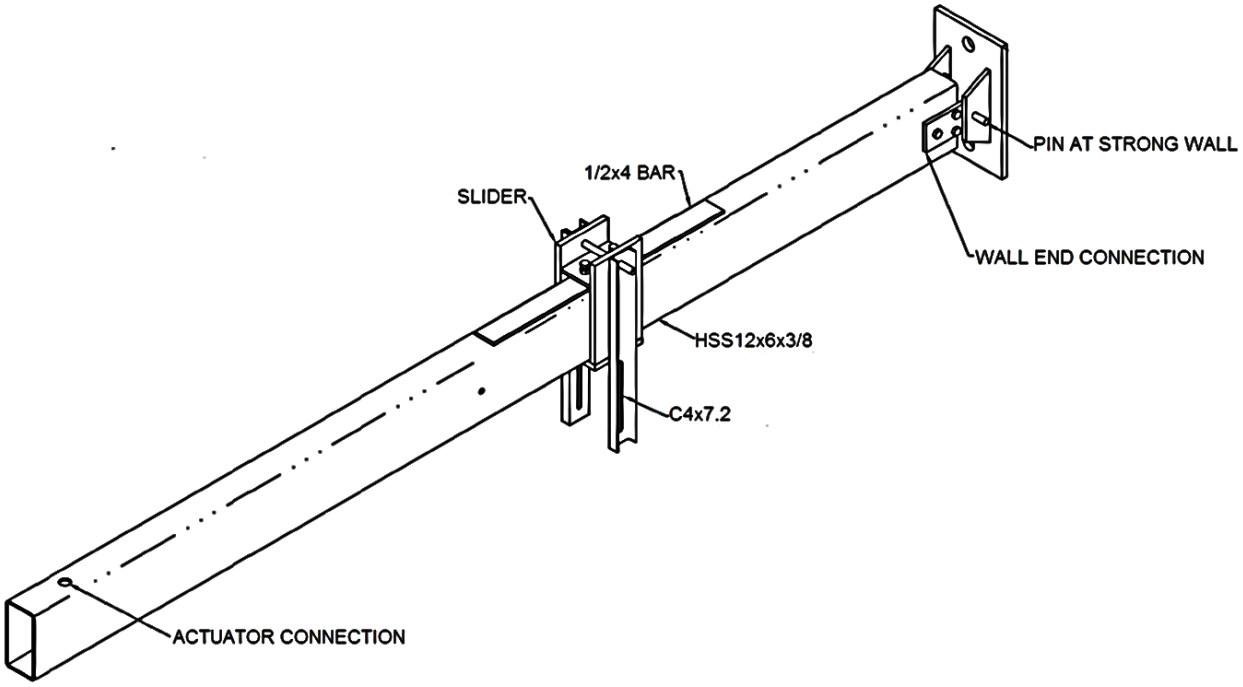

Figure 2-2: Orthographic view of vertical loading assembly.

The HSS section was selected to resist transverse torsional buckling caused by the torsional moment induced by friction in the pseudo-axle assembly. The beam acted as a lever in a vertical plane, allowing the full vertical axle load to be applied to the specimen with a 22 kip MTS servo controlled actuator. The section was designed to

carry the shear and moment induced by the actuator which acted in tension, and was braced against side sway between the third and fourth bearer bar.

The pin was attached to the strong wall by a bracket. It was designed to resist the largest expected shear force, which would occur when the pseudo axle assembly was halfway between the second and third bearer bars. The shear force was transferred to the wall by friction, and the bolts were designed to provide the frictional resistance.

The connection between the beam and the wall pin was designed so that on-site adjustment was possible during construction. This was advantageous in order to ensure the beam was loaded by the vertical actuator in its strong axis. One shear plate was welded to the end of the HSS section while the other was designed as a slip critical connection using three A490 bolts. This connection was designed for the worst case shear force as described previously.

The sliding assembly, shown in Figure 2-3, was designed to carry the full axle load from the HSS section to the vertical strut on the pseudo-axle assembly. The slider allowed the pseudo-axle to be moved from one location to another, allowing the versatility that was desired for each of the different test configurations. The slider was designed with clearance in the vertical and horizontal directions to allow it to slide freely on the HSS section. Once the slider was located at its appropriate position two set screws were used to raise the slider until its bottom surface was pressed against the bottom of the HSS beam. This prevented any unintentional movement of the slider as

load was applied. A plate of A36 steel was welded to the top of the loading beam between the second and third bearer bars to provide a more malleable material for these set screws to react against and to prevent the screws from damaging the HSS member.

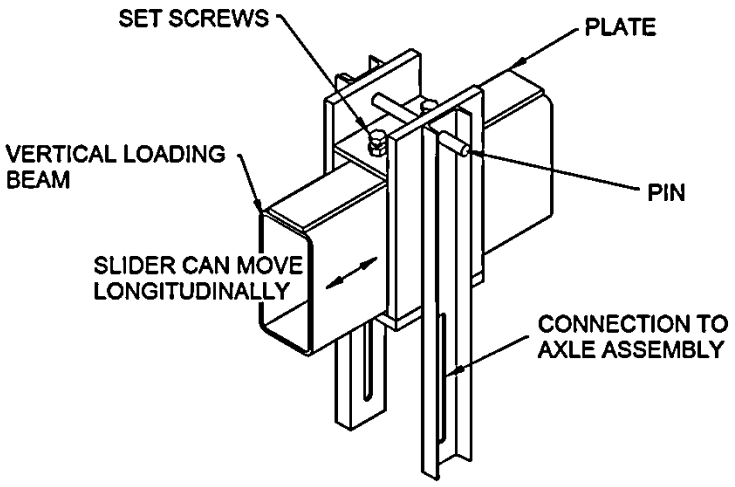

Figure 2-3: Orthographic view of slider assembly.

In order to provide a truly vertical force, the load from the slider to pseudo-axle assembly was transferred through a pin, set at the top of the slider. This allowed the pseudo axle assembly to hang freely under gravity once elevated above the rails. This pin was located at the top of the slider, above the centroid of the HSS section to avoid unintended torsional forces. In order to accommodate the elevation changes associated with moving the axle along the sloping rails, two slotted channels were used to transfer load from the slider pin to the vertical strut. These channels were designed to carry the vertical axle load, and prevent global buckling of the section.

The transverse wall brace was designed to carry 1 kip axial tension or compression. This corresponds to a friction coefficient in the pseudo-axle assembly of 3.5 %, which was twice the value that was estimated at the time of design. Because raising and lowering the beam produced a change in length and end slope of the brace, it was constructed from scaffolding props which provided the required adjustability and design strength. Rotation capacity was provided by attaching a clevis at each end.

2.4.2 Wing plate assembly

The wing plate assembly consisted of twelve stands, eight of which were affixed to the strong floor by plates anchored into hold downs by high strength rods. These stands supported two large wing plates that acted as surrogate box girders in the experimental regime. These wing plates were anchored into the strong floor by high strength rods at two locations to prevent uplift during testing. Figure 2-4 shows the stand arrangement and the axis of rotation of the specimen.

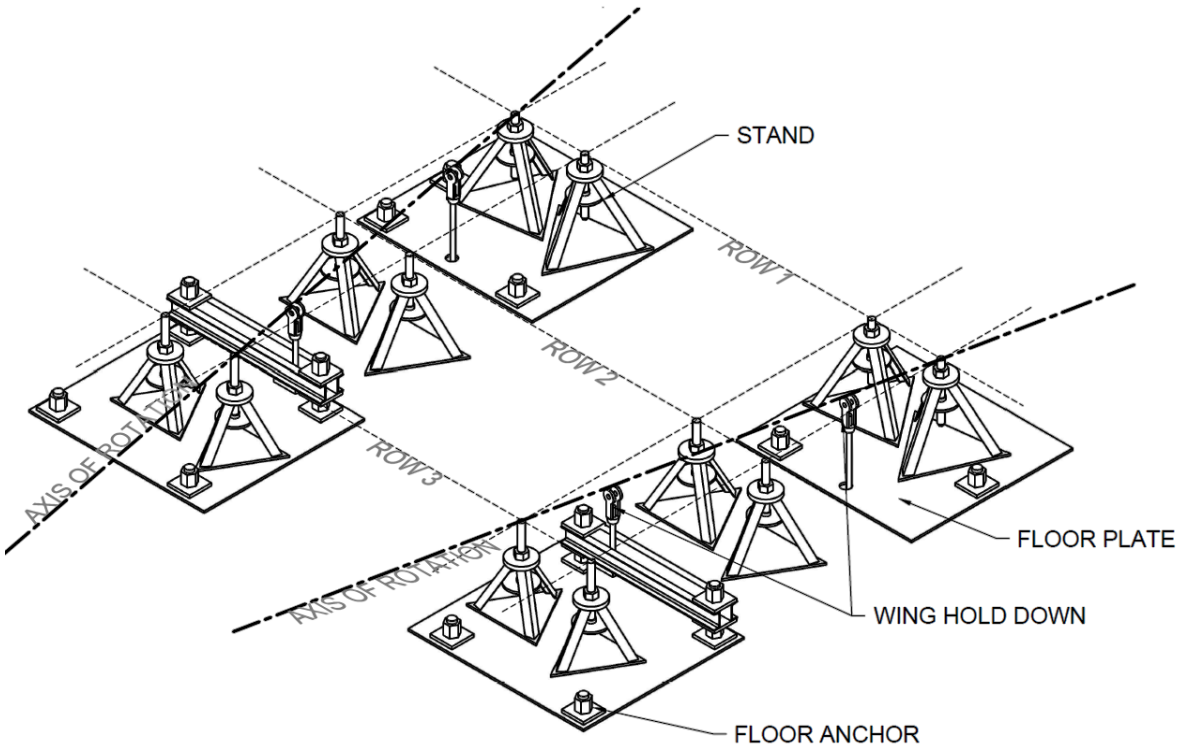

Figure 2-4: Orthographic view of stand configuration and old down system.

The stands were designed to be adjustable, so that the vertical height of each could be changed to produce the desired wing geometries. Each stand was designed to carry 20 kips of axial force and 1 kip of horizontal force. A 1.5 in diameter rod threaded through a nut on the top plate of the stand provided the adjustability and strength desired. The middle plate included a segment of pipe concentric with the threaded rod that prevented the rod from wobbling in the nut, effectively restraining translations of the wing. The stands were oriented in three longitudinal rows, each 48 inches apart. Because the apparatus was meant to be at a 4% longitudinal slope in its reference

condition the stands were designed at three different heights, one for each row, so that each stand had the same amount of adjustment about this reference state.

In the prototype, each wing rotates about an axis defined by the two stationary bearings on either the fixed or floating portion of the bridge. To replicate those rotations in the lab, the separation of the stands in the transverse direction was selected so that a diagonal from the first row to the third row coincided with the axis defined by these two bearings in the full-scale prototype.

Four stands under each wing were welded to floor plates, anchored to the strong floor via high strength rods. The center row was not affixed to the floor except through friction. Any shear and rotation of the wing was expected to be carried by the remaining two rows, which had the longest lever arm to prevent wing rotation about a vertical axis.

These stands supported the two wings, which were made from 1.5 in thick plate. They were used in place of the real welded box sections in the interests of simplicity and economy. They had recessed plates welded to their bottom surfaces to accept the stands' threaded rods and prevent the rods from sliding relative to the plate. The wing plate thickness was selected on the basis of deflections using simple one dimensional calculation.

Under each wing, two hold down plates were oriented so that holes passing through their centers were collinear with the imposed axis of rotation of the wing plate.

A hold down system, consisting of a clevis attached to a high strength rod, was connected to each of these projecting plates. In this fashion, the wing's orientation or rotation about the diagonal axis did not affect the location of the plate, and the clevis pin allowed the rotation to occur. The hold downs closest to the first row of stands coincided with an anchor location in the strong floor, and a turnbuckle was used to tighten the rod traversing from the clevis into the floor. The hold downs closest to the third row of stands did not coincide with an anchor location and two channels were installed across adjacent anchor locations to act as transfer beams. A plate washer and nut, located on the underside of these channels, allowed the hold downs to be tightened.

2.4.3 Pseudo-axle assembly

The pseudo-axle assembly is shown in Figure 2-5. The assembly consisted of four major components, and allowed the decoupling of the vertical and horizontal applied loads. If the pseudo-axle had been rigidly connected to the vertical loading system, the horizontal forces applied to the specimen would have been shared by both the rails and the vertical loading beam. Because this result was undesirable, a system was designed that allowed the pseudo-axle to translate transverse to the direction of the rails while still transmitting vertical load to the specimen.

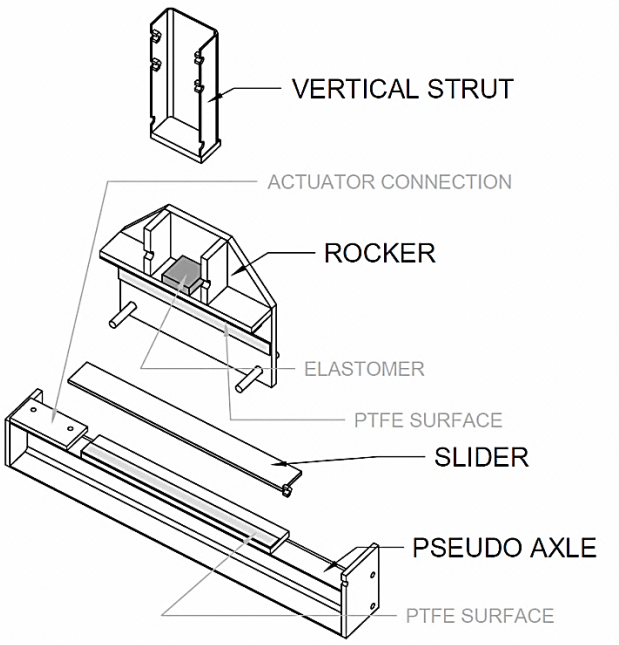

Figure 2-5: Exploded orthographic view of slider cross section.

The vertical strut was connected to the vertical loading assembly through a slip critical connection that consisted of four A490 bolts. The vertical strut transferred load from the vertical loading assembly to the rocker; the two were separated by an elastomeric bearing that distributed the load and allowed the pseudo axle to rock about a longitudinal axis.

The rocker's major purpose was to allow the pseudo-axle to be sloped transversely while the vertical strut remained purely vertical. This was particularly important for the roll test configuration that required two different wing centroid heights. In order to allow the pseudo-axle to translate transverse to the direction of the rails a sliding assembly was constructed that consisted of two polytetrafluoroethylene

(PTFE) surfaces, one on the underside of the rocker and one on the top of the pseudo-axle. Between these surfaces was a plate that had a stainless steel sheet welded to each side. While a simple PTFE surface would have provided the required sliding capacity, the benefit of such a configuration was that it allowed for the measurement of the friction coefficient between the paired surfaces. By welding a nut to one end of the slider, tests could be conducted, consisting of pulling the slider between the PTFE surfaces under a known vertical load.

The pseudo-axle transferred the vertical and horizontal forces to the specimen via the running rails. LRV wheel segments were welded on either end of the pseudo-axle to provide the correct wheel-rail contact surface to match the loading that the system would see in service. The wheel gage, measured from the back of the wheel flanges matched that of LRV's currently in service. Horizontal loads were applied to the pseudo-axle through a tapped plate welded to the top surface of the pseudo axle, the "actuator connection" in Figure 2-5. Although this vertical eccentricity induced a moment into the pseudo-axle, its affect was far outweighed by the forces caused by the vertical axle load.

Because friction forces were present, a brace was provided to the pseudo-axle assembly at the connection between the vertical loading assembly and the vertical strut. This brace was designed identically to the brace used for the vertical loading system. The scaffolding prop allowed for the adjustment necessary to accommodate different axle positions and provided the required axial strength. In the stiffness and friction

tests, in which load was applied in only one direction, an additional tension-only brace was provided to the rocker assembly to prevent transverse movements. This brace consisted of a 3.5 ton come-along anchored to the strong wall.

2.4.4 Horizontal Loading Assembly

In both the friction and stiffness tests, horizontal force was applied at the fourth bearer bar, the furthest from the wall. A separate system was designed, shown in Figure 2-6, in order to apply force to the system at this location. The horizontal loading assembly consisted of a vertical post welded to one of the wing plate assembly's floor plates, two floor anchors, and two tieback assemblies tightened by turnbuckles. The hydraulic ram provided horizontal force through a high strength rod attached to the pseudo axle. The ram reacted against the vertical post; loads were measured by a center-hole load cell situated between the reaction post and the ram. The reaction post was designed as a vertically oriented cantilever, with initial forces applied by the tieback assemblies for a maximum load of 12 kips.

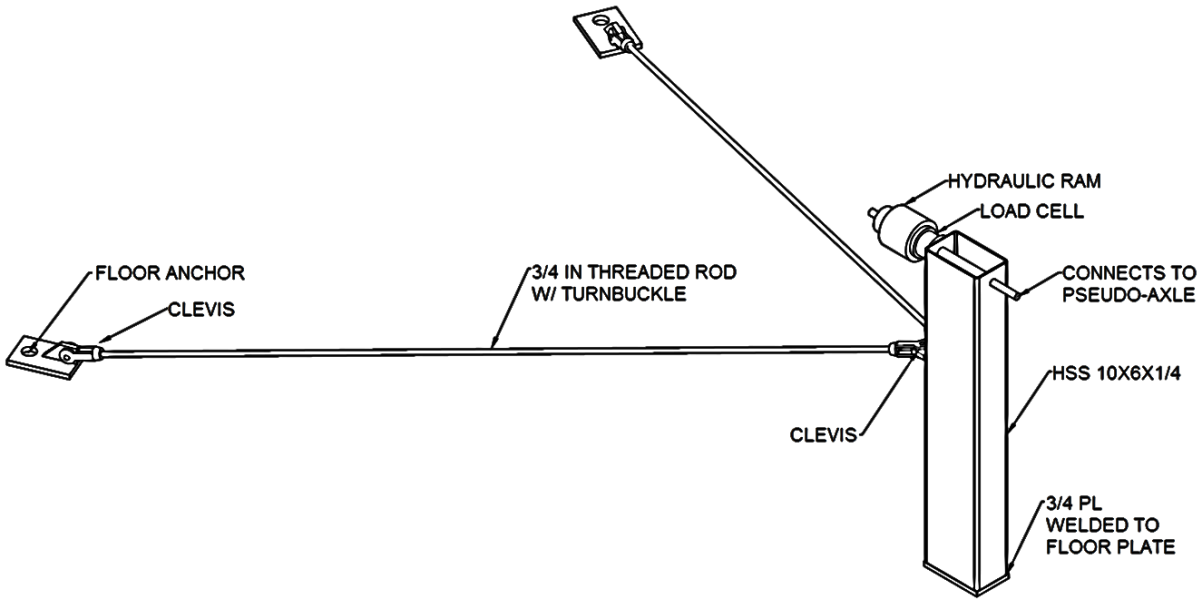

Figure 2-6: Orthographic schematic view of the horizontal loading assembly.

2.5 Test Specimen

The test specimen was based on the 65% design drawings, provided by Parsons Brinckerhoff. Although aspects of the design have been altered since this point, many conclusions about the basic behavior of the system and effectiveness of its components can still be made. Components of the specimen were constructed by Jesse Engineering in Tacoma, Washington who will fabricate the CESURA prototype. This allowed for an accurate appraisal of any issues arising from the specific fabrication and construction practices that will be used during construction.

The test specimen, shown in Figure 2-7, consisted of eight friction pendulum bearings, four bearer bars, and four short segments of rail. Both sets of rails were

fastened to the bearer bars using standard rail clips. The running rails were connected to the bearer bars through Amstead RPS Direct Fixation Fasteners, which were selected for the design because of their acoustic isolation properties, which are provided by the "sandwich" design, in which a layer of elastomer is bonded between the upper and lower steel plates of the fastener. The guard rails were attached to the bearer bars through Pandrol weld-on shoulders affixed to loose plates that were bolted through slip critical connections to the bearer bars.

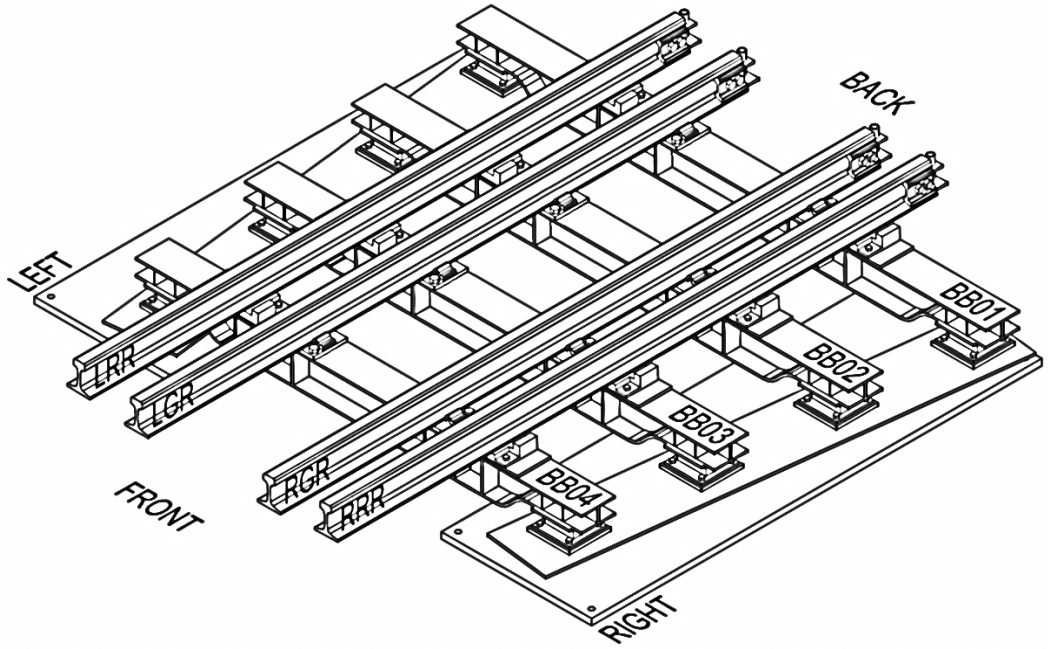

Figure 2-7: Orthographic schematic view of the specimen including element labels.

2.5.1 Friction pendulum bearings

The friction pendulum bearings used, shown in Figure 2-8, were specialized components designed for this particular application. These bearings are most commonly used for seismic isolation, but were selected for use here because they allow for a large amount of rotation and displacement in the transverse direction with respect to the rails, while preventing excessive rotation and displacement in the longitudinal direction of the rails. They accommodate these movements through rigid body sliding of the three components over one another, which causes the horizontal displacement, the vertical displacement and the rotation to be linked.

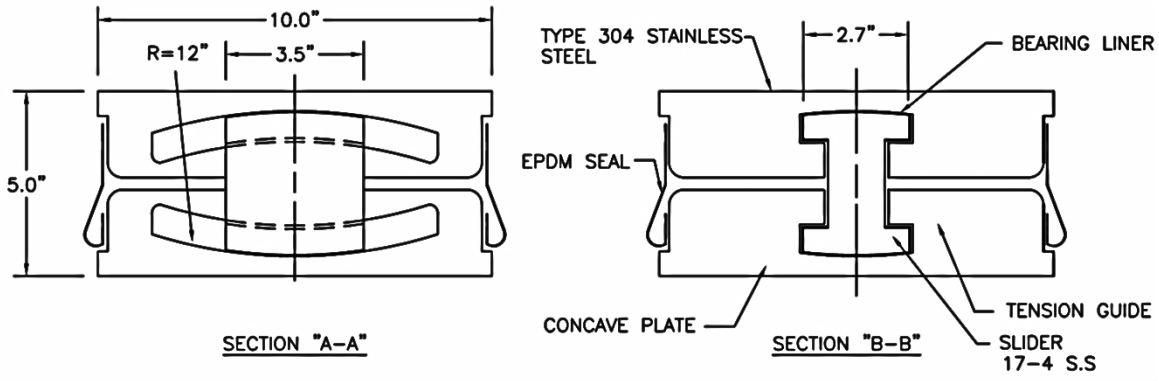

Figure 2-8: Front and side views of the friction pendulum bearing design.

These double friction pendulum bearings also possess a small rotation capacity about their vertical axis to allow for the yaw movement of the track bridge, and they prevent bearer bar uplift by the utilization of the “dogbone” shaped inner slider. The

uplift prevention feature is not normally used for seismic isolation and was developed specially for the bearings of this project.

The bearings are rated for an ultimate vertical load capacity of 50 kips in tension or compression, allow 3 inches of movement in the rail's transverse direction, 0.15 inches of displacement in the rail's longitudinal direction, 4 degrees of rotation about the rails' longitudinal axis, 0.5 degrees of rotation about the bearer bars' longitudinal axis, and 5 degrees of rotation about a vertical axis.

2.5.2 Bearer bars

The CESURA system's bearer bars take the place of standard ties on regular track work and are illustrated in Figure 2-9. The guard rail fasteners pictured are different than those used in the experiment because this detail was changed during the course of the experimental project. Each bearer bar consisted of a W8x31 section that was modified by coping at each end to accept a bent plate, welded to the section's web and bottom flange using complete penetration welds. By reducing the depth of the bearer bar at either end, the vertical height of the system could be reduced, making the concrete plinths used to approach the CESURA system more cost effective.

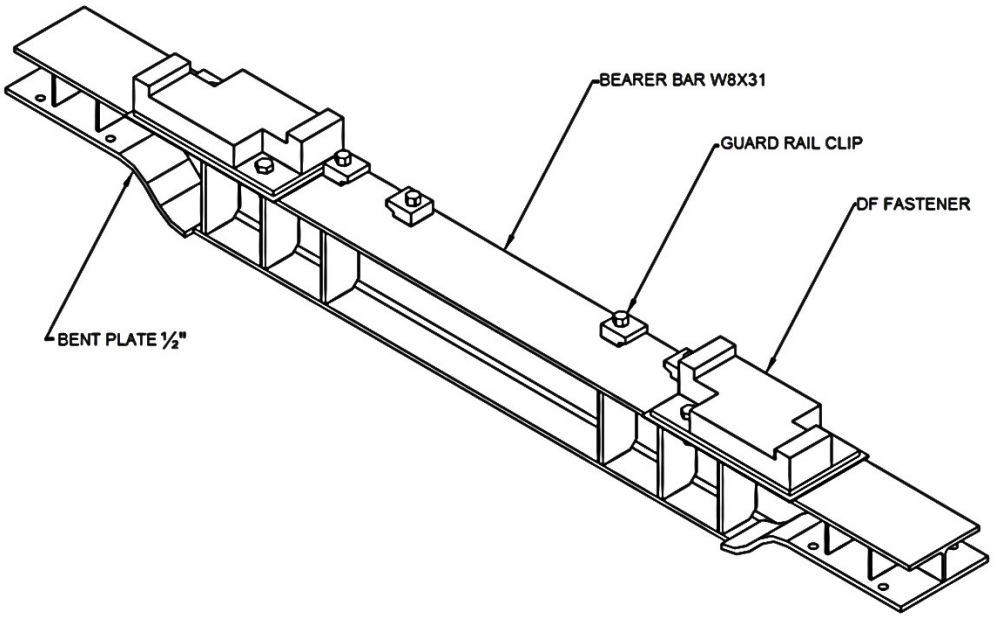

Figure 2-9: Orthographic schematic view of a typical bearer bar.

2.5.3 Rails

The rails used were standard A.R.E.A. 115 lbs/ yd rail segments, each 10 feet in length. At one end of the rails, a pin was constructed to allow each rail to rotate about its weak axis, as shown in Figure 2-10. Pins were located at the assumed point of lateral inflection of the rails, to simulate the restraint of the concrete plinths at the end of the track bridge structure. These pins consisted of a pipe welded to two standard joint bar segments, connected intermediately by two plate collars located at the joint bar's top and bottom flanges. This pipe was free to rotate about a threaded rod, oriented along the rails weak axis. Because the running rails had a 1:40 cant, the threaded rod was oriented at 0.025 radians to the vertical.

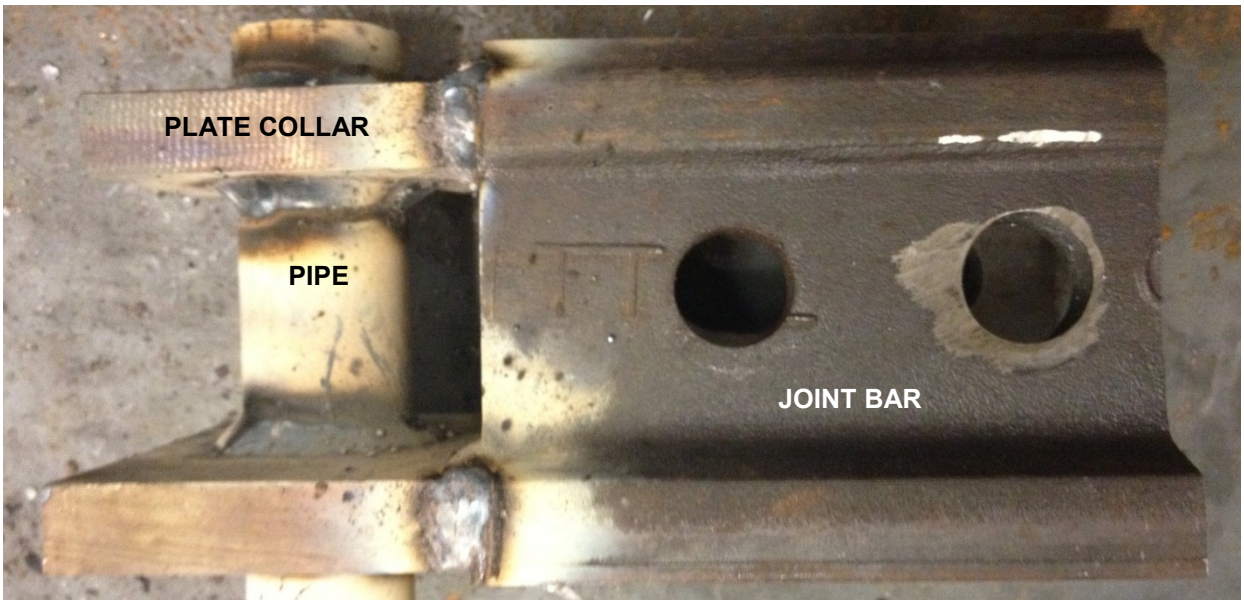

Figure 2-10: Photograph of the constructed rail end pin.

The free ends of the rails, opposite the rail end pins, were connected rigidly by a gage bar: a threaded rod that ran transversely between the rails. This rod's primary purpose was to ensure that gage, the transverse spacing of the rails, was maintained throughout the loading protocol, forcing the rails to remain parallel.

2.5.4 Rail clips

The rails were connected to the bearer bars through two types of rail clips, illustrated in Figure 2-11. The running rails, on which the LRV rides, were connected through elastomeric Direct Fixation (DF) fasteners provided by Amstead RPS. The DF fasteners consist of two steel cradles oriented like nested "U's" and separated by a layer of elastomer. This design allows for acoustic and electrical isolation between the track

work and the box girders. The rails were attached to the DF fasteners through “omega” clips, so named because of their shape. These torsional springs provide hold down forces through the turn of a bolt, tightened by torque wrench to the value specified by the manufacturer.

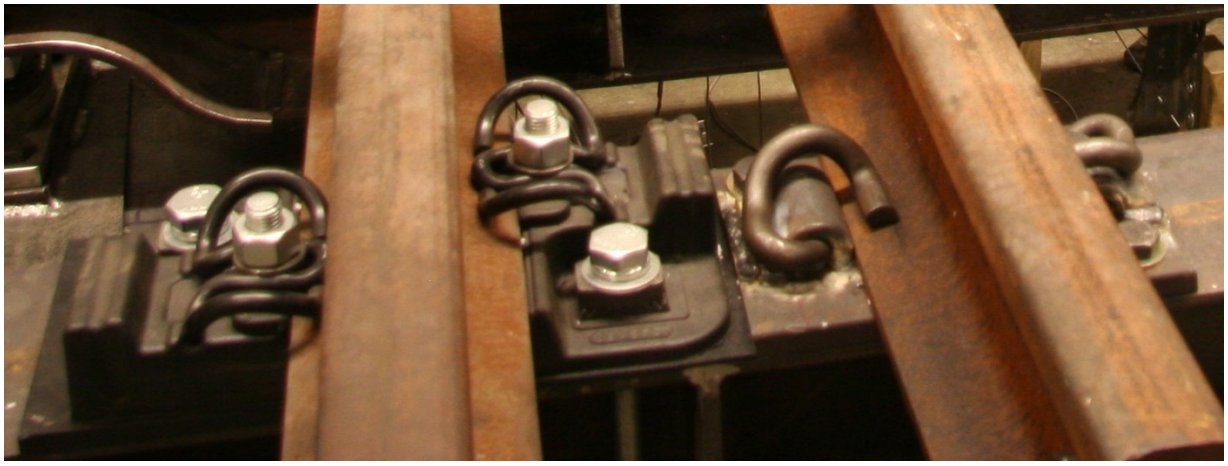

Figure 2-11: Photograph of the two rail fasteners used (*LEFT: DF fastener RIGHT: Weld on shoulder and “e” clip).*

Although bolted fasteners were specified on the design drawings, an alternative fastener was selected that was deemed to provide similar hold down characteristics, due to the difficulty in obtaining rail fasteners in small quantities. The guard rails were connected with Pandrol e-clips driven into weld-on shoulders that were welded onto loose plates. Each plate was then bolted to the flange of the bearer bars through slip critical connections using two 3/ 4 inch, A490 bolts. These clips also act as torsional springs; they are compressed by driving the stem of the spring through the question-mark shaped shoulders. The vertical pre-compression that they provide to the rail

depends on the accuracy with which the shoulder is welded down. If the shoulder lifts at all during welding, the torsional displacement of the clip, and hence its hold-down force, are reduced.

2.6 Specimen Construction

The test specimen was constructed following the completion and leveling of the wing plate assembly. First the friction pendulum bearings were located on the wing plates, using their relative positions to ensure the proper yoke geometry. Care was taken to place the bearings at identical locations on each wing plate in order to achieve matching vertical displacements in each of the pitch geometries. This was achieved by using a loose plate under each set of four bearings, to which the drilled and tapped bearing plates were welded after careful pre-positioning.

Bearer bars were then bolted to the bearings, maintaining the 29 inch spacing as specified in the design drawings. Rail fasteners were located on the bearer bars, and rails were seated into their fasteners. The rail end pins and gage bar were then installed, ensuring that the rails were in the proper longitudinal and transverse location and were at standard gage. With the DF fasteners and weld on shoulder plates loosely bolted to the bearer bars, the rail clips were tightened. Bolts between fasteners and bearer bars were then removed, shims were installed to ensure even bearing between the bearer bars, and fastener bolts were replaced and tightened to their minimum pretensions.

2.7 Construction issues

Constructing the specimen to the desired tolerances posed several problems. Although the fabricated components were within normal construction tolerances for steel components, the nature of the CESURA system made it extremely sensitive to small deviations from the specified dimensions. Issues that were encountered included the precise placement of the friction pendulum bearings on the wings surface, misfit between the bearer bars and the friction pendulum bearings, skew and slant of the welded bent plate at the ends of the bearer bars, bearer bar end section depth, achieving the correct wheel contact geometry with the supplied rail fasteners, and the guard rail clip alternative used. Many of these issues have already been addressed in the prototype design, but are worth discussing briefly.

2.7.1 Locating friction pendulum bearings

Several attempts were made to locate the friction pendulum bearings in the proper location. Initially, the bearings were attached to the bearer bars and the bearer bars were moved until their centerlines lay at the specified spacing. As will be described later, tolerances in the bearer bars prevented this process from being successful; the bearings' relative positions and rotations were incorrect and could not be rectified without detaching the bearings from the bearer bars.

This process was further complicated by the requirement that bearings be located in identical positions on the two wing plates. This is necessary to ensure that, as the

wings are positioned to new geometries, the ends of the bearer bars undergo the same elevation changes.

Subsequent attempts involved locating the first set of bearings by their longitudinal distance from a reference line and their transverse separation from each other. Each other bearing was located in turn from the one before it, using the relative distances required to produce the correct yoke geometry. Small measurement errors were compounded throughout this process and the variations between paired bearing's locations on the wings surface were unacceptable.

The solution was to make use of an additional plate on the wing, which also helped to easily achieve the yaw configuration. Bearings could be located relative to one another to reach the proper yoke geometry on the long plates on top of the wing plate's surface. Then the two loose plates could be adjusted to ensure that paired bearings were at identical locations on the wings surface.

For the prototype installation, it is recommended that, in place of the loose plate detail used in the test setup, a locating pin or recess be built into the center of the bottom surface of the bearing and a mating recess or pin located on the wing surface using a laser system. By locating the bearing center coordinates precisely in the machine shop before bearing installation, only the rotation about a vertical axis would remain to be aligned in the field, and that could be achieved through comparison with the paired bearing position on the opposing wing plate.

2.7.2 Bearer bar tolerances

The reduced section at the end of each bearer bar presented several construction challenges and produced an undesirable construction sequence. When the bearer bars were first placed onto the top of the friction pendulum bearings, a considerable gap was observed between the inner edge of the bearing and the bearer bar's bottom surface, as shown in Figure 2-12. Because of the large displacement capacity of the friction pendulum bearings and the desire for the wings' reference (flat) state to correspond to the bearing's neutral position, it was desirable to keep the shipping plates attached to the bearings until after the remainder of the system was constructed. The shipping plates connect the top and bottom surfaces of the bearing and prevent their relative translation. For the prototype installation, this allows the system to be built in a fabrication facility and shipped to the site in one piece.

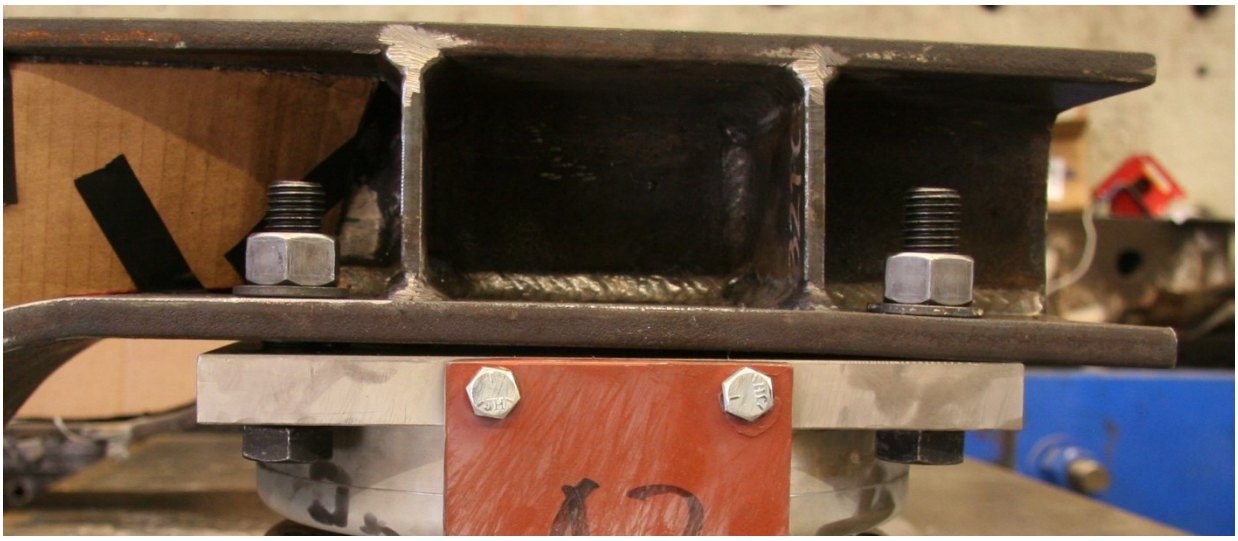

Figure 2-12: Bearer bar/bearing initial misfit *(NOTE: FPS bearing shipping plates are still attached)*.

To remedy this issue, the shipping plates were removed, and the gap was taken up by the rotation capacity of the bearing. This solution was undesirable, however, because it allowed the bearing to move freely in its remaining five degrees of freedom in addition to one that was desired. Those free movements made alignment difficult.

Additional problems were encountered with the reduced section of the bearer bar due to normal fabrication tolerances. Figure 2-13 shows the offset of the bent plate after the welding process. The holes that were meant for bolting the bearings top surface to the bearer bars were drilled into the plate before it was bent and subsequently welded to the wide flange section.

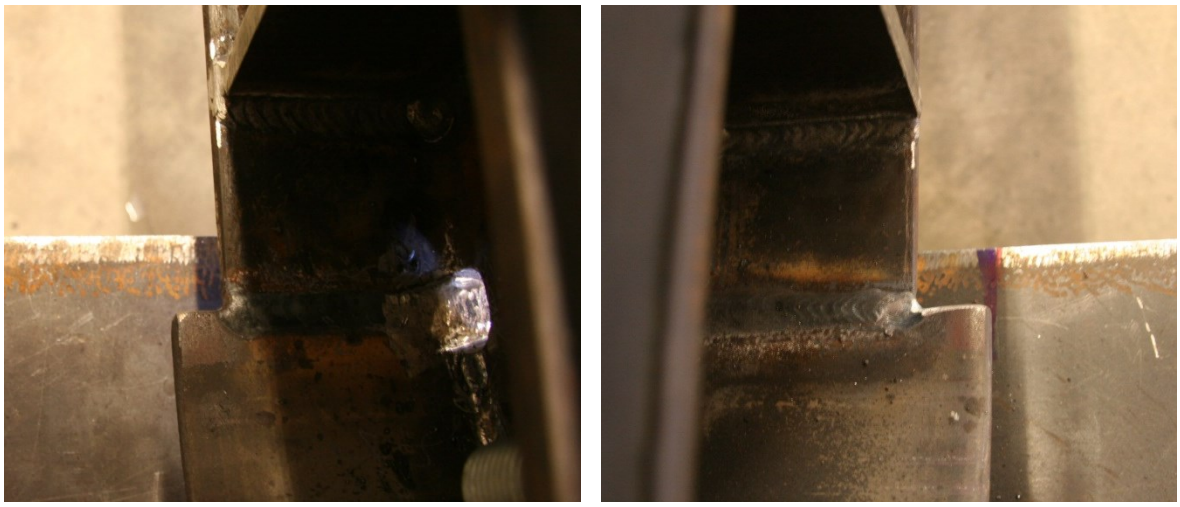

Figure 2-13: Bearer bar 01 bent plate offset *(NOTE: the difference in protruding length is 1/8th inch).*

This caused the hole pattern to be slightly offset in both the longitudinal and transverse directions of the bearer bar, and rotated about a vertical axis. The worst local longitudinal offset was 1/ 8th of an inch. The worst rotation occurred on bearer bar 04,

with a skew angle of one degree. The addition of these offsets to the original hole location tolerances on the flat plate made it impossible to locate the bearings to the specified tolerances and simultaneously attach the bearer bars to the bearings. This issue was remediated by reaming the holes in the bearer bars an additional 1/ 16th of an inch and changing the connection to be slip critical. By minimizing the maximum errors in a necessarily iterative process, the required tolerances were eventually achieved. These difficulties caused the process of erecting and connecting the specimen to take a total of ten days.

It is recommended for the prototype installation that the bent plates be fabricated thicker than specified so that they can be milled prior to final installation. In this manner the bearer bars will fit the bearings precisely and the bearing shipping plates can remain on the bearings until the system in installed on site. In addition, it is recommended that the holes in the bearer bars be drilled after the welding process is completed, so that the hole patterns can be located relative to the wide flange centerline rather than that of the bent plate.

2.7.3 Shimming procedure

Shimming of the rail fasteners is desirable, in order to prevent lack-of-fit stresses on the rails. This procedure was performed after the fasteners were connected to the rails, and before they were fully tightened to the bearer bars, while the specimen was in the level or flat condition. The fasteners were previously located on the bearer bars and

snug tightened to ensure their proper location on the rails. Shims of various thicknesses were manufactured, ranging from $1/8^{th}$ to $1/64^{th}$ of an inch, matching the plan dimensions of the rail fasteners. With the rails resting on the bearer bars shims were slid under the fasteners until no further shimming was possible. This process was performed iteratively until the rails rested level on the bearer bars. While this procedure was rather straightforward in the experimental specimen, consisting of four bearer bars, it will be necessarily more difficult when constructing the prototype.

For the prototype installation, it is recommended that the shimming procedure be conducted in a controlled environment, where the system can remain level and stationary throughout the shimming process. It may also prove to be advantageous to manufacture shims of varying thicknesses as was necessary in the test specimen.

2.7.4 Achieving the correct wheel contact geometry

Challenges were also faced when installing the pseudo-axle onto the specimen. Figure 2-14 shows the original and corrected wheel-rail contact profile.

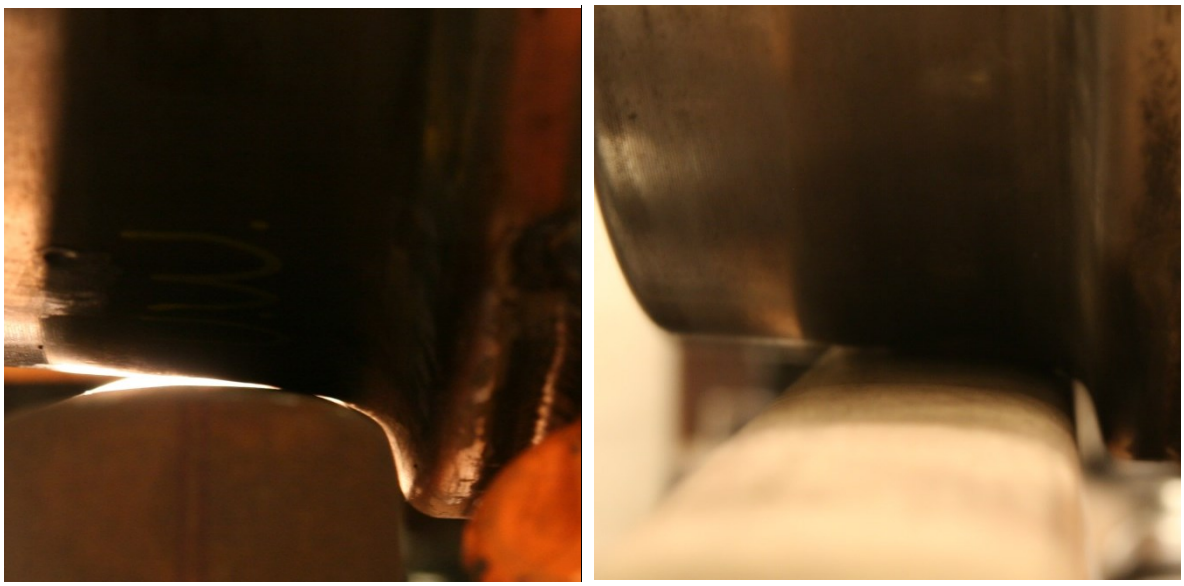

Figure 2-14: Wheel contact profiles (*LEFT: Original RIGHT: Corrected)*.

It was observed during the original installation that the wheel rested on a single point of the rail surface, whereas the contact profile that was desired mated the two surfaces over a much larger area. It was discovered that the provided rail fasteners that were on loan from a project in Buffalo, New York lacked the cant, or inwards slope of the rail, that is standard in Washington for LRT applications and necessary to match the wheel geometry. Achieving the correct contact profile was important because it affects how the forces are distributed to the rails and the global stability of the axle.

In order to produce the correct wheel contact geometry, high density polyethylene (HDPE) tapered shims were manufactured to be placed under the rail fasteners. This added an additional polymeric layer to the connection between rail and bearer bar, and provided an additional friction plane at which slip might occur. The

additional flexibility was deemed to be acceptable given that the specified fasteners were more flexible than those provided, and the displacement of the fastener was monitored during the transverse stiffness experiments to determine whether these shims allowed the fasteners to translate.

2.8 Instrumentation

2.8.1 Objectives

The objectives of the instrumentation system were to understand the behavior and effectiveness of the specific component members, identify the response of the system in global parameters, and ensure that the testing apparatus performed as intended. The specimen was extensively instrumented in order to achieve these objectives. Because of the lack of an experimental precedent, instrumentation locations were selected based on preliminary finite element modeling (performed by SC Solutions) as well as engineering judgment. The primary aim of this instrumentation strategy was to identify areas of interest that would be most applicable for the full scale prototype testing to be conducted by TTCI in Pueblo, Colorado in the Summer of 2013.

2.8.2 Specimen orientation and terminology

The specimen, shown in Figure 2-15, was essentially symmetric about the longitudinal (or "x") axis of the structure, and this symmetry was leveraged in the instrumentation strategy. This same strategy is recommended for the full scale prototype testing and the merits of this plan were investigated to assess whether or not

it would be appropriate for this test. By placing a large number of instruments on one side of the specimen (with some duplication on the opposite side), more information could be gathered with the same data acquisition resources. In the instrumentation manifest and elsewhere, the terms right, left, front, and back will be used informally to refer to one end of the specimen or a specific component.

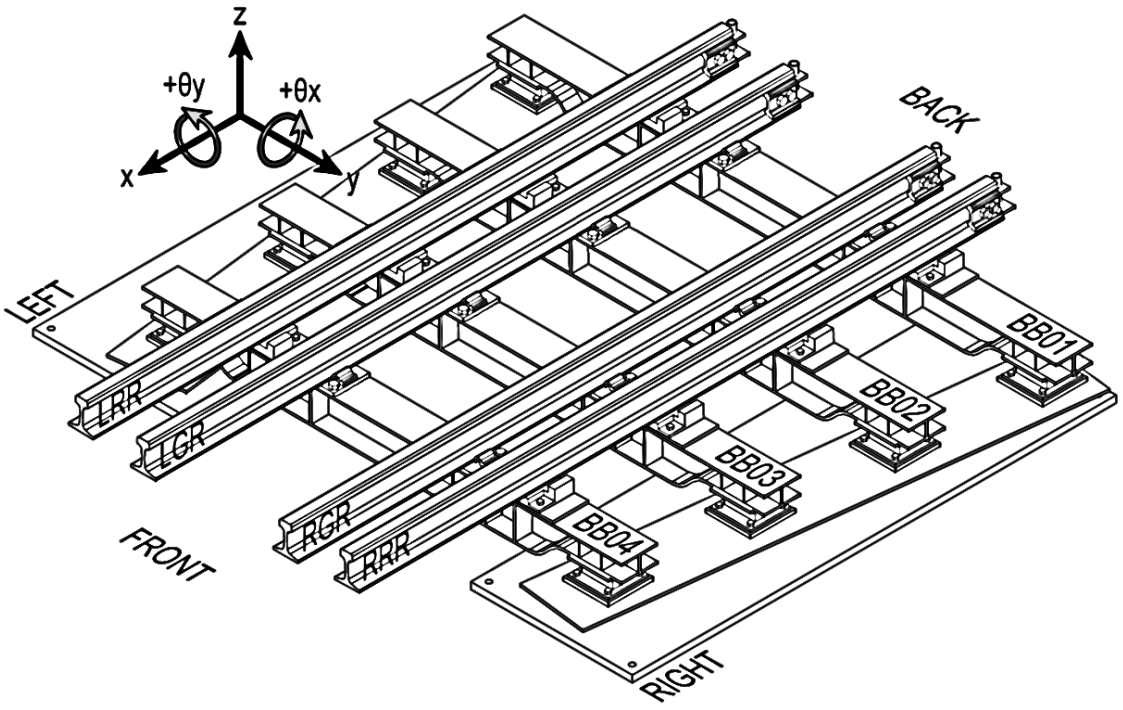

Figure 2-15: Specimen schematic view with defined coordinate axis

2.8.3 Instrumentation Identification Numbers

A rational instrument ID system was developed in order to locate specific gages within the specimen. The system that was used consists of an identifier to describe the

type of instrument, an identifier to describe the component on which the instrument is affixed and, following a dash, an identifier that describes the instrument location on the specific component and the direction of the measured quantity if applicable.

The instrument identifiers may be any of the following, noting that displacement measurements were not given an identifier of this type:

INC	inclinometer, measuring rotations
SL	linear strain gage, measuring strain along the longitudinal axis of the specific component
SR	strain gage rosette, measuring the strain state at a specific location

The component identifiers may be any of the following:

BB01 - BB04	Bearer bars, numbered in increasing order in the positive x-direction from the longest bearer bar which is located closest to the rail end pin (BB01) to the shortest bearer bar which is furthest from the rail end pin (BB04).
RRR & LRR	Right and Left running rails, the rails located the furthest from the systems centerline in the positive and negative y-directions (right and left) respectively. These rails transfer the load from the pseudo-axle to the bearer bars.
RGR & LGR	Right and Left guard rails, the rails located the closest to the centerline of the system, in the positive and negative y-directions (right and left) respectively. These rails are meant to guide the LRV vehicle in case of derailment and are not directly loaded by the pseudo-axle.
RWING & LWING	Right and left wing plates (right and left corresponding to the positive and negative y-direction)
RCKR	Rocker assembly which transferred vertical forces from the vertical loading beam to the pseudo-axle.
BEAM	Overhead, vertical loading beam that was used as a lever to apply vertical loads to the specimen.

For the rails three specific longitudinal locations between bearer bar 02 and bearer bar 03 were selected to place strain instruments. The indicators RRR, LRR, RGR, and LGR will be followed directly by a number to indicate this location.

01	six inches from the centerline of bearer bar 02 (the second bearer bar from the wall).
02	halfway between the centerlines of bearer bar 02 and bearer bar 03.
03	six inches from the centerline of bearer bar 03 (the third bearer bar from the wall).

The number following the dash indicates the location of the specific components. These locations can be identified in Figure 2-16 through Figure 2-22 and are described in the instrumentation manifest in Section 2.14.

2.9 Rotation

Rotations were monitored primarily by inclinometers. In a few cases they were also computed from pairs of potentiometers, spaced some distance apart. For a comparison of specifications of the inclinometers that were used see Section 2.13.2. Inclinometer locations are given in Figure 2-16.

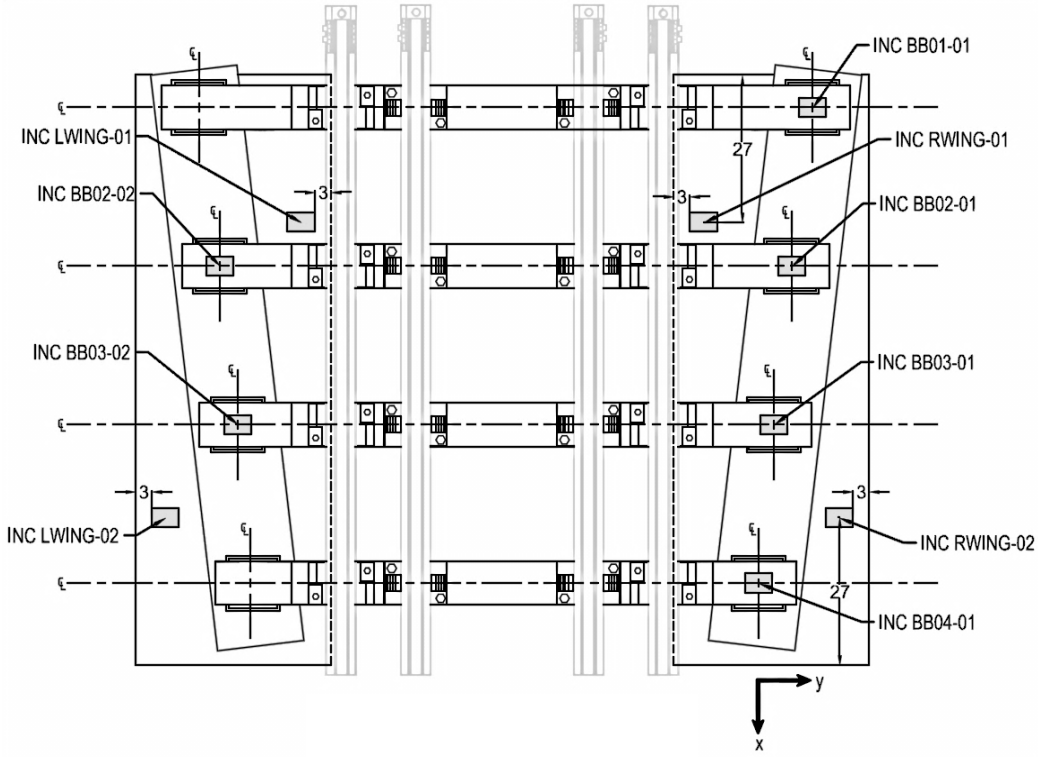

Figure 2-16: Inclinometer locations and designations

2.9.1 Bearer bar end rotation

Bearer bar end rotations were monitored by inclinometers on the right side of each bearer bar on the top flange above the center of the bearings top plate. Instruments

were duplicated on the left side of bearer bar 02 and bearer bar 03, because higher vertical forces and therefore larger end rotations were expected at these locations. Each instrument was capable of reading rotations in both the x and y-directions.

2.9.2 Wing rotation

Rotation of the wing plates was monitored in two separate locations. These instruments were mainly used as precision leveling instruments, used to adjust the wings into their different geometric configurations. They were also used to assess the deflection characteristics of the wing plate under vertical loads. These rotations were assumed to be small.

2.10 Displacement

2.10.1 Bearer bar displacement

Potentiometer locations measuring bearer bar displacements are given in Figure 2-17. Bearer bar transverse displacements (y-direction) were monitored on the right side of each bearer bar above the bent plate on the beams web. Vertical deflections (z-direction) were monitored at the center of the bottom flange of the bearer bars at mid span and also in three separate locations on the underside of bearer bar 02 and bearer bar 03 near the right friction pendulum bearing. These potentiometers were meant to capture the end rotations of the bearer bar, duplicating the inclinometer readings at this location. It was hoped that these potentiometers would also be able to be used to

determine the vertical change in bearing height caused by the coupling of its displacement and rotation.

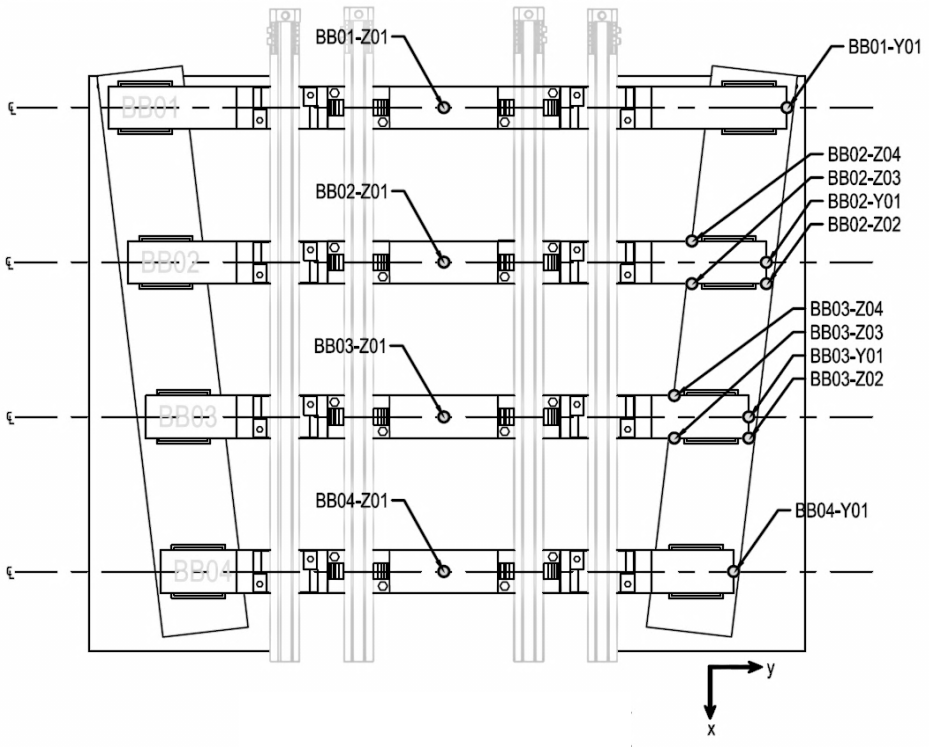

Figure 2-17: Specimen potentiometer locations and designations

2.10.2 Test apparatus displacement

Throughout the testing program, displacements of components of the testing apparatus were monitored in order to ensure acceptable levels of performance. In every test, wing longitudinal and transverse displacements were recorded at the front right and front left corner of the wing plates for the right and left wings respectively. Transverse displacements of the vertical loading beam and rocker assembly were also

monitored to assess the stability and safety of the apparatus. In the neutral (flat) stiffness tests, movement of the rail fasteners, rail end pins, and the vertical strut's slip critical connection were monitored. In the yaw configuration vertical displacements of the wing plates between the middle supports were recorded.

2.11 Stress

2.11.1 Shear stress in bearer bar transition region

Shear stresses were measured in the right transition region of each bearer bar. Figure 2-18 and Figure 2-19 detail the location of gages on the right side of bearer bar 03. Note that gage locations 01-04 are repeated on the remaining three bearer bars.

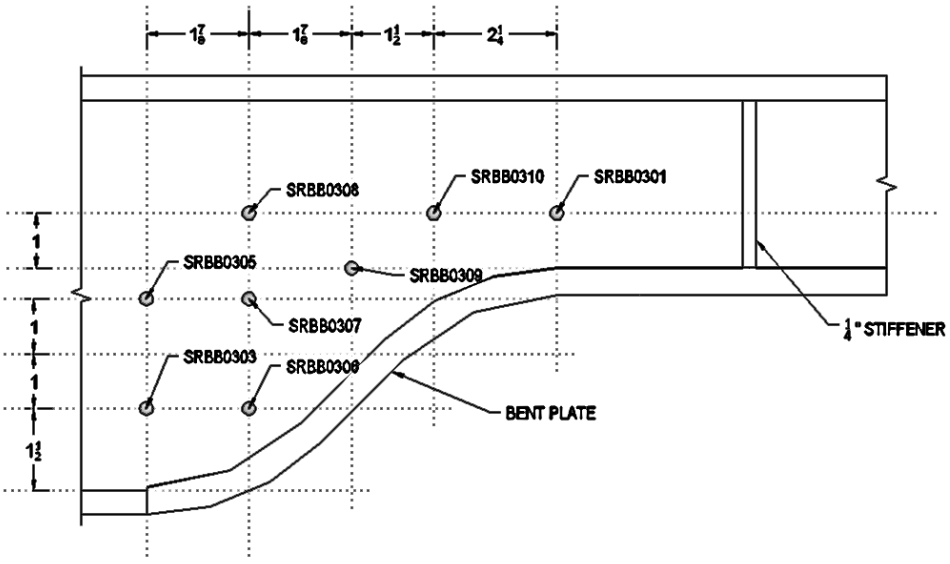

Figure 2-18: Strain rosette locations and designations on the front side of bearer bar 03.

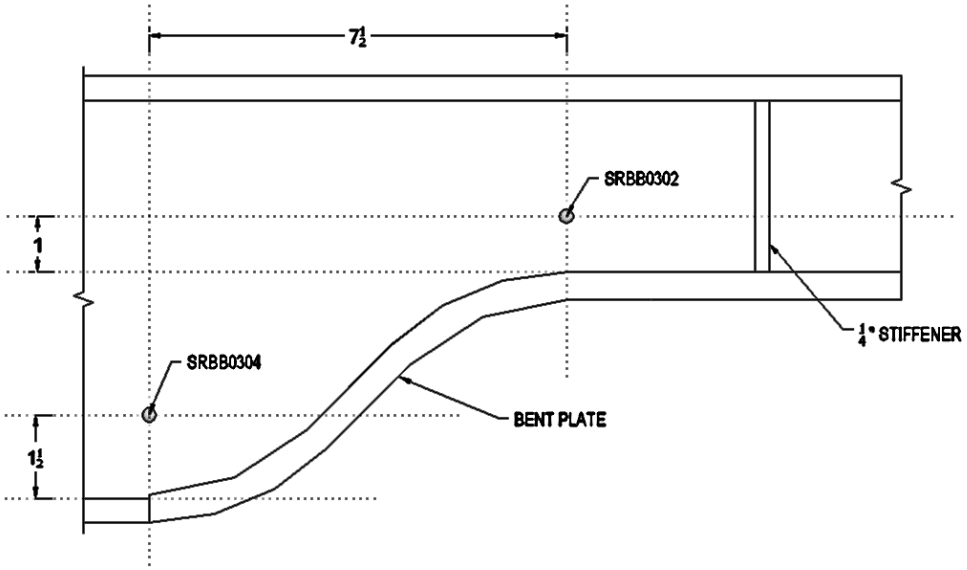

Figure 2-19: Strain rosette locations and designations on the back side of bearer bar 03.

Strain gage rosettes were used to capture the strain state in two locations that were deemed of particular interest because of the stress path through this region. Gages were placed on either side of bearer bar's web to investigate any stresses induced by torsional effects. Data acquisition resources were focused on the transition region of bearer bar 03 which was to be the most heavily loaded and which was therefore more heavily instrumented. The intent was to investigate the strain field in this region, to better understand the effects of the reduced section on local stresses, and to try to pinpoint regions of high stress that would be appropriate instrument locations for the prototype test. Unfortunately data acquisition resources and instrument malfunction did not allow readings to be taken from every strain instrument in every test configuration.

2.11.2 Bearer bar bending stress

Bearer bar bending stress was monitored at seven locations on bearer bar 02 and bearer bar 03 and five locations on bearer bar 01 and bearer bar 04. Figure 2-20 details the exact location of the gages in this region for Bearer bar 03. Note that the bearer bar is upside down in the figure and that the configuration of the gages was identical on each bearer bar with the caveat that gages 06-07 did not appear on bearer bar 01 or Bearer bar 04. Bending stresses were measured at the mid span of the bearer at the center of the bottom flange (Location 01 not pictured below) and near the right transition region. The instruments in the transition region were meant to capture the strains in this reduced section region, to pick up any stress concentrations or anomalies in this region, and pinpoint regions that would be of interest in the prototype test.

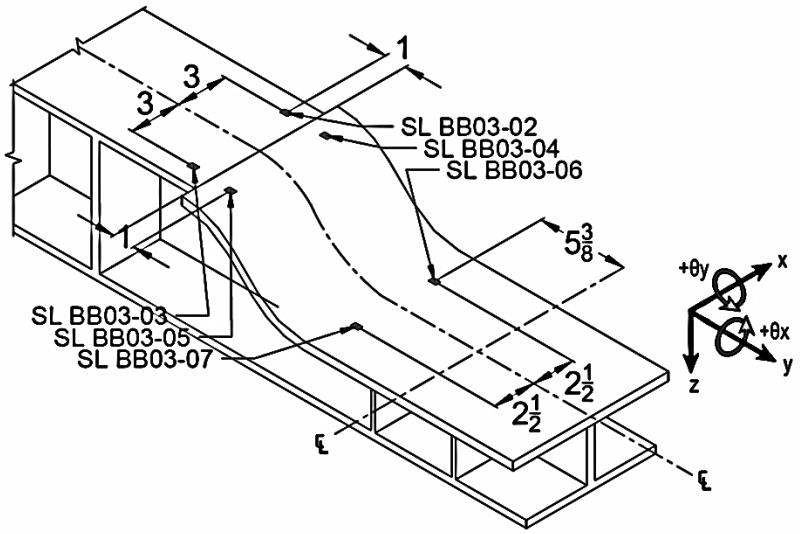

Figure 2-20: Linear strain gage locations and designations on the right side of bearer bar 03
(NOTE: the bearer bar is flipped upside down in the figure)

2.11.3 Rail Bending Stress

Rail bending stresses were monitored at three separate locations along the rail, as shown in Figure 2-21. Two locations were meant to capture the transverse moment in the rails; the remaining location was meant to capture the vertical moment cause by the application of the LRV axle load.

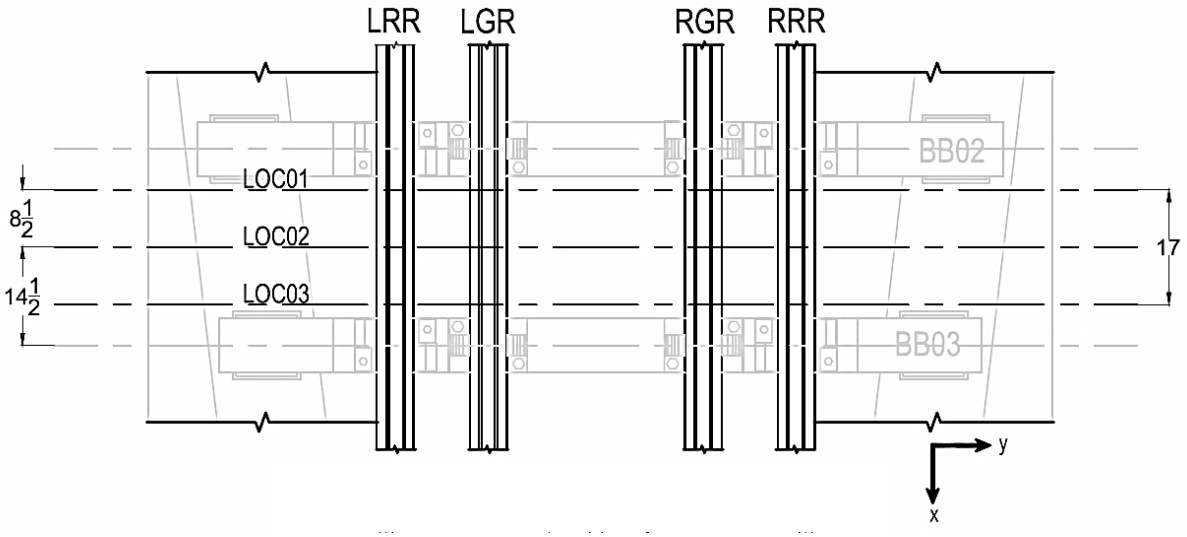

Figure 2-21: Longitudinal locations and designations for rail strain gages.

The transverse moment distribution of the rails was expected to exhibit a typical column moment diagram for a frame structure with concentrated moments at each rail fastener resulting from the interaction between the rails and the bearer bars. This concept was utilized in order to save data acquisition resources. Locations 01 and 03 were both offset two inches from the edge of the bearer bar. The intent was to use the gage pairs in these two locations to compute rail bending shears due to horizontal

forces. The transverse bending strains were monitored on the extreme edges of the bottom flange of the rail. From those strains the curvature, and hence the transverse moment could be computed.

The vertical moment strains were monitored halfway between bearer bar 02 and bearer bar 03. Strains were monitored at three locations, except on the right running rail that had an additional gage on the bottom flange to investigate the effective width of the bottom flange. The first location was at the center of the bottom flange, the remaining two were placed on the underside of the head of the rail above the sections neutral axis. Figure 2-22 details the exact location of the gages on the right running rail. These instruments are duplicated on the remaining three bearer bars, less gage 02-04 which is only present on the right running rail.

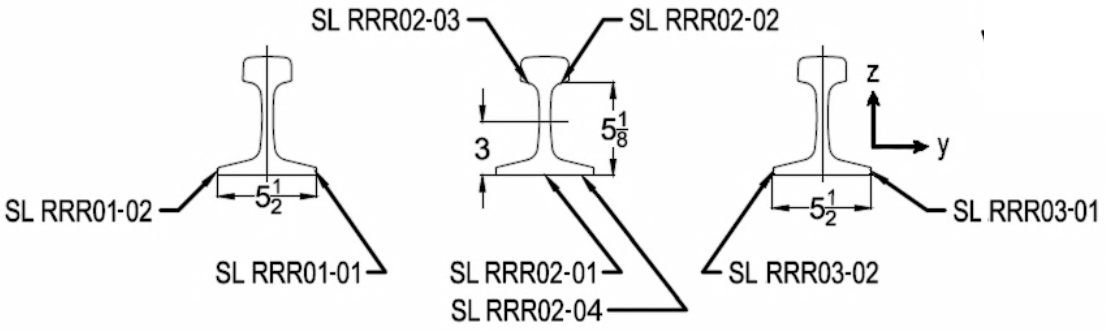

Figure 2-22: Location and designation of rail strain gages for right running rail
(LEFT TO RIGHT: Location 01, Location 02, and Location 03).

2.12 DMI Supplementary Instrumentation

In addition to the instruments supplied by the University of Washington, a supplemental instrumentation strategy was designed by Direct Measurement Incorporated (DMI). The purpose of this collaboration was to test the appropriateness and effectiveness of these instruments for the long term health monitoring of the track bridge, once it is completed and installed on the Homer Hadley Memorial Bridge. In order to establish direct comparisons, these instruments were installed to duplicate measurements from the instrumentation strategy previously described.

2.12.1 Bearing rotation

Rotations were monitored at the right end of bearer bar 03. Three single axis instruments inclinometers were installed on an aluminum bracket that connected by machine screws to the top surface of the friction pendulum bearing as shown in Figure 2-23. The tapped holes which were used previously to connect the shipping plates to the bearing were utilized extensively by the DMI instrumentation strategy, in order to simplify installation.

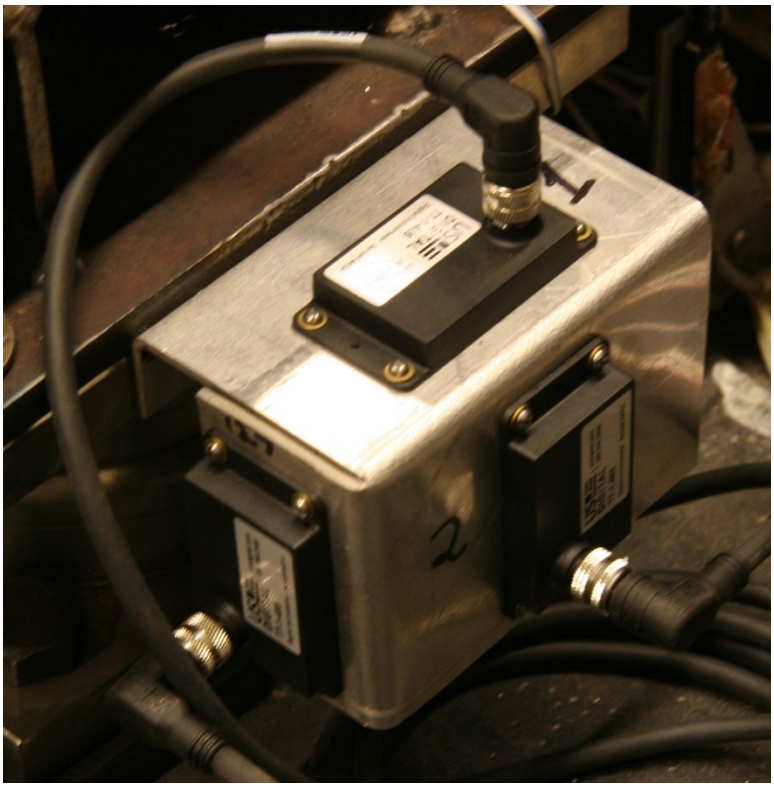

Figure 2-23: Photograph of inclinometer system used to measure bearing rotation.

2.12.2 Bearing transverse displacement

Transverse bearing displacements were monitored at the right end of bearer bar 03. Two LVDT's were mounted, in a crossing pattern, to aluminum brackets that were screwed to the top and bottom surfaces of the friction pendulum bearing as shown in Figure 2-24. Transverse translations of the bearing would result in one LVDT extending and the other retracting. Rotations of the bearing would result in both LVDTs extending or retracting. Through this configuration it was hoped that displacements and rotations could be measured with great precision.

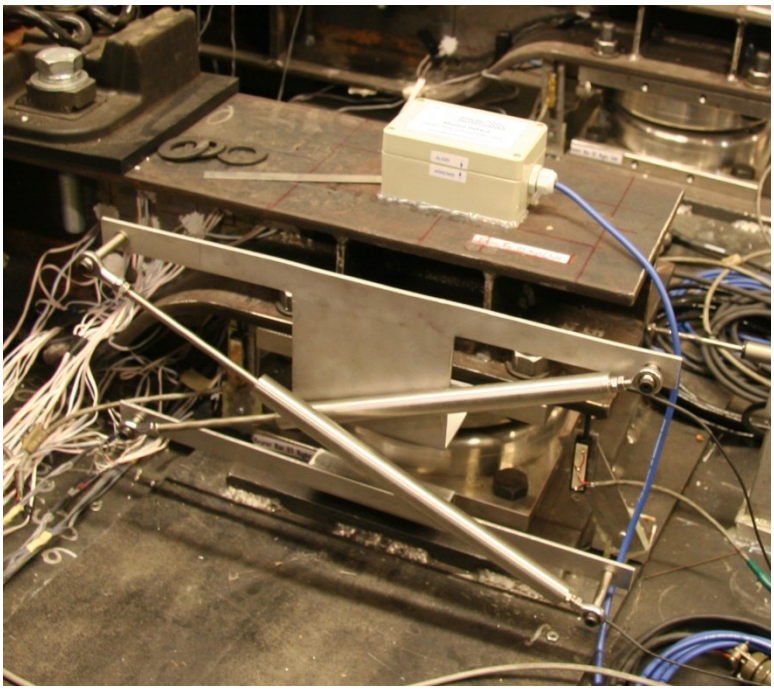

Figure 2-24: Photograph of “crossing” LVDT arrangement.

2.12.3 Rail Stresses

Rail stresses were monitored by optical sensors developed by DMI, and referred to as dual purpose sensors (DPS), for long term health monitoring. Several such sensors were affixed to the rail. Unfortunately, due to the curvature of the rail profile, some of gages were unreadable by the optical sensor, which needed to be in contact with a flat surface. Transverse rail stresses were measured on the right running rail between Locations 02 and 03 on the right edge of the bottom flange of the rail section. The intent of this instrument was to provide direct comparison of the optical system to traditional strain gages. Because conventional strain instruments were installed on this rail on

either side of this DPS gage, it was hoped that there would be good agreement between the strain determined by the optical gage and that found through interpolation from the traditional strain instruments.

2.13 Instrumentation technology

One component of the experiment was to pilot and develop effective instrumentation strategies for the CESURA system. A brief description of the instrument types employed in this experiment will be presented so that comparisons and conclusions can be drawn later about their effectiveness for the prototype tests.

2.13.1 Displacement

Two types of displacement instruments were used. Resistive potentiometers function by measuring the resistance across two ceramic resistors bridged by a conductive comb attached to a plunger. Linear variable differential transformers (LVDTs) act through the magnetic coupling among three solenoidal coils, one primary and two secondary. A ferromagnetic core moving through the coils causes the linkage between the primary and secondary coils to change, inducing voltages which can be interpreted as displacements.

2.13.2 Rotation

Two types of inclinometers were used. Electrolytic tilt sensors work by measuring the AC resistance of different paths throughout the instrument. Electrodes

are connected through a conductive fluid; as the instrument is tilted, the electrolytic fluid covers some electrodes while uncovering others. This technology lends itself to two axis measurement. Electrodes can be placed in four quadrants and the rotation in two orthogonal planes can be resolved from these measurements. In this experiment, analog instruments were used that converted AC resistances to DC outputs that were read by an analog to digital converter.

Digital inclinometers were also used. These devices measure tilt through integrated solid state accelerometers. These instruments are relatively inexpensive. In this experiment, the instruments communicated inclinations digitally through serial protocols. A comparison of the inclinometers used in this experimental project is presented in Table 2-2.

Table 2-2: Comparison of inclinometer technology utilized in instrumentation strategy

Brand:	Applied Geomechanics	US Digital
Model:	904-TH Clinometer Pak	T7 Networked Absolute Inclinometer
Technology:	Electrolytic tilt sensor	Solid state accelerometers
Range:	±10 degrees	360 degrees
Resolution:	0.005 degrees	0.01 degrees

2.13.3 Strain

Both electrical resistance strain gages and optical sensors were used to measure strains in the specimen. Dual Purpose Sensors, manufactured by Direct Measurement

Incorporated are optical instruments that were developed for long term monitoring of crack initiation and growth. The optical instrument works by measuring the elongation of a polymer gage that is imprinted with a pattern resembling a standard bar code. The width of each bar on the gage can be determined from the optical sensor and the strain of the material can be determined over the width of the gage. Since each bar of the gage constitutes an individual strain measurement, small cracks can be detected and monitored. In this experiment, no cracks occurred and only the average strain was utilized. Because the sensor relies on optics, the data acquisition rate is limited to one reading/ second which is practical for long term health monitoring, but is impractical for real-time data acquisition of dynamic response.

2.14 Instrumentation Manifest

2.14.1 Primary Instrumentation System

In the following tables, a complete list of the instrumentation with its ID designation and a brief description are presented. Instruments that were either damaged during testing or provided erroneous data are highlighted in the tables.

2.14.2 Rotations

Rotations were measured at the ends of the bearer bars situated above the center of the top plate of each FPS bearing. Each instrument was given a designation that indicates the bearer bar number and the end at which the rotation is measured. The positive direction for rotation is a global quantity so, for symmetric bending due to vertical load on the bearer bar, the end rotations will have equal magnitudes but opposite signs.

Table 2-3: Inclinometer designations and descriptions

Name	*Vars.*	*Description*
Wing Plates		
INC RWING-01	ΘX,ΘY	Rotations of the right (+y dir) wing plate between BB01 and BB02
INC RWING-02	ΘX,ΘY	Rotations of the right (+y dir) wing plate between BB03 and BB04
INC LWING-01	ΘX,ΘY	Rotations of the left (-y dir) wing plate between BB01 and BB02
INC LWING-01	ΘX,ΘY	Rotations of the left (+y dir) wing plate between BB03 and BB04
Bearer Bars		
INC BB01-01	ΘX,ΘY	Rotations of BB01 at right end (+y dir.) centered above FPS bearing top plate
INC BB02-01	ΘX,ΘY	Rotations of BB02 at right end (+y dir.) centered above FPS bearing top plate
INC BB02-02	ΘX,ΘY	Rotations of BB02 at left end (-y dir.) centered above FPS bearing top plate
INC BB03-01	ΘX,ΘY	Rotations of BB03 at right end (+y dir.) centered above FPS bearing top plate
INC BB03-02	ΘX,ΘY	Rotations of BB03 at left end (-y dir.) centered above FPS bearing top plate
INC BB04-01	ΘX,ΘY	Rotations of BB04 at right end (+y dir.) centered above FPS bearing top plate

2.14.3 Displacement

Lateral (y-direction) displacements were measured at the ends of each bearer bar above the bottom flange, and vertical (z-direction) displacements were recorded at the mid span. Each potentiometer was given a designation that indicates its location and direction on the specific bearer bar. Deflections of the wing plates and loading assembly were also monitored.

Table 2-4: Potentiometer designations and descriptions

Name	***Vars.***	***Description***
Wing Plates		
RWING-X01	ΔX	x-displacement of right wing at front (+x dir) right (+y dir) corner
RWING-Y01	ΔY	y-displacement of right wing at front (+x dir) right (+y dir) corner
LWING-X01	ΔX	x-displacement of left wing at front (+x dir) left (-y dir) corner
LWING-Y01	ΔY	y-displacement of left wing at front (+x dir) left (-y dir) corner
Bearer Bars		
BB01-Y01	ΔY	y-displacement of web of BB01 on the right end (+y dir.)
BB01-Z01	ΔZ	z-displacement of center of bottom flange of BB01 at midspan
BB02-Z02	ΔZ	z-displacement of bot flange of BB02 at right end (+y dir.) front (+x dir.)
BB02-Z03	ΔZ	z-displacement of bot flange of BB02 left of (-y dir.) FPB front (+xdir.)
BB02-Z04	ΔZ	z-displacement of bot flange of BB02 left of (-y dir.) FPB back (-xdir.)
BB02-Y01	ΔY	y-displacement of web of BB02 on the right end (+y dir.)
BB02-Z01	ΔZ	z-displacement of center of bottom flange of BB02 at midspan
BB03-Z02	ΔZ	z-displacement of bot flange of BB03 at right end (+y dir.) front (+x dir.)
BB03-Z03	ΔZ	z-displacement of bot flange of BB03 left of (-y dir.) FPB front (+xdir.)
BB03-Z04	ΔZ	z-displacement of bot flange of BB03 left of (-y dir.) FPB back (-xdir.)
BB03-Y01	ΔY	y-displacement of web of BB03 on the right end (+y dir.)
BB03-Z01	ΔZ	z-displacement of center bottom flange of BB03 at midspan
BB04-Y01	ΔY	y-displacement of web of BB04 on the right end (+y dir.)
BB04-Z01	ΔZ	z-displacement of center of bottom flange of BB04 at midspan
Loading Assembly		
RCKR-Y01	ΔY	y-displacement of top of rocker
RCKR-X01	ΔX	x-displacement of bottom of rocker
BEAM-Y01	ΔY	y-displacement of loading beam at mid height

2.14.4 Stresses

Bending stresses were measured in the rails and in the bearer bars for both horizontal and vertical cyclic loads.

Table 2-5: Linear strain gage designations and descriptions

Name	*Vars.*	*Description*
Bearer bars		
SL BB01-01	εY	longitudinal bending strain at midspan of BB01 (bottom flange)
SL BB01-02	εY	strain at weld before right curved transition of BB01 (front bottom flange)
SL BB01-03	εY	strain at weld before right curved transition of BB01 (back bottom flange)
SL BB01-04	εY	strain at weld after right curved transition of BB01 (front bottom flange)
SL BB01-05	εY	strain at weld after right curved transition of BB01 (back bottom flange)
SL BB02-01	εY	longitudinal bending strain at midspan of BB02 (bottom flange)
SL BB02-02	εY	strain at weld before right curved transition of BB02 (front bottom flange)
SL BB02-03	εY	strain at weld before right curved transition of BB02 (back bottom flange)
SL BB02-04	εY	strain at weld after right curved transition of BB02 (front bottom flange)
SL BB02-05	εY	strain at weld after right curved transition of BB02 (back bottom flange)
SL BB02-06	εY	strain at FPB of right side of BB02 (front bottom flange)
SL BB02-07	εY	strain at FPB of right side of BB02 (back bottom flange)
SL BB03-01	εY	longitudinal bending strain at midspan of BB03 (bottom flange)
SL BB03-02	εY	strain at weld before right curved transition of BB03 (front bottom flange)
SL BB03-03	εY	strain at weld before right curved transition of BB03 (back bottom flange)
SL BB03-04	εY	strain at weld after right curved transition of BB03 (front bottom flange)
SL BB03-05	εY	strain at weld after right curved transition of BB03 (back bottom flange)
SL BB03-06	εY	strain at FPB of right side of BB03 (front bottom flange)
SL BB03-07	εY	strain at FPB of right side of BB03 (back bottom flange)
SL BB04-01	εY	longitudinal bending strain at midspan of BB04 (bottom flange)
SL BB04-02	εY	strain at weld before right curved transition of BB04 (front bottom flange)
SL BB04-03	εY	strain at weld before right curved transition of BB04 (back bottom flange)
SL BB04-04	εY	strain at weld after right curved transition of BB04 (front bottom flange)
SL BB04-05	εY	strain at weld after right curved transition of BB04 (back bottom flange)
Rails		
Location 01 – near BB02 (6 inches from centerline of bearer bar)		
SL RRR01-01	εX	transverse bending strain on right running rail (right side +y dir.)
SL RRR01-02	εX	transverse bending strain on right running rail (left side -y dir.)
SL LRR01-01	εX	transverse bending strain on left running rail (right side +y dir.)
SL LRR01-02	εX	transverse bending strain on left running rail (left side -y dir.)
SL RGR01-01	εX	transverse bending strain on right guard rail (right side +y dir.)
SL RGR01-02	εX	transverse bending strain on right guard rail (left side -y dir.)

Name	*Vars.*	*Description*
SL LGR01-01	ε X	transverse bending strain on left guard rail (right side +y dir.)
SL LGR01-02	ε X	transverse bending strain on left guard rail (left side -y dir.)
Location 02 – halfway between BB02 and BB03 (14.5 inches from centerline of bearer bar)		
SL RRR02-01	ε X	longitudinal bending strain on right running rail (middle of bottom flange)
SL RRR02-02	ε X	longitudinal bending strain on right running rail (under head right +y dir.)
SL RRR02-03	ε X	longitudinal bending strain on right running rail (under head left -y dir.)
SL RRR02-04	ε X	longitudinal bending strain on right running rail (on bottom flange edge)
SL LRR02-01	ε X	longitudinal bending strain on left running rail (middle of bottom flange)
SL LRR02-02	ε X	longitudinal bending strain on left running rail (under head right +y dir.)
SL LRR02-03	ε X	longitudinal bending strain on left running rail (under head left -y dir.)
SL RGR02-01	ε X	longitudinal bending strain on right guard rail (middle of bottom flange)
SL RGR02-02	ε X	longitudinal bending strain on right guard rail (under head right +y dir.)
SL RGR02-03	ε X	longitudinal bending strain on right guard rail (under head left -y dir.)
SL LGR02-01	ε X	longitudinal bending strain on right guard rail (middle of bottom flange)
SL LGR02-02	ε X	longitudinal bending strain on right guard rail (under head right +y dir.)
SL LGR02-03	ε X	longitudinal bending strain on right guard rail (under head left -y dir.)
Location 03 – near BB03 (6 inches from centerline of bearer bar)		
SL LRR03-01	ε X	transverse bending strain on right running rail (right side +y dir.)
SL LRR03-02	ε X	transverse bending strain on right running rail (left side -y dir.)
SL RRR03-01	ε X	transverse bending strain on left running rail (right side +y dir.)
SL RRR03-02	ε X	transverse bending strain on left running rail (left side -y dir.)
SL RGR03-01	ε X	transverse bending strain on right guard rail (right side +y dir.)
SL RGR03-02	ε X	transverse bending strain on right guard rail (left side -y dir.)
SL LGR03-01	ε X	transverse bending strain on left guard rail (right side +y dir.)
SL LGR03-02	ε X	transverse bending strain on left guard rail (left side -y dir.)

In addition to the bending stresses, strain gage rosettes were used to quantify the shear stresses in the variable depth regions at the right end of the bearer bar under vertical loading.

Table 2-6: Strain gage rosette designations and descriptions

Name	***Vars.***	***Description***
Bearer bars – in the right transition region (+y dir.)		
SR BB01-01	εz, εy, εyz	Strain state near FPB of BB01 (front of web +x dir.)
SR BB01-02	εz, εy, εyz	Strain state near FPB of BB01 (back of web -x dir.)
SR BB02-01	εz, εy, εyz	strain state near FPB of BB02 (front of web +x dir.)
SR BB02-02	εz, εy, εyz	strain state near FPB of BB02 (back of web -x dir.)
SR BB02-03	εz, εy, εyz	strain state near weld of BB02 (front of web +x direction)
SR BB02-04	εz, εy, εyz	strain state near weld of BB02 (back of web -x dir.)
SR BB03-01	εz, εy, εyz	shear strains near FPB of BB03 (front of web +x dir.)
SR BB03-02	εz, εy, εyz	strain state near FPB of BB03 (back of web -x dir.)
SR BB03-03	εz, εy, εyz	strain state near weld of BB03 (front of web +x dir.)
SR BB03-04	εz, εy, εyz	strain state near weld of BB03 (back of web -x dir.)
SR BB03-05	εz, εy, εyz	strain state near weld at middepth of BB03 (front of web +x dir.)
SR BB03-06	εz, εy, εyz	strain state right of weld near bottom flange of BB03 (front of web +x dir.)
SR BB03-07	εz, εy, εyz	strain state right of weld at midpan of BB03 (front of web +x dir.)
SR BB03-08	εz, εy, εyz	strain state between weld and FPB of BB03 (front of web +x dir.)
SR BB03-09	εz, εy, εyz	strain state left of FPB of BB03 (front of web +x dir.)
SR BB03-10	εz, εy, εyz	strain state left of FPB of BB03 (front of web +x dir.)
SR BB04-01	εz, εy, εyz	strain state near FPB of BB04 (front of web +x dir.)
SR BB04-02	εz, εy, εyz	strain state near FPB of BB04 (back of web -x dir.)

2.15 DMI Supplementary Instrumentation System

The instrumentation that was installed by Direct Measurements Incorporated (DMI) on the test specimen in parallel with the UW sensors is presented in the following tables with its ID designation and a brief description.

2.15.1 Bearing relative movements

Lateral (y-direction) and vertical (z-direction) displacements and rotations were measured by two "crossing" LVDT's mounted on the front side of bearer bar 03 on the right side.

Table 2-7: LVDT designations and descriptions

Name	*Vars.*	*Description*
LVDT BB03-01/ 02	ΔY, ΔZ, ΘY	Y-displacement, z-displacement, y-rotation of the FPB on the right side (+y dir.) of BB03

2.15.2 Rotations

Rotations about the bearings' three local coordinates were measured at the end of the bearer bar 03 by three inclinometers, attached to the back side of the friction pendulum bearing.

Table 2-8: DMI inclinometer designations and descriptions

Name	*Vars.*	*Description*
INC BB03-03	ΘX	X-rotation of the FPB on the right side (+y dir.) of BB03
INC BB03-04	ΘY	Y-rotation of the FPB on the right side (+y dir.) of BB03
INC BB03-05	ΘZ	Z-rotation of the FPB on the right side (+y dir.) of BB03

2.15.3 Stresses

Transverse bending stresses were measured in the rails for horizontal cyclic loads by a DPS sensor located two inches from location 03 on the right running rail.

Table 2-9: DPS sensor designations and descriptions

Name	*Vars.*	*Description*
DPS RRR04-01	εx	Transverse bending strain on right running rail (right side +y dir.)

Chapter 3 Observed Data

3.1 Geometric Adjustment

The specimen accommodated the geometric configurations without observable negative consequences. Figure 3-1 shows the specimen in the reference condition, including the 4% longitudinal slope and no transverse rotation of the wing plates. Tests REF01, REF02, FRK02, FRK03, STF02, and REF03 were all performed in this configuration. The axle placement as pictured is typical for the REF02 and REF03 tests. The STF02, FRK02, and FRK03 tests were conducted with the axle over fourth bearer bar 4 (to the extreme left as viewed in the photo). The REF01 test was performed with the pseudo-axle midway between bearer bars 2 and 3.

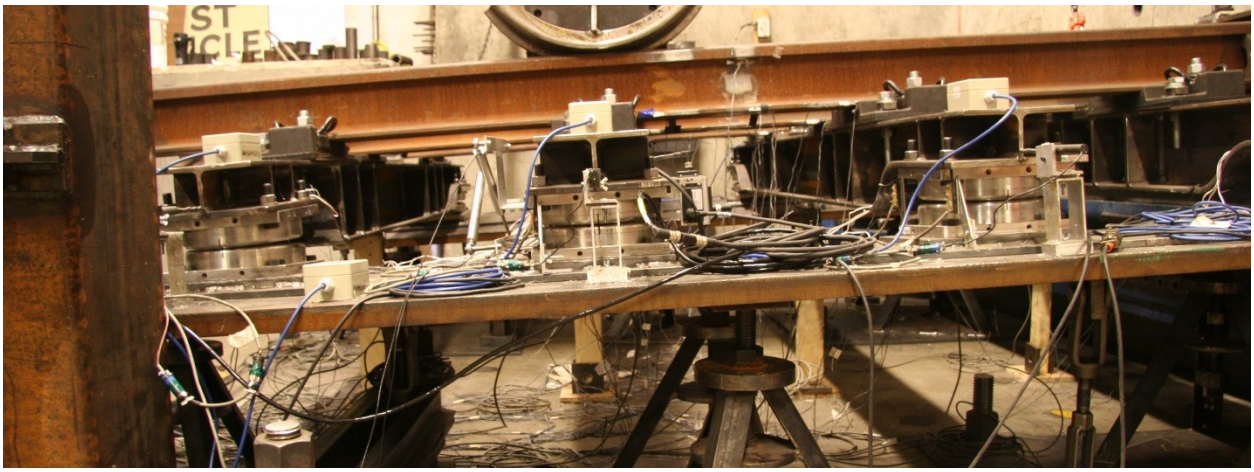

Figure 3-1: Right wing, viewed from the right, in the reference condition.

Figure 3-2 shows the specimen in the PIT02 condition with the wing plates rotated about a longitudinal axis, away from one another, three degrees.

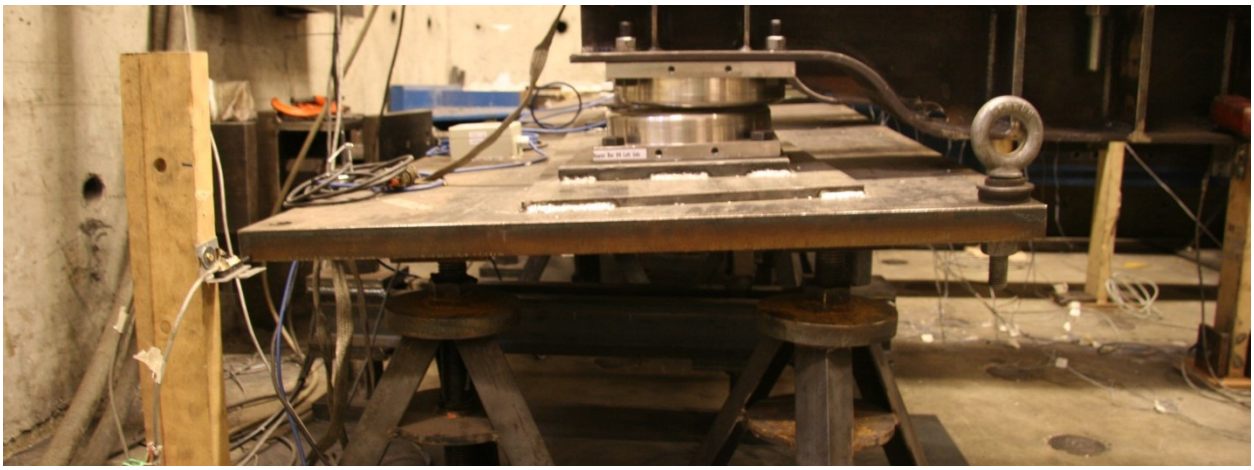

Figure 3-2: Left wing, viewed from the front, in the PIT02 configuration.

Transverse displacements of the bearing's bottom plate caused by the rotation of the wing plates were accommodated by the friction pendulum bearings, whose new neutral position had no observable effects ton the system's behavior. The bearer bars and rails remained stationary during geometric adjustment. Figure 3-3 shows the friction pendulum bearing in the PIT01 configuration with the wings rotated about a longitudinal axis, towards one another, three degrees. Note the small initial transverse offset caused by the geometric condition of the wing plates.

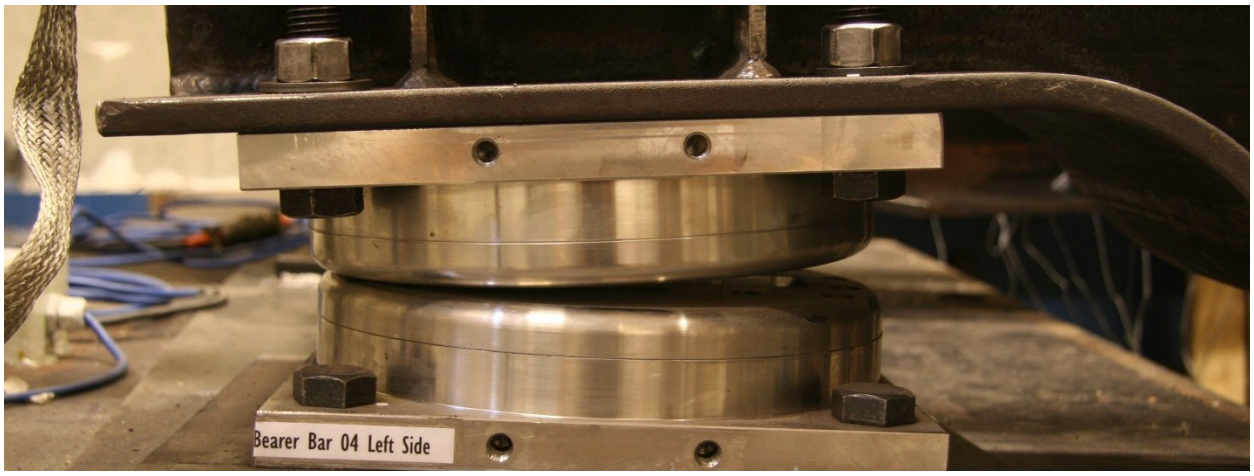

Figure 3-3: Bearer bar 04 left bearing, viewed from the front, in the PIT01 configuration.

3.2 Loading Protocols

Throughout the loading protocols no audible noises were heard that would indicate that the friction pendulum bearings were binding or the top surfaces of the bearings were rocking on the top of the inner "dog bone" sliders.

The testing apparatus and specimen responded elastically, displacements and forces were in the ranges that were expected. The pseudo axle remained seated and did not ride up on the rails. The frame that comprise the bearer bar-rail system visibly deformed into a parallelogram shape, which was confirmed by the potentiometers' measuring bearer bar deflections, as observed in Section 4.5. The rail pins at the wall, allowed the rails to rotate, but prevented their translation in the transverse direction. The gage bar at the free end of the system and the fasteners kept the rails parallel and at the proper gage distance during the loading protocols.

The axle assembly allowed transverse displacements of the specimen to occur independent of the vertical loading structure, and the braces restricted transverse displacements of the vertical strut and vertical loading beam.

Chapter 4 Measured Data

The sliding components of the rig introduced some friction, which was unavoidably included in the measured load. Therefore separate friction tests were conducted so that, during the tests simulating horizontal motion of the system, the friction force could be estimated reliably and subtracted from the load measurements to give the true system resistance. Those friction tests are described first, and are followed by descriptions of the responses to vertical and horizontal loading.

4.1 Friction

The friction coefficient of the PTFE sliding interface was measured three times throughout the testing program. The typical response of the system is reported in Figure 4-1. The slider was re-greased before REF02, PIT02, and STF02. Friction measurements were taken initially and before STF02, just before re-greasing and just after. Despite the difference in the number of cycles and times after re-greasing, the friction coefficient remained constant, implying that the level of residual grease retained in the dimpled PTFE surface was adequate to provide effective lubrication even after many cycles of horizontal load. The response includes an initial peak, after which the friction coefficient remained relatively constant. The peak coincides with static, or "breakaway", friction and the constant region corresponds to sliding friction.

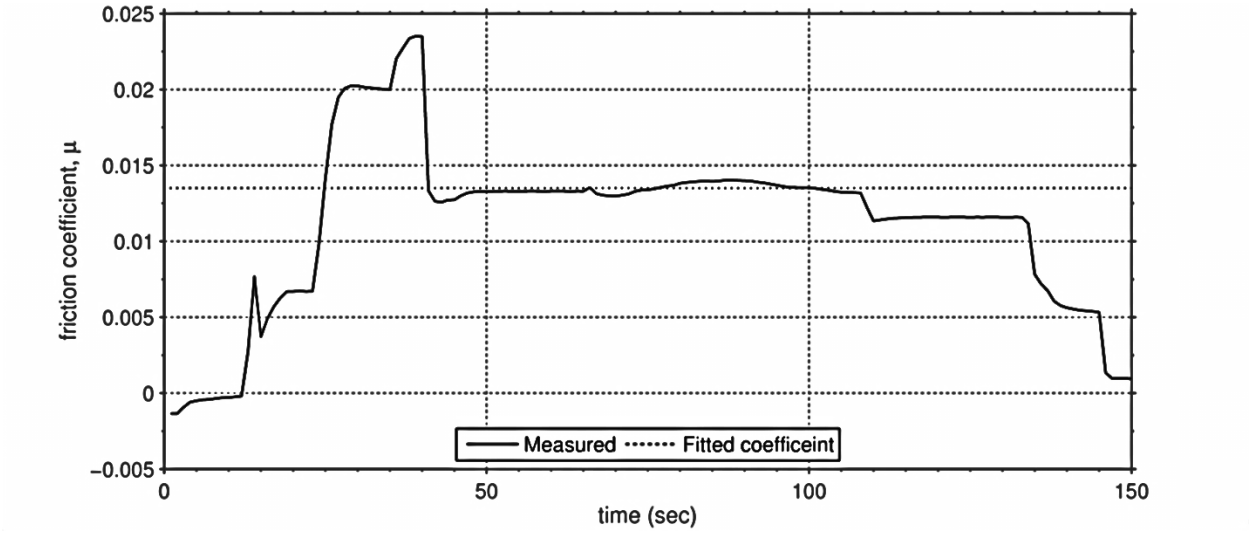

Figure 4-1: Typical friction test plot (FRK02c before STF02 after re-greasing).

4.2 Experimental Apparatus

Local displacements between nominally rigid components of the experimental apparatus were, in general, small. In the stiffness tests, the transverse displacements of the rail fasteners relative to the bearer bars were monitored. These displacements were on the order of 0.001 inches. The slip critical connection between the loading apparatus and the pseudo axle assembly was also monitored for slip. Although this instrument responded to the elastic bending of the channel section, the displacement returned to zero at the end of loading, indicating no slip had occurred. The rail pin at the wall was monitored for transverse displacements relative to the wall plate. The readings that were recorded for the slip of the connection and the transverse displacement of the pin were less than 0.01 inches in magnitude. Due to the geometry of the pin and friction

between the potentiometer plunger and the steel tube, the actual translation of the rail pin could much smaller.

Throughout the geometric tests the vertical loading beam was monitored for sidesway between bearer bars 03 and 04. Although measures were taken to properly brace the beam, some transverse displacements were expected in the horizontal experiments. These arose largely because the brace connections had to allow vertical movement, so they consisted of pins and bolts, which inevitably allowed some local movement. The maximum transverse deflection of the beam was roughly a quarter of an inch.

The pseudo axle assembly was also monitored for movement and rotation. Transverse displacements of the rocker and vertical strut did occur, roughly matching those of the vertical loading beam. In some of the geometric tests the assembly rotated about the transverse axis (i.e. torsion rotation of the pseudo axle). These rotations were gradual and small, the assumption being that the axle was not perfectly level at the start of the experiment.

The displacements of the corner of the wings plates in both the x and y-directions are reported in Figure 4-2 for the PIT02 horizontal test, which exhibits the typical behavior seen throughout the geometric configuration testing protocols. Both the longitudinal and transverse peak-to-peak displacements of the wing plates were less than 2 % of the actuator peak-to-peak displacement during the geometric tests (less than

0.01 inches). The maximum wing displacements were less that 5% of the overall system displacement in the stiffness tests. . The displacements were an order of magnitude smaller in the vertical tests in comparison to those measured under transverse loads.

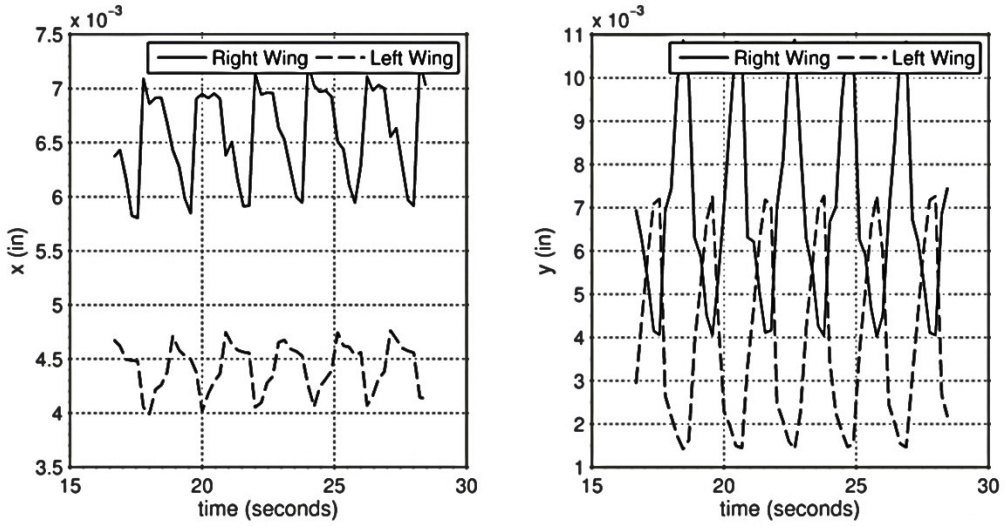

Figure 4-2: Typical right and left wing corner x and y-displacements for horizontal tests.

The vertical deflection of the wing plates directly under the FPS bearings for bearer bar 03 are reported in Figure 4-3 for the YAW01 configuration. This position corresponded to roughly the center of the wing plate, between the two center stands. The vertical deflection of the wing in this configuration was less than 0.01 inches.

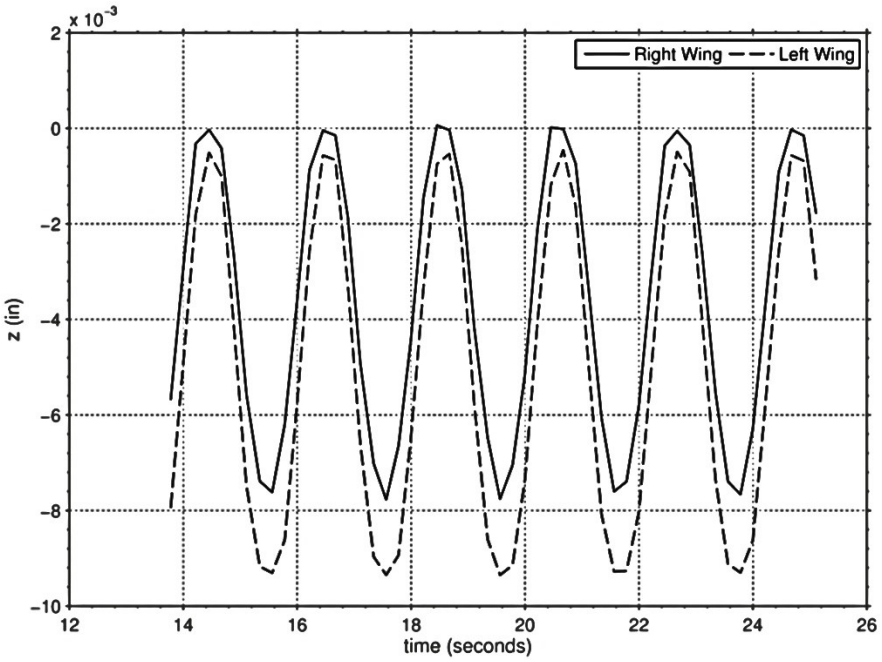

Figure 4-3: Center wing plate z-deflections for YAW01 vertical test.

4.3 System Transverse Stiffness

The transverse stiffness of the system was measured both with and without the guard rails fastened to the bearer bars. Figure 4-4 shows the response of the system with and without the guard rails. The stiffness of the system was influenced little by the presence of the guard rail. At a displacement of roughly 1.7 inches a drastic increase in stiffness was observed.

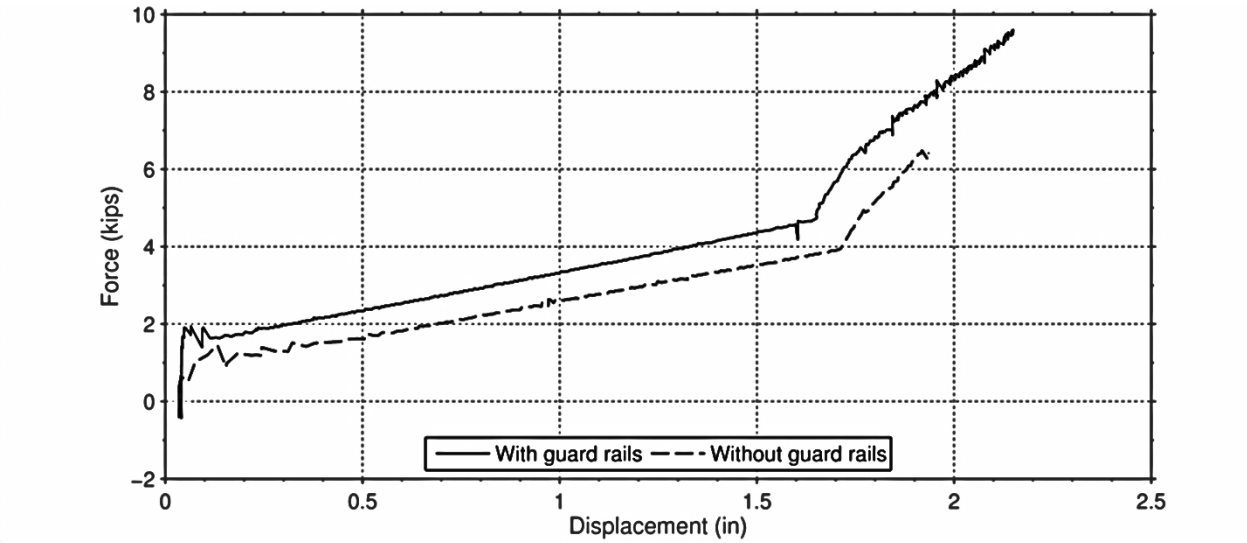

Figure 4-4: System stiffness curves with and without the guard rails attached to the bearer bars.

Several possible explanations were hypothesized as the cause for the secondary stiffness observed. Binding of the FPS bearing was of primary concern, but this would likely cause an additional friction force, rather than the elastic behavior recorded. Other sources that were identified included the rail fasteners and the rail end pin. The rail end pin was disregarded because the contribution from additional rotational resistance at the wall would be too small to produce the magnitude of the stiffness increase recorded.

The corresponding rail shears between bearer bars 02 and 03 for the right and left running rails are reported in Figure 4-5. The purpose was to determine whether the stiffness increase was associated with the behavior of the fasteners. If it was, the transverse shear forces in the rails would be expected to increase. It should be noted

that the displacement axis in this figure corresponds to the relative displacement between bearer bars 02 and 03.

Because the rails rotated about the wall pin essentially as rigid bodies, the correlation between the relative displacement, Δ, and the system displacement can be determined by similar triangles. For the specimen, the relative displacement between bearer bars is roughly 28% of the system displacement at bearer bar 04. For a system displacement of 1.7 inches, this corresponds to a relative displacement of 0.48 inches.

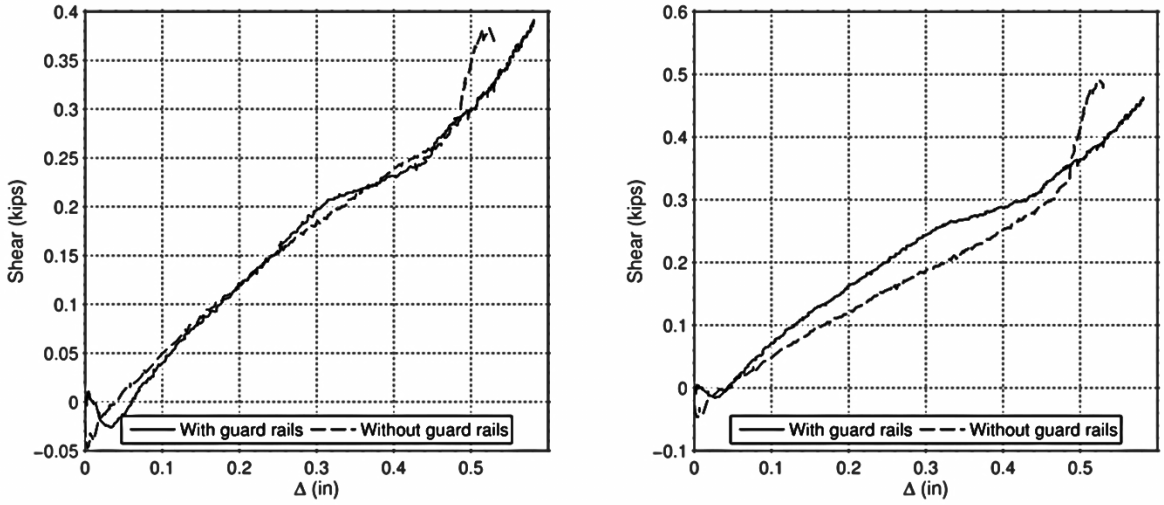

Figure 4-5: Measured rail shears rails for the right and left running rails respectively.

Curiously, it was observed that the rail shears and strains increased at the same displacement as the increase in global stiffness, only when the guard rails were not present. Although this data provides some insight into the fastener's contribution to the overall system behavior, additional gages would be necessary in the adjacent spans to have a complete picture of the rails' influence.

Figure 4-6 shows a cross section of a typical DF Fastener. The basic design of the fastener consists of two steel plates, separated by a layer of elastomer. Shear forces are transferred from the rail to the bottom plate through two uprights on the transverse sides of the rail clip, as seen to the right in the figure.

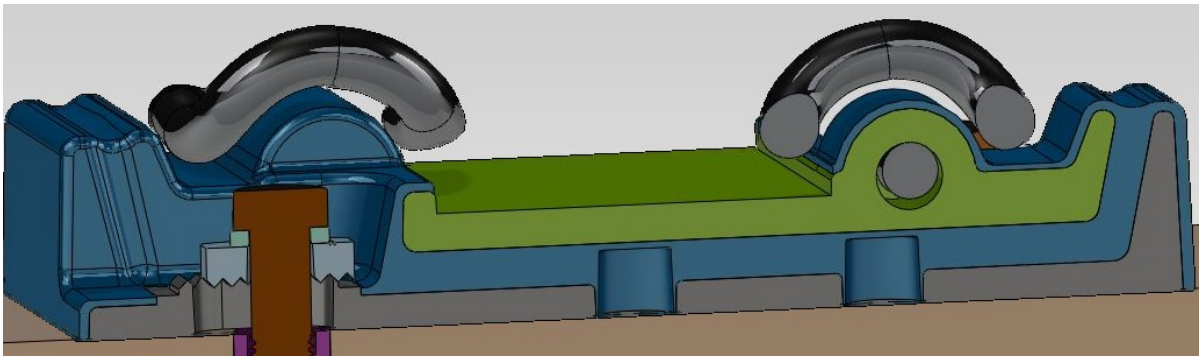

Figure 4-6: Cross section of a typical DF Fastener.

Because of the fasteners asymmetric design, the direction of rotation about a vertical axis dictates the characteristics of the response. Rotating the rail about a vertical axis counterclockwise, as seen in the figure, compresses the rubber between the uprights, while a clockwise rotation causes tension in the rubber. This asymmetric behavior may be one possible reason that a sharp increase in stiffness was observed.

After the transverse load was released, a significant residual displacement remained. The initial, maximum and final displacement of the left bearing of bearer bar 04 for STF01 is shown in Figure 4-7.

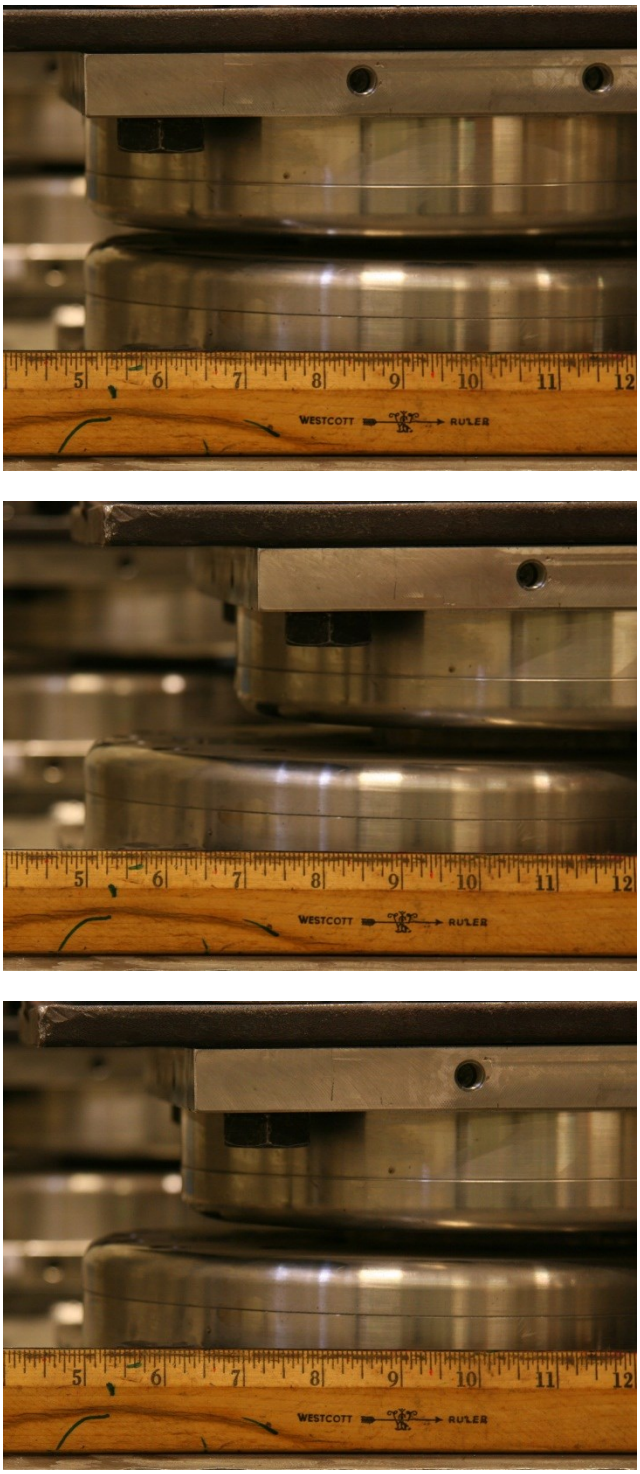

Figure 4-7: Displacement of left FPS bearing of BB04 in STF 01.
Top: initial displacement
Middle: maximum displacement
Bottom: residual displacement

4.4 Response to Vertical Load

The vertical response of the system was recorded for each of the geometric conditions. The response of the system was nearly identical for each of the configurations, and a typical response is reported subsequently. Refer to Appendix B for additional plots from each of the geometric configurations. Each figure reproduces the same time interval from the same test, near the midpoint of the loading protocol, unless otherwise noted.

4.4.1 Loading History

The vertical load on the specimen is reported in Figure 4-8. In this configuration the axle load was directly over bearer bar 03. The vertical load on the specimen was determined using the vertical actuator's MTS load cell and the appropriate lever arm from the wall pin. The weight of the loading assembly and pseudo axle assembly were also included in this calculation. The load on the specimen was determined by,

$$P = (1/L_1)(\, F\, L \, + \, \omega\, L^2/2\,) + W \qquad (4\text{-}1)$$

Where

P = Vertical Load on the specimen (kips)
F = MTS Actuator Force (kips)
W = Weight of the pseudo axle assembly (kips)
ω = Weight of the vertical loading beam (kips/in)
L = Length of the vertical loading beam (in)
L_1 = Length from the wall pin to the pseudo axle (in)

In order to prevent uplift of the axle, a modest (0.5 kips) tension force remained in the vertical actuator at the minimum of the applied cyclic load, to prevent separation. This corresponded to roughly four kips of vertical force on the specimen.

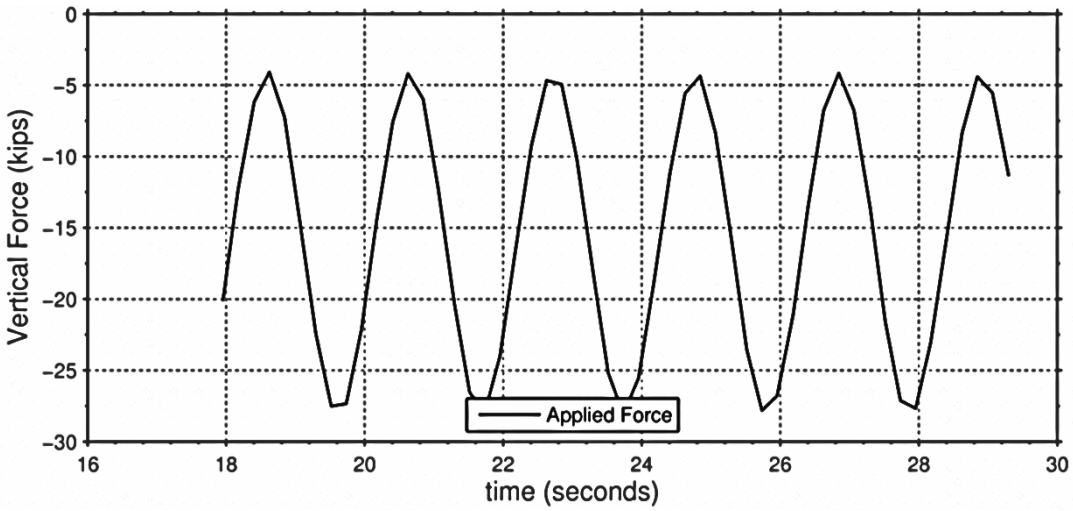

Figure 4-8: Typical vertical loading time history (ROL01).

4.4.2 Bearer bar displacement

The vertical deflections of the bearer bars at their midspans are reported in Figure 4-9. The displacements for bearer bars 02-04 were found to be very similar, despite their differing bending stiffness.

To check the magnitude of these deflections, assume that one-quarter of the axle load of 28 kips was applied to a single prismatic W8x31 bearer bar as two concentrated loads applied at a separation of 59 inches (gage spacing plus 2.5 inches to account for the wheel-to-rail contact points). Taking the average length of the bearer bars to be

102.5 inches, the mid span deflection would be 0.03 inches. Given that the recorded deflections include any deflections of the wing plates and the fact that the bearer bars are more flexible due to the reduced section, the measured displacements appear reasonable.

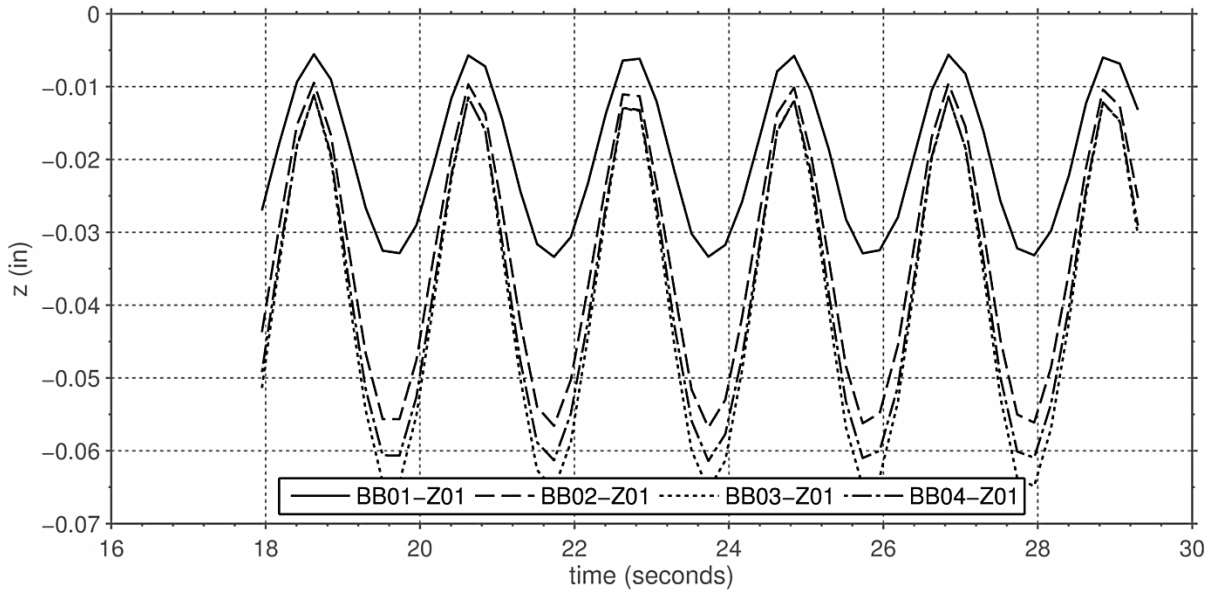

Figure 4-9: Typical bearer bar z-displacement time history for vertical tests (ROL01).

4.4.3 Bearer bar mid span stresses

The strong axis bending stresses of the bearer bars at mid span are reported in Figure 4-10. These stresses were computed from strain readings by multiplying the measured value by Young's modulus. Anomalously bearer bar 02 showed smaller mid span bending stresses, despite having similar deflections to bearer bars 03 and 04. The stresses of bearer bar 04 were higher, consistent with the observation of its deflection

and its higher stiffness. The stresses never exceeded 6 ksi, and were slightly higher in the pitch configurations.

The magnitude of these stresses can be checked using the same assumptions presented in the previous section. For a prismatic bearer bar with a length of 102.5 inches, the mid span bending moment is found to be 76 kip-inches, and the corresponding stress at the bottom flange, assuming shear deformations are negligible, would be 2.8 ksi. Using the length of bearer bar 04 instead, this value would be 2.2 ksi. The fact that the measured stress of bearer bar 04 is much larger indicates that it carried a majority of the vertical load.

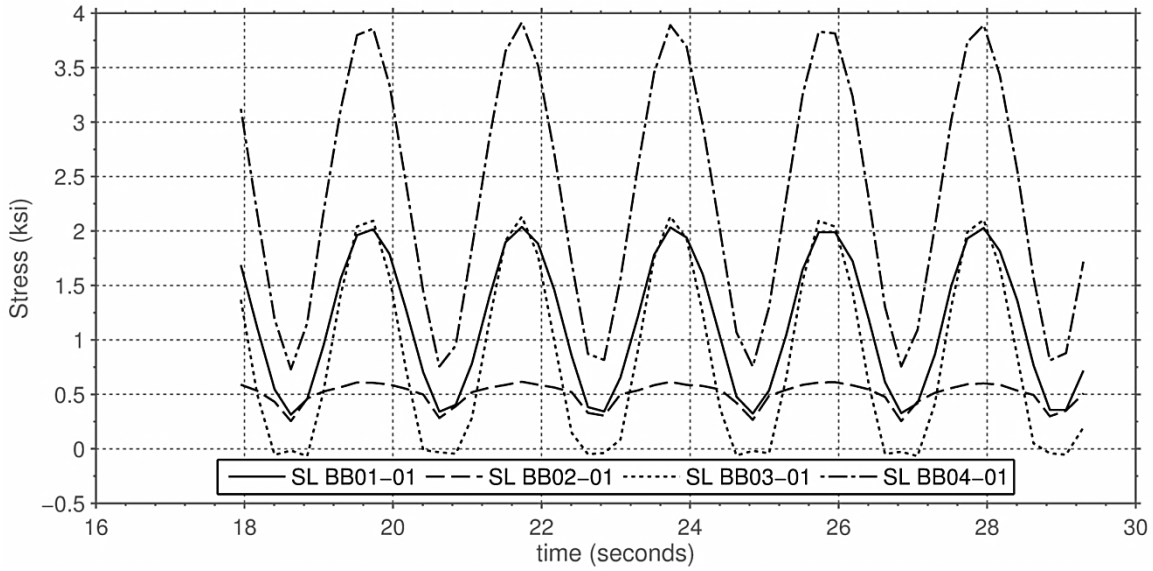

Figure 4-10: Typical bearer bar mid span stress time history for vertical tests (ROL01).

4.4.4 Bearer bar end rotations

The strong axis rotations of the ends of the bearer bars are reported in Figure 4-11. Anomalously the ends of bearer bar 02 showed rotation in the same direction, while those from bearer bar 03 showed rotations in opposite directions. The instrument located on bearer bar 04 malfunctioned during the test, and these results are not shown. The magnitudes of these rotations differed slightly from geometry to geometry, but these trends persisted.

Again a simple check can be performed to assess whether the magnitudes of these rotations are reasonable. Returning to the prismatic W8x31 bearer bar with a length of 102.5 inches, and assuming one quarter of the axle load is applied at two points spaced of 59 inches apart, the end rotations of the beam would be 0.06 degrees. This result is very close to the measured data, despite the bearer bars being more flexible than the assumed prismatic section. It is believed that bearer bar 04 carried a considerable portion of the total load, and therefore it may not be as surprising that the measured rotations for bearer bars 01 and 02 are smaller than would be expected.

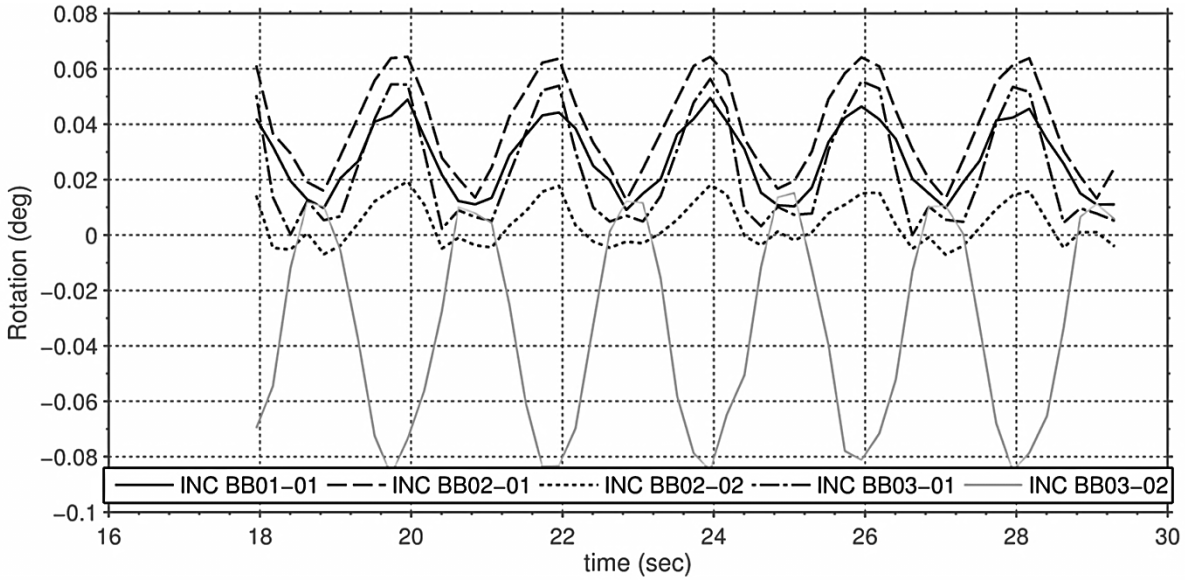

Figure 4-11: Typical bearer bar end y-axis rotations for vertical tests (ROL01).

The twisting rotations of the ends of the bearer bars are reported in Figure 4-12. With the load over bearer bar 03, small twisting rotations were observed in both bearer bar 02 and bearer bar 03. As the vertical load was increased, bearer bar 02 rotated as a rigid body consistent with the rail deflecting downward between bearer bars 02 and 03. No trend was observed in the rotations of bearer bar 03 although small fluctuations were recorded.

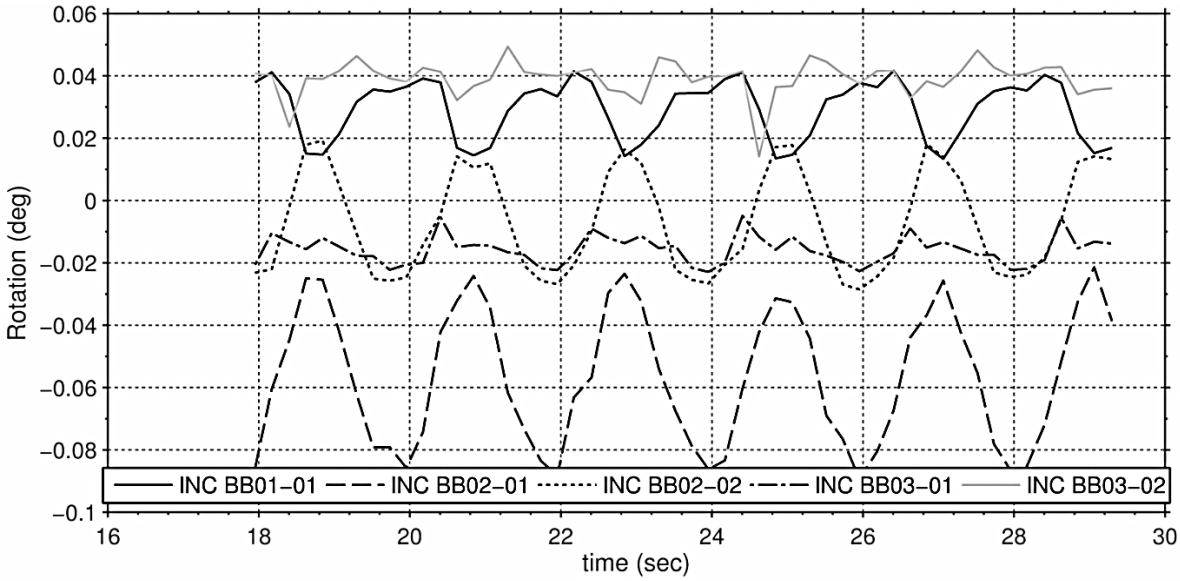

Figure 4-12: Typical bearer bar end x-axis rotations for vertical tests (ROL01).

4.4.5 Rail Stresses

The strong-axis mid span rail bending stresses between bearer bars 02 and 03 are reported in Figure 4-13. Several strain instruments malfunctioned during the test, namely one gage on the head of the right running rail and two gages on the head and the bottom flange of the right guard rail. It was observed that the stresses in the running rails were close to twice those in the guard rails. For each geometric condition, the bottom flange of the section was in tension and the head of the rail was in compression, consistent with a downward deflection and positive bending moment of the rails at mid span. In no case was the stress greater than 4 ksi. In the prototype, the values are expected to be lower than that, because the wheel load will be spread over more than four bearer bars.

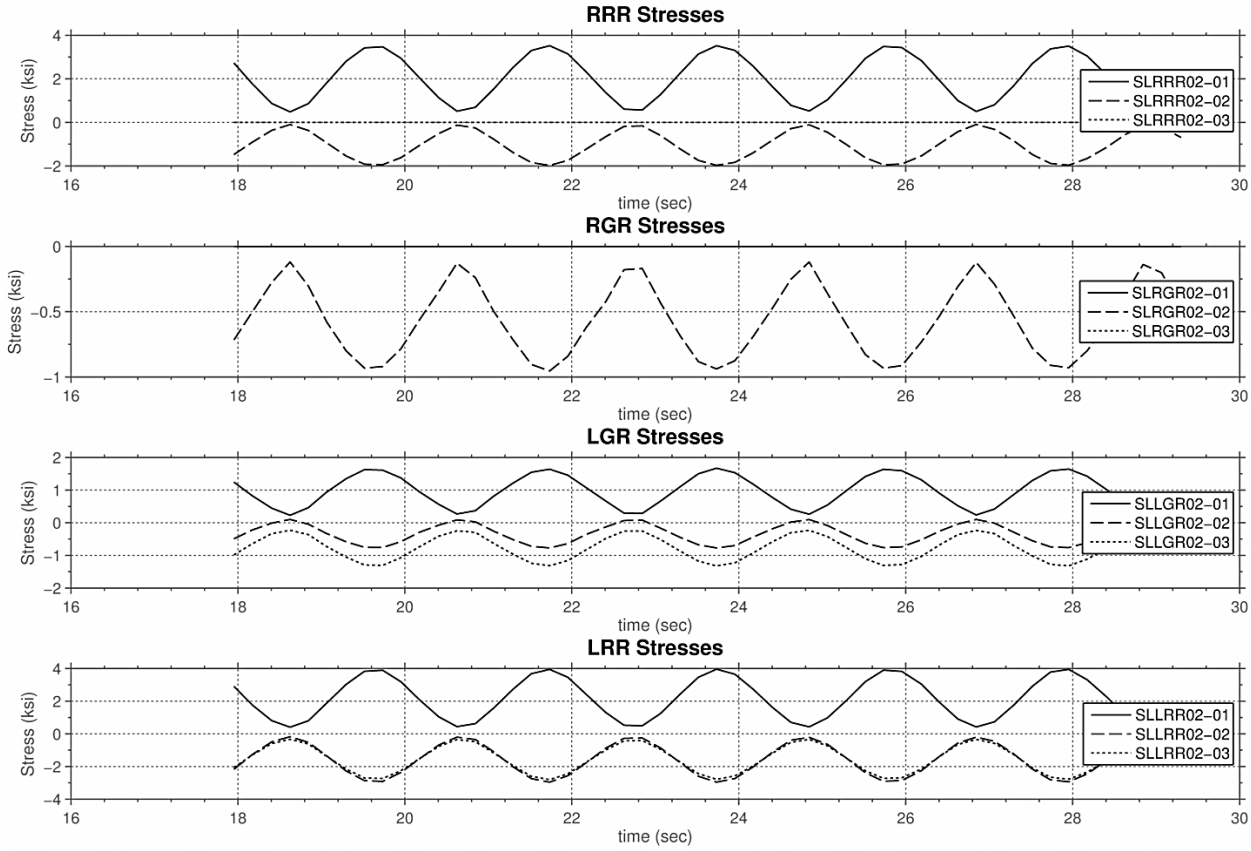

Figure 4-13: Typical mid span rail stresses for vertical tests (ROL01).

4.4.6 Bearer Bar Transition Stresses

The interpolated von Mises stress field in the transition region of bearer bar 03 is reported in Figure 4-14. It was observed that web stresses were highest near the ends of the transition zone, and significant shear forces were carried by the bent plate in the center of the transition region as evidenced by the decrease in web stresses. For each geometric condition, the stresses were all less than 6 ksi.

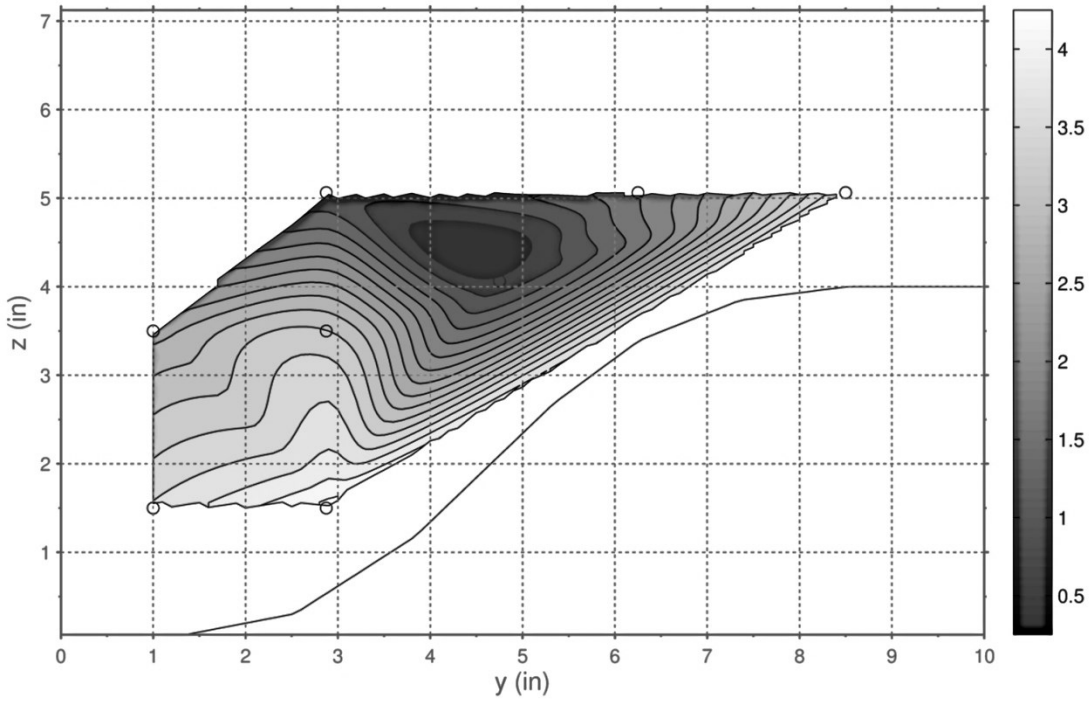

Figure 4-14: Typical BB03 transition zone von Mises stress field for vertical tests (ROL01).

Gages located on the bottom flange of the bearer bar adjacent to the transition region also showed low levels of stress, however, the pattern of the stresses was curious. The effects of the bearer bar weld access hole are discussed further in Section 6.5.5.

The shear stresses in the transition regions of the bearer bars are reported in Figure 4-14. It should be noted that the shear stresses increase from one end of the system to the other, with the highest shear stress measured in bearer bar 04. Because of gage failure and the limited data acquisition resources, the reported values of bearer bars 01, 02 and 04 vary in both location and number.

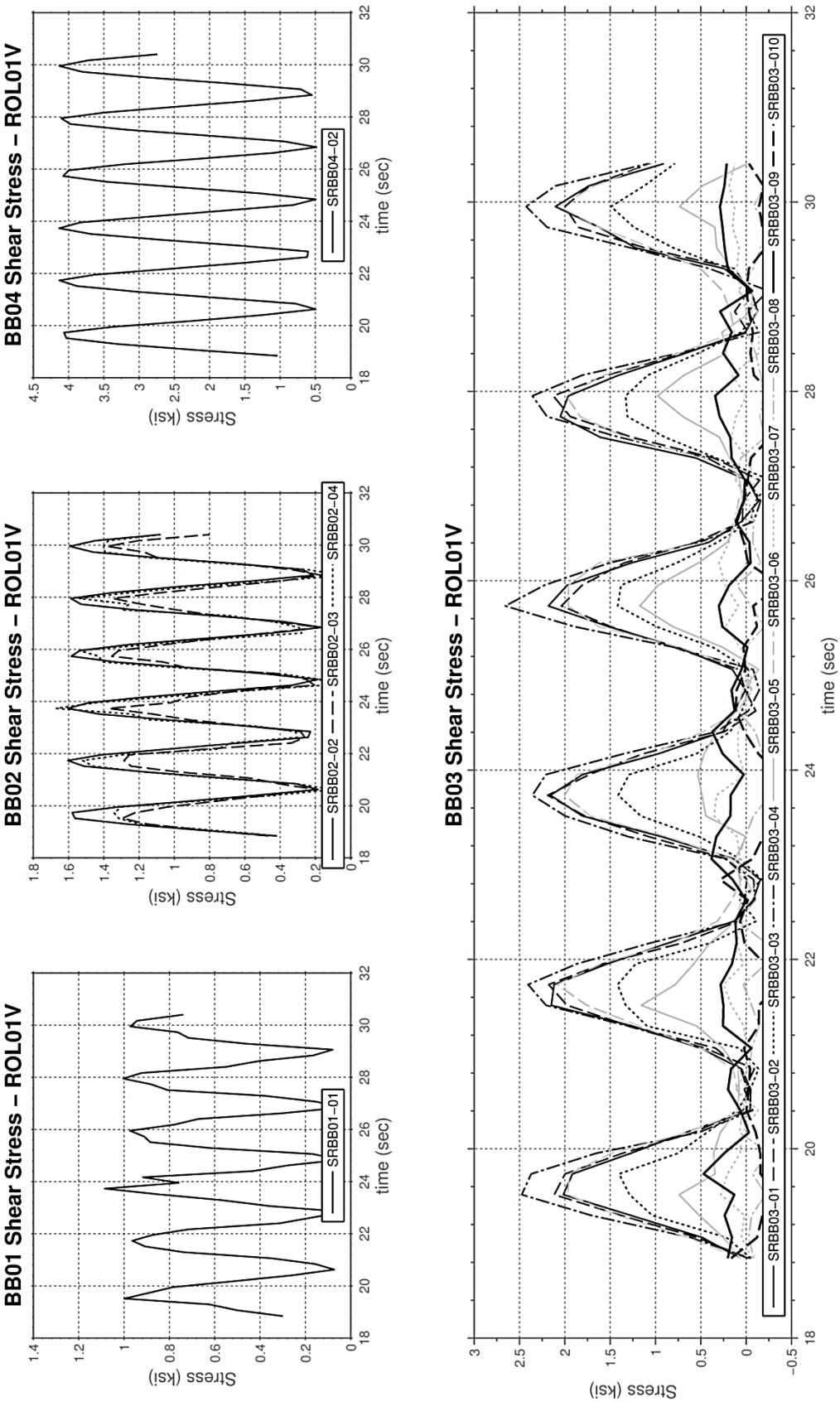

Figure 4-15: Typical bearer bar transition zone shear stresses for vertical tests (ROL01).

4.4.7 Bearer Bar Transverse Displacements

In several of the vertical loading tests, a small initial transverse displacement of the system was imposed before vertical cycling commenced. The transverse displacement time history of the bearer bars is reported in Figure 4-16. Although cyclic vertical loads did have a beneficial effect on the re-centering of the system, the re-centering was an order of magnitude smaller than initial drift displacements observed in the horizontal tests.

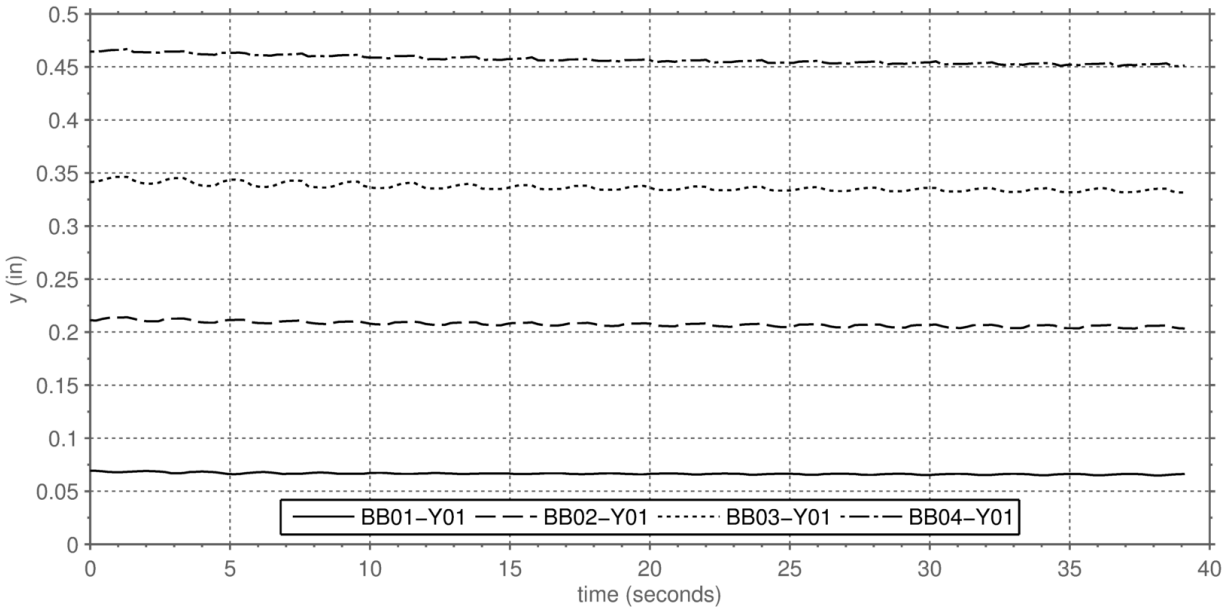

Figure 4-16: Bearer bar y-displacements for vertical test with initial transverse offset (PIT02).

4.5 Response to Horizontal Load

The transverse response of the system was recorded for each of the geometric conditions. The response of the system was nearly identical for each of the configurations, and a typical response is reported in this section. Refer to Appendix B for additional data from each of the geometric configurations. Each figure reproduces the same time interval in the same test unless otherwise indicated, near the midpoint of the loading protocol.

4.5.1 Loading History

The horizontal load on the specimen and the displacement at the pseudo axle are reported in Figure 4-17. The friction force, resulting from the PTFE slider in the axle assembly, has been removed from these measurements. These values were recorded by the MTS LVDT and load cell respectively. In the reported response the pseudo axle was directly over bearer bar 03. The vertical load on the specimen was held constant at 28 kips as determined using Equation 4-1. The maximum displacement and the maximum load were slightly offset in time, with the maximum displacement occurring slightly after the maximum load. This characteristic was independent of the data sampling frequency.

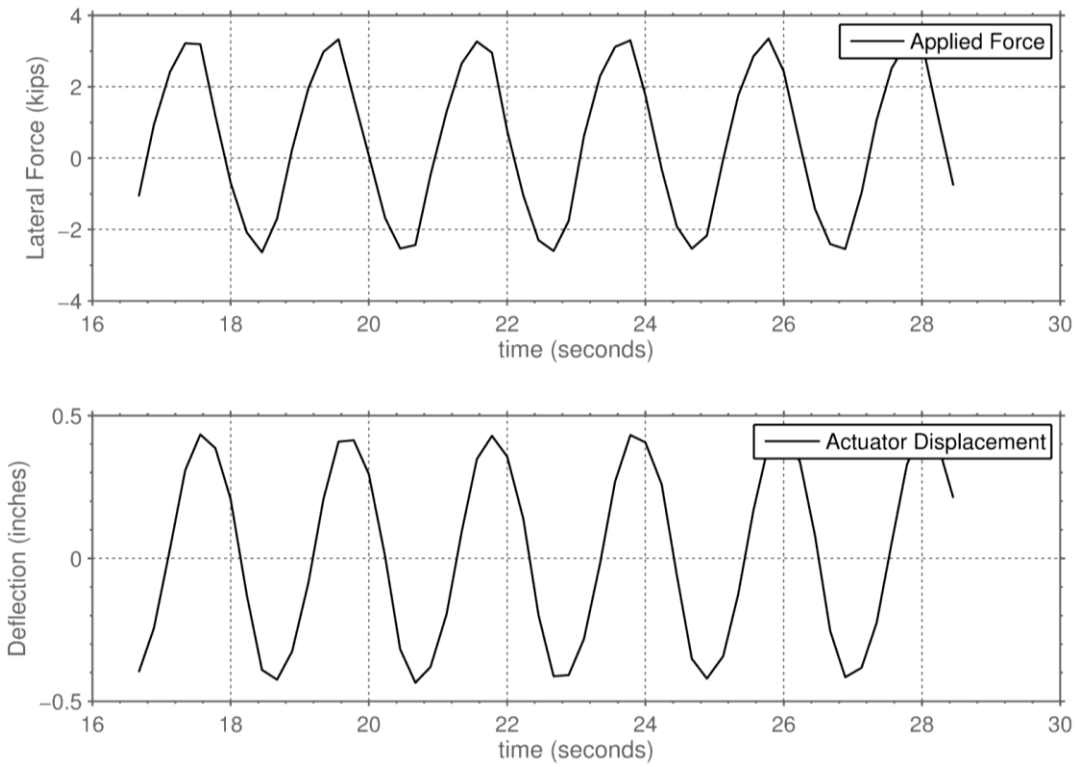

Figure 4-17: Typical transverse loading time history for horizontal test (PIT02).

4.5.2 System Hysteresis

The horizontal load on the specimen is plotted against the displacement at the pseudo axle in Figure 4-18. Again, the friction forces present in the experimental apparatus have been subtracted from the horizontal forces using the measured friction coefficient. The hysteresis plot shows that after the horizontal force was removed, significant displacements were still present. It also shows significant energy dissipation per cycle. It should be noted that the lack of continuous rails makes the experimental apparatus more susceptible to residual displacements.

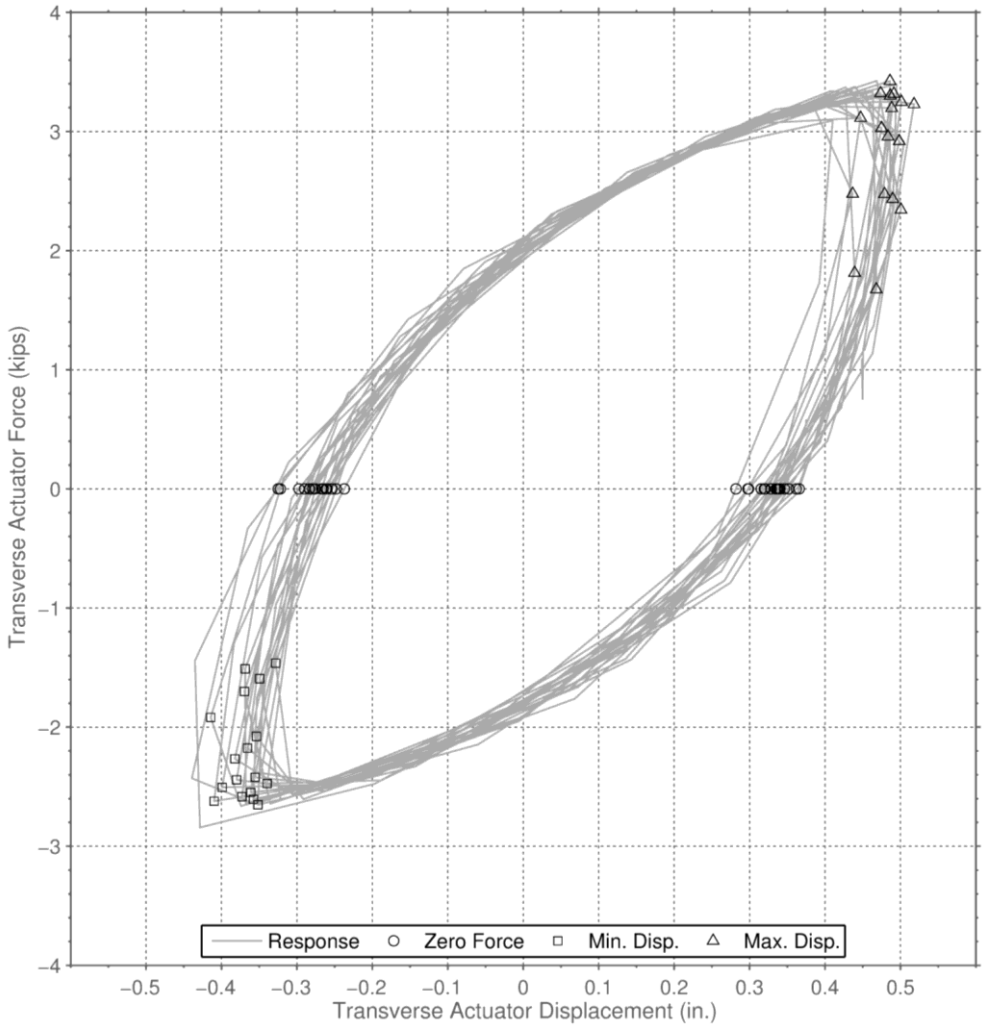

Figure 4-18: Typical load-displacement plot for horizontal tests (PIT02).

4.5.3 Bearer Bar Transverse Displacements

The displacements of the bearer bars versus time are reported in Figure 4-19. The rails rotated essentially as rigid bodies about the wall pins, with the displacements increasing nearly linearly from the pin to the free end.

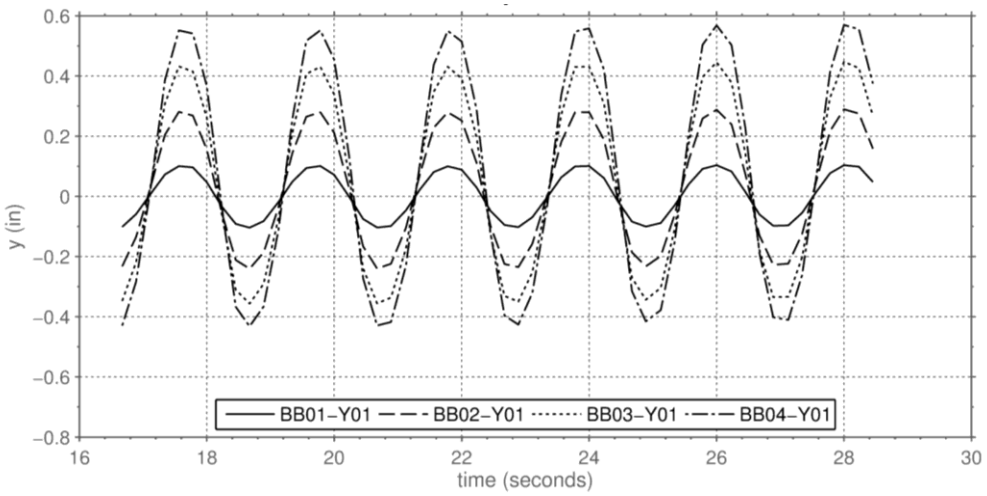

Figure 4-19: Typical bearer bar y-displacement time history for horizontal tests (PIT02).

In tests conducted under force control, initial cycles caused increasing transverse displacements. This initial drift is reported in Figure 4-20 for the PIT01 test in which this behavior was most dramatic. The amplitude of the sinusoidal force applied to the specimen was constant during this time. The specimen displayed an initial transient response which decayed to zero after only several oscillations; subsequent bearer bar displacement cycles followed the path of the cycle previous to it.

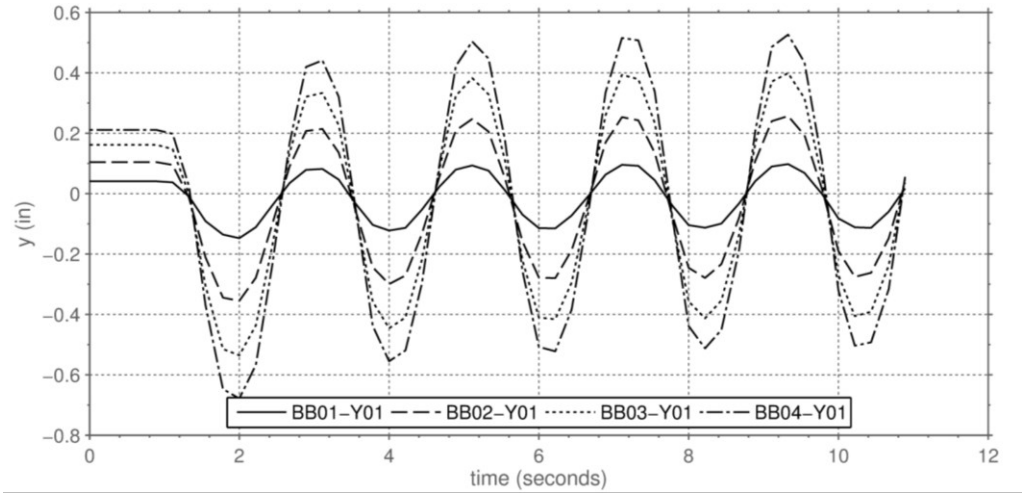

Figure 4-20: Initial transverse system drift for horizontal tests (PIT01).

The maximum, minimum, and initial displacements of the bearer bars versus the longitudinal distance from the wall pin are reported in Figure 4-21. It was observed that as the system displaced from its neutral position the relative bearer bar displacements became less linearly related to distance from the pin. This is attributed to lateral bending of the rails. It should be noted that this test was conducted under load control, and this is reflected in the symmetric pattern of the maximum and minimum displacements.

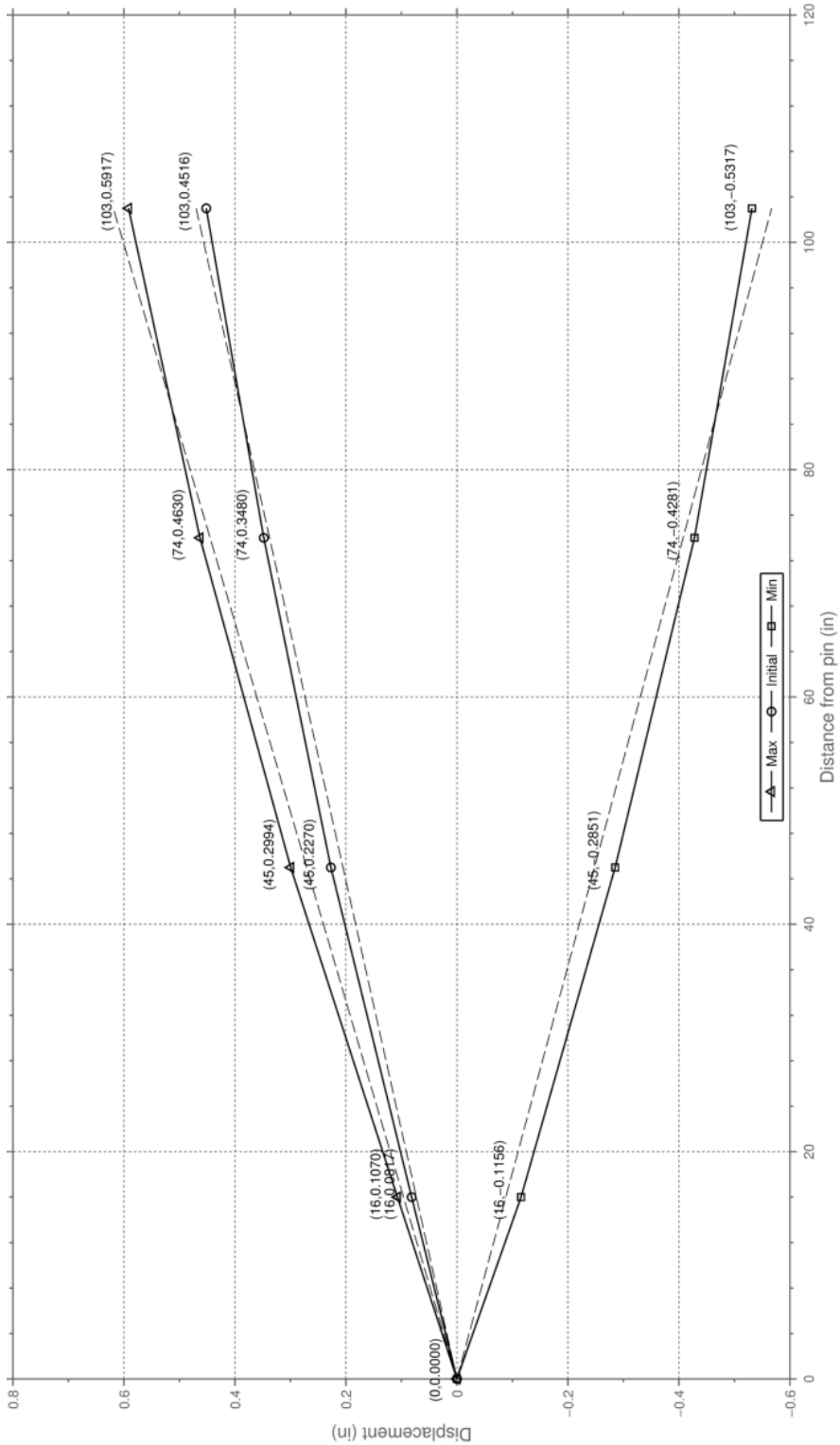

Figure 4-21: Typical bearer bar maximum and minimum displacements for horizontal tests (PIT02).

4.5.4 Rail Stresses

The weak axis rail bending stresses between bearers 02 and 03 are reported in Figure 4-22. Gages were located 17 inches apart, centered about mid span. One strain instrument malfunctioned during the reported test on the left guard rail. It was observed that the stresses in the left running rail were close to twice those in the other rails; this finding was consistent throughout the geometric testing program. For each condition, stresses were compressive on one side of the rail neutral axis, and tensile on the other. This finding was consistent with the rail deflected shape presented in Section 4.5.3. In all geometries, all rails stresses remained below 15 ksi.

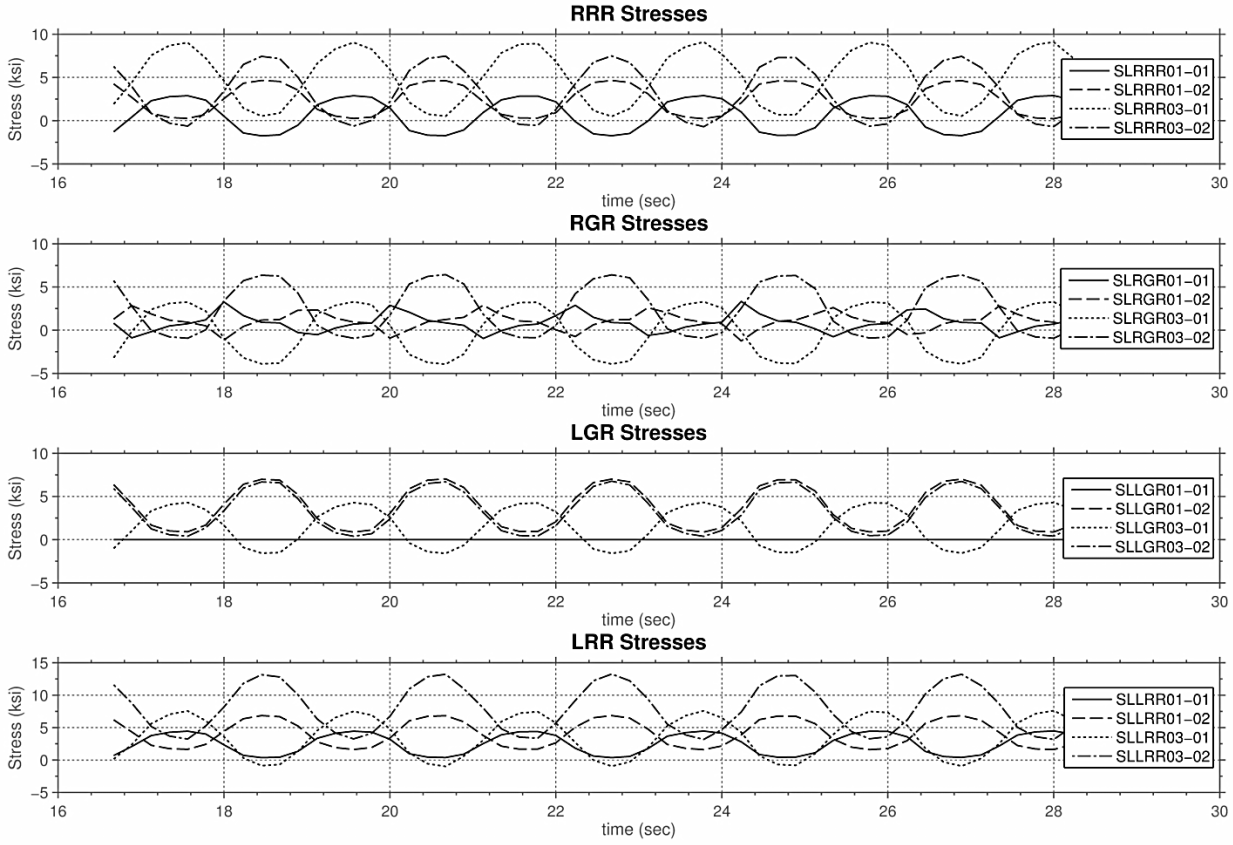

Figure 4-22: Typical transverse rail shear time history for horizontal tests (PIT02).

4.5.5 Bearer bar end rotations

The inclinometers that were used to determine the bearer bar end rotations function by measuring the direction of gravity in an inertial reference frame. Unfortunately, this makes them highly sensitive to accelerations in addition to inclination. This was deduced only after testing was complete. Inclinometer readings were taken during the horizontal tests, but they are not reported here because they do not represent the true rotations.

4.5.6 One sided time history

In the YAW01 geometric configuration, the specimen was subjected to repeated loading in a single direction. The time history of the MTS load and displacement are reported in Figure 4-23. The cyclic amplitude of the control signal was adjusted, and after four complete cycles, the design transverse load was reached. It was observed that the displacement of the system stabilized after which further load displacement cycles followed the path of the one previous to it.

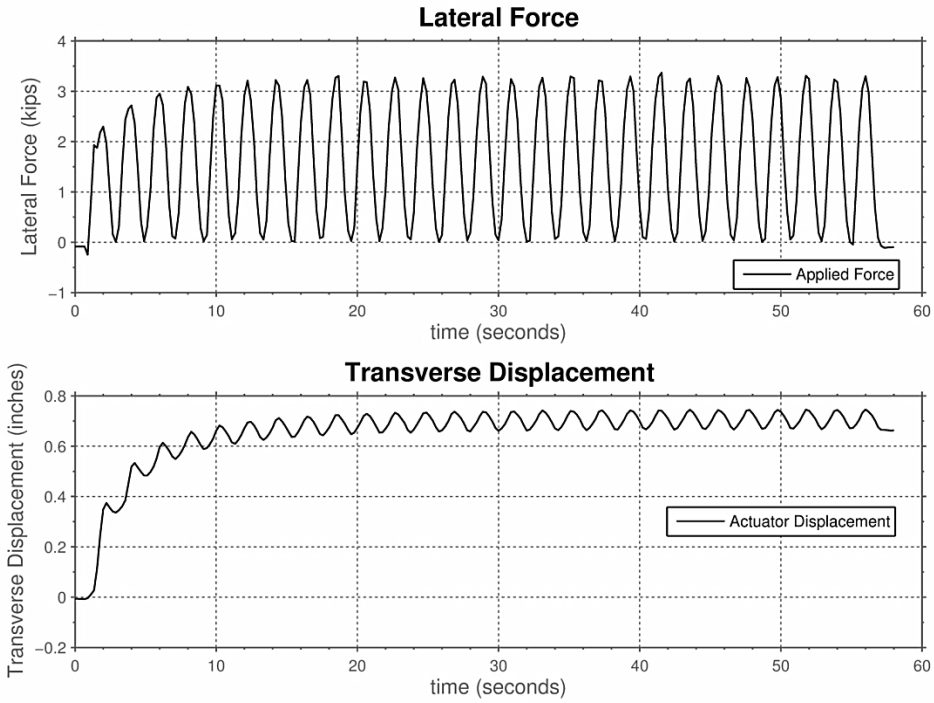

Figure 4-23: One sided time history for a repeated horizontal load (YAW02).

Chapter 5 Data Analysis

5.1 Sliding Interface Friction

The friction coefficient between the PTFE sliding surfaces in the pseudo–axle assembly was measured at four separate times throughout the testing protocol, and was found to be consistent both before and after re-greasing the assembly. The friction coefficient was determined by dividing the instantaneous transverse force required to displace the stainless steel slider by the instantaneous vertical axle load computed using Equation 4-1. Table 5-1 reports the friction coefficients that were fitted to the data measured after the initial stiction peaks and before the release of the transverse forces.

Table 5-1: Measured friction coefficients

Test	***Friction coefficient, μ***
FRK01	1.45%
FRK02a	1.32%
FRK02b	1.40%
FRK02c	1.35%
Average	**1.4%**

Because of the consistency of the measured values, it was presumed that the friction coefficient remained constant throughout the experimental testing regime and was subsequently subtracted from all horizontal forces imposed on the system. All horizontal force values that are presented herein have been adjusted to remove these friction forces.

5.2 Experimental Apparatus

Overall, the experimental apparatus performed as anticipated. Rail fastener displacements were negligible; the proper gage distance between rails was maintained throughout the testing program. The loading beam and pseudo-axle assembly were stable and remained at the same point in space as the axle moved transversely beneath them.

The transverse displacements of the wing relative to the floor that were recorded were roughly 1% of the displacement of the bearer bars relative to the wing for the cyclic tests. In subsequent data, these small displacements will be ignored.

The vertical deflections of the wing plates under cyclic vertical load were larger than anticipated. The deflections of the wing plates constituted approximately 10% of the observed deflection of bearer bar 03. Although this data is important for interpreting the measured response, a more detailed picture of the wing plate deformations would be needed to use this information to correct the bearer bar deflections.

5.3 System Stiffness

The stiffness of the system was nearly bi-linear. Figure 5-1 reproduces the response of the system to monotonic load in the STF01 and STF02 experiments, and includes the bilinear fitted values and the predicted response of a single FPS bearing to the same motions under the full axle load, using the known bearing geometry and 8% friction.

Figure 5-1: Force displacement behavior for STF01 and STF02 with predicted FPS bearing behavior.

An initial force of around 2 kips was required to break the static friction forces of the various components of the system, after which the system behaved elastically with a stiffness of nearly 2 kips/ inch. When the guard rails were attached to the bearer bars, additional frictional forces were present. This response is closely related to the response specified by the friction pendulum bearing manufacturer. It can be shown that given the

bearings' geometry, the tangent translational stiffness can be expresses using Equation 5-1.

$$K = W/L \tag{5-1}$$

where

K = Transverse bearing stiffness (kips/in)
W = Vertical force on the friction pendulum bearing (kips)
L = Effective pendulum length (in)

For the bearings used in the specimen, the effective length was specified as 20.5 inches. This value was also confirmed by measuring the internal components of one of the bearings and computing the effective length from geometric principles. For the vertical axle load of 28 kips, this corresponds to a translational stiffness of 1.4 kips / in. The frictional coefficient specified by the manufacturer was 8% ± 6%. Figure 5-1 shows the response using the design friction value of 8%. However, the friction coefficient achieved must have been lower. In the absence of the guard rails, the initial measured breakaway force shown in Figure 5-1 is approximately 0.7 kips, or about one third of the predicted frictional resistance of the bearing, which must therefore have been no greater than 2.7%. If the running rail fasteners contributed in any way to that initial breakaway resistance, the bearing friction would have been smaller still. The internal slider in the bearing is made from a proprietary woven polymer, for which the friction is likely to depend on the contact stress, as is the case for most polymers. Thus, if the wheel load

were to be distributed among more than the four bearer bars used in these tests, the individual bearing loads will be smaller and the friction would be higher.

The remaining tangent stiffness is attributed to frame action between the rails and bearer bars. This behavior is highly dependent on the characteristics of the rail fasteners. At a displacement of 1.63 and 1.71 inches for STF01 and STF02 respectively the system stiffened significantly, to over seven times the initial stiffness. Table 5-2 summarizes the results of the stiffness tests. The entries highlighted in bold are the values plotted in Figure 5-1.

Table 5-2: Fitted stiffness coefficients for STF01 and STF02 tests

Test	*y-intercept*	*Primary stiffness*	*Secondary stiffness*
STF01a[2]	1.8 kips	2.2 kips/ in	
STF01b[2]	1.8 kips	2.0 kips/ in	
STF01c[1]	**1.3 kips**	**2.0 kips/in**	**15.5 kips/in**
STF02a[3]	0.7 kips	1.9 kips/ in	
STF02b[1]	**0.7 kips**	**1.9 kips/in**	**16.8 kips/in**
STF02c	0.7 kips	1.8 kips/ in	
Average		1.9 kips/ in	16.1 kips/ in

1. The reported results, shown in bold, are presented in Figure 5-1
2. Tests were terminated before reaching secondary stiffness due to floor anchor slip in the experimental apparatus
3. Test was terminated before reaching secondary stiffness, due to instrument failure

The stiffness decreased slightly throughout the testing program, but was observed to be consistent, even without the guard rails. The noticeable difference in the fitted y-intercept shows that the behavior of the guard rail fasteners, which were included in Test STF01 but not STF02, was highly frictional.

5.4 Vertical Response

Measured data from the vertical load tests was investigated in order to compare the system's behavior between the different geometric configurations. The expected mid span deflections of the bearer bars were calculated using the method of virtual work, assuming that the axle load was transferred to the bearer bars solely through the running rails and was equally distributed amongst them. Figure 5-2 shows both the calculated moment of inertia and assumed moment diagram that was used to perform these computations.

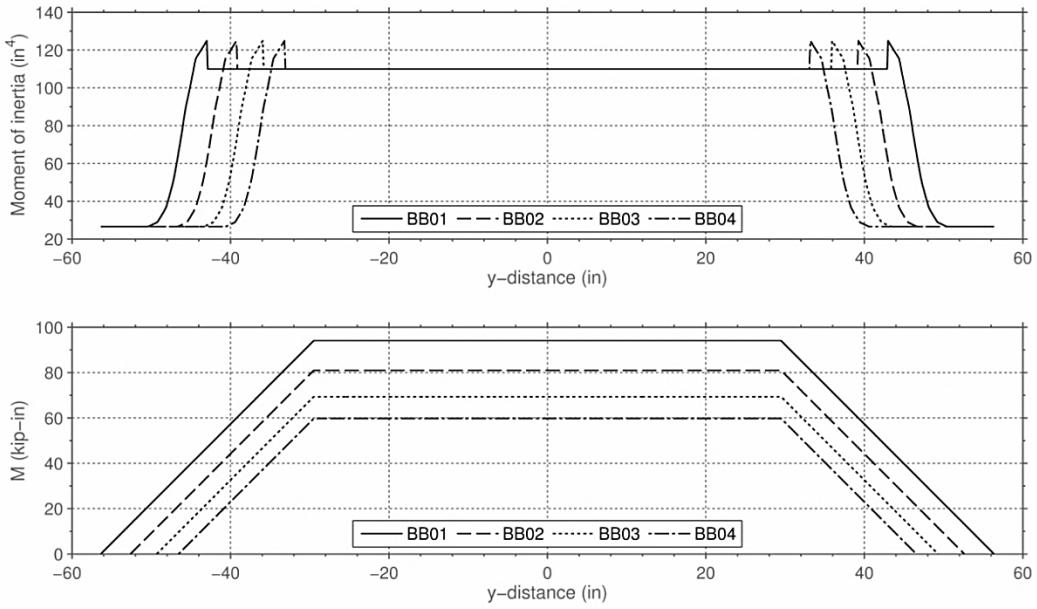

Figure 5-2: Bearer bar moment of inertia and assumed moment distribution used to compute average stiffness.

It was found that the expected bearer bar mid span deflections were 0.044 in, 0.034 in, 0.026 in, and 0.020 in for bearer bars 01-04 respectively. This same computation

was repeated for a range of vertical loads, and the vertical mid span stiffness of each bearer bar was computed as the slope of the resulting line. Figure 5-3 and Table 5-3 sumarize the results of these computations, including the calculated average bearer bar stiffness for the experimental specimen. The applied load refers to the total load applied to the bearer bar at the two running rail locations, separated by the standard gage. The stiffness is computed as the applied load divided by the individual mid-span deflection.

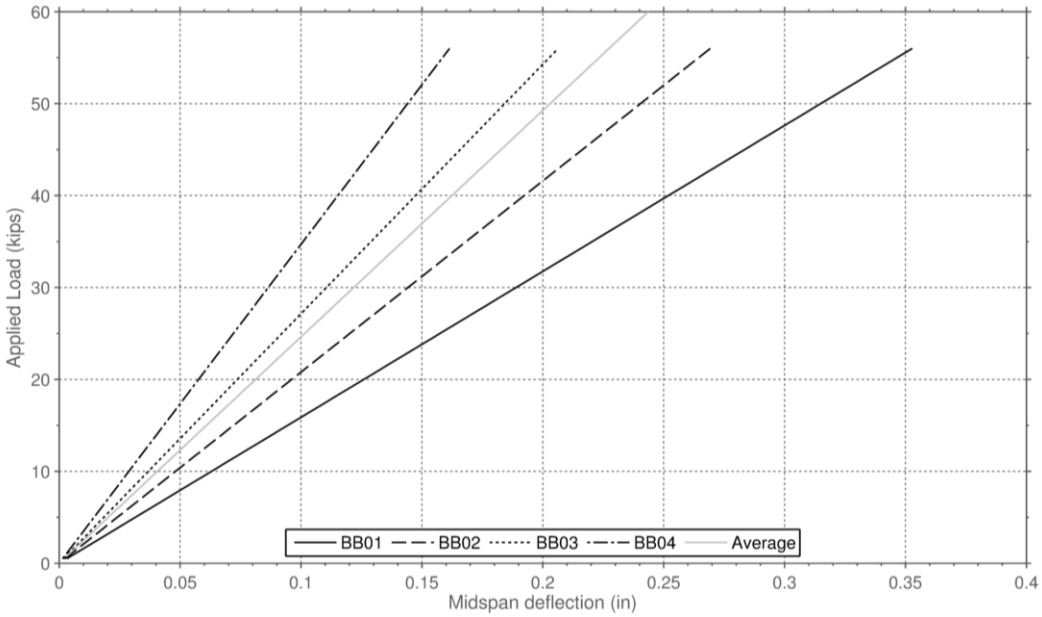

Figure 5-3: Computed mid span bearer bar deflections for the applied loads, average bearer bar stiffness.

Table 5-3: Computed bearer bar mid span stiffness

Bearer Bar	*Length between bearing centers*	*Stiffness*
01	112.75 in	158.7 kips/ in
02	105.25 in	208.0 kips/ in
03	98.625 in	271.3 kips/ in
04	93.125 in	347.0 kips/ in
Average	**102.4 in**	**246.3 kips/in**

The stiffness values presented in Table 5-3 include the total load applied to the system at the running rails and the resulting deflections at mid span. Although these two measures appear to be incompatible, this approach allows for the development of a simple model for comparison with experimental data.

The rail-bearer bar system was modeled as a beam on an elastic foundation (BoEF) as pictured in Figure 5-4. The ends of the beam were assumed to be free. The combined moment of inertia for all four rails was lumped at center of the system, I = 4 I_{rail} = 262 in^4. The foundation stiffness was computed by dividing the average effective stiffness of the bearer bars by the bearer bar spacing, k = (246.3 kips/ in)/ (29 in) = 8.5 kips/ in^2.

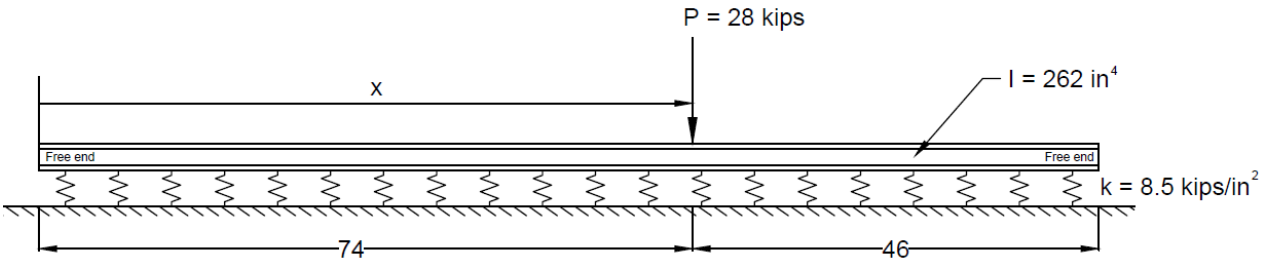

Figure 5-4: Beam on an elastic foundation model for the test specimen

The characteristic length of the system was computed using Equation 5-2.

$$1/l_c = \sqrt[4]{k/_{4EI}} = \sqrt[4]{\frac{8.5 \text{ kips/in}^2}{4\,(29{,}000 \text{ ksi})(262 \text{ in}^4)}} \rightarrow \; l_c = 43.5 \text{ in} \qquad (5\text{-}2)$$

The behavior of such a system largely depends of the dimensionless parameter L/l_c, where L is the length of the rail segment. In this discussion the length of the rail is taken to be 120 inches, consistent with the specimen. In this case $L/l_c, = 2.75$, indicating the beam is of medium length and the stiffnesses of both the rail and the bearer bars are important.

5.4.1 Bearer bar vertical deflections

The maximum bearer bar deflections were recorded for each of the geometric tests and are shown in Figure 5-5. The deflection predicted by the finite beam on an elastic foundation model is also presented. The general pattern of the deflections in tests where the pseudo axle was directly over bearer bar 03 was consistent throughout the testing program and matched that predicted by the simple BoEF model. The displacement pattern is different in the REF01 test because of the different point of load application, between bearer bars 02 and 03.

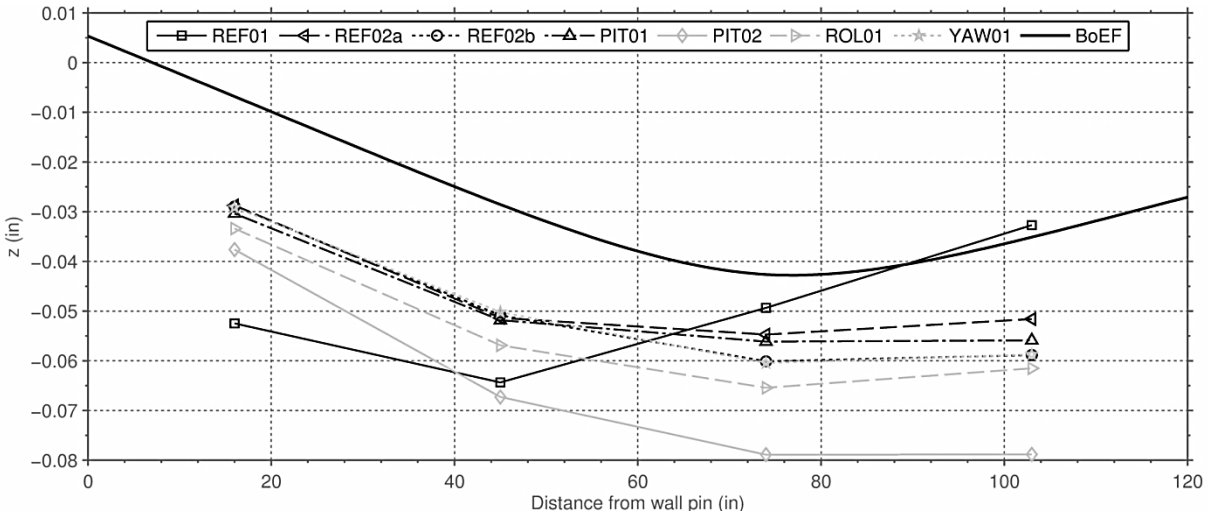

Figure 5-5: Bearer bar maximum mid span deflections and predicted deflections from simple beam on elastic foundation model.

These measured deflections include the wing deformations, the bearer bar displacements, as well as the vertical displacement of the ends of the beam due to the rotation of the friction pendulum bearings. Independent of the geometric configuration, the pattern and magnitude of the deflections are quite similar. The measured deflections' being larger than those predicted by the BoEF model reflects the fact that the BoEF model does not include the wing and bearing deformations. Furthermore, the BoEF model shows an upwards slope at the right end (Bearer Bar 04) which is less apparent in the measured data. This is attributed to the fact that the higher numbered bearer bars were longer and therefore more flexible, but the BoEF model was based on an average bearer bar stiffness. Given these approximations, the fit between the measured and predicted values is considered acceptable.

More importantly, the measured deflections are too small to have a significant effect on the vertical alignment of the track bridge.

5.4.2 Bearer bar mid span stresses

The maximum bearer bar mid span stresses were recorded for each of the geometric tests and are shown in Figure 5-6. With the exception of test REF01, the pseudo axle was directly over bearer bar 03, and in those tests the general pattern of the response was similar in almost all the different configurations. The implication is that the system configuration has almost no effect on the bearer bar stresses. Test PIT02 appears to be an exception. The reasons for its very different behavior are unknown.

In test REF01, the load was applied half way between bearer bars 02 and 03. The response pattern is similar in principle to that observed in the other tests, but, as might be expected, the stresses are higher nearer the wall and lower at bearer bar 04.

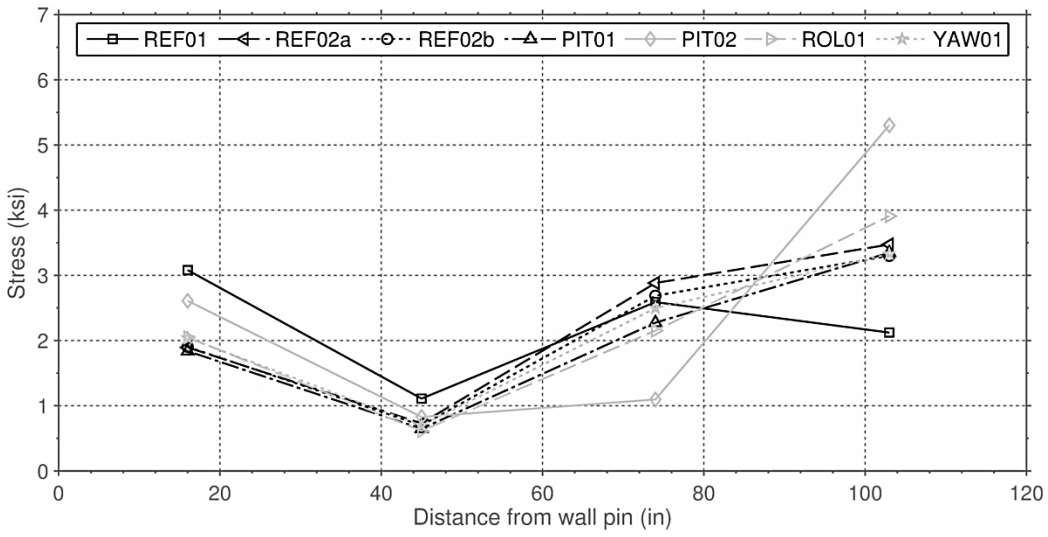

Figure 5-6: Bearer bar mid span stress against distance from wall pin.

The stresses experienced by bearer bar 02 were much lower than anticipated. It is possible that shimming affected these measurements, gage failure occurred, or the gages on bearer bars 01 and 02 were mislabeled and should be reversed in the figure. None of these possibilities are very likely; great care was taken in installing and labeling the instruments and the shimming process was performed iteratively under controlled conditions. The cause of this anomaly is unknown.

What was observed was that the geometric configuration, had no effect on the bearer bar mid span stress. The measured stresses were below 12% of the yield stress of the material, well below tolerable limits for the design.

5.4.3 Rail stresses

The maximum rail stresses midway between bearer bars 02 and 03 for three of the rails were recorded for each geometric configuration, and are presented in Figure 5-7. The right guard rail values are not presented, because of strain gage failure. The bending stress predicted by the beam on elastic foundation model is also shown. The simple model under-predicts the stress in the running rails and over-predicts those of the guard rails. This result is unsurprising given that the rails were all lumped in a single element in the model, but in the test setup the running rails were loaded directly and stress was induced in the guard rails only indirectly through their interaction with the other elements in the framework.

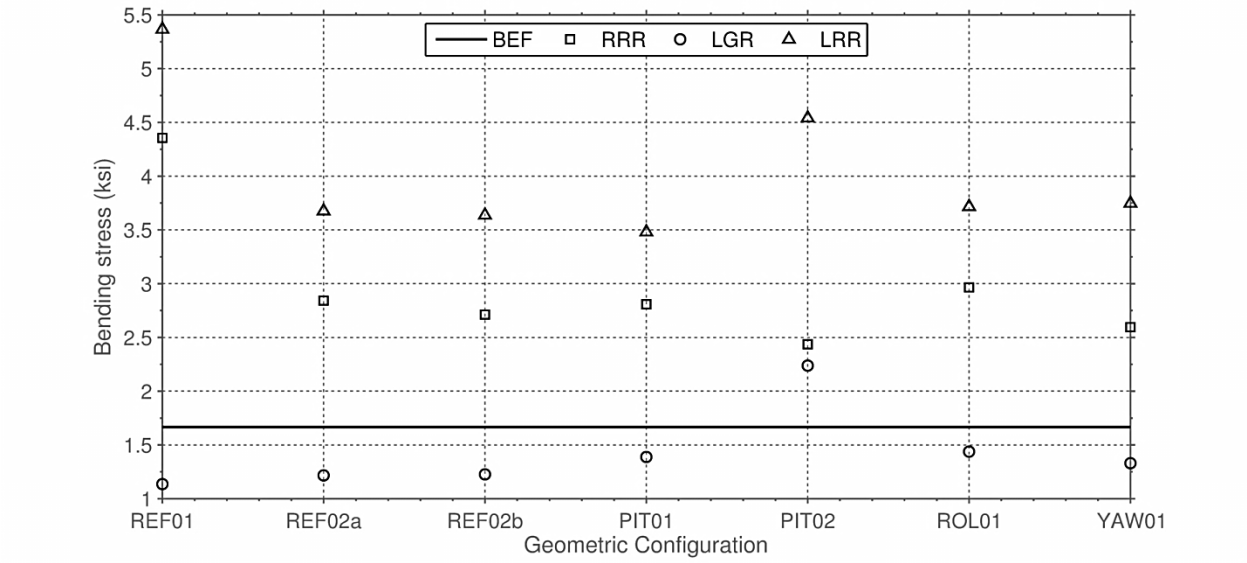

Figure 5-7: Maximum bending stress on bottom flange of rail and predicted value from simple BoEF model.

The rail observed stresses were similar in all the geometric configurations except REF01 and PIT02. In REF01 the load was placed at mid-span between bearer bars 2 and 3, which is where the gages were located, so the larger stresses in that case are not surprising. The response in configuration PIT02 is anomalous, as it was for the bearer bar stress measurements. It appears that some error existed in the test setup for that test. Overall, the stresses in the rails were less than 5% of the estimated yield stress of the rails.

5.5 Horizontal Response

Two features of the specimen are investigated in order to compare the system's behavior between geometric configurations. Both dimensionless parameters have implications for the performance of the CESURA prototype.

5.5.1 Normalized crossover displacement

Crossover displacements were computed to assess the ability of the system to re-center itself after it was displaced by a transverse force. This measure allowed comparisons between the experiments, despite unintended variations in the maximum and minimum force and displacement present in the loading protocols.

The normalized crossover displacement (NCD), given by Equation 5-3, is a dimensionless parameter that compares the system's displacement at zero force to the system's maximum displacement, as illustrated in Figure 5-8.

$$\text{NCD} = \frac{\Delta_{\text{Crossover}}}{\Delta_{\text{Maximum}}} \tag{5-3}$$

A perfectly elastic system would have an NCD of 0.0, while a perfectly frictional system would have an NCD of 1.0. If a system is constructed with both elastic and frictional components, as the CESURA system is, it should behave as shown in Figure 5-8 with $0.0 < \text{NCD} < 1.0$. The ratio of elastic and frictional components must be balanced in the CESURA system in order to achieve the greatest performance.

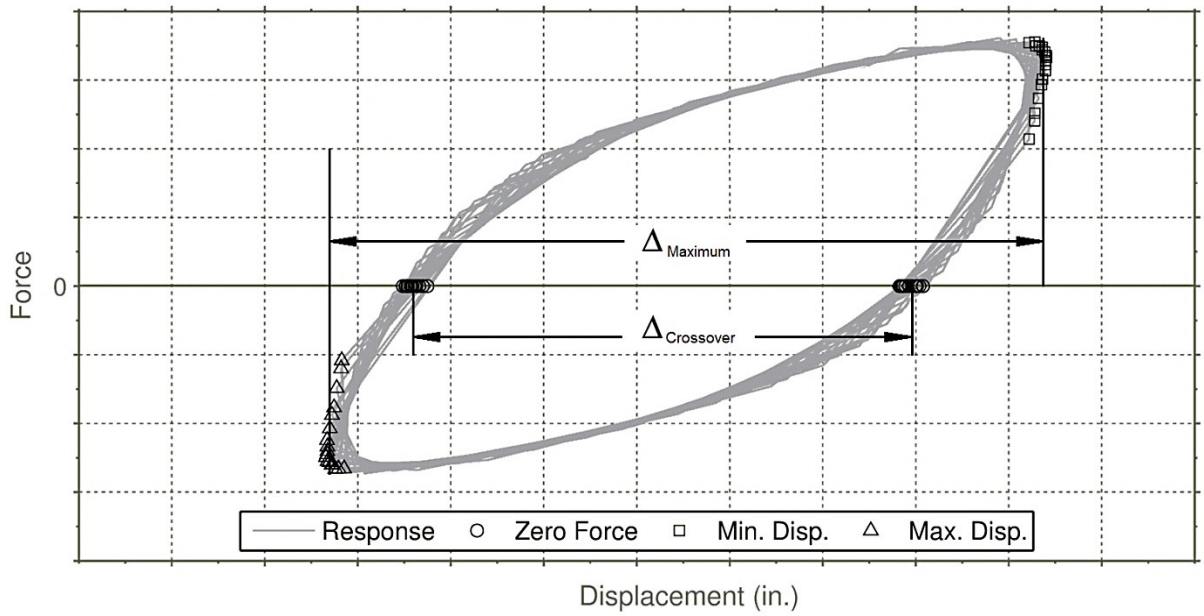

Figure 5-8: Crossover displacement definition.

Table 5-4 reports the computed NCD for each of the component geometries. Test REF02 was performed twice, once under load control and once under displacement control, to examine the effects of the control measure. These results show that the experimental apparatus behaved similarly, independent of the geometry of the wing plates.

Table 5-4: Computed normalized crossover displacements

Test	***Normalized Crossover Displacement***
REF01	0.693
REF02a	0.749
REF02b	0.658
PIT01	0.737
PIT02	0.701
ROL01	0.701
YAW01	0.727
Average	**0.709**

The average NCD of 0.71 would indicate that the frictional elements of the system (bearings, rail fasteners, PTFE sliding assembly) far outweigh the elastic elements (elastic frame action between rails and bearer bars). While this behavior is true of the specimen, the conclusion for the prototype may be different. It contains an important additional re-centering element in the form of the rails, which are fixed against translation at each end of the track bridge. Any transverse movement induces elastic bending in the rails, which thus promote re-centering. The rails in the test setup were pinned at one end and free at the other, so lateral displacement in the form of rigid body rotation could occur freely, without inducing any stresses that would result in re-centering.

5.5.2 Equivalent viscous damping

The equivalent viscous damping ratio (EVDR) was also used to compare the behavior of the specimen in the different geometric configurations. The EVDR is related to the energy dissipation of the experimental system per cycle and also has implications for the performance of the prototype track bridge. The more energy that is dissipated, the smaller the oscillations of the system will be due to train hunting forces: transverse impact loads between the LRV wheels and the running rails.

The equivalent damping ratio for each of the geometric configurations was computed using Equation 5-4.

$$\zeta = \frac{2}{\pi} \frac{A_{loop}}{A_{box}} \tag{5-4}$$

This particular formulation uses the force-displacement loop area and its circumscribing rectangle, as shown in Figure 5-9.

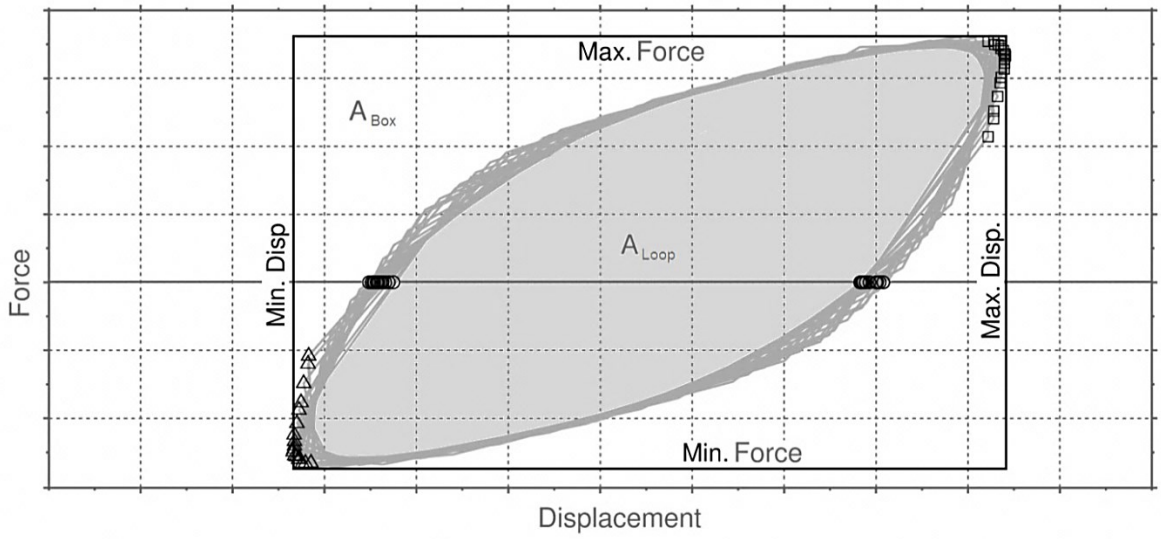

Figure 5-9: Equivalent viscous damping definition

Table 5-5 reports the computed EVDR for each of the geometric tests. These results show that the experimental apparatus behaved similarly, independent of the rotation of the wing plates.

Table 5-5: Computed equivalent viscous damping values

Test	*Equivalent viscous damping*
REF01	0.403
REF02a	0.437
REF02b	0.411
PIT01	0.414
PIT02	0.417
ROL01	0.411
YAW01	0.425
Average	0.417

The average value 0.417 indicates that significant damping was present in the system. The FPS bearings were originally conceived for seismic isolation, and in that environment friction damping is desirable. In the track bridge true viscous damping would be desirable to damp out any vibrations due to vehicle passage. True viscous damping does not inhibit re-centering. However, friction damping does inhibit re-centering, and it can be shown that an FPS bearing, when released in a pull-back test, will theoretically stop sliding a distance μL from the origin, where μ is the friction coefficient and L is the effective pendulum length. Here, L = 20.5 inches. If μ is taken as 3%, the bearing might be expected to reach zero lateral load at a distance of 0.615 inches

from the center. This value is supported by the behavior that was observed in the STF02b test shown in Figure 5-10.

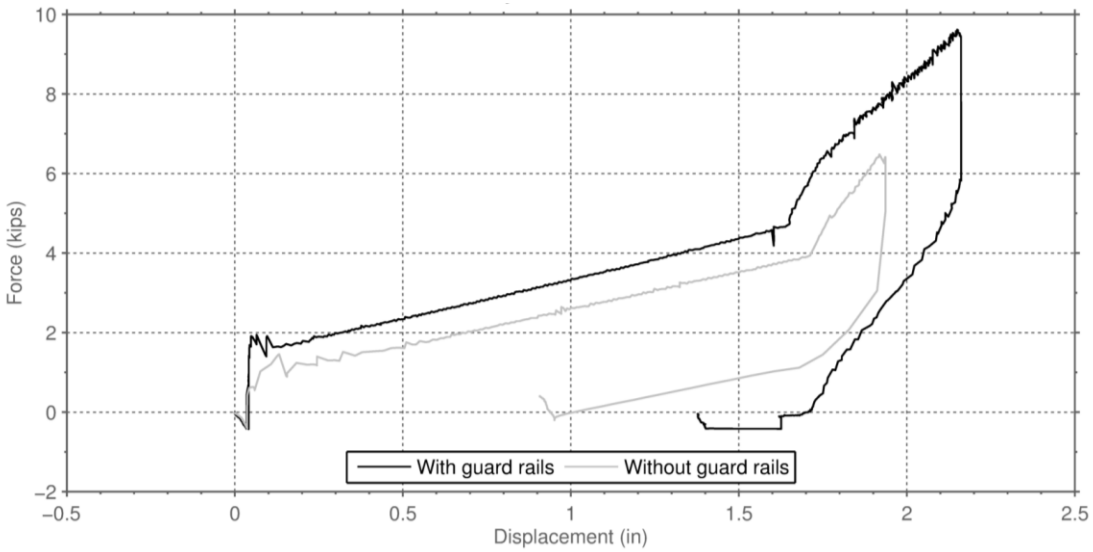

Figure 5-10: Force displacement behavior of the system after unloading the specimen.

In this configuration the transverse load was released abruptly and the system was allowed to reach equilibrium. The fact that the residual displacement is greater than that computed for a single bearing is unsurprising. The vertical forces on the rails were distributed throughout eight bearings, each of which underwent displacements proportional its longitudinal distance from the wall pin. Thus a displacement of 0.9 inches at bearer bar 04 corresponds to a displacement of only 0.13 inches at bearer bar 01. The system, in addition, also had other frictional components that prevented re-centering.

Figure 5-11 shows the load-displacement time history for the PIT01 test, representing the typical behavior of the specimen when subjected to transverse loads. In the horizontal tests the system was not displaced greater than 0.6 inches as is seen in the figure. The lack of re-centering of the specimen is consistent with the observation that the system did not displace further than the theoretical threshold beyond which re-centering would occur due to the friction pendulum bearings geometry alone.

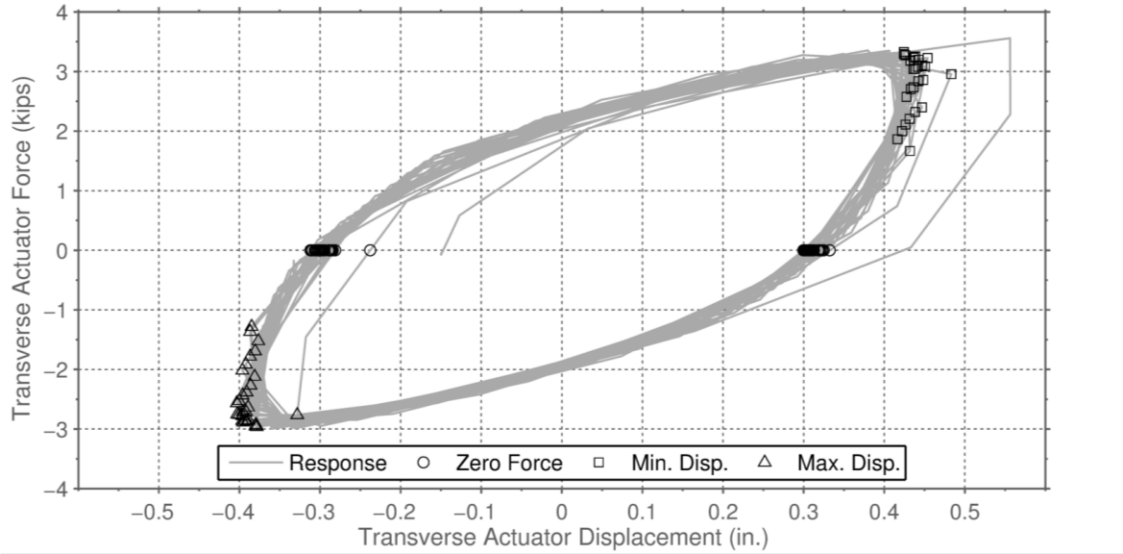

Figure 5-11: Typical force displacement history under cyclic transverse loads (PIT01).

In practice, vibration in the structure generally reduces the residual displacement in an elastic system with friction damping. That fact, combined with the additional elastic restoring forces from rail bending, suggests that re-centering will be less problematic in the prototype than these test results indicate at first sight. However, because re-centering is an important feature of the system, the effects of the restoring

elements and friction elements should be investigated carefully using the prototype geometry, prior to proceeding with final design.

Chapter 6 Discussion of Results

6.1 CESURA Yoke Geometry

In Section 1.5 an introduction to the kinematics of the CESURA system was presented, assuming that the center support bearing was directly over the bridges hinge location. Through this analysis, a method was introduced to ensure slope continuity through the track bridge given a pitch rotation of the joint. In most applications, having the center support over the joint is impractical, because the required substructure is not present. Figure 6-1 shows an idealized version of one side of the CESURA system subjected to a pitch motion with the center bearing offset from the hinge location.

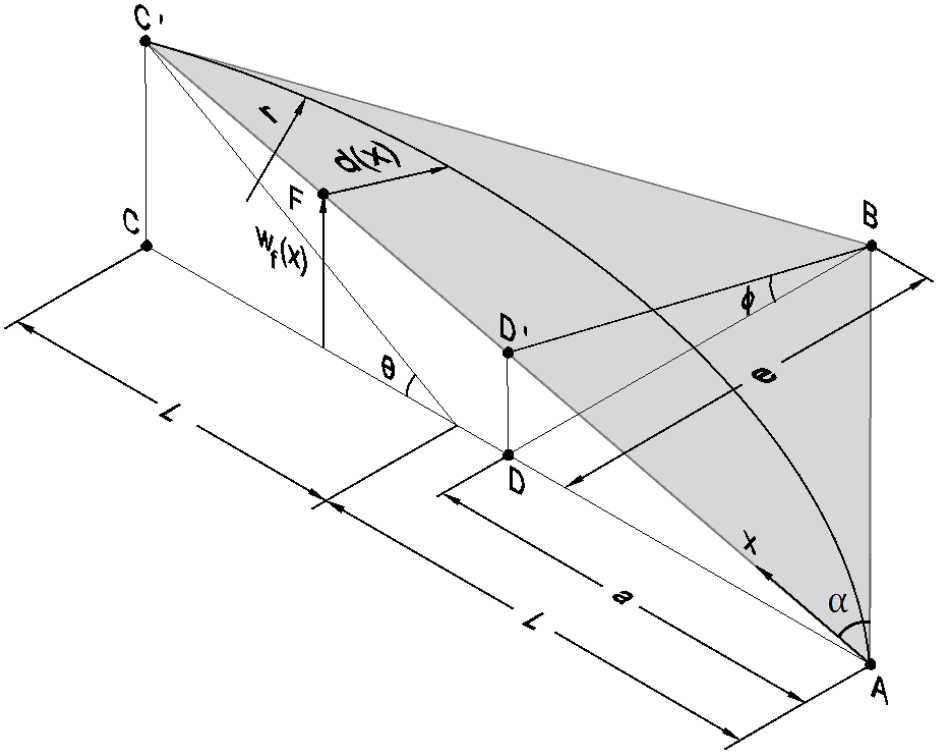

Figure 6-1: Idealized CESURA system with longitudinally offset center bearing.

Points *A, B* and *C* represent the location of the wings plate's supports on the bridges surface in the reference condition. Points *D* and *B* are both offset from the joint that joins the transition span to the fixed or floating portions of the bridge. In this picture, the lines *AC* and *DB* are perpendicular. Points *C'* and *D'* are points on the wings surface after the joint has undergone a pitch rotation of magnitude θ. In this configuration, rails would run along a path parallel to the line *AC*. The parameter, α, represents the angle between the lines *AC* and *AB*. Assuming that the pitch angle, θ, is small, the length *CC'* and *DD'* are given by

$$CC' = L\theta \qquad DD' = \frac{a\,\theta}{2} \tag{6-1}$$

The twist angle of the wing, ϕ, is then

$$\phi = \frac{DD'}{e} = \frac{a\,\theta}{2e} \tag{6-2}$$

Assuming that the bearings yoke is given by a circle with radius, *r*, and define *x* to be the distance from point *A* along the line *AC'*. Then the distance, *d*, as a function of *x* is given by,

$$d(x) = \sqrt{r^2 - L^2 - x^2 + 2Lx} - \sqrt{r^2 - L^2} \tag{6-3}$$

Defining $w_f(x)$ to be the vertical displacement due to a pitch rotation of an arbitrary point, *F*, along the path defined by *d*, it can be shown that:

$$w_f(x) = \frac{\theta\,x}{2} - \frac{a\,\theta}{2e}\left(\sqrt{r^2 - L^2 - x^2 + 2Lx} - \sqrt{r^2 - L^2}\right) \tag{6-4}$$

Which is an elliptical arc joining the two trajectories. The slope of this vertical curve at the boundary $x = 2L$, should match the slope of the transition span, θ.

$$w_f'(2L) = \theta = \frac{\theta}{2} - \frac{a\,\theta(-2(2L)+2L)}{2\,e\sqrt{r^2 - L^2 - (2L)^2 + 2L(2L)}} \tag{6-5}$$

This implies in order to have continuous slopes at the end of the CESURA system, the relationship between the bearing eccentricity, *e*, the length of the system, 2*L*, and the FPS bearing's yoke radius must be

$$r = L\sqrt{1 + \left(\frac{a}{e}\right)^2} \;\; \therefore \;\; \sin\alpha = L/R \tag{6-6}$$

For a bearing eccentricity, e = 3.17 feet, a CESURA half length, L = 21 feet, and a bearing location, a = 18 feet this reduces to

$$r = 21\text{ft}\sqrt{1+\left(\frac{18\text{ ft}}{3.17\text{ ft}}\right)^2} = 121\text{ ft} \tag{6-7}$$

This method allows for the design of the yoke radius of the system based on the pitch motion, but does not account for the complexities of the roll motion, which is harder to conceptualize in this fashion.

6.2 CESURA parametric kinematic studies

In order to investigate the kinematics of the system in greater detail, MATLAB routines were developed to perform kinematic calculations. In these computations, all elements of the system except the rails were assumed to move as rigid bodies. Figure 6-2 shows the graphical output of the program.

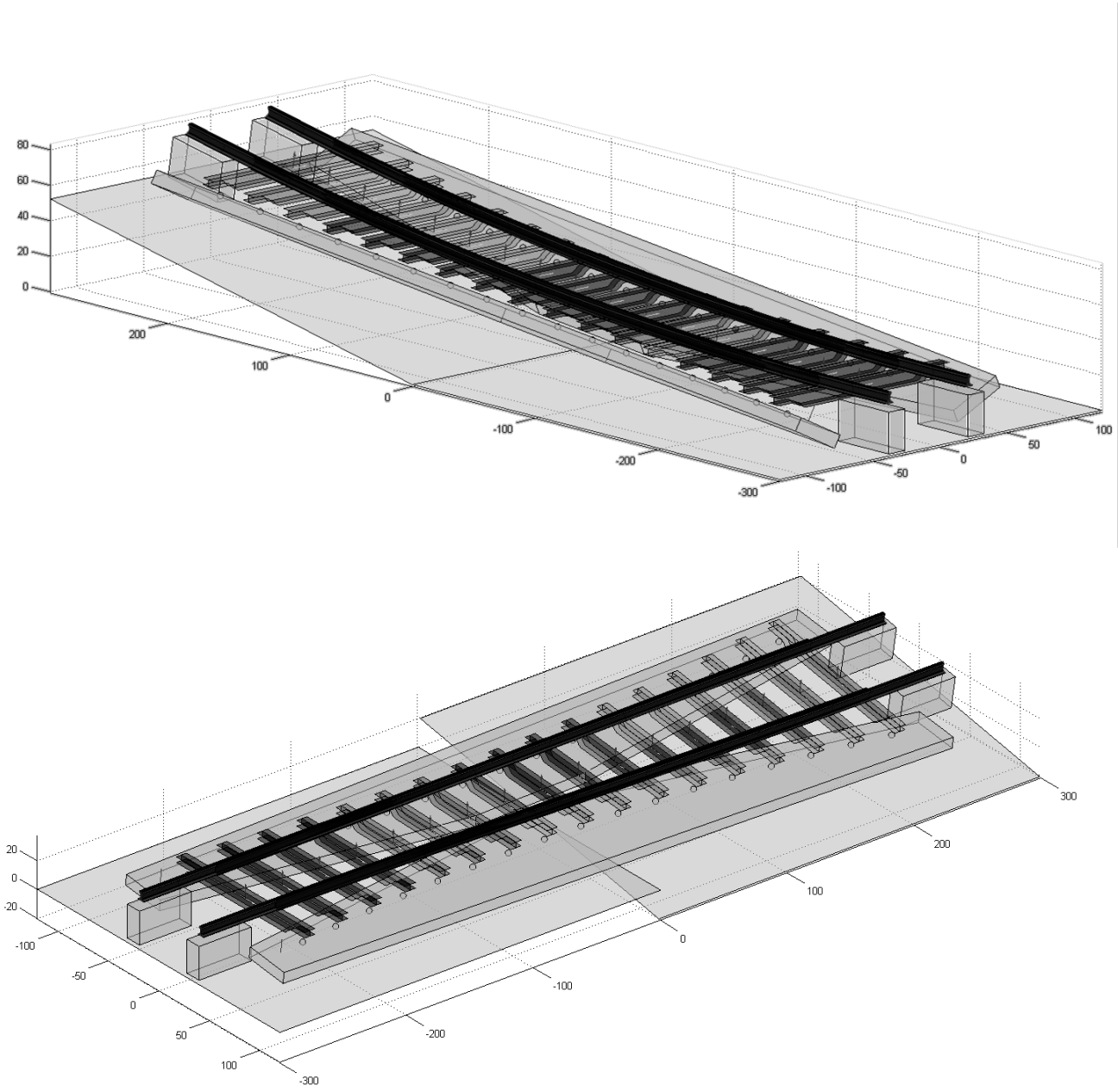

Figure 6-2: CESURA kinematic studies for pitch (top) and roll (bottom) motions (highly exaggerated)

The program calculated the displaced wing support locations and plinth locations on the bridge deck given arbitrary amounts of pitch, roll, and yaw. All

movements were assumed to occur in one span, while the other remained stationary; only relative motions were investigated. Rotations were investigated separately to avoid questions of rotation order. All rotations were assumed to occur about orthogonal axes originating from the center of the track bridge, although rigid body displacements of the displaced span were also programmed into the framework to allow rotations about arbitrary points if desired. The CESURA system was assumed to be centered longitudinally over the hinge location, so that the center of the track bride was directly over the joint.

The wings' end support on the stationary span was assumed to remain fixed. The location of the wings' end support on the displaced span defined their longitudinal axis. The actual wing support-to-support distance was used to compute the wing's displaced support location, determining the displacement of the guided bearing due to the rotation at the joint. The wings' center support was also located on the stationary span, defining the wings transverse axis. The support offset was used to locate the wing support on the stationary span. Small angle approximations were not used in these calculations.

The location of the wing was plotted using the dimensions provided for the box girder and the support bearing thicknesses, using the wings' local coordinates. The friction pendulum bearings bottom half locations were also located on the wings top surface using the local coordinates defined by the support locations.

To properly orient the bearer bars, the curves that define the FPS bearings' locations on the wing were projected into the global CESURA longitudinal-vertical plane. The normal to this curve was found at each of the FPS bearing locations on either wing, and the average of these two directions was used to orient the bearer bar's local weak-axis direction. The line adjoining paired bearings between the wings defined the bearer bar's longitudinal axes.

The height of the friction pendulum bearings, bearer bars, rail fasteners, and rail centroids were all projected above the bearing location on the wing's surface in each bearer bar's weak-axis direction. The gage distance was used to locate the rails between these two points.

Additionally, a cubic curve was fitted between the plinth locations on the two spans, based on the end locations and slopes. These locations represent the first rail supports on either end of the CESURA system, and this line would represent the rails' deformed shape if it was not connected to the track bridge at intermediate locations.

In this treatment, the required relative displacements of the friction pendulum bearings could be computed, but their geometric complexity was ignored. Because the vertical deflections of the bearings are small, they were neglected in the subsequent analysis, and the bearing height was taken as 5 inches nominally. It was found that with the given yoke radius the bearings had ample displacement capacity to accommodate the design motions.

6.2.1 Pitch

Figure 6-3 summarizes a parametric study, where the radius of the bearing yoke was varied to investigate the ideal radius for slope continuity given a center bearing longitudinal distance, a = 18 feet, and a bearing offset, e = 3.17 feet.

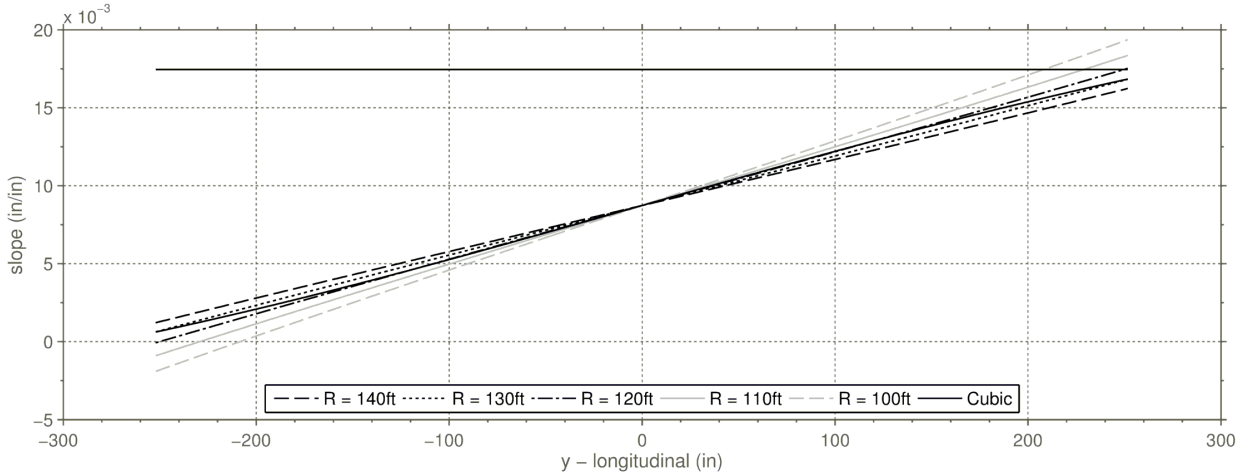

Figure 6-3: Longitudinal slope over the length of the track bridge for various yoke radii and a cubic rail alignment under a 1° pitch rotation about the center of the track bridge.

The radius of 120 feet most closely matched the slope of both the stationary span and the rotated span, whose slope is shown in solid black for reference. This result is consistent with the ideal radius of 121.08 found previously using simple geometric arguments and assuming small-deflection. It should be noted that because the first plinth is located beyond the ends of the track bridge, the cubic has not yet reached the required slope at the extremities of the graph.

6.2.2 Roll

In order to assess the effectiveness of each of the radii in the roll configuration, the centripetal acceleration was computed along the length of the track bridge, based on the instantaneous curvature of the path defined by the rails location on the bearer bars and the design speed of 60 mi/ hr. The reported centripetal accelerations are for a particle moving with a constant velocity along the curve defined by the rails position. In actuality the ride quality of the system would be determined by the suspension system of the LRV. Figure 6-4 reports the centripetal accelerations along the track bridge for several bearing yoke radii, given a center bearing longitudinal distance, a = 18 feet, and a bearing offset, e = 3.17 feet subjected to a roll rotation of one degree. Although the centripetal acceleration does not directly determine ride quality, it can provide insight into the fundamental mechanics of the system.

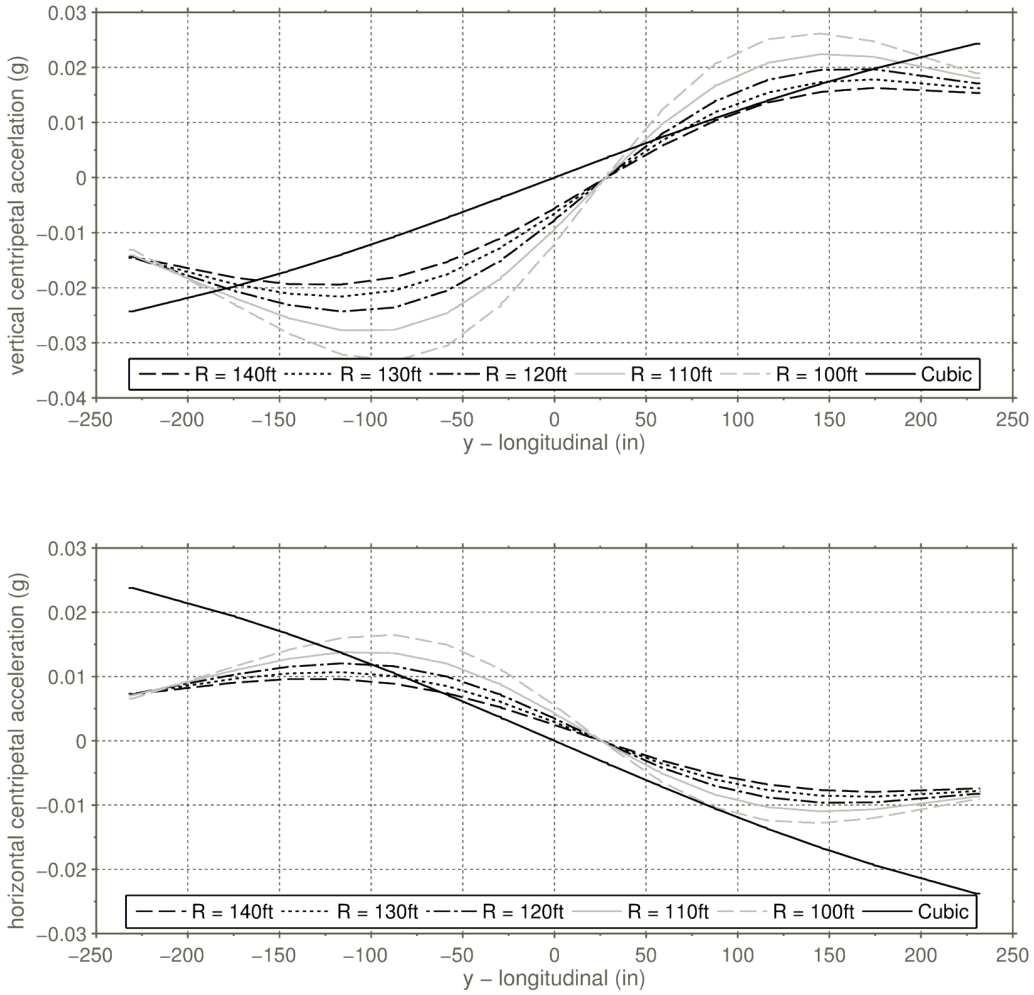

Figure 6-4: Centripetal acceleration over the length of the track bridge for various yoke radii and a cubic rail alignment under a 1° roll rotation about the center of the track bridge.

For the circular bearing geometries investigated, the plots are very similar. Because of the assumption that the end bearing on the stationary span remains fixed, the plots are not symmetric. As was expected the largest bearing yoke radius has the smallest accelerations.

Figure 6-5 shows the transverse slope of the rails for the five bearing yoke radii from the stationary to the displaced span. The transverse slope of the displaced span is shown as a horizontal black line for reference. The transverse slope of the system was calculated using the coordinates of two rail centroids over the track bridge.

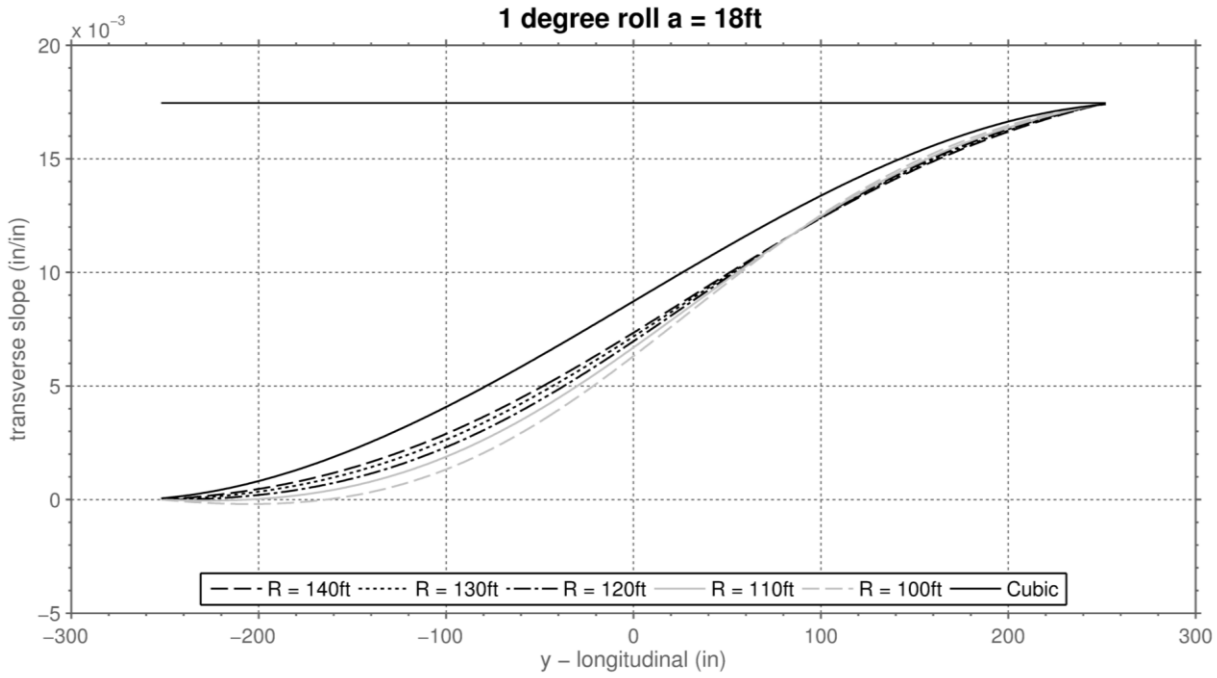

Figure 6-5: Transverse slope over the length of the track bridge for various yoke radii and a cubic rail alignment under a 1° roll rotation about the center of the track bridge.

The radii all provide smooth transitions from one slope to the other, but some appear to be more advantageous than others. The smaller radii, R= 100 feet especially, have the interesting feature of initial negative slopes, which seems ineffective. The radius of 120 feet appears to provide the smoothest transition, with a smaller initial and

final curvature than the higher radii while still maintaining a strictly positive slope throughout the transition.

6.2.3 Yaw

The program that was developed assumes that the bearer bars are always centered about the friction pendulum bearing locations on the surface of the wings. In actuality they will move under the forces of the rails, until the minimum energy state is reached. Although this assumption works well for the pitch and roll configurations, the yaw geometry requires the translation of the bearer bars to assume a smooth horizontal alignment, and therefore is out of the scope of this investigation.

6.3 Choice of CESURA bearing yoke geometry

Although the designers chose a circular path for the bearing yoke geometry to produce a near circular vertical curve, other yoke geometries were investigated to optimize specific desirable attributes of the system.

Figure 6-6 shows a schematic elevation view of the CESURA system, after it has undergone a pitch rotation of θ. In the interests of simplicity, the whole system has been subjected to a rigid body rotation so that the deformed configuration is symmetric.

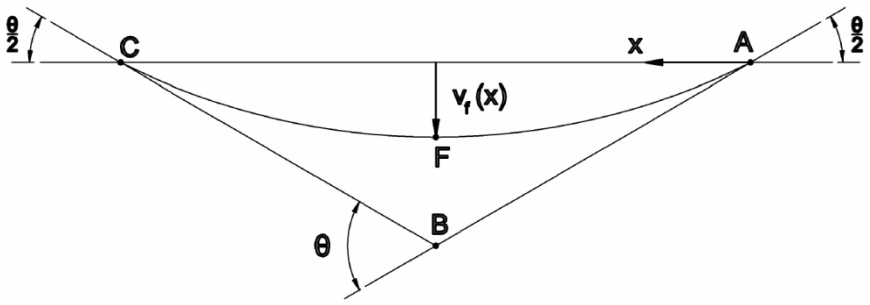

Figure 6-6: CESURA diagram for polynomial yoke curve fitting

In this picture, line AB represents the fixed or floating span, and line BC represents the transition span. The CESURA end supports, located at points A and C, define the wings' longitudinal axis, and the distance along this axis is denoted by x as before. In order to ensure continuity at the ends of the system, the equation $v_f(x)$ that defines the rotated bearing yoke along the wing has, for small θ, the boundary conditions

$$v_f(0) = 0 \qquad v_f(|AC|) = 0$$
$$v_f'(0) = -\theta/2 \qquad v_f'(|AC|) = \theta/2$$

Denoting $|AC|$ as $2L$, the unique cubic between these points is given by

$$\mathrm{v_f(x)} = \frac{\theta}{4\mathrm{L}}\mathrm{x}^2 - \frac{\theta}{2}\mathrm{x} \tag{6-8}$$

Returning to the geometric arguments of Section 6.1, the relationship between $v_f(x)$ and $d(x)$, the equation of the bearing yoke on the wings surface is given by,

$$\mathrm{d_3(x)} = -\frac{2\mathrm{e}}{\mathrm{a}\theta}\mathrm{v_f(x)} = -\frac{\mathrm{e}}{2\mathrm{aL}}\mathrm{x}^2 + \frac{\mathrm{e}}{\mathrm{a}}\mathrm{x} \tag{6-10}$$

which is independent of the imposed pitch motion. Additional constraints can be added to the system, and arbitrary boundary conditions satisfied. Adding the condition that the curvature be zero at the boundary,

$$v_f''(0) = 0 \qquad v_f''(|AC|) = 0$$

The resulting 5th order polynomial becomes

$$v_f(x) = -\frac{\theta}{16L^3}x^4 + \frac{\theta}{4L^2}x^3 - \frac{\theta}{2}x \tag{6-11}$$

And the equation of the bearing yoke on the wing is given by

$$d_5(x) = \frac{e}{8aL^3}x^4 - \frac{e}{2aL^2}x^3 + \frac{e}{a}x \tag{6-12}$$

6.3.1 Pitch

Figure 6-7 summarizes a parametric study, where the shape of the bearing yoke was varied to investigate the difference in system behavior given a center bearing longitudinal distance, a = 18 feet, and a bearing offset, e = 3.17 feet.

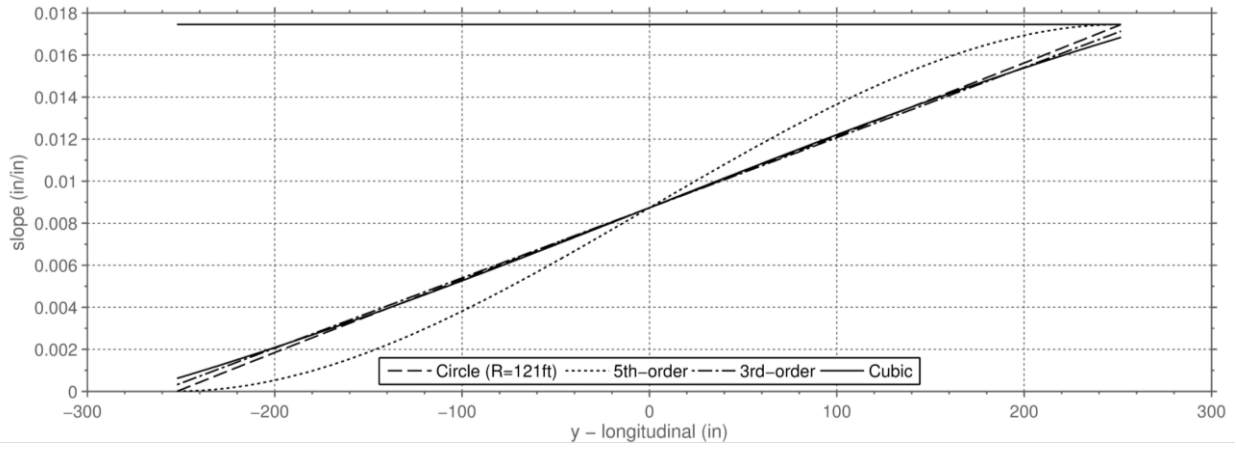

Figure 6-7: Longitudinal slope over the length of the track bridge for various yoke shapes and a cubic rail alignment under a 1° pitch rotation about the center of the track bridge.

The radius of 121 feet and the 5th-order polynomial most closely matched the slope of both the stationary span and the rotated span, whose slope is shown in solid black for reference. The 3rd-order polynomial did not appear to have any real benefit over the circle when comparing its slope to that of the cubic fit between plinths. The 5th-order polynomial, however, appears to provide a more gentle transition on either end of the track bridge.

6.3.2 Roll

Figure 6-8 reports the centripetal accelerations along the track bridge for several bearing yoke geometries, given a center bearing longitudinal distance, a = 18 feet, and a bearing offset, e = 3.17 feet subjected to a roll rotation of one degree. The centripetal acceleration was computed for a particle travelling along the path defined by the rails location on the bearer bars along the length of the track bridge, based on the instantaneous curvature and a constant velocity of 60 mph.

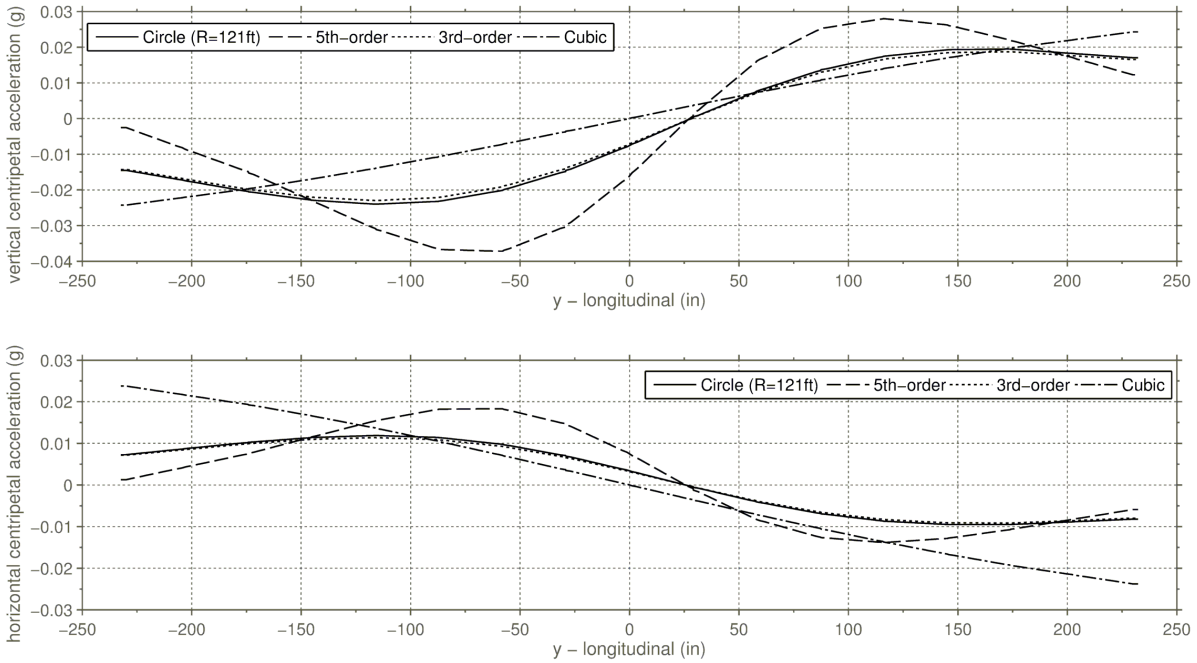

Figure 6-8: Centripetal acceleration over the length of the track bridge for different bearing yoke shapes and a cubic rail alignment under a 1° roll rotation about the center of the track bridge.

The 3rd-order polynomial followed closely that of the circular yoke with non-zero accelerations on either end of the track bridge. In contrast the 5th-order polynomial's centripetal acceleration approaching the end of the CESURA system approached zero, more closely on the side of the wing which was held fixed against translation.

Figure 6-9 shows the transverse slope of the rails for the three bearing yoke geometries from the stationary to the displaced span. The transverse slope of the displaced span is shown as a horizontal black line for reference. The transverse slope of the system was calculated using the coordinates of the two rail centroids over the track bridge.

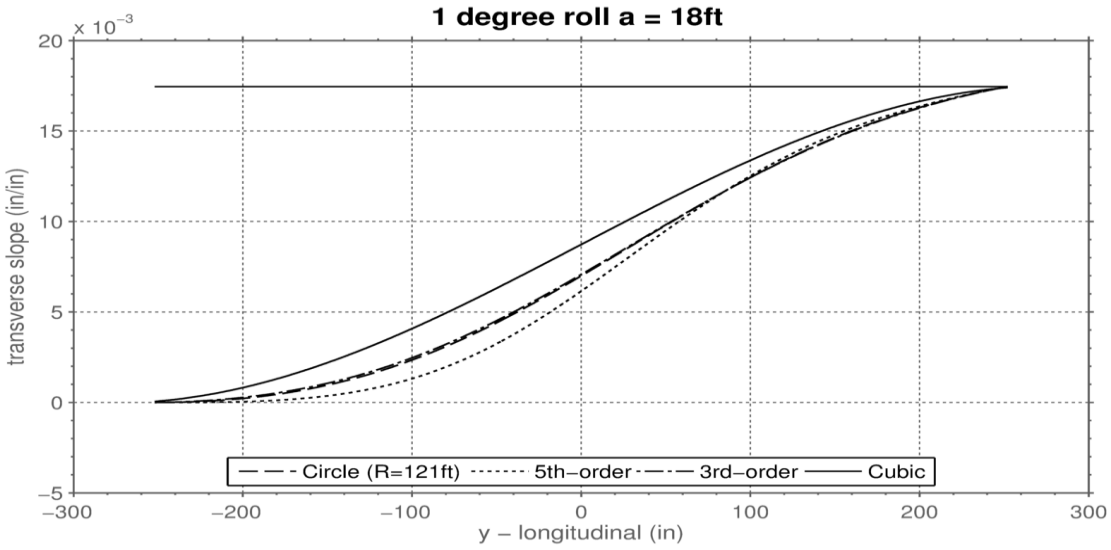

Figure 6-9: Transverse slope over the length of the track bridge for different bearing yoke equations and a cubic rail alignment under a 1° roll rotation about the center of the track bridge.

Each of the yoke geometries provides a smooth transition from one transverse slope to the other. As was noticed previously, the 5th–order polynomial appears to provide a gentler transition at the fixed end, while increasing the curvature near the middle. Independent of the chosen yoke geometry, the slopes converge near the end of the system, on the displaced span, although the curvature of the 5th-order polynomial is somewhat smaller.

6.3.3 CESURA Yoke Geometry Summary and Conclusions

The physical realities of the designed system including the wing support conditions and the bridges structural layout affect the optimum design of the track bridge. A simple numerical model was developed to understand the kinematics of the

system, and geometric design arguments were tested. Given a center support bearing's eccentricity, e = 3.17 feet, and a center bearing longitudinal distance, a = 18 feet, the most effective radius was determined to be r = 121 feet. It was also found that using higher order curves could allow the designer to choose the characteristics of the resulting vertical curve that may be beneficial to ride quality and passenger comfort. Member deflections were not accounted for in this analysis and may have measurable influences on the optimum geometric design.

Figure 6-10 shows the bearing yoke curves versus the normalized distance along the longitudinal distance of the CESURA system. If the central bearing is offset from the transition span, so that a = 18 feet with an overall length L = 42 feet and a yoke radius of 140 feet, then selection of the correct radius for slope continuity requires moving the bearings so that e = 2.73 feet, which represents a movement of 0.44 feet or less than six inches from their present position. This change would only minimally affect the design of the box girders and would likely lead to lower rail stresses at the extremities of the CESURA system. The selection of a third order polynomial does not appear to have any additional benefits over the circle.

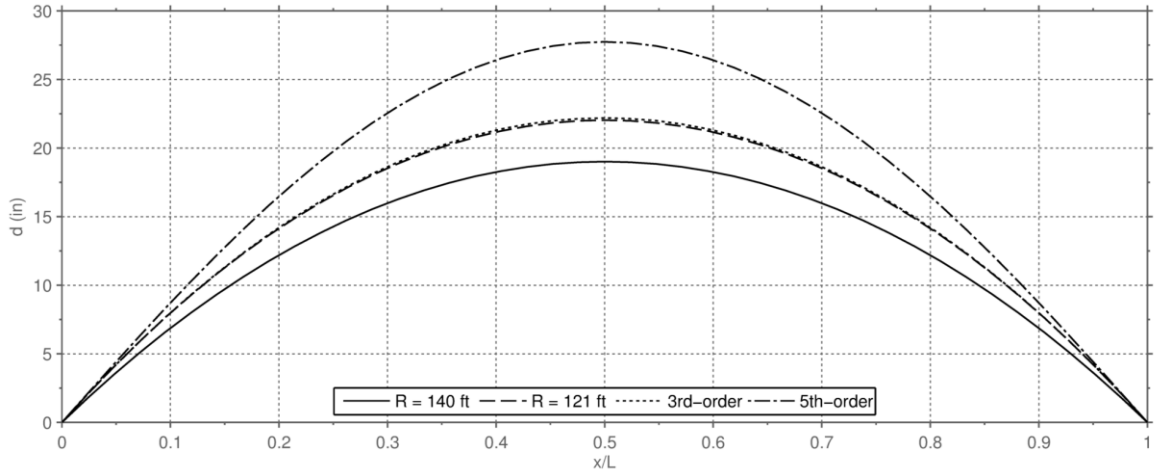

Figure 6-10: Comparison of FPS bearing yoke geometries

Although the fifth order polynomial may require additional reconfiguration of the wing box girders, the benefits of this system appear numerous. In both the roll and pitch configurations, the transverse and longitudinal slope conditions were satisfied. Furthermore, the transitions in both configurations between straight portions of rail, resting on fasteners atop concrete plinths, into the curved rail, resting on both flexible fasteners and bearer bars, were much more gradual. This would likely have measurable benefits to the rail continuity at the extreme ends of the system, and to the ride quality of the LRV, by slowly increasing the accelerations felt by passengers. Finite element modeling should be performed to assess the influence of component deflections and the interaction with the LRV suspension system.

6.4 Instrumentation

The instrumentation strategy employed in this experiment is of particular importance, because of the implications it has for the prototype tests that will be performed at the Transportation Technology Center Incorporated (TTCI) in Pueblo, Colorado. Two separate instrumentation strategies were employed, and comparisons between these strategies are presented here. Shortcomings of the instrumentation are also discussed, with strategies for successful measurement in the full scale experiments.

6.5 DMI Supplementary Instrumentation

Direct Measurements Incorporated (DMI) have been engaged to provide long-term monitoring instrumentation on the prototype bridge after its installation. The company is tasked with installing trial instrumentation for the test at TTCI in Pueblo, and they provided pilot instruments for the UW component testing program. That instrumentation was installed on the test specimen in parallel with the UW sensors. In this section, the two systems are evaluated and compared.

6.5.1 Inclinometers

Figure 6-11 displays the inclination readings recorded by both instrumentation strategies for the YAW01d supplementary horizontal test. The figure also displays the instantaneous arctangent of the bearer bar pseudo-acceleration and the acceleration of gravity. This test was performed specifically to compare the instrumentation measurements.

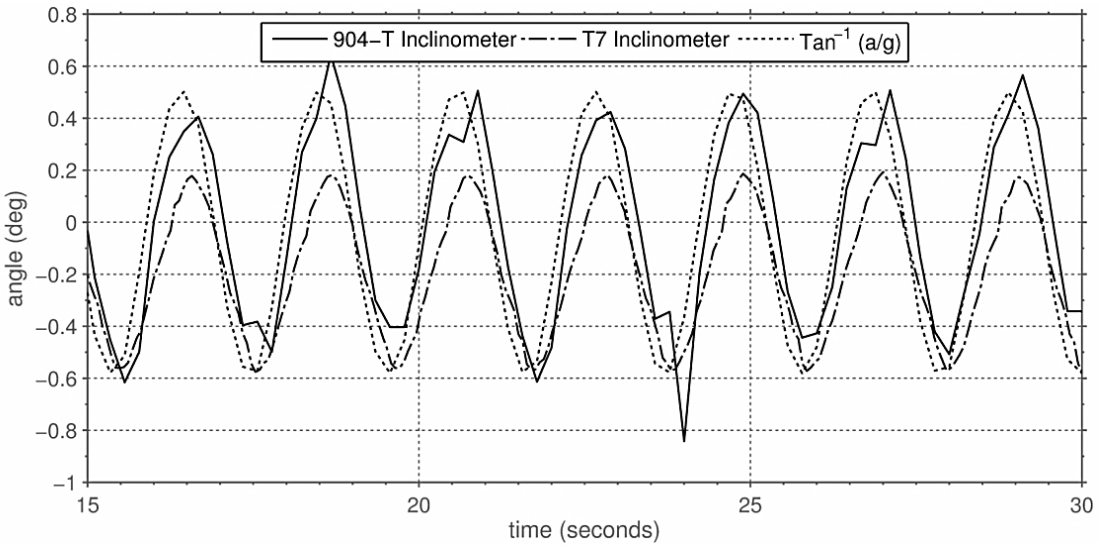

Figure 6-11: Measured and calculated fictitious rotations at the right end of bearer bar 03 (YAW01d).

The Applied Geomechanics 904-T dual axis model employed in the University of Washington (UW) instrumentation strategy was more sensitive to inclination, with a resolution of 0.005 degrees and was read using a 16-bit A/ D converter. The US Digital T-7 inclinometer employed in the Direct Measurements Incorporated (DMI) strategy had a resolution of 0.01 degrees and was read through a virtual serial bus using software supplied by the manufacturer. The T-7 inclinometer appeared to be less prone to vibratory noise, and produced a smoother signal. Both instruments work by measuring the inclination of the force of gravity. This was particularly problematic in the horizontal tests, where loads were applied transversely. The accelerations of the bearer bars were recorded as rotations by both instruments, contrary to the belief that the rotations should be nearly zero.

6.5.2 "crossing" LVDT arrangement

Transverse bearing displacements were monitored at the right end of bearer bar 03. Two LVDT's were mounted, in a crossing pattern, to aluminum brackets that were screwed to the top and bottom surfaces of the friction pendulum bearing as shown in Figure 6-12.

Figure 6-12: Photograph of "crossing" LVDT arrangement

The intent of using the crossing LVDT arrangement was to be able to measure both transverse displacement and rotation of the end of bearer bar. This objective is stymied by the coupling of the six degrees of freedom of the friction pendulum (FPS) bearings. In particular, the longitudinal and vertical displacements and the rotation about the transverse axis are coupled. Thus, theoretically, only two degrees of freedom

remain and the two crossing LVDTs should be sufficient to determine all three motions. However, the coupling equations for the FPS bearings require the starting position to be known, and in most cases this was not available. The bearings were not centered exactly with respect to their local axes when the global displacement was taken as zero, because of slight misfits during assembly of the rig. Had the crossing LVDTs had a third sensor, all three motions could have been deduced with only small errors associated with assuming that the bearings displacements in its other degrees of freedom are negligible.

Figure 6-13 displays both the measured and calculated bearer bar 03 transverse displacements from both instrumentation strategies for the YAW01d supplementary horizontal test. In the horizontal tests, where the rotation of the ends of the bearer bars could be neglected, the calculated bearer bar displacement was nearly identical to that measured by the potentiometer at the end of the bearer bar. In Figure 6-13 it is nearly impossible to tell the two apart. This is further evidence that the inclinometer rotation readings were purely acceleration based. If the rotation of the end of the bearer bar was to change due to transverse displacements, than the computed readings would show significant error.

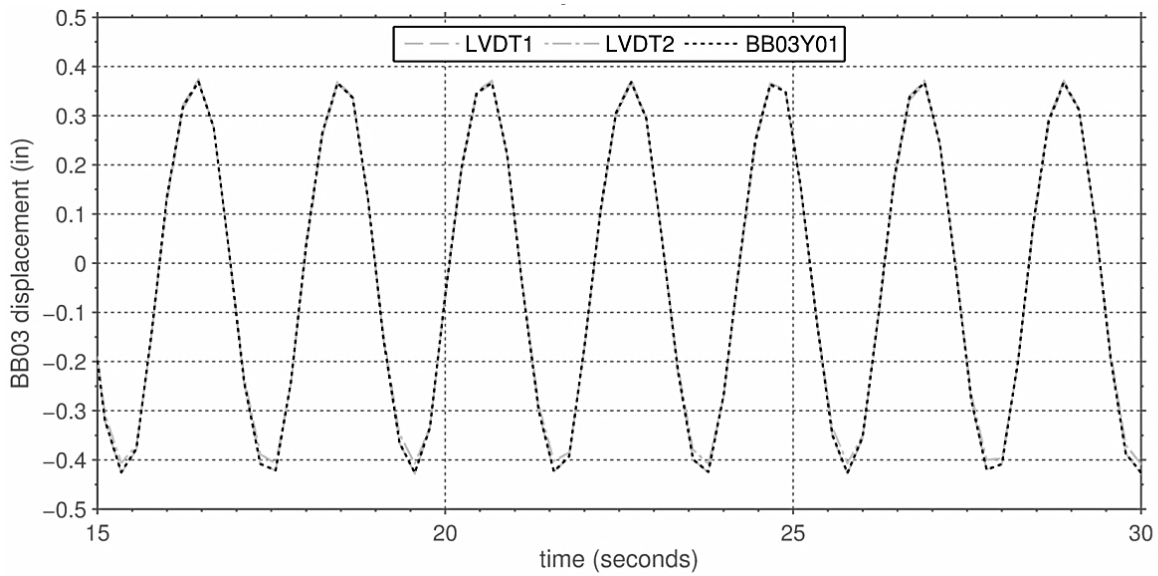

Figure 6-13: Measured and calculated bearer bar 03 transverse displacements assuming zero rotation of the bearer bar (YAW01d).

In vertical tests where the bearing both rotated and translated, the calculated quantities showed significant error in both the measured displacement and rotation. The change in length of the LVDT's is highly sensitive to the bearings initial configuration and the accurate determination of this position is difficult given the nature of the bearings and the method of installing them. If these sensors could be placed before removing the shipping plates on the bearings, then the neutral condition could be established, and they may have been more effective.

6.5.3 Dual-Purpose Sensor (DPS)

Figure 6-14 displays the both the measured and calculated right running rail stress at the DPS sensor location for the STF01a test. The strain was measured and

multiplied by Young's Modulus to give stress. The DPS reading reported is based on the average strain across the instrument. This test was chosen to compare the instruments, because the loading protocol was much slower than in the horizontal tests.

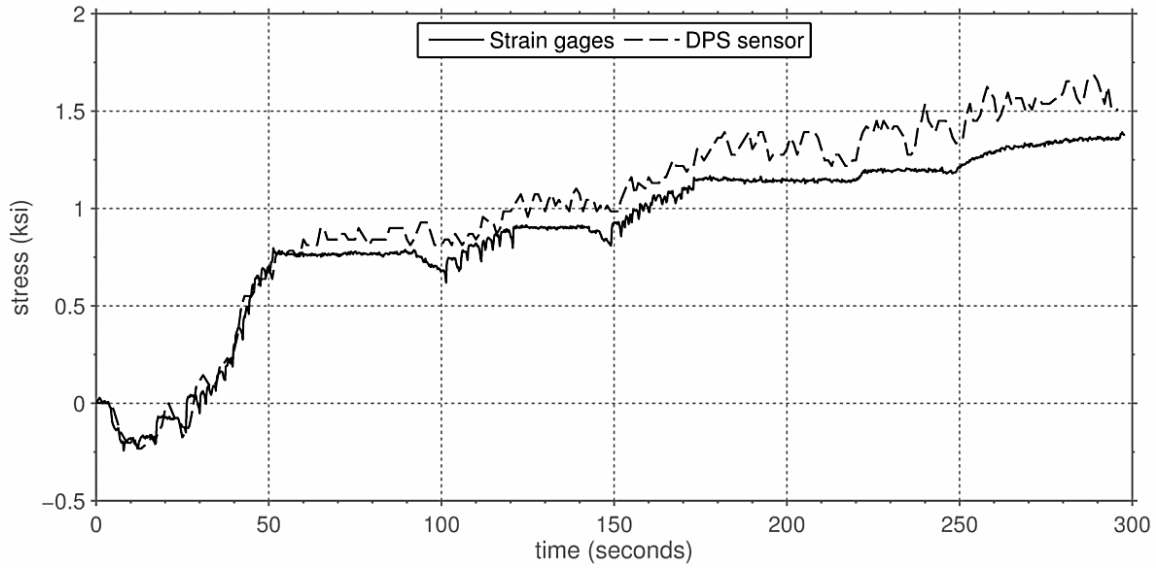

Figure 6-14: DPS measured stress and interpolated stress at DPS location (STF01a)

Because the DPS sensor uses optical technology the acquisition speed is much slower than that of traditional analog instruments. It should be noted that the flat segments of the plot are actually pauses in the loading protocol. The strain at the location of the DPS sensor was computed by linear interpolation between gages SLRRR0301 and SLRRR0101. It can be seen that the gages performed quite similarly throughout the test, especially in the initial region. It was noticed that the noise in the sensor was higher than the traditional electrical resistance strain gage, but the offset between readings was never greater than 0.5ksi.

Because these instruments are designed for crack detection and long term health-monitoring these results are favorable. DPS sensors could be used on the CESURA system to monitor regions of high anticipated stress for signs of fatigue and failure. They are suitable for measuring long-term strain, but not instantaneous strain, because of their slow reading time.

6.5.4 End rotations from vertical potentiometers

Three potentiometers were installed as shown in Figure 6-15 on bearer bar 02 and 03 to measure the vertical displacement and rotation of the end of the bearer bar relative to the wing plate. They were installed so that their plungers rested on the bottom flange of the bearer bar, 0.5 inches from the outer edges of the bottom flange. Because the top half of the bearing was intended to translate at most one inch in either direction, the potentiometers were offset from the edges of the FPS bearing by 1.25 inches.

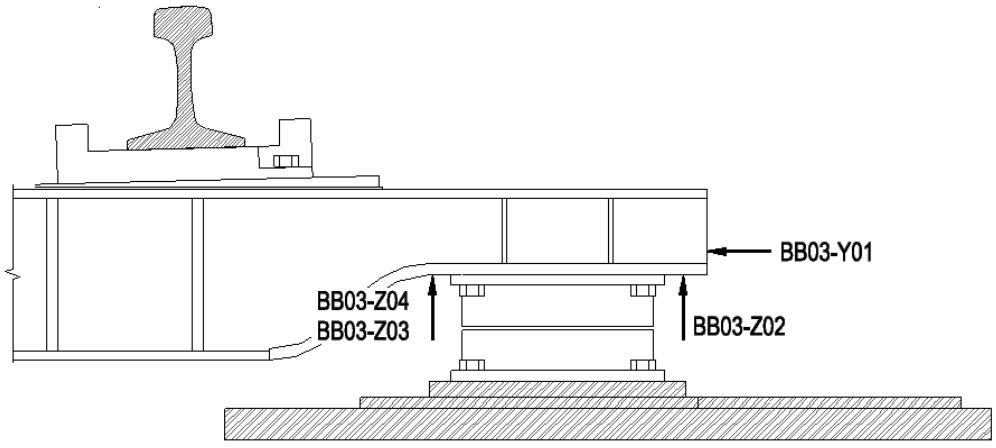

Figure 6-15: Vertical potentiometer locations for bearer bar 03 (identical to those on bearer bar 02)

Unfortunately this strategy was ineffective at measuring the rotation and change in height of the FPS bearings because of the curved geometry and rough steel surface of the bottom flange of the bearer bar. The potentiometers were at fixed locations and, as the bent portion of the plate moved over the sensor, it caused artificial displacement readings because it depressed the plunger in the sensor. The roughness of the steel plate's surface also caused the potentiometer to tilt, and possibly caused the plunger to bind by pushing the side of the plunger transversely as the bearer bar translated. This problem could be rectified by instead taking measurements on the underside of the top plate of the friction pendulum bearing, however, installing instruments in this location would be impossible in the prototype installation because of the ethylene propylene diene monomer (EPDM) seal that will encapsulate the bearing.

6.5.5 Bearer bar bottom flange bending stresses

The bearer bar transition region presents an atypical bending strain pattern due to presence of the bent plate and the weld access hole. As was reported in Section 4.4.6, the von Mises stresses in the web decrease toward the center of the transition and are highly concentrated near the bottom of the web at either end. This stress pattern, although caused by the geometry of the section in this region, is exacerbated by the location of the weld access hole.

Additionally, the bending stress on the bottom flange of the bearer bar also shows the effect of bent plate transition. Figure 6-16 shows both the location and sign of

the stresses on the bottom flange. Because of the tortuous load path at the transition the stress pattern is unsurprising. The stresses were strictly less than 3 ksi, but the sensor readings do not adequately detect the quantities of interest in the prototype.

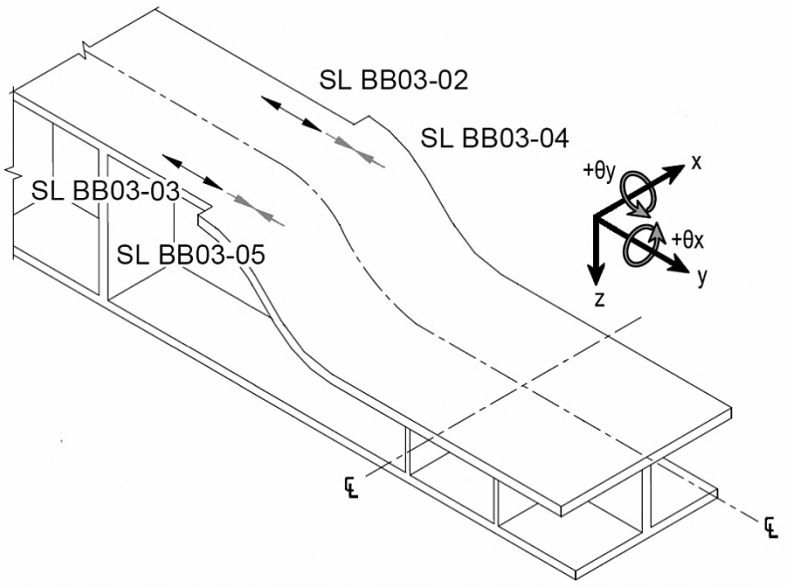

Figure 6-16: bearer bar 03 strain gage locations and signs of recorded longitudinal stresses

Figure 6-17 reports the bending stresses on either side of the weld for three cycles of vertical loading for the ROL01 geometric test. Gages just before the transition region register tensile stresses, while those just after the weld register compressive stresses. Again, the recorded data is expressed as stresses. In fact the strains were recorded and were converted to stresses prior to plotting.

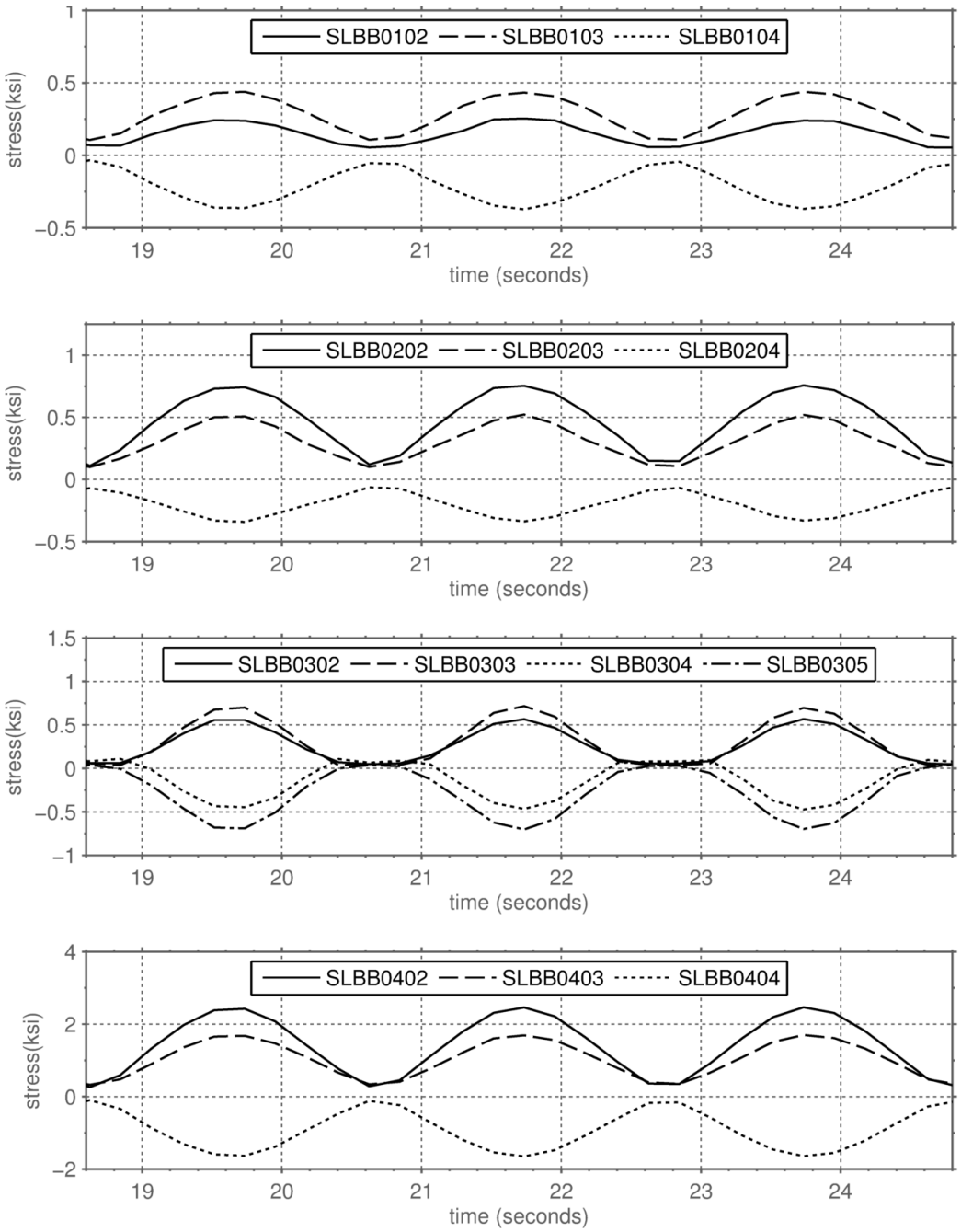

Figure 6-17: Recorded bearer bar bottom flange stresses on either side of bent plate butt weld.(ROL01)

6.5.6 Friction pendulum displacement measurements

As was commented on in Sections 6.2.1 and 6.2.2, measuring the displacements and rotations of the friction pendulum bearings posed serious challenges and the three methods that were investigated all had their own unique problems. An alternate concept for measuring the relative displacements and rotations of the FPS bearings was developed, independent of those tested. This method eliminates the need for inclinometers and avoids the issues encountered with the curved surface of the underside of the bearer bar. It has the potential to be installed after the shipping plates are removed; a baseline, or neutral measurement, is not necessary. This eliminates the problems encountered by trying to compute the highly coupled, non-linear behavior of the system from non-unique displacement data.

Figure 6-18 shows the instrumentation concept that was developed. This method ignores the inner workings of the friction pendulum bearing, and focuses instead on the position of the bearing top plate relative to that of the bottom plate.

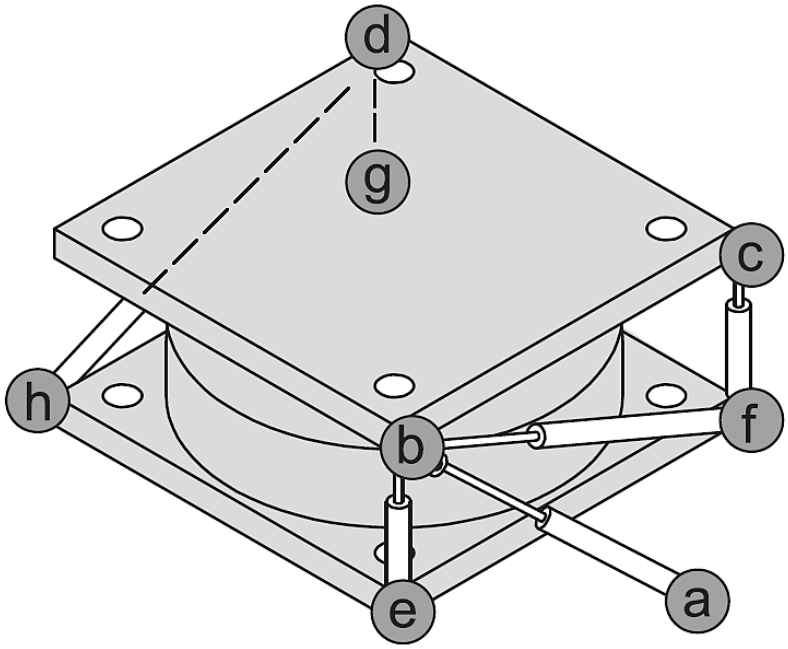

Figure 6-18: Instrumentation arrangement for measuring displacements of FPS bearings.

The system works by measuring the lengths between 8 points, 7 that are located on the friction pendulum bearing itself. In this picture the longitudinal axis of the bearer bar would run parallel to the line *bc*. Because the bearing has a large displacement capacity in this direction, no instruments were placed on these faces. Instead point *a* was offset from the side of the bearing in order to locate point *b*.

The lengths that are required to compute the FPS bearings relative motions are summarized by Table 6-1.

Table 6-1: Displacement sensor arrangement

Instrument	*Start Point*	*End Point*
L1	*a*	*b*
L2	*e*	*b*
L3	*f*	*b*
L4	*f*	*c*
L5	*g*	*d*
L6	*h*	*d*

The system works by using the lengths *L1, L2* and *L3* to locate point *b*. Point *a* must not be coplanar with points *e*, *f,* and *b* in order to do this. Because the distance between points *b* and *d*, the diagonal of the top plate, is known point *d* can be located in turn, and subsequently point *c*. Thus the location of three corners of the top plate are located and rotation and displacement of the two halves of the bearing can be computed, without knowledge or accuracy of the initial position of the system or the behavior of the bearing itself. This also allows for the measurement of these displacements in the case of uplift or rocking of the bearing, where the kinematics of the system changes.

Two major challenges facing the implementation of this system are the accurate location of the seven points on the FPS bearing and the calibration of the displacement measurement devices. The location of the points could be achieved by drilling holes accurately located in the top and bottom plates of the bearing during manufacturing. Suitable devices should be selected, with large displacement capacities and suitably calibrated so that lengths can be read from analog outputs. Because the motions will

occur in three dimensional space, the ends of the sensors should be equipped with spherical swivels.

6.5.7 Instrumentation summary

The instrumentation strategies that were employed illuminated areas for improvement for the full scale prototype test at TTCI in Colorado.

Bearer bar web stresses are highest at either end of the transition region and the stresses on the bottom flange near the change in flange width show an unusual pattern. Gages should be placed in regions away from the anomalies encountered in the component tests, to better understand the system behavior.

Bearer bar end rotations should be measured by displacement instruments, rather than inclinometers that are highly sensitive to dynamic motions.

FPS bearing relative displacements are challenging to measure for several reasons. Given the characteristics of the system, the initial conditions of the bearing are hard to identify once the bearing is free to move. The kinematics of the FPS bearing are highly sensitive to its initial condition and couple the six degrees of freedom of the system. The two strategies employed were not effective in computing the vertical rise or rotations of the bearings, although transverse displacements were able to be calculated.

An alternative approach was presented to replace the inclinometer and potentiometer systems used to measure relative bearing motions. This system does not rely on the kinematics of the bearing, and is therefore not sensitive to the initial

configuration of the system. It also has the benefit that is can be installed on site without tedious measurement.

6.6 CESURA System Behavior

The tested components are discussed briefly, specifically the consequences of their behavior observed in the laboratory for the prototype. Components that are deemed important for further experimental investigation are identified. The re-centering behavior of the prototype is investigated.

6.7 Effectiveness of chosen components

6.7.1 Friction pendulum bearings

The friction pendulum bearings were able to accommodate the exaggerated geometric conditions that were tested in the laboratory. Under transverse loads, the bearings proved to have adequate translation and rotation capacity and provided the primary restoring force in the specimen. Although they are traditionally used in seismic isolation applications that require energy dissipation, the friction present in the bearings was found to inhibit the re-centering of the system. This effect could be lessened by reducing the effective pendulum length or by decreasing the internal friction coefficient. The reduction of the pendulum length is likely the easier of the two options, and would also be beneficial because it would also increase the transverse stiffness of the bearing, which would be desirable.

6.7.2 Running rail fasteners

The running rail fasteners behaved largely elastically in response to rotations about a vertical axis as seen in the horizontal tests. Their vertical flexibility helped to distribute the vertical load between the bearer bars. These two responses are both desirable. When compared with the guard rail clips, their general behavior was more advantageous for this particular application. However, the direct determination of the characteristics of the fasteners, including their rotational stiffness, was not possible in this experiment. It was hoped that these properties could be indirectly determined. Unfortunately, due to the distribution of stresses in the rails, and the lack of sufficient instruments to characterize this distribution, this characterization was not possible.

6.7.3 Guard rail fasteners

The guard rail fasteners that were used for this experiment were designed for freight traffic. The hold down characteristics and rotational behavior are likely unimportant in most applications involving relatively stable rail alignments. In this particular application, the frictional characteristics of the fasteners were problematic because they actively combated the elastic elements of the system, and helped to prevent its re-centering. Again the indirect computation of the exact properties of the fasteners was not possible because of the need for additional strain instruments on the rails to characterize the distribution of shear forces.

Although other elastic elements will be present in the prototype, namely the continuous rails, this frictional behavior is still undesirable. If the guard rails were instead pinned at the bearer bars, so that rotations were unimpeded by the fasteners, only the elastic contribution of the continuous rails would be included. If some other rolled shape was used, instead of rails, the elastic bending stiffness of these rails could be optimized to produce the desired level of re-centering in the prototype.

6.7.4 Bearer bars

Although the coped ends of the bearer bars provided extra vertical flexibility, the deflections were still strictly less than 0.1 inches, and may have been less than one 1/ 16th of an inch if the bending of the wing plates and vertical deflections caused by the rotation of the FPS bearings are considered. In the prototype, these deflections will certainly be smaller because of the presence of seventeen bearer bars and the relatively rigid boundary elements: the concrete plinths at either end of the CESURA system. This result is advantageous, because this amount of deflection would likely have little effect on the vertical rail alignment imposed by the geometry of the system.

Although the resulting pattern of stresses in the bearer bars are more complex compared with those of a standard rolled section, the bearer bar stresses were less than 10% of the yield strength of the material. The stresses in the transition region were influenced by the presence of the relief hole to permit the welding process between rolled section and bent plate. This created stress concentrations in a region that was

already subjected to higher stresses due to the bent plate geometry. If this relief hole could be positioned away from the change in section depth, the magnitude of the stresses in an already critical region could be reduced.

6.8 Areas for further investigation

Additional running rail fastener tests are needed to fully determine their influence on the behavior of the system. These properties are significant; they have implications on the re-centering of the system, the deflection of the components under vertical load, and the properties of the transition at either end of the track bridge.

The fasteners' rotation stiffness directly influences the stiffness contribution of the frame action of the system. If the system is meant to re-center, this stiffness plays an important role. This stiffness and the fastener behavior is likely dependent on the vertical load, and this feature would also be useful to characterize.

The vertical flexibility of these fasteners plays an important role in the distribution of vertical forces and the geometric alignment of the prototype. The marriage of running rails connected to the bearer bars through flexible fasteners and guard rails attached more rigidly is beneficial. The presence of elements both flexibly and rigidly conned to the bearer bars will lead to a greater distribution of vertical forces. This would like lead to smaller deflections of the bearer bars. If the fasteners are too flexible, this beneficial effect may be counteracted by the deflections in the fasteners themselves.

The rotational stiffness of the fasteners about a transverse axis also has important implications for the behavior of the system. This will affect how much of the imposed twisting rotations on the bearer bars by the rail geometry is taken up by the fastener and the friction pendulum bearing respectively. It will also affect the characteristics of the transition from concrete plinths to CESURA system at either end. If the fasteners are rather flexible under these rotations, then the end slope of the prototype may have little consequence on the performance of the system. Conversely, if they are fairly rigid the end slope and end deflection may become a serious design consideration.

6.9 Re-centering behavior of the prototype

An approximate scheme for extending the experimental results to the prototype system is presented. The relative stiffness of each of the components of the system is computed and the implications of these stiffness values to the re-centering characteristics of the prototype are described.

6.9.1 Frame action of the running rails

The running rail-bearer bar system can be thought of as an equivalent shear beam with a stiffness characterized by the parameter *GA*. Figure 6-19 shows the recorded right running rail shear versus the relative displacement between bearer bar 02 and 03 for the PIT01 configuration.

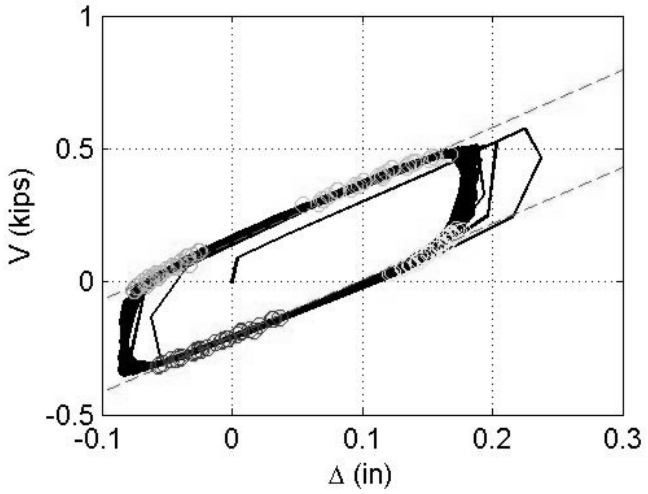

Figure 6-19: Shear force displacement time history for the right running rail

Taking the tangent stiffness as 2.5 kips/ inch the resulting value for GA = (2 rails)(2.5 kips/ in)(29 in) = 145 kips. It should be noted that this value is meant only as an approximation to illustrate the behavior of the system. Because the rail shears are only known in one bay of the system, this reliability of this value is relatively low.

Extending this characteristic parameter to the prototype, and assuming a concentrated transverse load is applied to the system at mid span, the stiffness of the system in terms of the mid span deflection is given by

$$k_{frame} = \frac{4GA}{L} = \frac{4(145 \text{ kips})}{42 \text{ ft}(12 \text{ in/ft})} = 1.15 \text{ kips/in} \quad (6\text{-}12)$$

6.9.2 Elastic bending of the rails

Assuming that both the guard rails and running rails are attached to the bearer bars through pinned connections and are fixed against rotation at the ends of the

system, the elastic bending stiffness of the rails at mid span if a transverse load is applied at mid span is given by

$$k_{rails} = 4 \cdot \frac{192\ EI}{L^3} = 4 \cdot \frac{192\ (29{,}000\ ksi)(10.7\ in^4)}{(42\ ft \cdot 12\ in/ft)^3} = 1.86\ kips/in \qquad (6\text{-}13)$$

6.9.3 Friction pendulum bearings

From Equation 5-1, the stiffness of a single friction pendulum bearing under the full axle load is

$$k_{FPS} = \frac{28\ kips}{20.5\ in} = 1.37\ kips/in \qquad (6\text{-}14)$$

6.9.4 Effective re centering of the system

If the guard rails are truly pinned, than the only major frictional element left in the system is the FPS bearings. Assuming a bearing friction coefficient of 3% the resulting friction force would be 0.84 kips if the full axle load acts only on one bearing. If the stiffness of each of the components acts in parallel, the estimated residual displacement from a simple pullback test would be.

$$\Delta = \frac{0.84\ kips}{(1.15 kips/in)+(1.86 kips/in)+(1.37 kips/in)} = 0.19\ inches \qquad (6\text{-}15)$$

This value is one third that which was calculated for the experimental specimen. Because of the dynamic forces of the light rail vehicle and the vibrations of the bridge due to lake conditions and traffic, the residual displacements could be much lower. More importantly over the length of the track bridge, this displacement is equivalent to

a concentrated rotation of 0.04 degrees at the ends of the CESURA system. This value is likely well within operating conditions.

The guard rails appear to be the most sensible choice for optimization in this regard. If the A.R.E.A 115 lbs/ yd rails were replaced by a standard rolled section, than the stiffness could be chosen to provide an arbitrary level of re-centering, within the geometric limitations of the system.

If the guard rails were instead fixed against rotation at the connection to the bearer bars, the resulting stiffness from the frame action would be two orders of magnitude higher than the other components described previously. Although this would seem to solve issues regarding the re-centering of the system, it would also hinder the intended horizontal bending of the rails required in the yaw configuration.

Chapter 7 Summary, Conclusions, & Recommendations

7.1 Summary

An experimental research project was conducted to investigate the effectiveness of components that will be used in an expansion joint track bridge system that will allow the completion of Sound Transit's East Link Light Rail Expansion project. The system is the Curved Element Supported Rail System, referred to by the acronym CESURA. An experimental apparatus was designed and a test specimen consisting of approximately one-quarter of the system at full scale was constructed. It consisted of four bearer bars (which play approximately the role of railroad ties), two running rails, which carry the wheels, and two guard rails, which carry no applied load under normal operating conditions. An instrumentation strategy was developed and analyzed. Challenges encountered during construction were articulated, and implications for the prototype and potential solutions were developed.

Vertical and transverse cyclic loads were applied to the specimen under five simulated geometric configurations, such as pitch, roll and yaw, and the measured datasets were compared. The transverse stiffness of the system was also measured under monotonic loading. A kinematic model was developed and parametric studies were performed to determine the effects of the system’s geometry on the resulting vertical and horizontal response to load.

7.2 Conclusions on the CESURA System as Implemented

7.2.1 Testing Observations

The specimen behaved largely as anticipated and revealed no major shortcomings once it had been assembled within tolerances. The friction pendulum bearings successfully accommodated the changes in geometry and the behavior of the system was largely independent of the imposed geometric configuration.

The internal mechanism of the Friction Pendulum Bearings causes their three major rigid body sliding motions (rotation and vertical and horizontal displacement) to be linked by a constraint equation. Thus, for example, arbitrary combinations of horizontal displacement and end rotation will result in some vertical displacement. While the magnitude of the vertical motion is small, and is an essential to the bearings' normal function of providing seismic isolation, it is a less desirable feature in the present application.

In the vertical loading experiments, the LRV axle load was distributed over all four bearer bars. The bearer bars were always in compressive contact at both the rail fasteners and FPS bearings. The maximum stresses in the bearer bars and rails were on the order of 5 ksi. The stresses near the butt weld, joining the bent plate to the bottom flange of the W-section, were affected by the presence of a weld access hole in the web.

Cyclic vertical loads were found to promote the re-centering of the system, but the magnitude of the effect was small, such that the residual displacement after removal of the load was on the order of 90% of the peak displacement.

In the horizontal load experiments, the LRV design wind load was found to displace the experimental specimen by about 0.6 inches at the fourth bearer bar. The rail stresses were found to be less than 15 ksi. When subjected to a repeated load in a single direction, the system displacement initially increased progressively with cycling, but then stabilized.

Although the experimental system was unable to re-center after horizontal load was released, the specimen lacked the continuous rails that are the largest elastic element of the CESURA system. Therefore the prototype is expected to have better re-centering properties. The extent of re-centering of the prototype is highly dependent on how the components are attached, and the relative stiffnesses of internal features of the system. Some features promote re-centering (continuous rails, geometry of the friction pendulum bearings, and frame action between rails and bearer bars) and some are detrimental to it (friction in the rail fasteners and friction pendulum bearings). The choice and balance of these components are essential to produce an optimal design.

During the test program, it was learned that the designers were considering changing the guard rail and its attachment system from the one used in the tests. The

change is likely to have a major effect on the elastic transverse stiffness, and therefore on the degree of re-centering possible, in the prototype.

7.2.2 Design Observations

If a circular bearing yoke is chosen, than the bearing eccentricity and longitudinal location should be selected to satisfy the slope continuity expression given by Equations 1-7 and 6-6. Bearing yokes that are non-circular, particularly a fifth-order polynomial, may increase ride quality by providing gentler transitions at either end of the CESURA system.

The re-centering behavior of the prototype is largely dependent on the chosen section of the guard rails and how they are fastened to the bearer bars. If the guard rails are fixed to the bearer bars, preventing relative rotation, then their transverse stiffness contribution far outweighs any other source in the design. If they are instead pinned to the bearer bars, then their contribution is entirely dependent on the chosen section and will be of the same order of magnitude as the other elements promoting the re-centering of the system.

7.2.3 Construction Issues

The CESURA system is highly sensitive to accuracy of fabrication. Although the components were fabricated within their individual tolerances, assembly of the bearer bars within the required global tolerances was not possible. Achieving the latter

required reaming out holes in the bearer bars and changing the bolted connection between bearings and bearer bars to be slip critical.

To connect the bearer bars, the friction pendulum bearings' shipping plates had to be removed. This left the bearings free to translate and rotate, which greatly complicated the assembly process.

Although the rail fasteners that were procured for this experiment did not have the correct cant, the rail was inclined to the vertical and the correct wheel-rail contact profile was achieved by custom-manufacturing and installing tapered HDPE shims. These shims provided some additional vertical flexibility, which may have affected the distribution of the wheel load among the four bearer bars. In principal, flexibility in these connections is beneficial because it reduces the potential for uplift in the bearings and the deflections of the bearer bars. Because the rail fasteners contain a soft, internal elastomeric layer, designed to provide acoustic isolation, they appear to be significantly more flexible than the HDPE shim. The effect of the shim is thus expected to have little practical effect on the performance.

Weld-on shoulders were supplied for use in attaching the guard rails to the bearer bars, instead of the bolted clips that were specified in the design drawings. These fasteners were intended to have hold down characteristics similar to those of the clips that were specified. However, the two clip systems use different methods of attachment and in reality they affect the service performance. The weld-on shoulders

provided hold down forces that were highly dependent on the welding procedure and proved to have highly frictional rotation behaviors.

7.2.4 Instrumentation

The instrumentation system employed to study the behavior of the system was largely successful. Areas for improvement were identified, and those improvements are recommended for use in the track bridge prototype.

Inclinometers proved to be problematic given the dynamic forces that were applied to the system. An effort was made to develop methods for determining the relative movements across the bearings using displacement measurements. However, they were found to be ineffective because they either relied on the bearing geometry, in the case of the "x-pattern" LVDT arrangement, or on the global positions of potentiometer plungers on moving, curved surfaces. Data analysis was performed to attempt to reconcile these issues, however the uncertainty of the assumptions employed in these analyses prevented the adequate correction of the data.

The transition region of the bearer bars, where the depth varies, was initially expected to cause a complex stress field and possible high stresses. It was heavily instrumented and the von Mises stresses were found to be less than 5ksi. The complex pattern of stresses, although not surprising, makes the measured behavior hard to interpret without comparison to finite element models. The stresses are highest on the

two ends of the transition near the bottom flange, where shear stresses are transferred from the web into the diagonal bottom flange of the bearer bar.

7.3 Recommendations

7.3.1 Prototype design

It may be advantageous to extend the butt welds in the bottom flange of the bearer bars to a region where the section depth is constant, to reduce the stress concentration present at the transition region.

The guard rails should be fastened to the bearer bars using connections that are either fully fixed or completely free to rotate. The presence of clips, whose characteristics are highly dependent on welding procedure and behave frictionally, both inhibits re-centering and confounds the effective modeling of the system.

The effects of the bearing yoke geometry should be investigated using finite element modeling that includes the deformation of the components. The radius should be selected to avoid slope discontinuities at the ends of the CESURA system. Passenger comfort and local rail stress concentrations may both be improved by selecting higher order curves for the layout of the friction pendulum bearings, similar to those presented in Section 6.1.2.

7.3.2 Construction

The construction sequence should facilitate the precise placement of the elements of the system. The component tolerances should be modified to be consistent with the specified global tolerances.

The shimming procedure for ensuring the correct rail height should be carried out under controlled conditions, where accurate appraisals of shimming requirements are possible.

For installing the FPS bearings in the prototype, it is recommended that, in place of the loose plate detail used in the test setup, a locating pin or recess be built into the center of the bottom surface of the bearing and a mating recess or pin located on the wing surface using a laser system. The purpose is to hold the location of the bearing in the horizontal plane while still permitting rotation about a vertical axis for the purpose of aligning the bearer bars.

It is also recommended that the bent plates at the ends of the bearer bars be fabricated thicker than specified so that they can be accurately milled prior to final installation. The bolt holes in the bearer bars should also be drilled after welding is complete.

7.3.3 Instrumentation

For the prototype installation, it is recommended that inclinometers not be used to measure bearer bar end rotations because of their sensitivity to accelerations. Instead,

a set of displacement instruments should be used, similar to the configuration described in Section 6.2.4. That system has the potential to provide accurate rotation and displacement measurements without prior knowledge of the initial configuration of the system.

Strain instruments should be placed on the bearer bar web on either side of the transition region near the bottom flange and on the center of the bottom of the bent plate in several longitudinal locations.

Bibliography

Hetenyi, M. Beams on Elastic Foundation: Theory with Applications in the Fields of Civil and Mechanical Engineering. Ann Arbor: University of Michigan Press, 1946. Print.

KPFF. "Homer Hadley Interstate 90 Floating Bridge Test Program for Light Rail Transit Draft Test Report". [2005].

Parsons Brinckerhoff. "East Corridor HCT – Summary of I-90 Floating Bridge (Homer Hadley) Studies Final Report" [2006].

Rao, Ranganatha R., Sanghvi, Sudhir "Design of continuous welded rail on a suspension Bridge". *Proceedings from the 2000 AREMA Annual Conference*. [2000]

Appendix A Supplemental Test Data

This Appendix contains the reduced, measured data from both vertical and horizontal tests for the five geometric conditions (REF, PIT01, PIT02, ROL, YAW). It also includes figures which show the time history of the presented data.

The time history plots show how the response quantity in question varies as the load is cycled. The tables of numerical values show the amplitude of the cyclic response. These values may be compared with responses of a numerical model subjected to the same loading.

A.1 RMS values

In order to best reduce the time history data to values that can be easily compared with finite element results, equivalent sinusoidal amplitudes were computed using the root mean square (RMS) of the given signals.

This allows for the slight variation in peak amplitudes from cycle to cycle caused by sampling the data at discrete points and reduces the inherent variability in these peaks caused by background noise. Because many of the measured quantities were small, these noise characteristics were not insignificant. By using this procedure the effect of this noise is reduced, and the time history can be condensed to two numbers, the mean value and the effective amplitude.

The RMS for a sinusoid with amplitude, a, and offset (or mean), μ, is given by

$$RMS = \sqrt{\mu^2 + (a^2/2)} \tag{A-1}$$

Thus, by computing the mean and the RMS of a given signal, the equivalent sinusoidal amplitude can be determined by solving the above expression for a.

A.2 Measured RMS values

The mean and equivalent sinusoidal amplitudes for the five different geometric conditions (REF, PIT01, PIT02, ROL and YAW) are given in the tables below. The tables are separated according to the loading regime. The vertical tests had cyclic vertical loads and no horizontal load and the horizontal tests had a constant vertical load and a cyclic horizontal load. The maximum and minimum values of a given parameter can be obtained by adding and subtracting the amplitude from the mean. The first value given for each channel of data is the mean denoted by, μ, and shaded to distinguish it from the equivalent sinusoidal amplitude, denoted by a. In most cases the cyclic amplitude is the simplest value with which to evaluate the response, since some initial stresses and deformations existed in the system due to stresses locked in during to the assembly process and the initial displacements at the start of loading. These affect the mean, but not the cyclic amplitude.

Some values are left blank intentionally because instruments and gages malfunctioned between or during tests and were no longer considered reliable. Although every effort was made to ensure consistent instrumentation, the volume of data made it difficult to catch some of these malfunctions during testing.

Instrument names are consistent with those listed in Table 1 through Table 4 and with those given in Appendix A. Please refer to these sources for the exact location and description of the gages.

A.2.1 Vertical tests (loading in Z-direction)

Each test was conducted with the axle over Bearer Bar 03 and performed by cycling vertical the vertical load about the mean value given. It should be noted that the vertical load did not cycle from max to zero, this was to prevent unsafe conditions in the laboratory due to the potential for actuator uplift. Rather, a constant load of about 16 kips was applied, with an additional sinusoidal load of approximately +/ - 12 kips. Thus the minimum load during cycling was approximately 4 kips. All of these tests were performed under load control.

Table A-1: Reduced Measured Values for the Five Geometric Conditions under Cyclic Vertical Load
Table A.2-2

VERTICAL		***REF***	***PIT01***	***PIT02***	***ROL***	***YAW***
No of cycles		24	16	19	24	19
Vertical load (kips)	μ:	-16.0932	-15.6920	-15.7271	-16.0073	-16.0345
	a:	11.8997	12.0792	12.0272	11.9930	11.9900
BEARER BAR MIDSPAN VERTICAL DEFLECTIONS (IN)						
BB01-Z01	μ:	-0.0174	-0.0202	-0.0206	-0.0203	-0.0177
	a:	0.0127	0.0104	0.0172	0.0140	0.0125
BB02-Z01	μ:	-0.0294	-0.0309	-0.0370	-0.0345	-0.0300
	a:	0.0225	0.0216	0.0300	0.0233	0.0212
BB03-Z01	μ:	-0.0358	-0.0345	-0.0439	-0.0404	-0.0359
	a:	0.0253	0.0235	0.0347	0.0269	0.0253
BB04-Z01	μ:	-0.0358	-0.0344	-0.0447	-0.0384	-0.0358
	a:	0.0245	0.0231	0.0337	0.0249	0.0240
BEARER BAR MIDSPAN BENDING STRESS (KSI)						
SL BB01-01	μ:	1.1358	1.2180	1.4757	1.2062	1.2105
	a:	0.8408	0.6612	1.1461	0.8756	0.9011

SL BB02-01	μ:	0.4366	0.4509	0.7209	0.5017	0.4595
	a:	0.1935	0.1763	0.1538	0.1473	0.1967
SL BB03-01	μ:	1.3145	0.9555	0.5246	0.8874	1.1534
	a:	1.3717	1.2616	0.5834	1.1786	1.3159
SL BB04-01	μ:	1.9987	1.9680	3.1734	2.4053	2.0369
	a:	1.3278	1.4060	2.1250	1.5672	1.3488
BEARER BAR END Y ROTATION (DEG)						
INC BB01-01Y	μ:	0.0249	0.0353	0.0281	0.0283	0.0544
	a:	0.0196	0.0230	0.0239	0.0181	0.0194
INC BB02-01Y	μ:	0.0412	0.0416	0.0467	0.0402	0.0699
	a:	0.0303	0.0287	0.0371	0.0244	0.0304
INC BB02-02Y	μ:	0.0073	0.0069	0.0090	0.0045	0.0343
	a:	0.0140	0.0136	0.0213	0.0108	0.0128
INC BB03-01Y	μ:	0.0290	0.0276	0.0402	0.0245	0.0561
	a:	0.0406	0.0358	0.0459	0.0274	0.0393
INC BB03-02Y	μ:	-0.0596	-0.0406	0.0001	-0.0359	-0.0215
	a:	0.0458	0.0417	0.0076	0.0506	0.0441
INC BB04-01Y	μ:					
	a:					
VERTICAL MIDSPAN RAIL BENDING STRESS (KSI)						
SL RRR02-01	μ:	1.8964	1.8057	1.6738	2.0781	1.8732
	a:	1.3847	1.4424	1.2063	1.5087	1.3907
SL RRR02-02	μ:	-1.2179	-1.1588	-0.9498	-1.0859	-1.0739
	a:	0.8648	0.9169	0.8063	0.9278	0.7766
SL RRR02-03	μ:					
	a:					
SL RGR02-01	μ:					
	a:					
SL RGR02-02	μ:	-0.4313	-0.4169	-0.2851	-0.5827	-0.3677
	a:	0.3015	0.3650	0.3271	0.3928	0.2459
SL RGR02-03	μ:					
	a:					
SL LGR02-01	μ:	0.7720	0.7924	1.3762	0.9943	0.8645
	a:	0.6091	0.6896	1.0258	0.6888	0.6365
SL LGR02-02	μ:	-0.4324	-0.3484	-0.8564	-0.3596	-0.5479
	a:	0.3700	0.4421	0.7753	0.4303	0.4501
SL LGR02-03	μ:	-0.4952	-0.6958	-0.8056	-0.7881	-0.5623
	a:	0.4519	0.5244	0.8701	0.5471	0.4920
SL LRR02-01	μ:	2.1937	2.0538	2.6537	2.2047	2.2555
	a:	1.7673	1.7228	2.1599	1.7725	1.8256

SL LRR02-02	μ:	-1.7189	-1.5855	-1.8848	-1.5933	-1.7710
	a:	1.3819	1.3784	1.7158	1.3882	1.4309
SL LRR02-03	μ:	-1.4039	-1.3684	-1.4598	-1.5773	-1.4966
	a:	1.2011	1.1221	1.4885	1.2222	1.2593
BEARER BAR TRANSITION REGION SHEAR STRESS (KSI)						
SR BB01-01	μ:	0.5825		0.4681	0.5706	0.6177
	a:	0.4125		0.4112	0.4490	0.4325
SR BB02-02	μ:	0.9414	0.9279	0.8728	0.9306	0.9177
	a:	0.6421	0.6408	0.6061	0.6922	0.6519
SR BB02-03	μ:	0.7683	0.9332	0.7094	0.8073	0.8817
	a:	0.6162	0.6028	0.4917	0.5392	0.6571
SR BB02-04	μ:	0.9140	0.8740	0.8642	0.8793	
	a:	0.6464	0.5997	0.5500	0.6711	
SR BB03-01	μ:	1.2244	1.1008	0.9639	0.8777	1.1900
	a:	1.3841	1.2967	1.0814	1.1185	1.4473
SR BB03-02	μ:	1.2622	1.0634	0.9091	0.8715	1.0797
	a:	1.4169	1.3219	1.0764	1.1426	1.3573
SR BB03-03	μ:	0.9277	0.6667	0.6036	0.6034	0.9131
	a:	0.9887	0.8952	0.7782	0.8152	0.9882
SR BB03-04	μ:	1.3396	1.2017	1.1427	0.9936	1.2838
	a:	1.5727	1.4467	1.3005	1.3595	1.5469
SR BB03-05	μ:	0.4850	0.1902	0.2392	0.3586	0.1460
	a:	0.5367	0.5312	0.4273	0.4177	0.5138
SR BB03-06	μ:	1.0730	0.8633	0.9314	0.9135	1.0217
	a:	1.1901	1.0439	1.0017	1.0511	1.1749
SR BB03-07	μ:	0.1856	0.1015	0.1370	0.0791	0.1578
	a:	0.2088	0.1887	0.1292	0.1572	0.2148
SR BB03-08	μ:	-0.0458	-0.0898	-0.0408	-0.0761	-0.0042
	a:	0.1119	0.1040	0.1563	0.1375	0.1121
SR BB03-09	μ:	0.4811	0.3198	0.0356	0.1898	0.2154
	a:	0.2467	0.2298	0.1758	0.1790	0.2830
SR BB030-10	μ:	-0.1403	-0.1008	-0.0991	-0.0696	-0.0992
	a:	0.1724	0.1555	0.2063	0.2194	0.1697
SR BB04-02	μ:	2.1181		2.5030	2.3853	1.9472
	a:	1.5964		2.0280	1.7999	1.5000

A.2.2 Horizontal tests (loading in Y-direction)

Each test was conducted with the axle over Bearer Bar 03 and was performed by holding the vertical load constant and cycling the horizontal load about the mean value. It should be noted that, at the start of the cyclic loading, the system was not at the bearings' neutral position (i.e. bearing top plates centered over bottom plates) but was at some initial offset caused by a combination of the assembly tolerances, the applied vertical load and previous horizontal test cycles. These values are reported in order to properly define the initial conditions of the system before the application of the horizontal force.

The values are also slightly affected by the fact that Tests REF, ROL, and YAW were conducted under displacement control, where tests PIT01 and PIT02 were conducted under load control. Although this affects the shapes of the plots presented subsequently, and in particular the initial offsets, the amplitudes are comparable indicating that the difference in control methods had little effect on the systems behavior.

Table A-2: Reduced Measured Values for the Five Geometric Conditions under Cyclic Horizontal Load

HORIZONTAL		***REF***	***PIT01***	***PIT02***	***ROL***	***YAW***
No of cycles		14	30	21	22	21
Mean Vertical load (kips)		28.2123	27.8568	27.7256	27.8751	27.9458
Horizontal force (kips)	μ:	0.1847	-0.1461	0.3587	-0.4499	0.1997
	a:	3.3227	3.1269	2.9901	3.3590	3.6979
Actuator Displacement (in)	μ:	0.3125	-0.0576	0.0029	0.2368	0.0865

	a:	0.2802	0.4351	0.4470	0.3892	0.3717
INITIAL LATERAL DEFLECTIONS (IN)						
BB01-Y01		0.0576	0.0409	0.0817	0.0640	0.0087
BB02-Y01		0.1658	0.1045	0.2270	0.1873	0.0379
BB03-Y01		0.2693	0.1616	0.3480	0.3139	0.0729
BB04-Y01		0.3687	0.2112	0.4516	0.4549	0.1293
LATERAL DEFLECTIONS (IN)						
BB01-Y01	μ:	0.0628	-0.0085	-0.0001	0.0686	0.0043
	a:	0.0724	0.1120	0.1075	0.1024	0.0959
BB02-Y01	μ:	0.1687	-0.0061	0.0230	0.1911	0.0217
	a:	0.1758	0.2784	0.2755	0.2512	0.2337
HORIZONTAL		REF	PIT01	PIT02	ROL	YAW
BB03-Y01	μ:	0.2529	-0.0008	0.0379	0.3003	0.0415
	a:	0.2614	0.4260	0.4208	0.3726	0.3539
BB04-Y01	μ:	0.3331	0.0132	0.0633	0.4146	0.0687
	a:	0.3247	0.5475	0.5299	0.4683	0.4442
Y ROTATION (DEG)						
INC BB01-01Y	μ:	0.0583	0.0406	0.0585	0.0552	0.0800
	a:	0.0993	0.1373	0.1427	0.1313	0.1340
INC BB02-01Y	μ:	0.0758	0.0730	0.0900	0.0757	0.1062
	a:	0.2330	0.3431	0.3569	0.3142	0.3080
INC BB02-02Y	μ:	0.0188	0.0122	0.0278	0.0068	0.0437
	a:	0.2226	0.3332	0.3468	0.3023	0.3005
INC BB03-01Y	μ:	0.0682	0.0618	0.0999	0.0574	0.0976
	a:	0.3401	0.5219	0.5546	0.4580	0.4605
INC BB03-02Y	μ:	-0.1119	-0.0960	-0.0002	-0.0905	-0.0696
	a:	0.3434	0.5405	0.5586	0.4745	0.4640
INC BB04-01Y	μ:					
	a:					
LATERAL RAIL BENDING STRESS (KSI)						
SL RRR01-01	μ:	3.0620	0.3863	0.6448	1.5162	1.4835
	a:	2.3042	2.3776	2.6069	2.7252	2.5773
SL RRR01-02	μ:	0.2852	2.2458	2.4238	2.4540	1.6112
	a:	2.1314	2.2846	2.4800	2.5392	2.3728
SL RRR03-01	μ:	8.1869	4.9580	4.8357	6.6006	6.4465
	a:	3.7682	4.1293	4.4487	4.4937	4.3550
SL RRR03-02	μ:	1.1257	3.2453	3.3889	3.1315	2.6802
	a:	3.5301	3.9151	4.2583	4.1883	3.9837
SL RGR01-01	μ:	1.2257	1.2492	0.8716	2.8527	1.5147
	a:	1.1592	1.2677	1.4556	1.4555	1.1680

SL RGR01-02	μ:	0.1255	-0.0614	1.0278	-0.2787	0.0617
	a:	1.0591	1.2249	1.3545	1.3000	1.1776
SL RGR03-01	μ:	2.5045	-0.8533	-0.1977	0.7897	
	a:	3.3691	3.8188	3.9699	3.7400	
SL RGR03-02	μ:	-0.2334	3.0564	2.6682	2.6272	1.6716
	a:	3.2368	3.6497	4.0975	3.6804	3.2220
SL LGR01-01	μ:	3.8204				
	a:	3.2506				
SL LGR01-02	μ:	-0.7516	3.2040	3.8716	2.1077	4.0384
	a:	3.1464	3.6696	3.3815	3.9537	3.3652
SL LGR03-01	μ:	2.1006	0.2457	1.4520	1.1691	0.1359
	a:	3.3971	3.3807	3.1785	3.8005	3.3444
SL LGR03-02	μ:	-0.1115	1.7434	3.4231	1.7227	2.3200
	a:	3.4109	3.3917	3.4246	3.8681	3.3612
SL LRR01-01	μ:	3.5188	1.1414	2.4297	2.2564	2.2936
	a:	2.0331	2.2742	2.2613	2.3295	2.3367
SL LRR01-02	μ:	1.2570	3.2019	4.1736	3.5794	2.8965
	a:	2.2847	2.5134	2.8750	2.7438	2.4291
SL LRR03-01	μ:	4.3767	1.7129	3.3157	3.1745	2.8777
	a:	3.4281	4.1333	4.3901	4.1774	4.1527
SL LRR03-02	μ:	4.7920	6.6618	8.1550	7.2655	6.7715
	a:	3.8952	4.6531	5.1676	4.7790	4.5096

A.3 Response to Loading: Plotted Values

For the quantities given in Table 4 and Table 5, time history plots were produced for several cycles of the loading quantity. These plots are intended to be a representative portion of the experimental data and serve to more readily interpret the tabulated values. It also acts to exemplify the nature of the experimental data and why the RMS reduction method was used to produce the mean and effective sinusoidal amplitudes reported.

A.4 Friction Tests

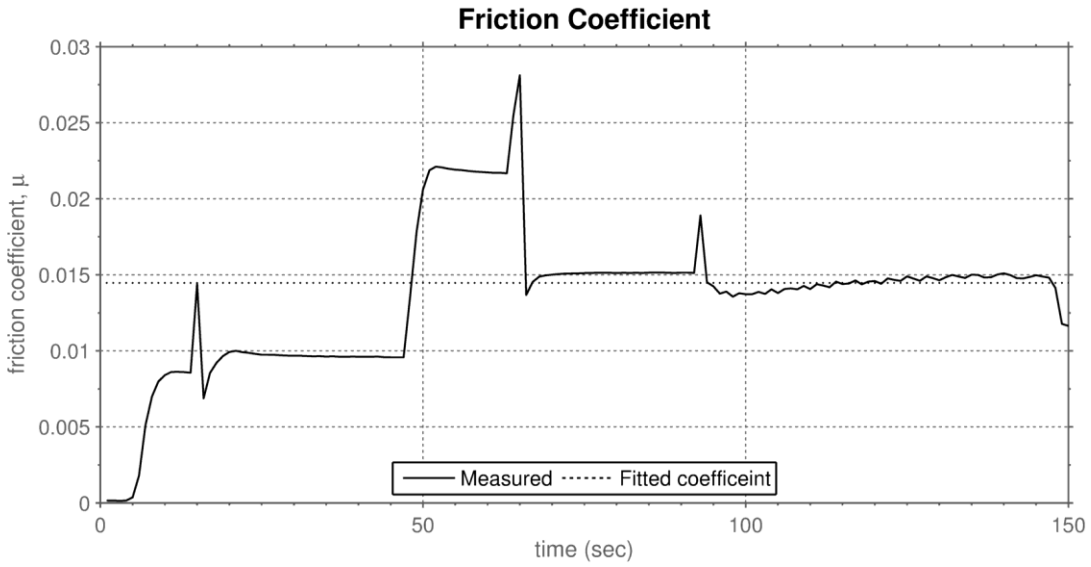

Figure A-1: Measured and Fitted Friction Coefficient for the FRK01 test

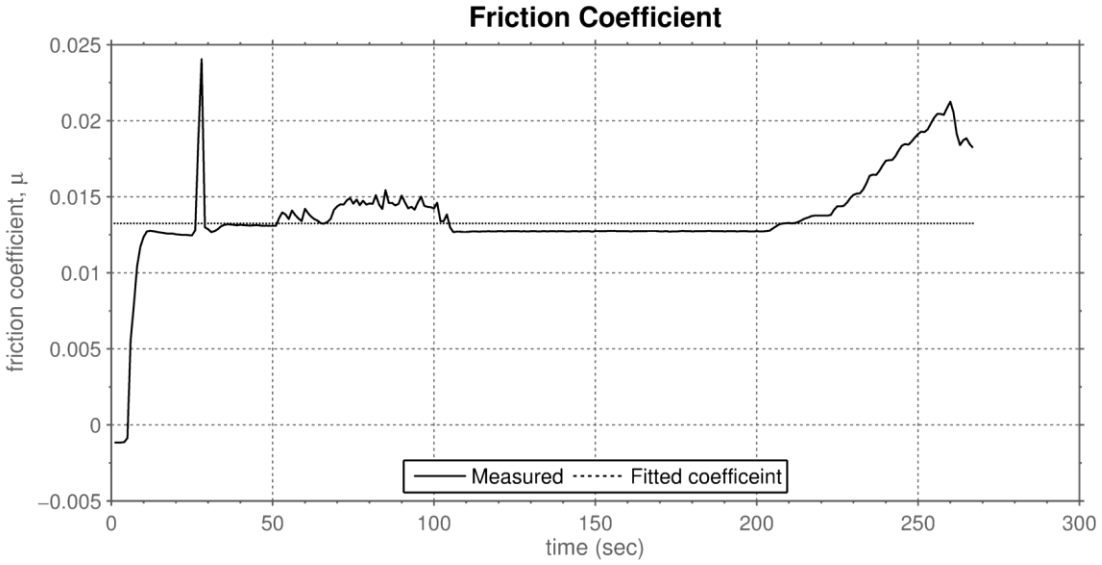

Figure A-2: Measured and Fitted Friction Coefficient for the FRK02a test

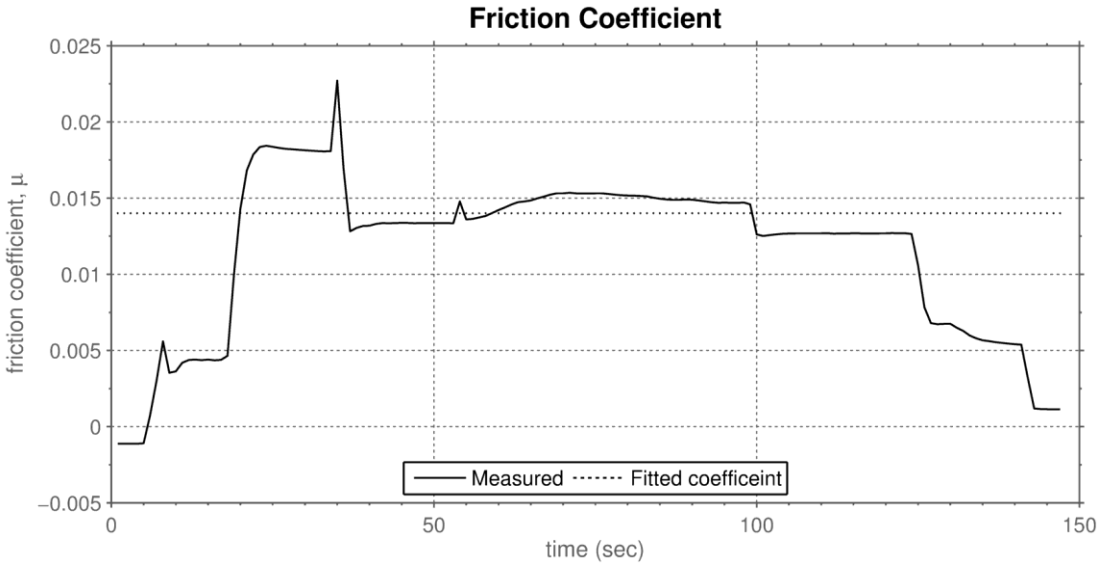

Figure A-3: Measured and Fitted Friction Coefficient for the FRK02b test

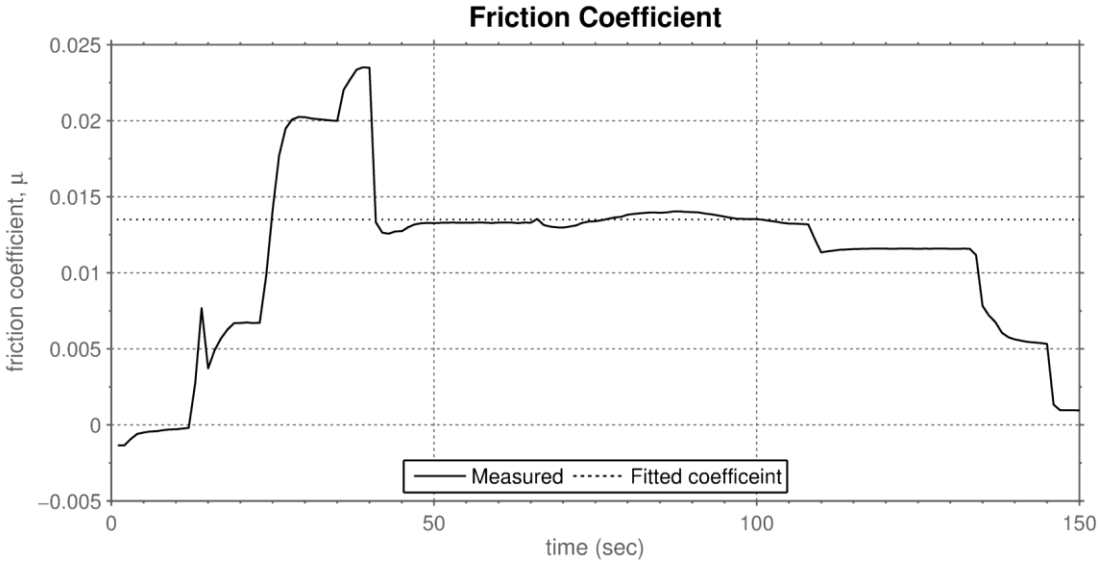

Figure A-4: Measured and Fitted Friction Coefficient for the FRK02c test

A.5 Vertical Tests (Loading in Z-direction)

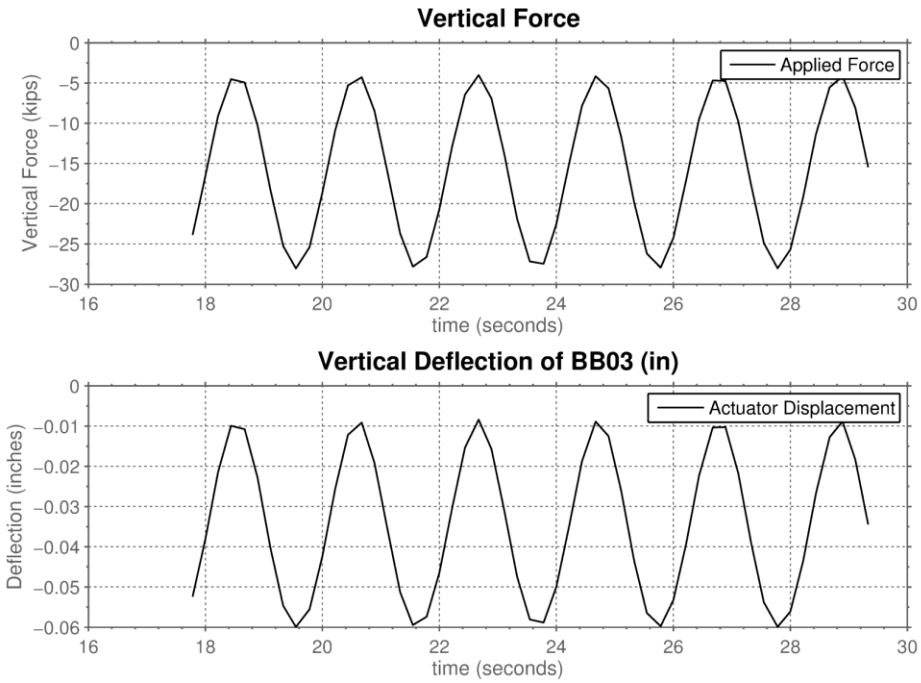

Figure A-5: Vertical Load and BB03 Displacement Time History for REF Test

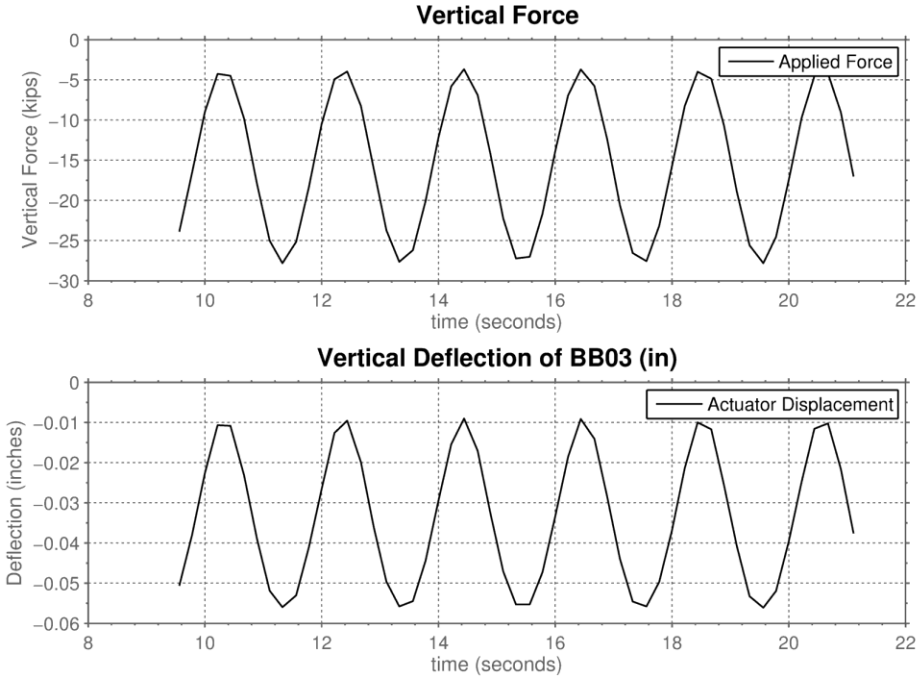

Figure A-6: Vertical Load and BB03 Displacement Time History for PIT01 Test

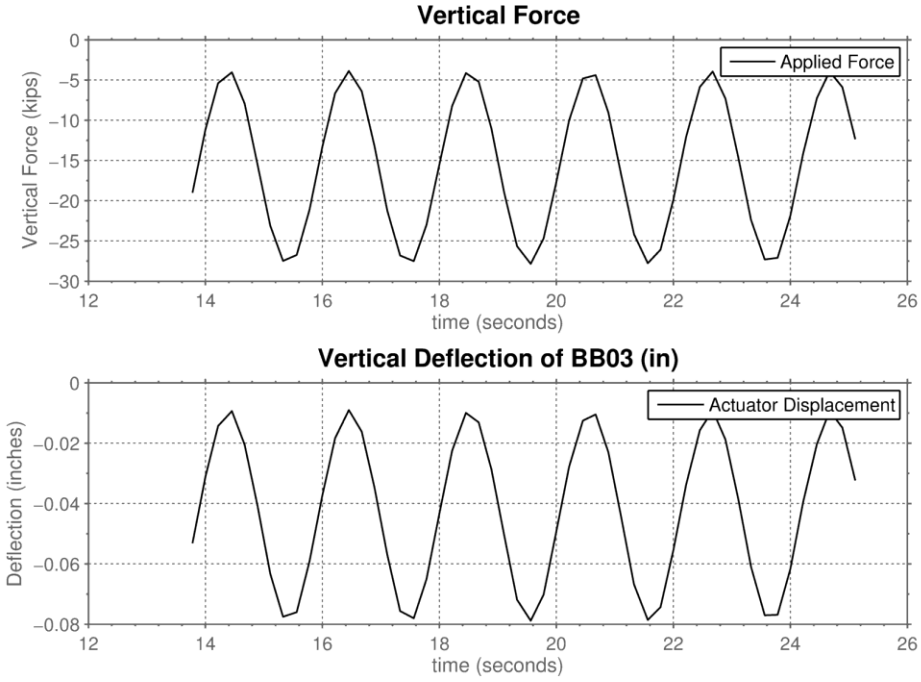

Figure A-7: Vertical Load and BB03 Displacement Time History for PIT02 Test

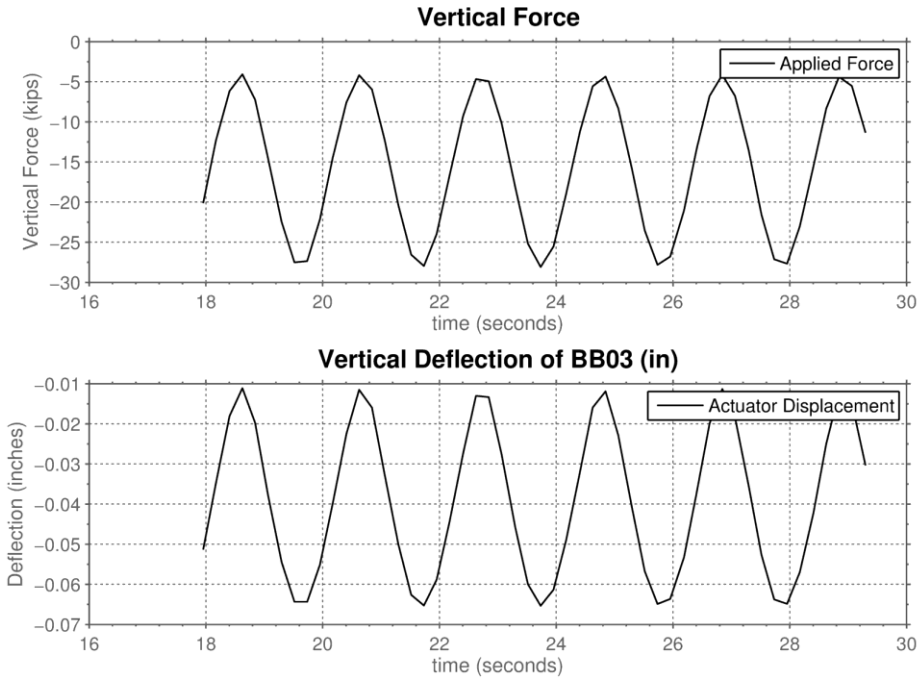

Figure A-8: Vertical Load and BB03 Displacement Time History for ROL Test

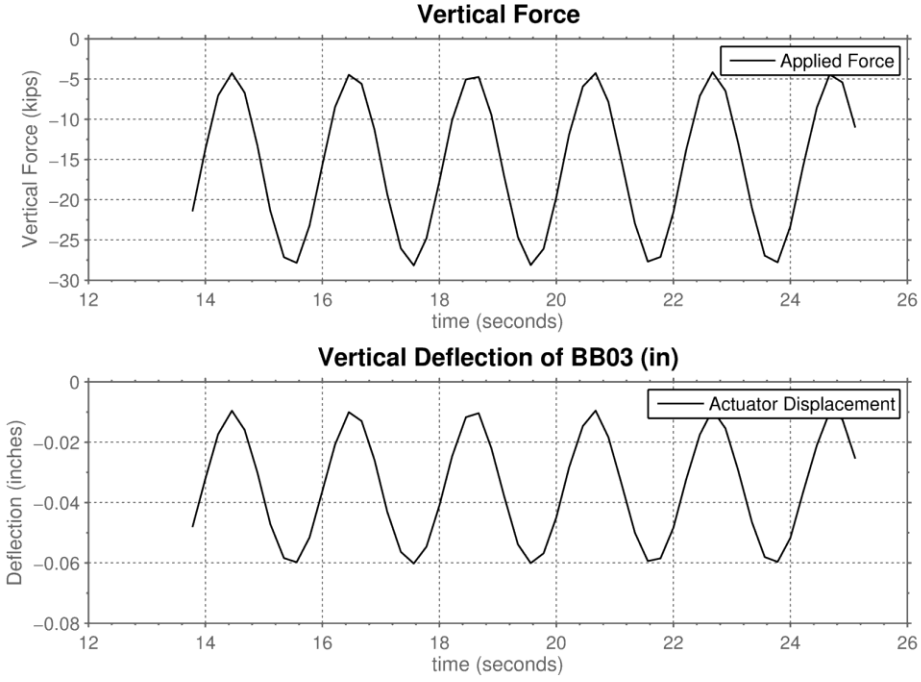

Figure A-9: Vertical Load and BB03 Displacement Time History for YAW Test

A.5.1 Rail Stresses

The time history plots for the vertical bending stresses in each rail in the CESURA geometric conditions are presented below. It should be noted that some of the plots have lines which are zero for the entirety of the time period. This is due to the fact that a lead wire has broken and the gage is malfunctioning and should not be interpreted as the rail reading a zero strain value.

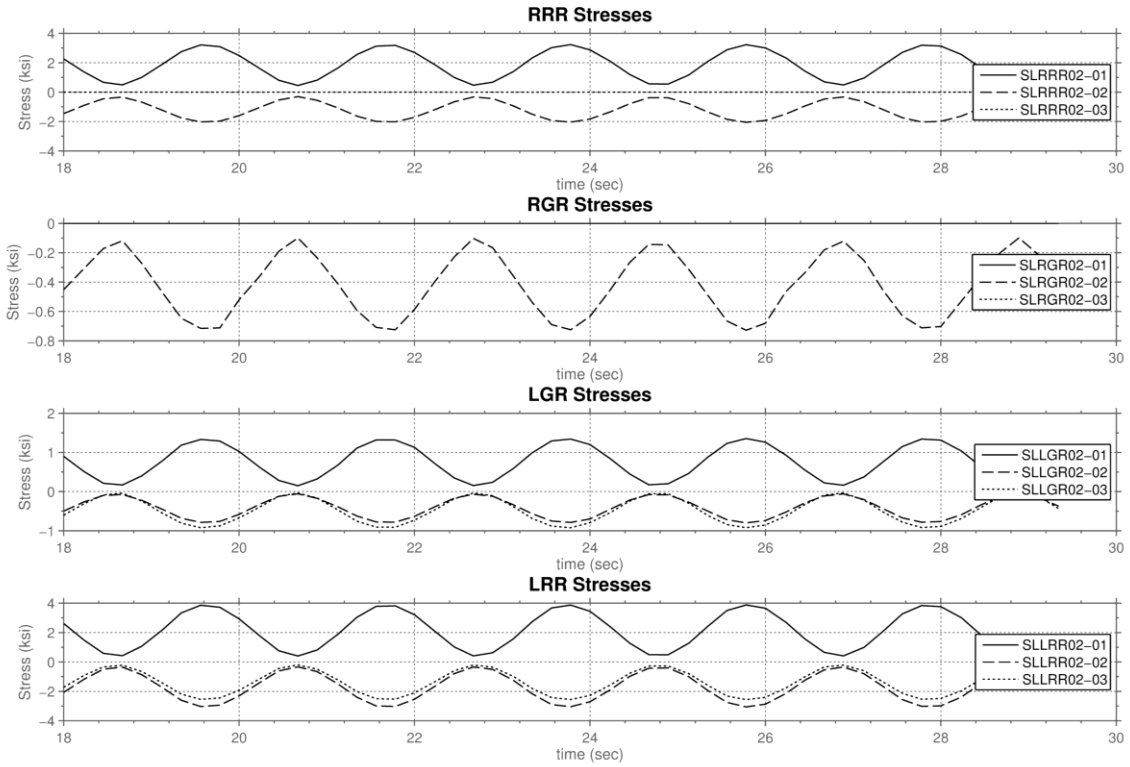

Figure A-10: Rail Stress Time History for the REF Test (Disregard gages SL RRR02-03, SL RGR02-02, and SL RGR02-03)

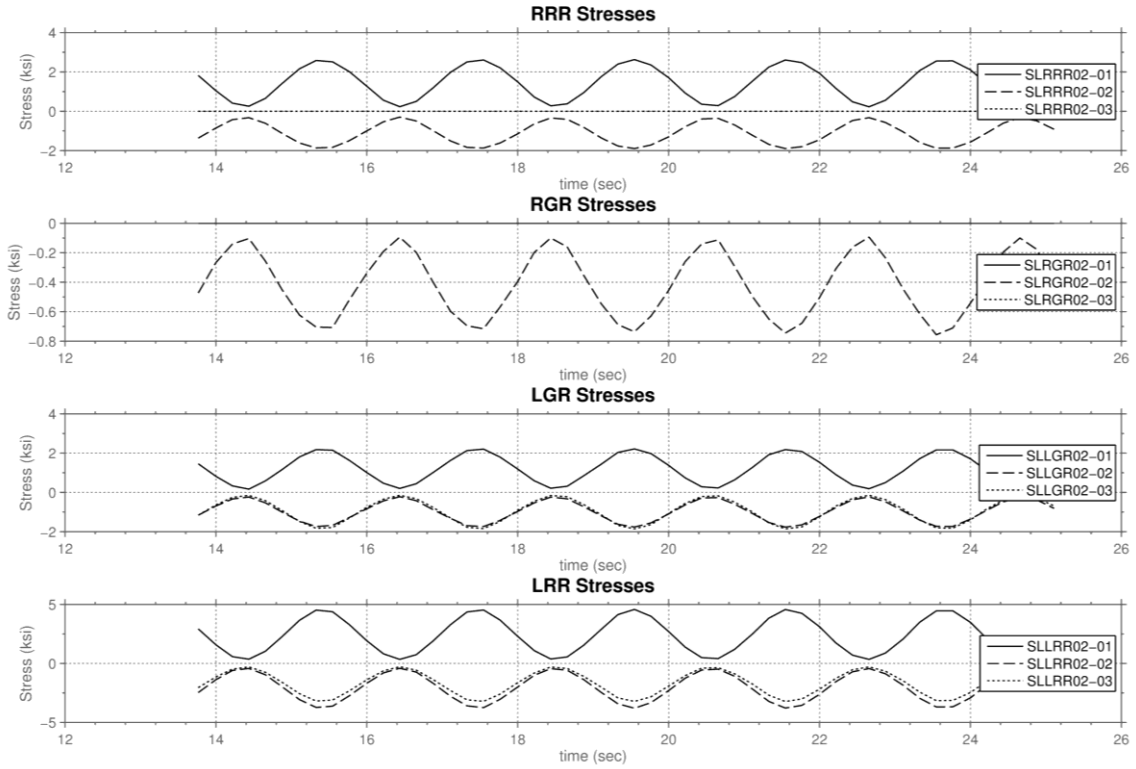

Figure A-11: Rail Stress Time History for the PIT01 Test (Disregard gages SL RRR02-03, SL RGR02-02, and SL RGR02-03)

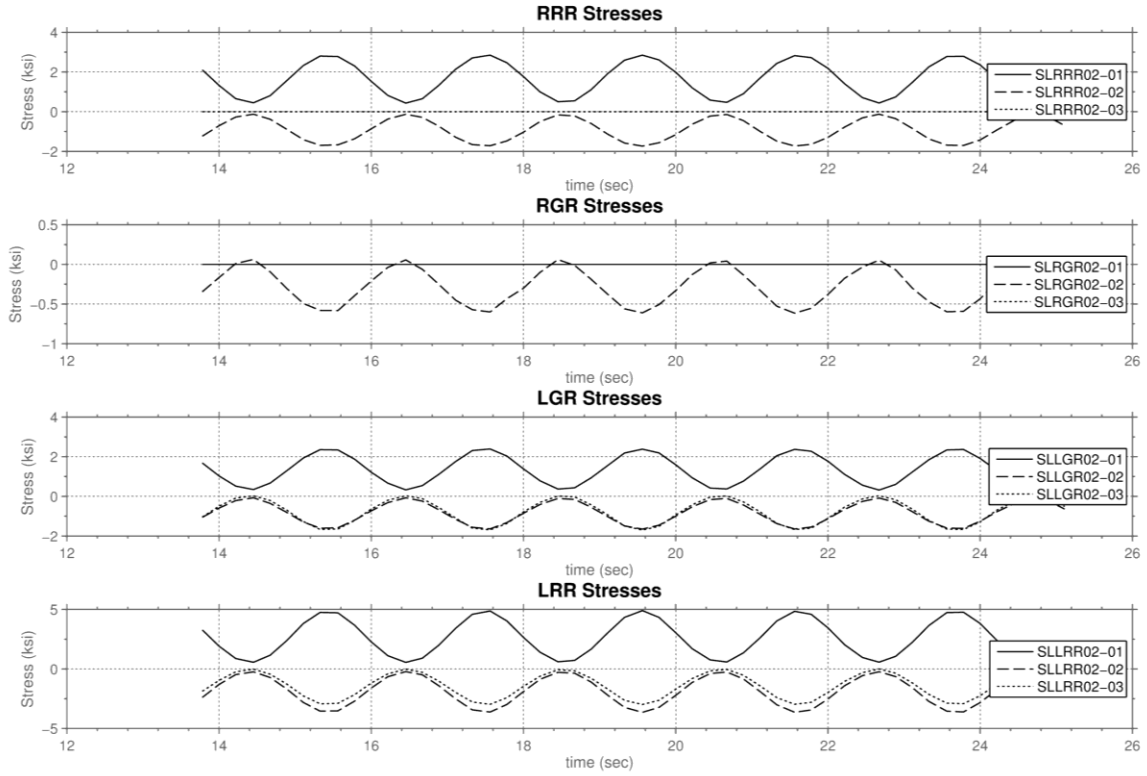

Figure A-12: Rail Stress Time History for the PIT02 Test (Disregard gages SL RRR02-03, SL RGR02-02, and SL RGR02-03)

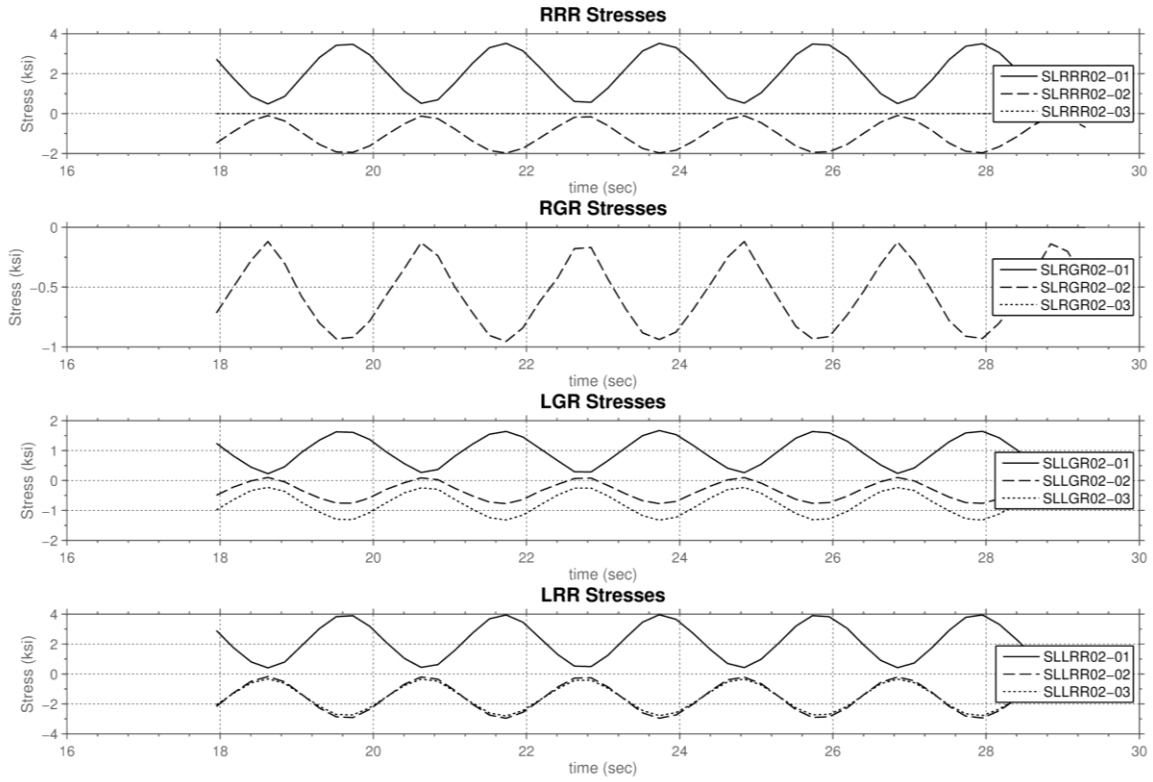

Figure A-13: Rail Stress Time History for the ROL Test (Disregard gages SL RRR02-03, SL RGR02-02, and SL RGR02-03)

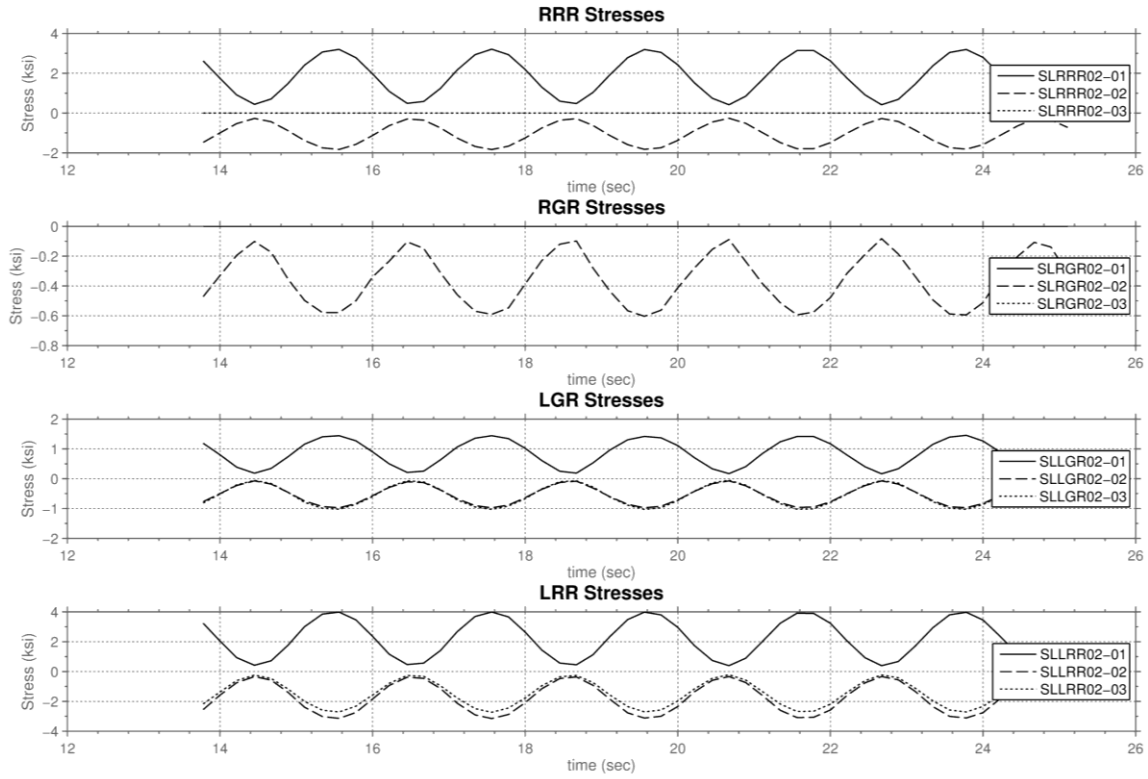

Figure A-14: Rail Stress Time History for the YAW Test (Disregard gages SL RRR02-03, SL RGR02-02, and SL RGR02-03)

A.5.2 Bearer Bar Displacements

The time history plots for the vertical deflection of the four bearer bars in each of the CESURA geometric conditions are presented below. From these plots it can be seen that Bearer Bar 03 and Bearer Bar 04 have similar displacements. The colors correspond to the different bearer bars, with the darkest being Bearer Bar 01 and the lightest being Bearer Bar 04.

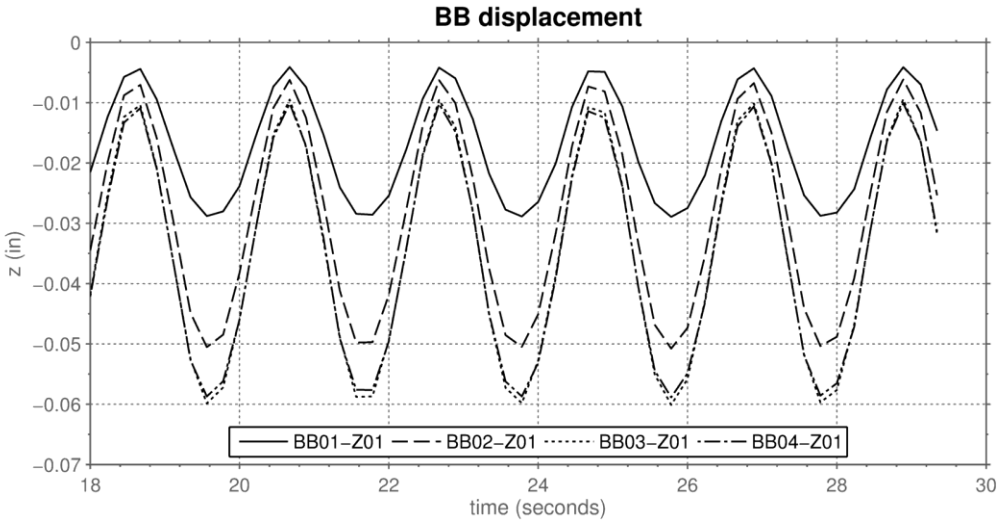

Figure A-15: Bearer Bar Displacement Time History for the REF Test

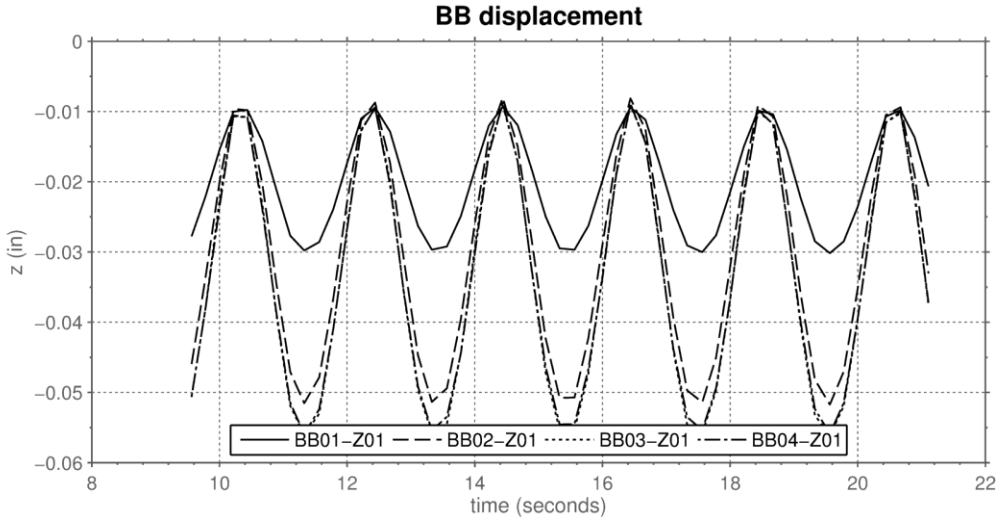

Figure A-16: Bearer Bar Displacement Time History for the PIT01 Test

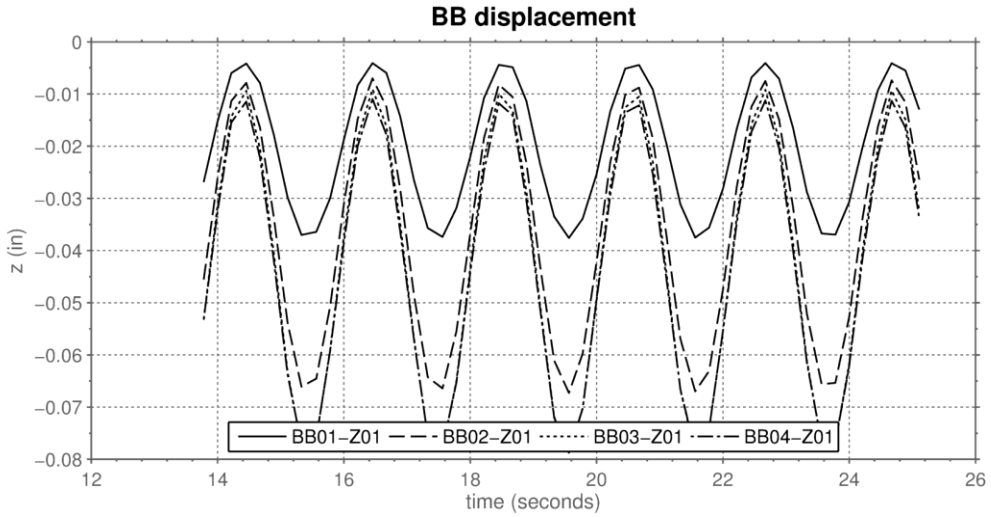

Figure A-17: Bearer Bar Displacement Time History for the PIT02 Test

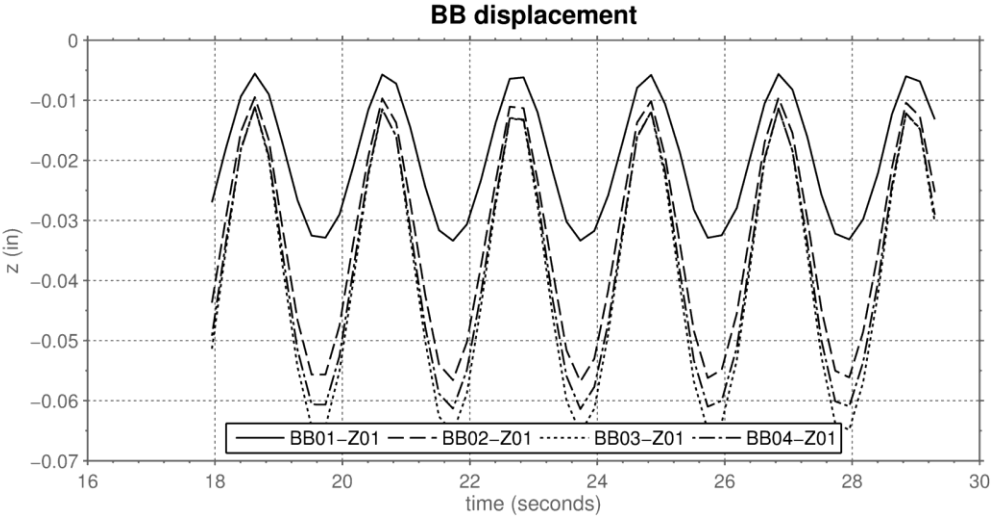

Figure A-18: Bearer Bar Displacement Time History for the ROL Test

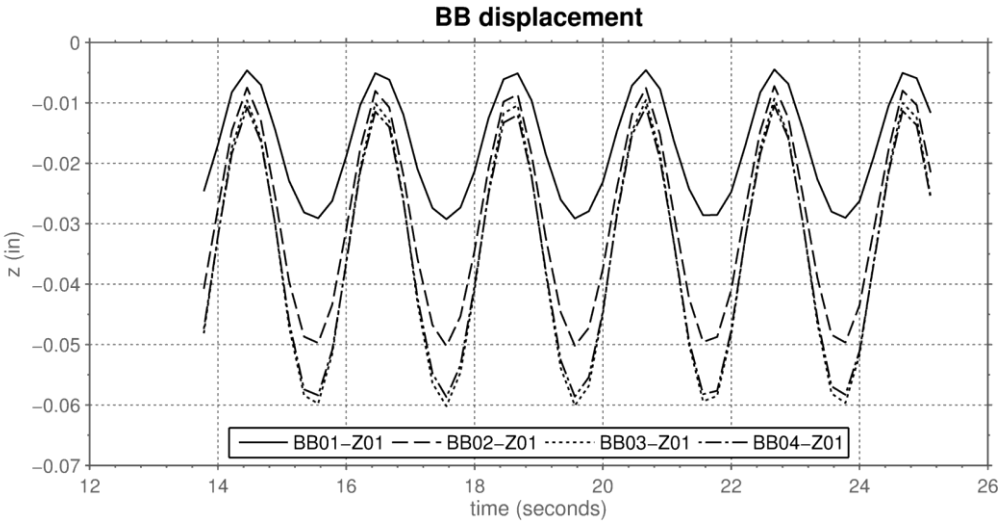

Figure A-19: Bearer Bar Displacement Time History for the YAW Test

A.5.3 Bearer Bar End Rotations

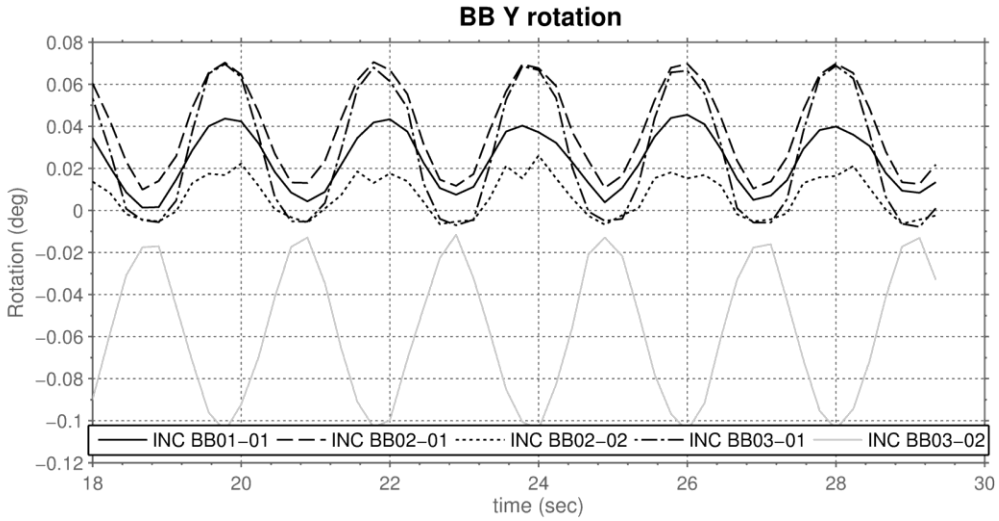

Figure A-20: Bearer Bar End Rotation Time History for the REF Test

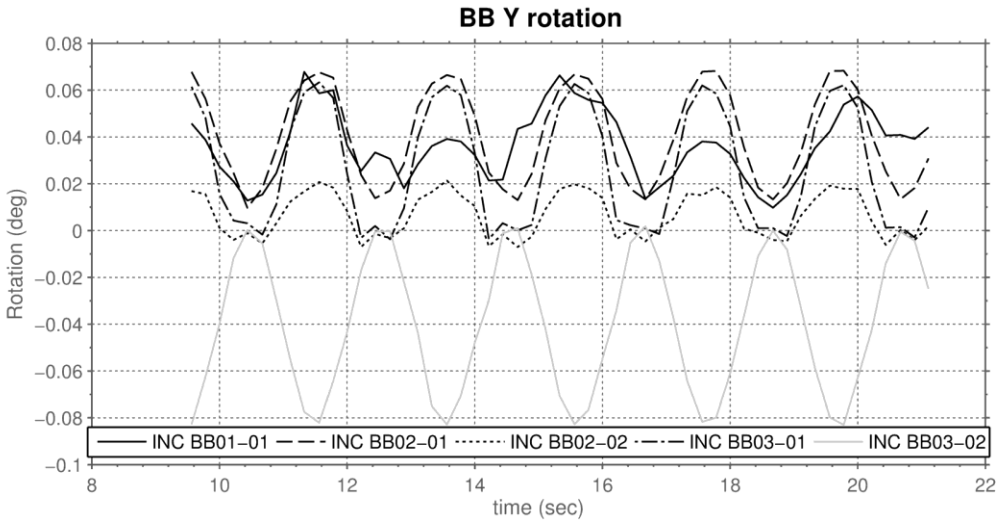

Figure A-21: Bearer Bar End Rotation Time History for the PIT01 Test

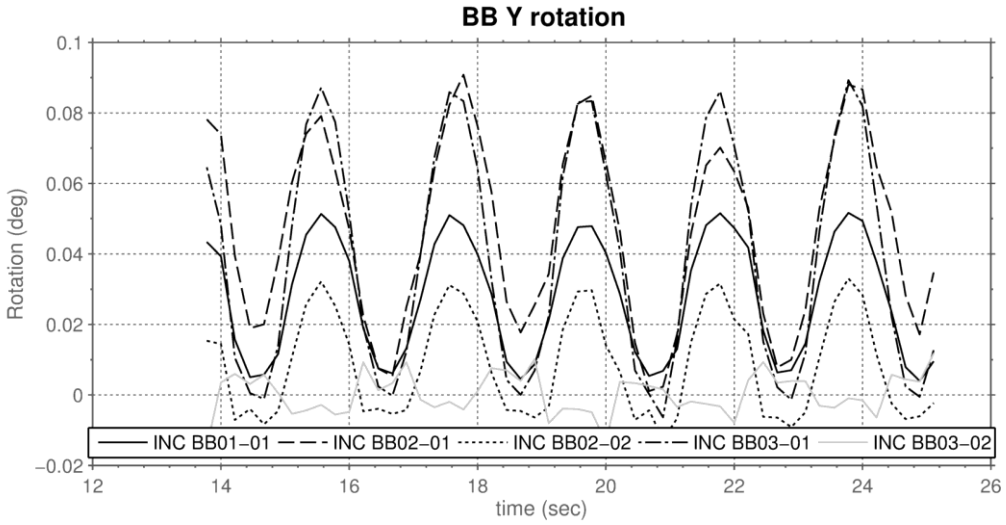

Figure A-22: Bearer Bar End Rotation Time History for the PIT02 Test

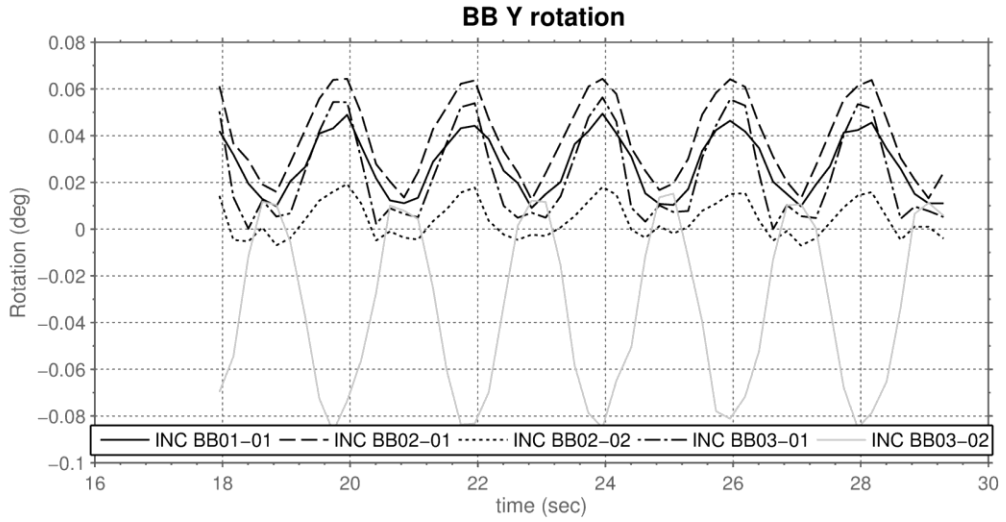

Figure A-23: Bearer Bar End Rotation Time History for the ROL Test

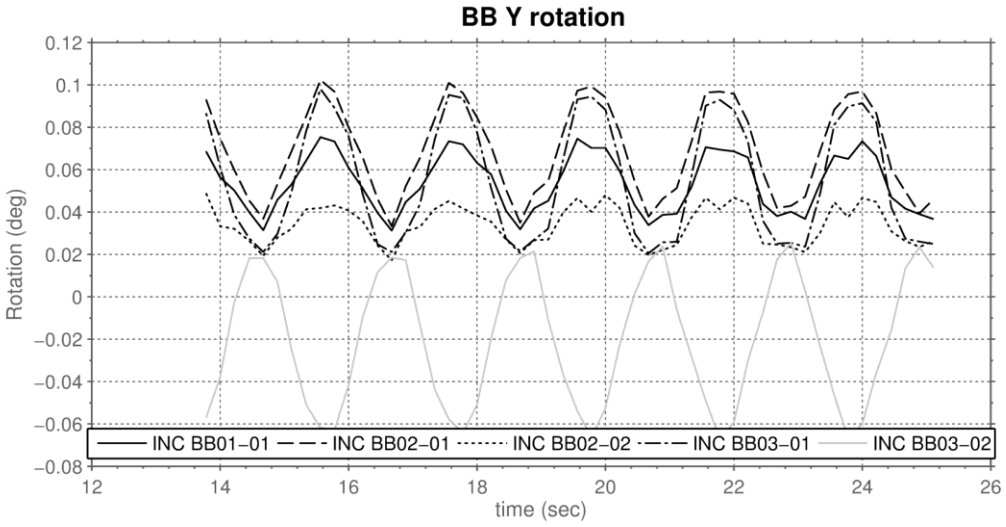

Figure A-24: Bearer Bar End Rotation Time History for the YAW01 Test

A.5.4 Bearer Bar Midspan Stresses

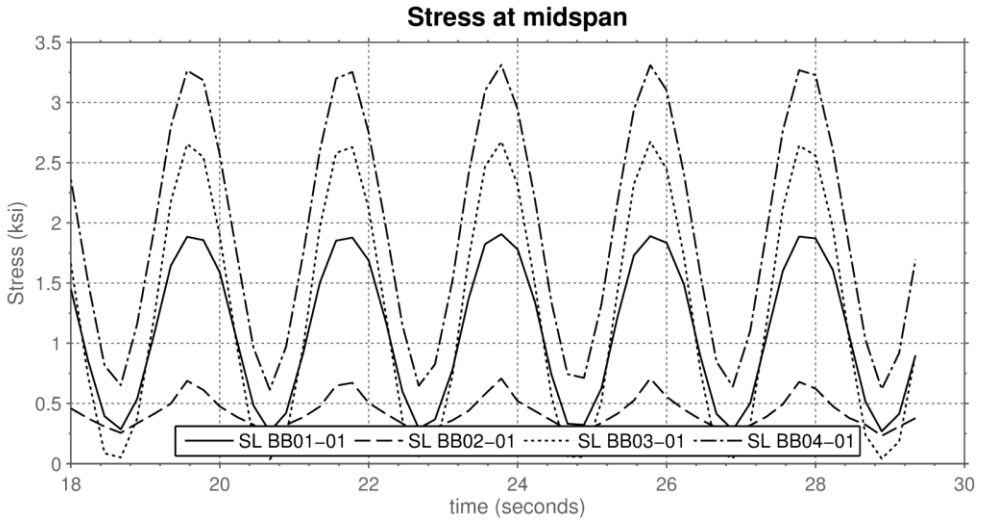

Figure A-25: Bearer Bar Mid span Bending Stress Time History for the REF Test

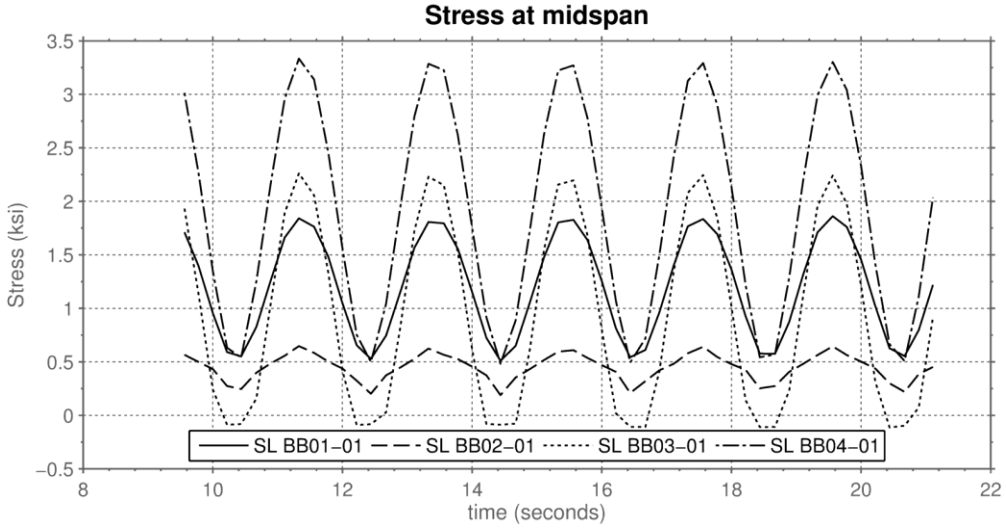

Figure A-26: Bearer Bar Mid span Bending Stress Time History for the PIT01 Test

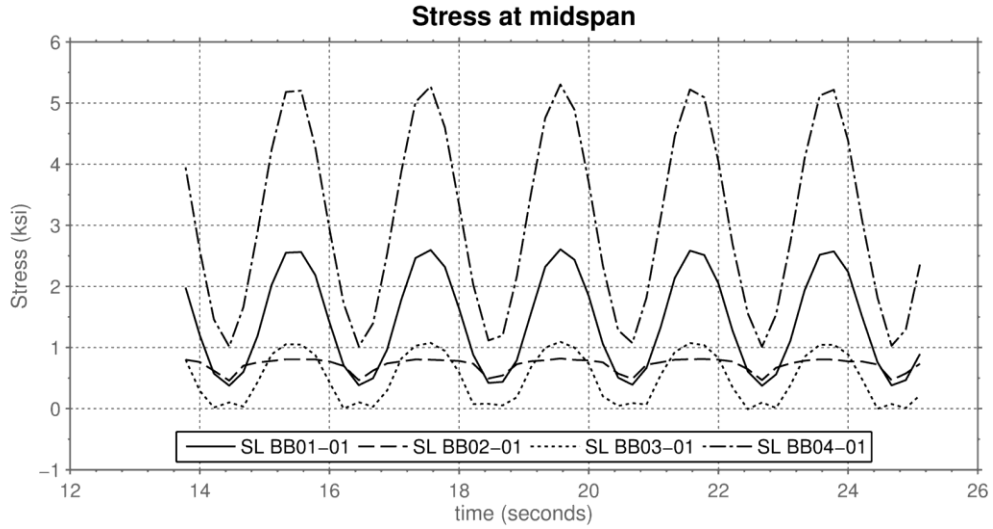

Figure A-27: Bearer Bar Mid span Bending Stress Time History for the PIT02 Test

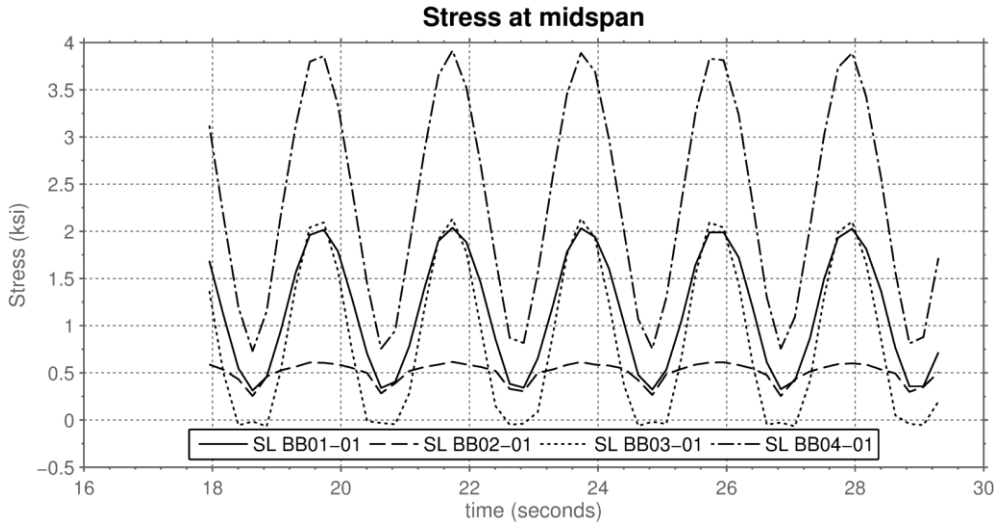

Figure A-28: Bearer Bar Mid span Bending Stress Time History for the ROL Test

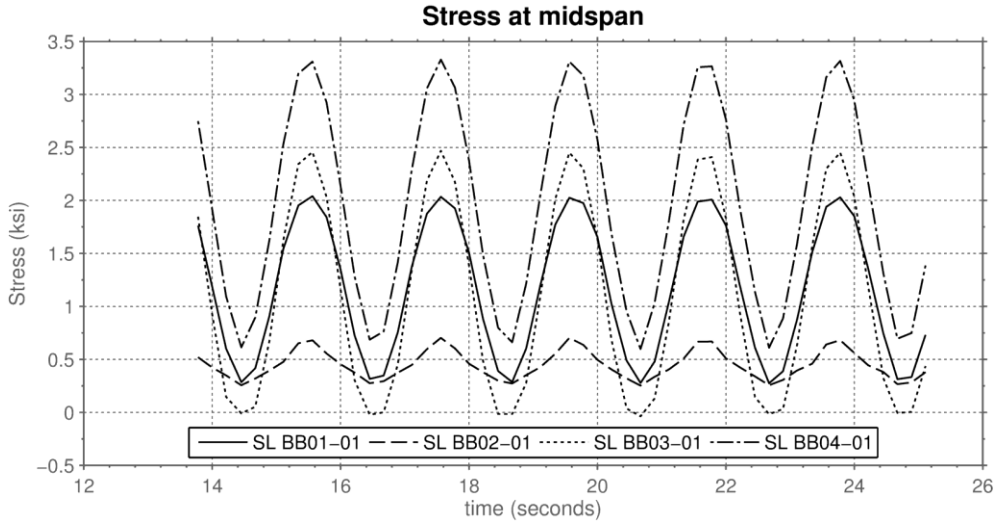

Figure A-29: Bearer Bar Mid span Bending Stress Time History for the YAW Test

A.5.5 Bearer Bar Transition Region Shear Stresses

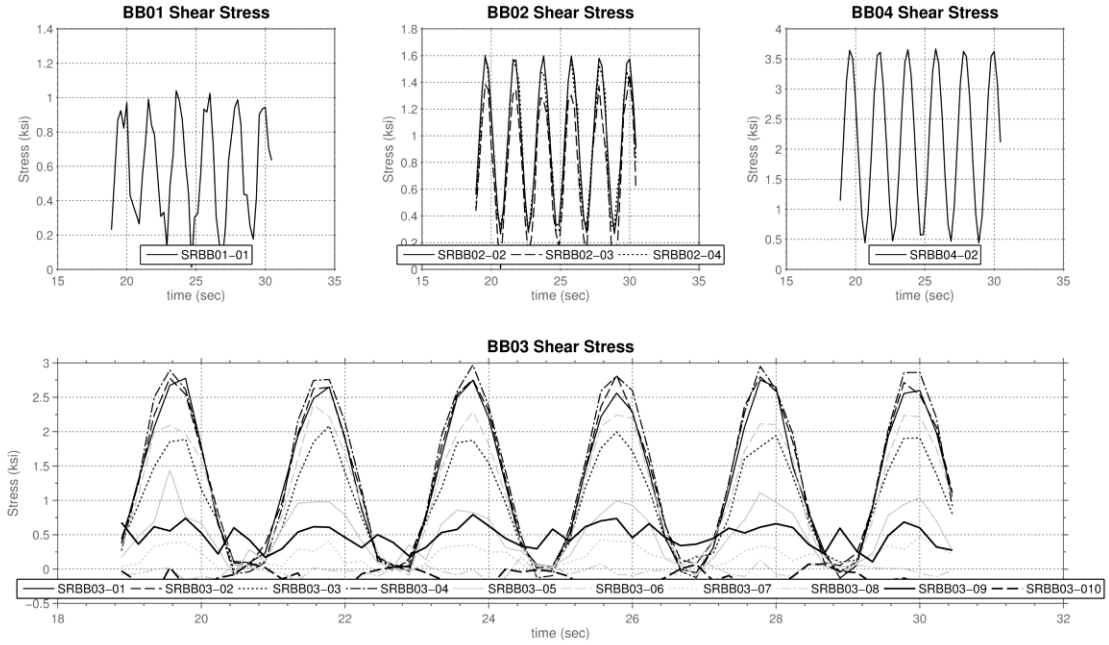

Figure A-30: Bearer Bar Shear Stresses in Transition Region Time History for the REF Test

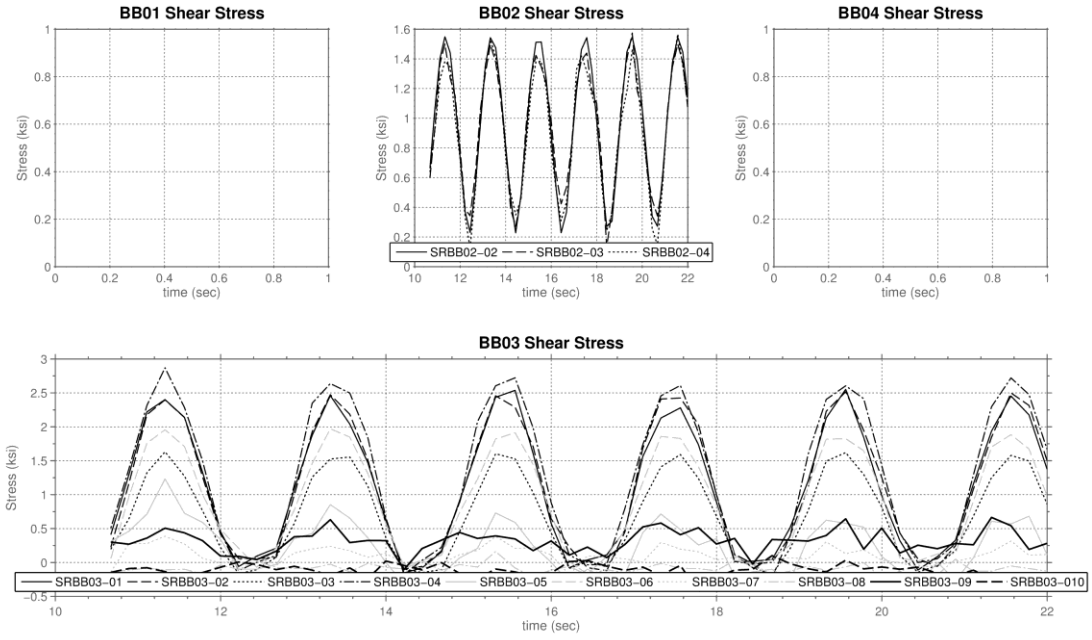

Figure A-31: Bearer Bar Shear Stresses in Transition Region Time History for the PIT01 Test

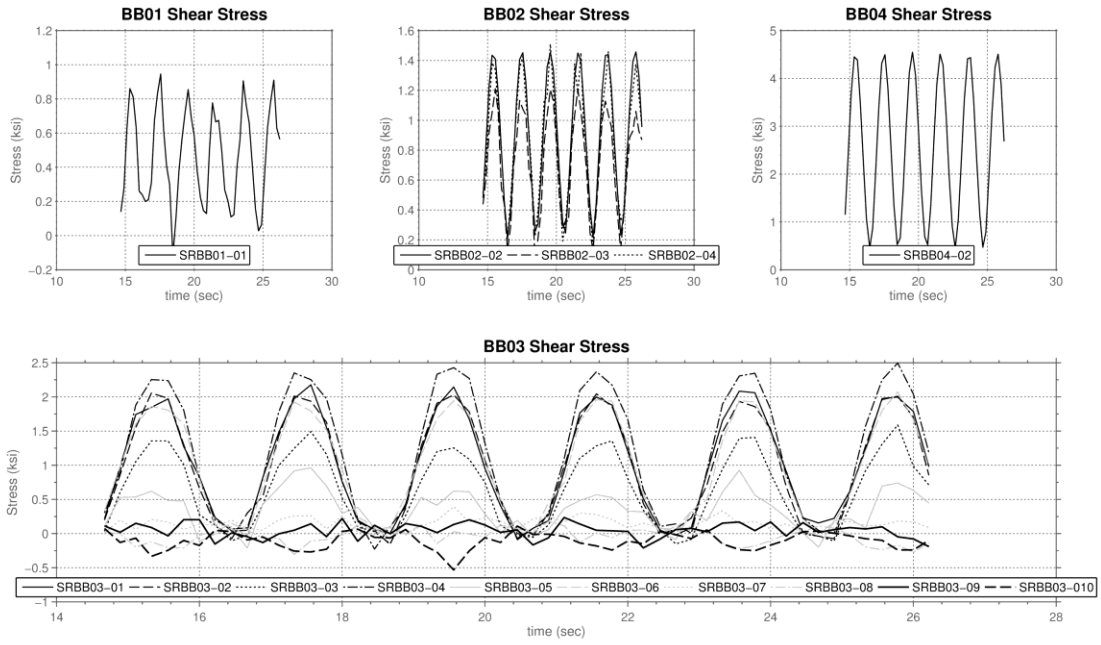

Figure A-32: Bearer Bar Shear Stresses in Transition Region Time History for the PIT02 Test

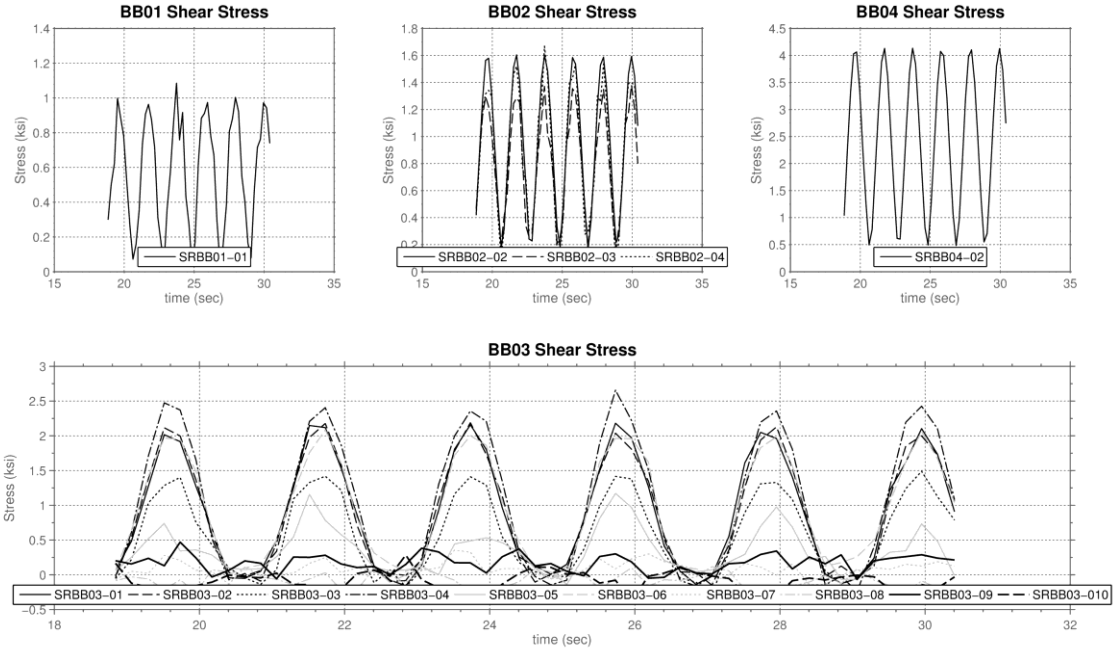

Figure A-33: Bearer Bar Shear Stresses in Transition Region Time History for the ROL Test

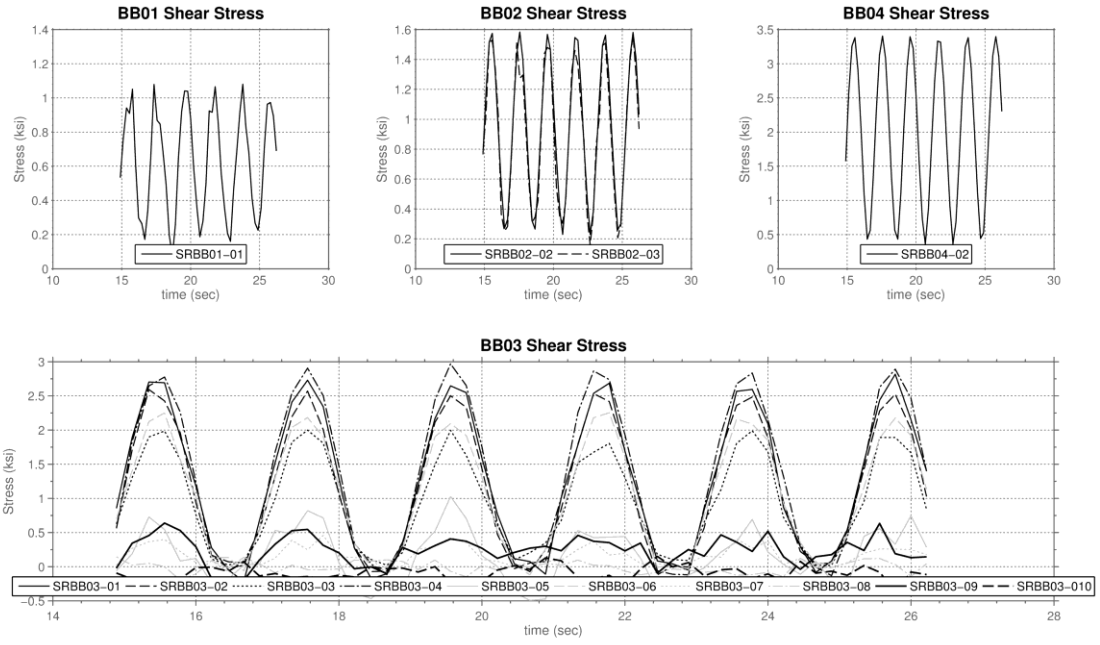

Figure A-34: Bearer Bar Shear Stresses in Transition Region Time History for the YAW Test

A.6 Horizontal Tests (Loading in Y-direction)

A.6.1 Horizontal Load and Displacement Time History

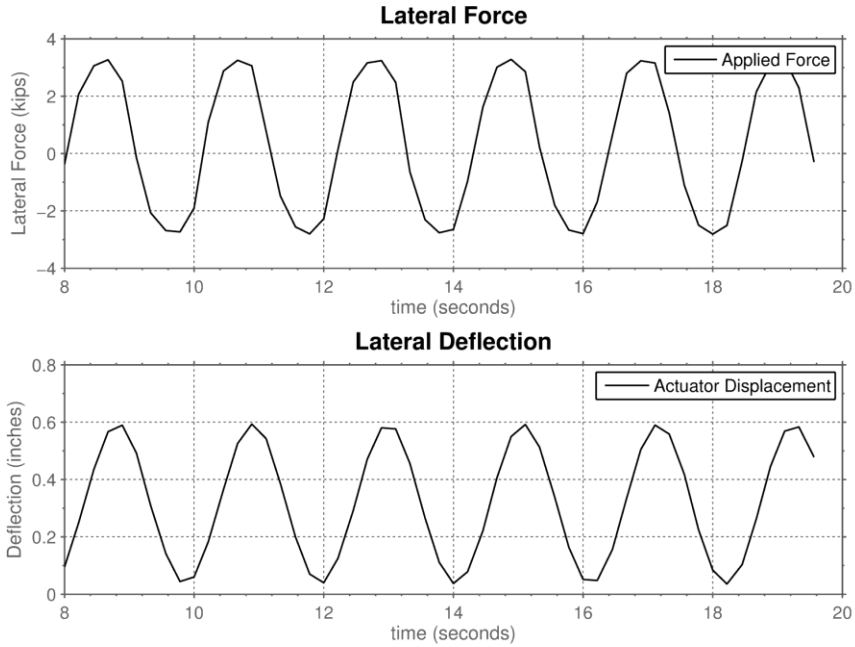

Figure A-35: Horizontal Load and Actuator Displacement Time History for REF Test

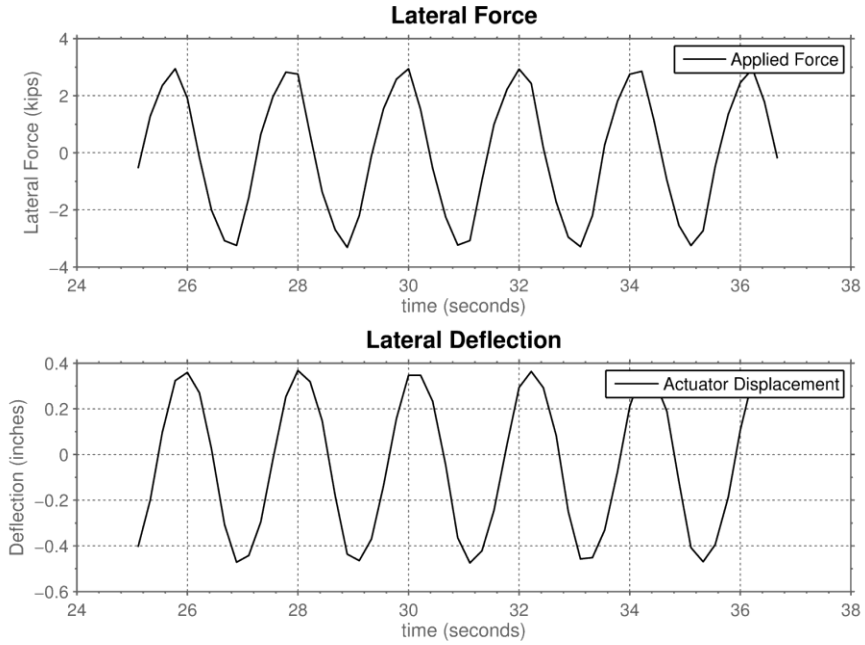

Figure A-36: Horizontal Load and Actuator Displacement Time History for PIT01 Test

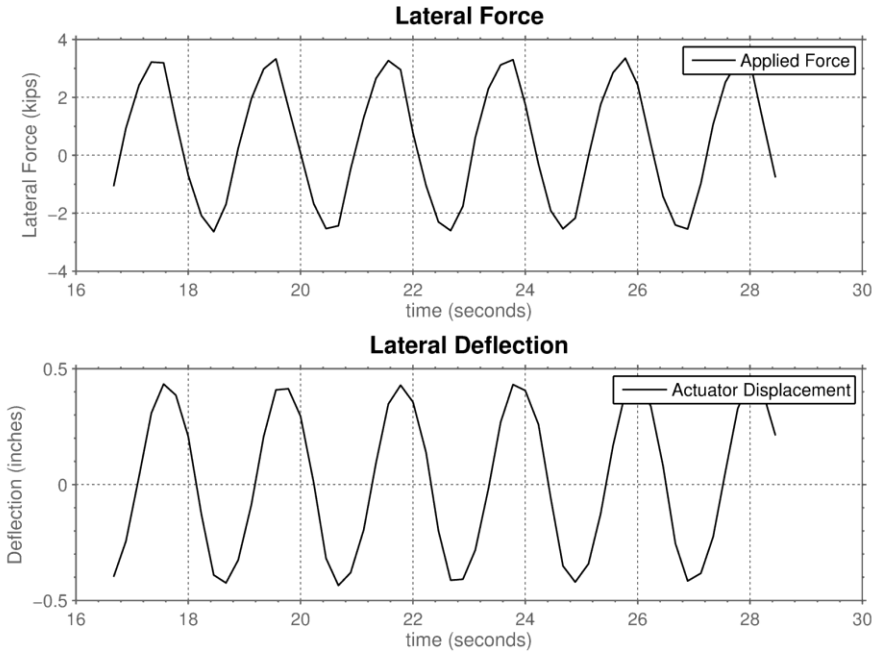

Figure A-37: Horizontal Load and Actuator Displacement Time History for PIT02 Test

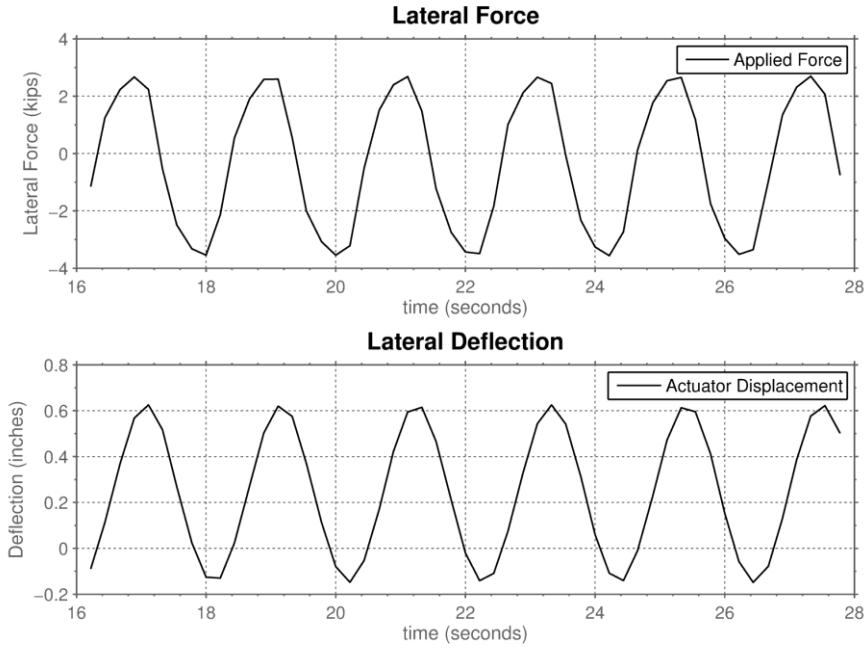

Figure A-38: Horizontal Load and Actuator Displacement Time History for ROL01 Test

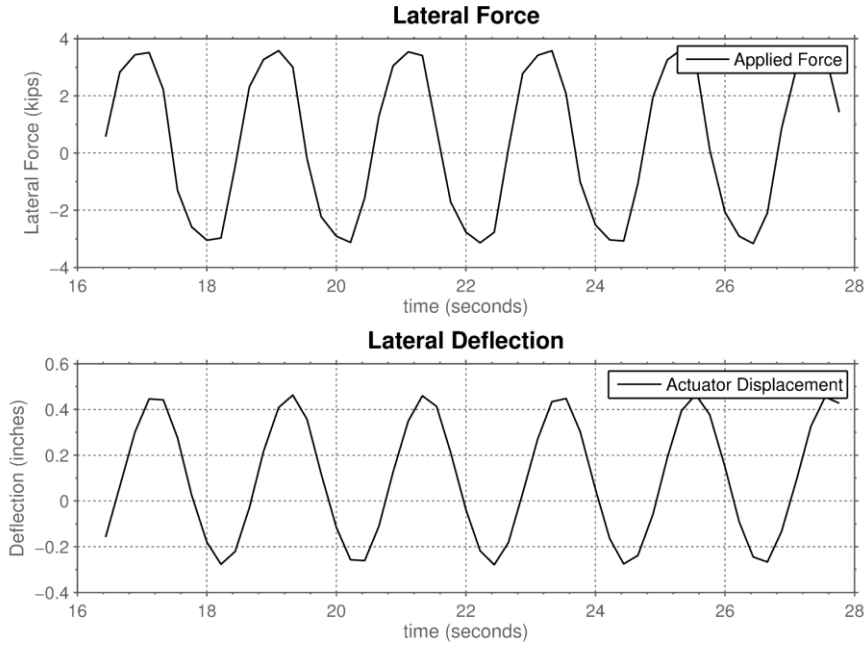

Figure A-39: Horizontal Load and Actuator Displacement Time History for the YAW Test

A.6.2 Load-Displacement Response

The load versus displacement responses for each geometric configuration is presented. Displacements have been shifted so that the line representing the average secant stiffness passes through the origin.

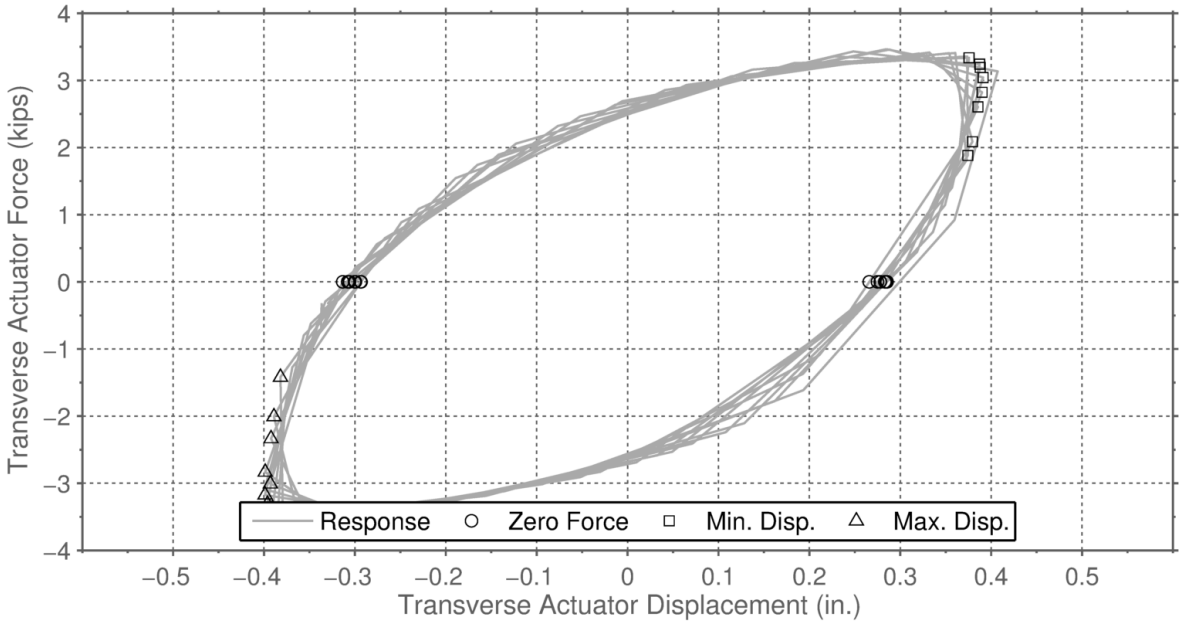

Figure A-40: Horizontal Force-Displacement Curve for the REF Test

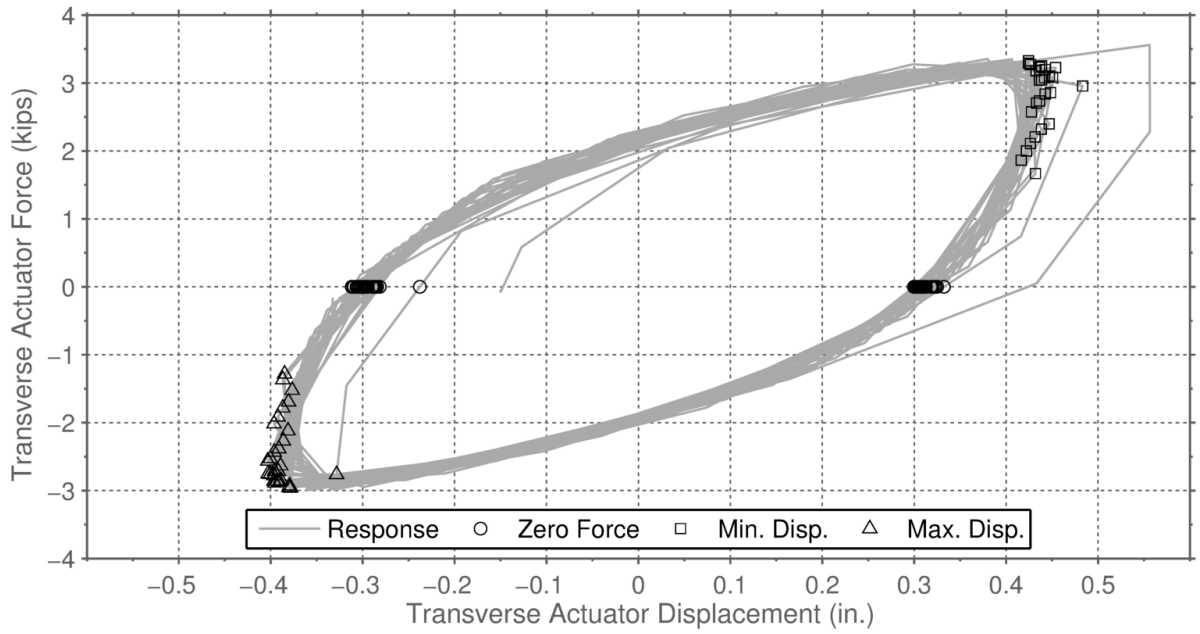

Figure A-41: Horizontal Force-Displacement Curve for the PIT01 Test

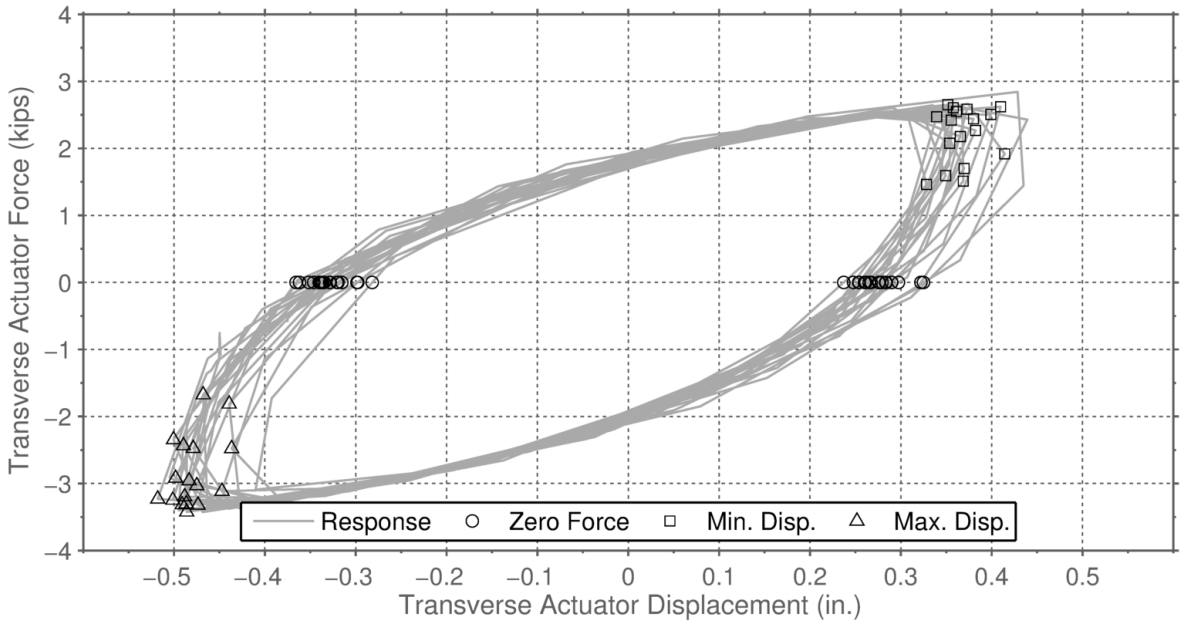

Figure A-42: Horizontal Force-Displacement Curve for the PIT02 Test

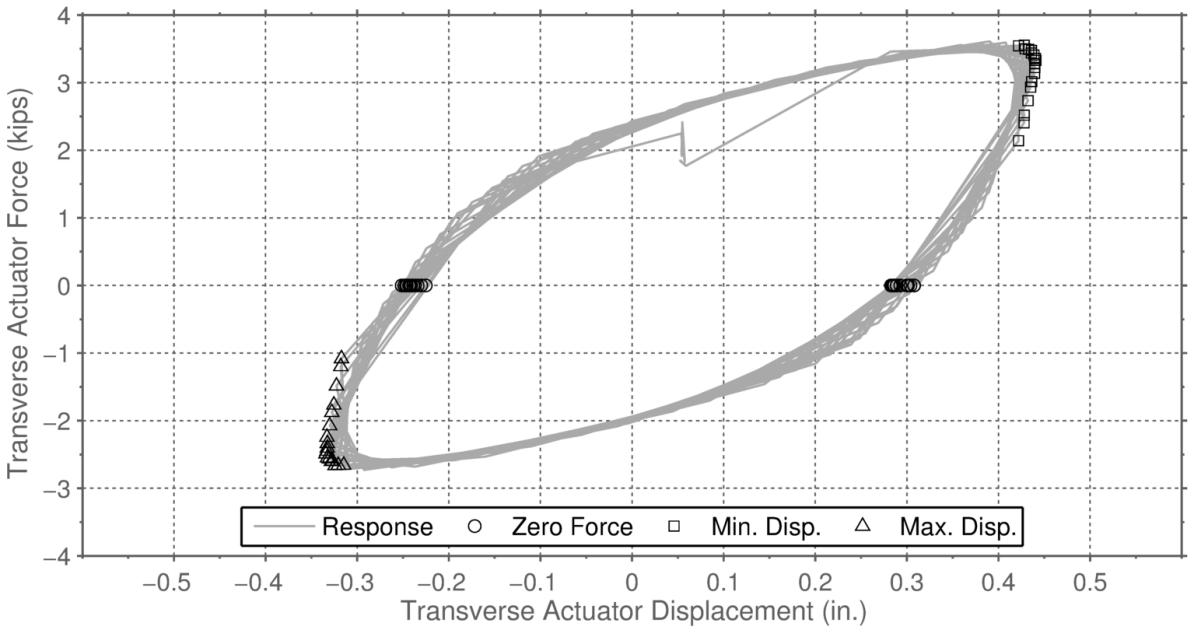

Figure A-43: Horizontal Force-Displacement Curve for the ROL Test

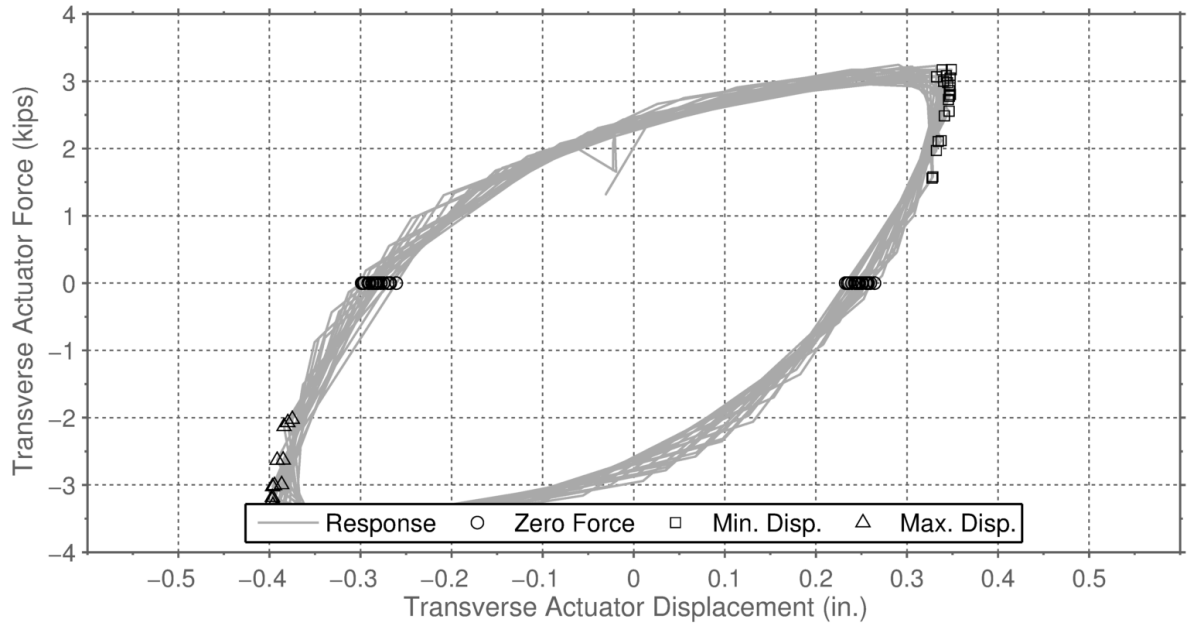

Figure A-44: Horizontal Force-Displacement Curve for the YAW Test

A.6.3 Bearer Bar Displacements and Rail Deformations

The displaced shapes of the rails in the initial, maximum and minimum positions of the bearer bars are presented in the figures below, with their linear fits. For each rail position, the data points (bearer bar y-displacements) were all collected at exactly the same time. These plots show that the motion of the rails, and the bearer bars connected to them, can be closely represented by a rigid body rotation about the pin at the wall. The linear fit curves show that rigid body motion, and the difference between the linear fit and the measured values represents the bending deformations of the rails. Those bending deformations are caused by horizontal forces, which are provided by the resistance to transverse movement provided by the FPS bearings and other sources. Note that the resistance of an FPS bearing is proportional to the vertical load acting on it. Values are presented for ease of comparison.

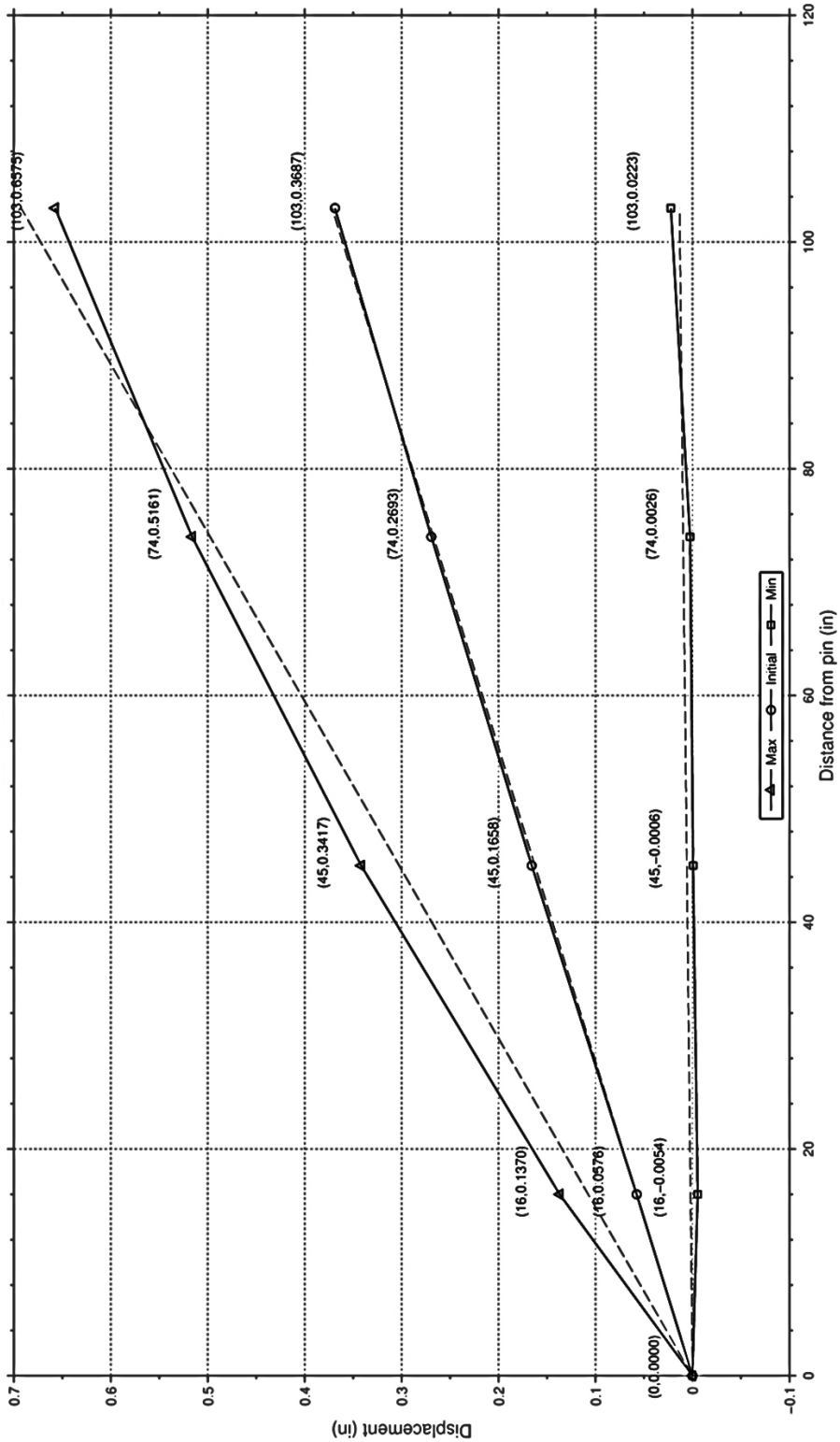

Figure A-45: Bearer Bar Y-Displacement at Peak Values for REF Test

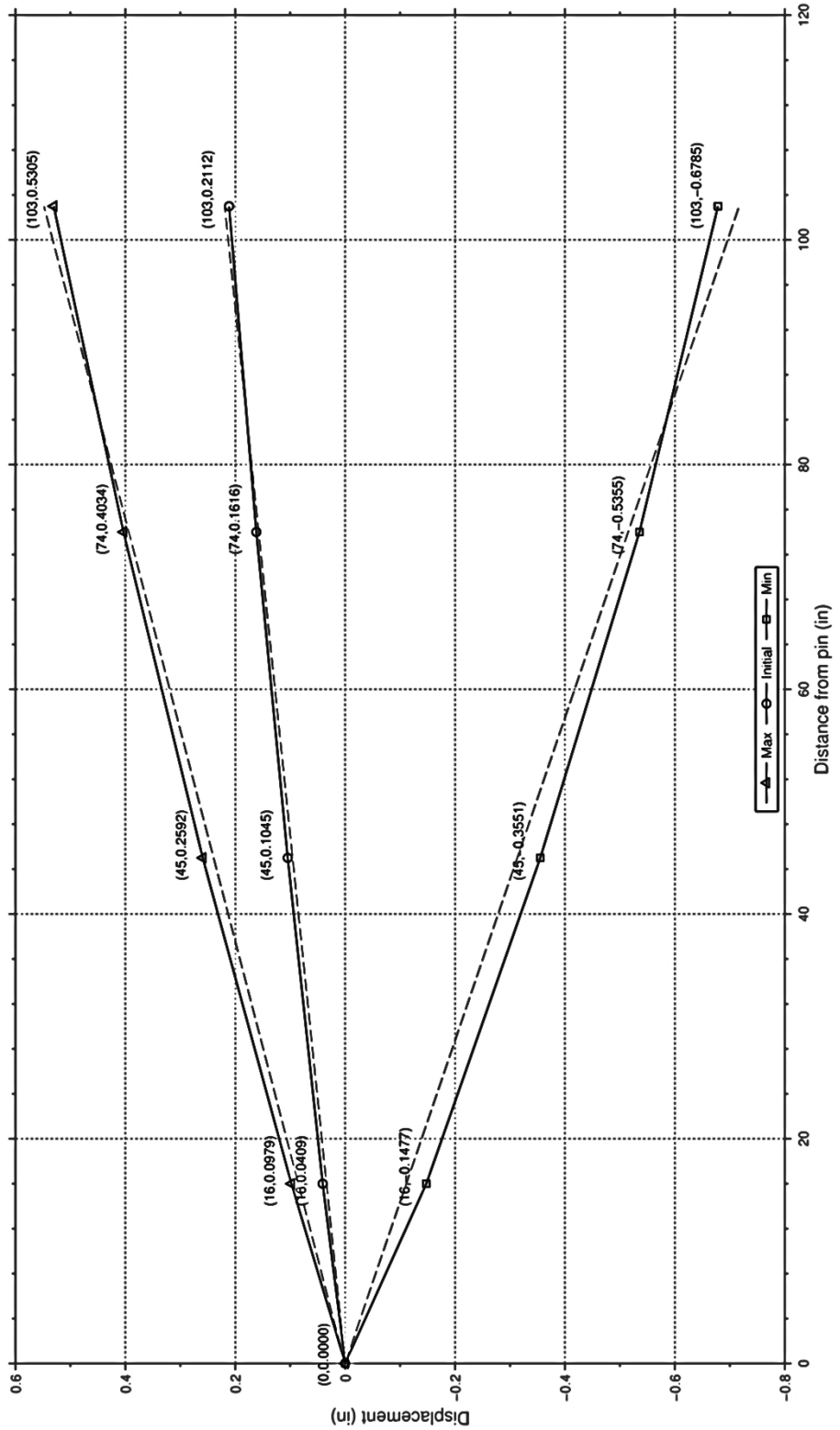

Figure A-46: Bearer Bar Y-Displacement at Peak Values for PIT01 Test

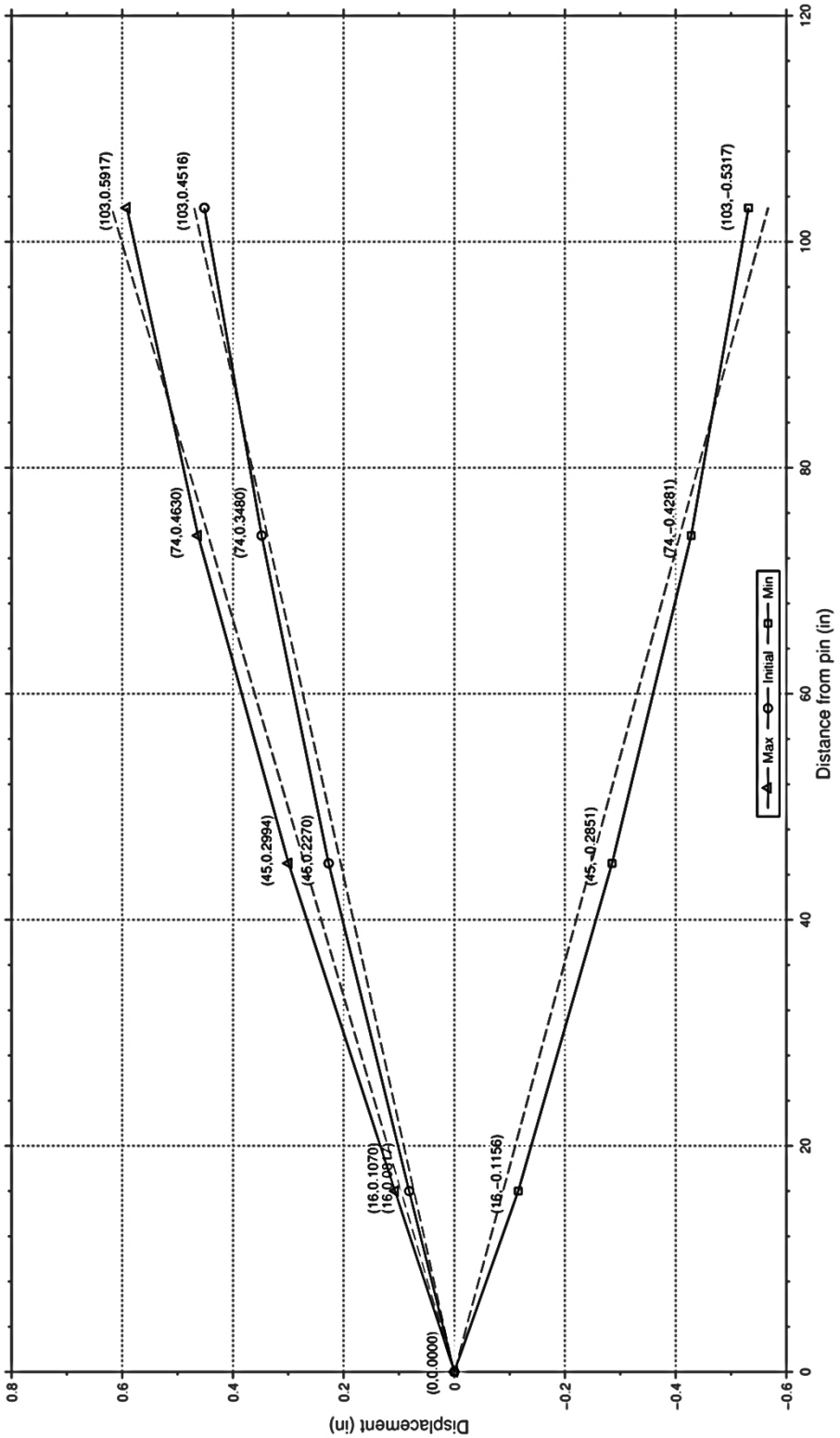

Figure A-47: Bearer Bar Y-Displacement at Peak Values for PIT02 Test

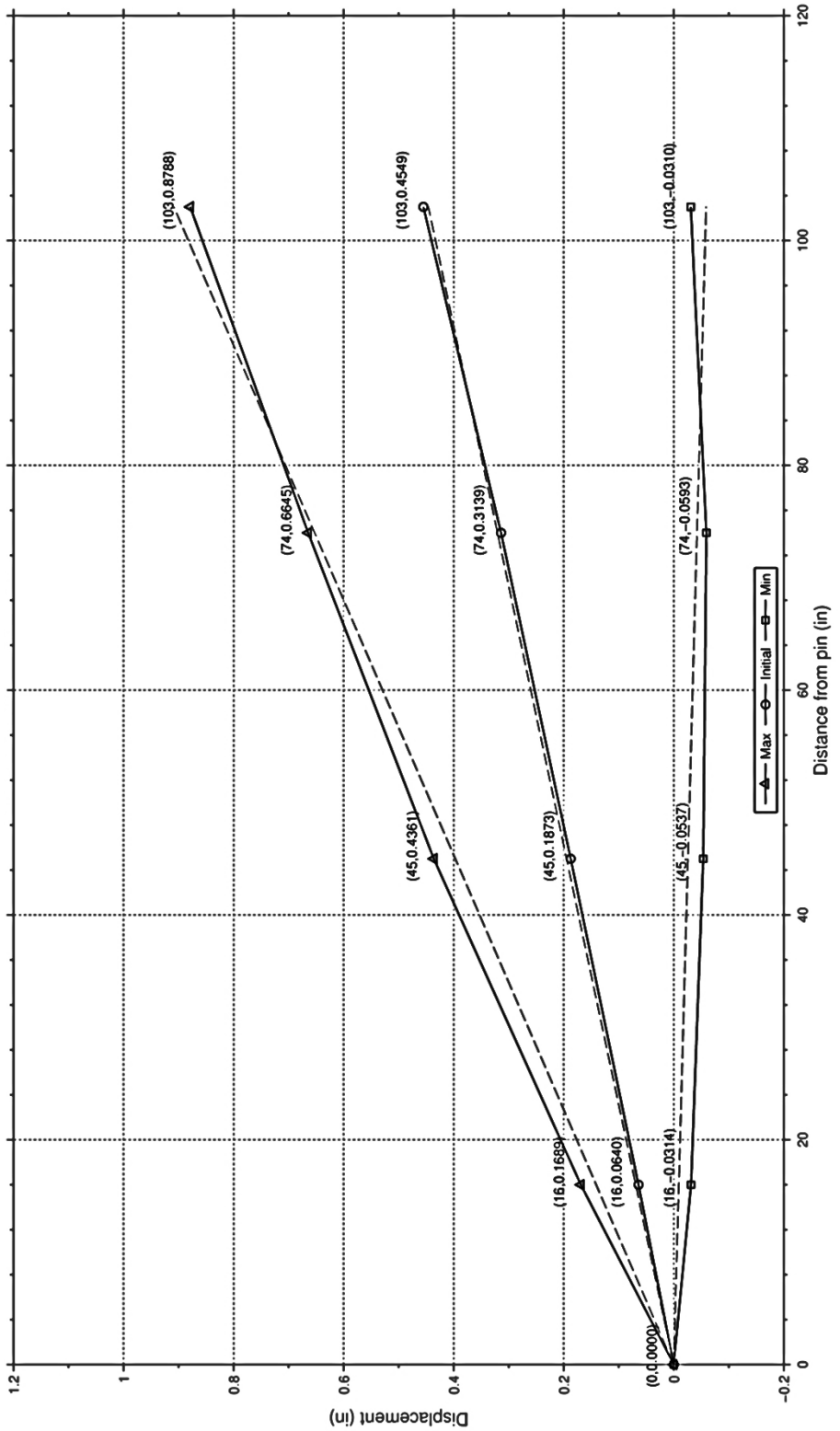

Figure A-48: Bearer Bar Y-Displacement at Peak Values for ROL Test

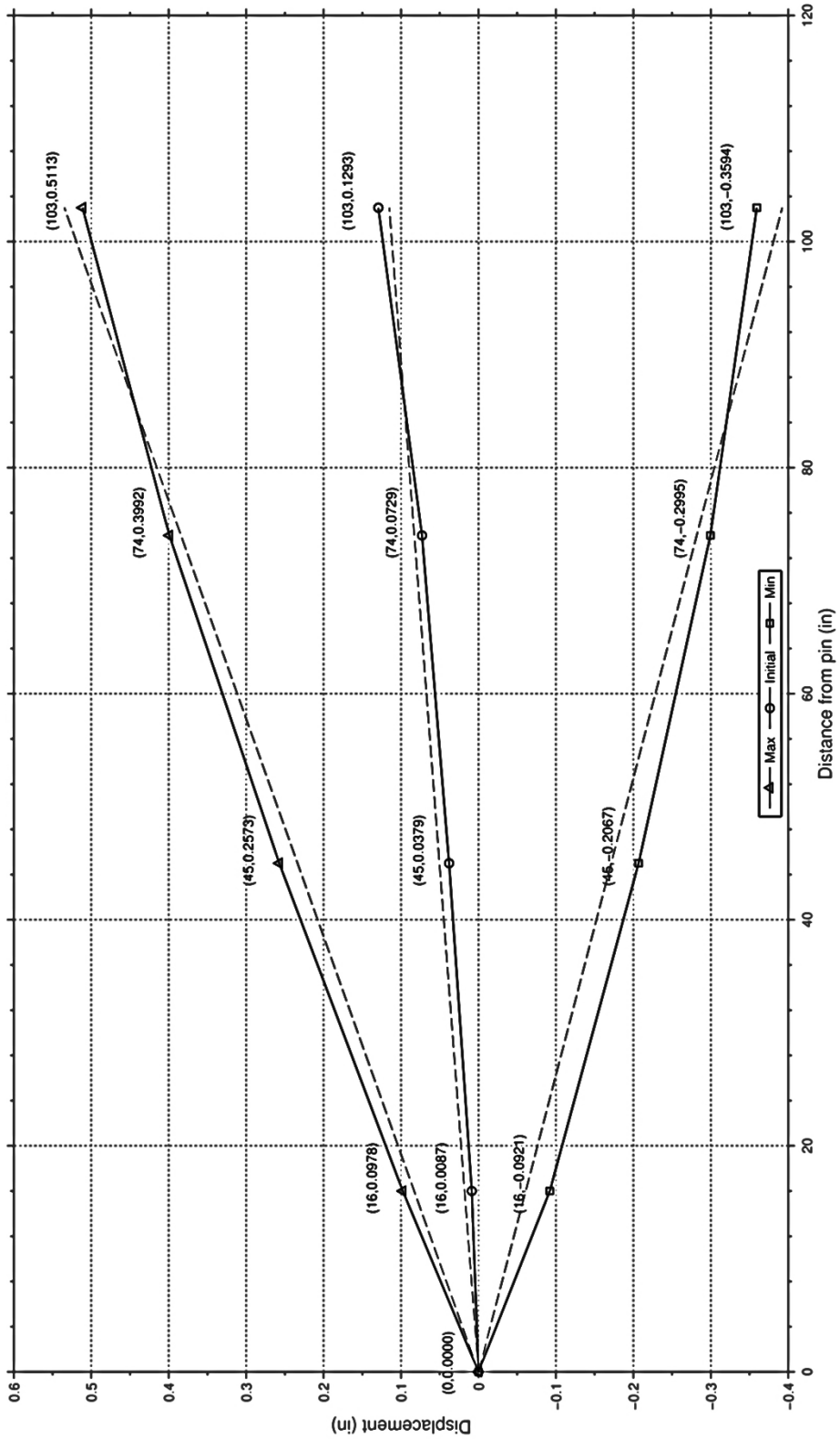

Figure A-49: Bearer Bar Y-Displacement at Peak Values for YAW Test

A.6.4 Bearer Bar Displacements: Time Histories

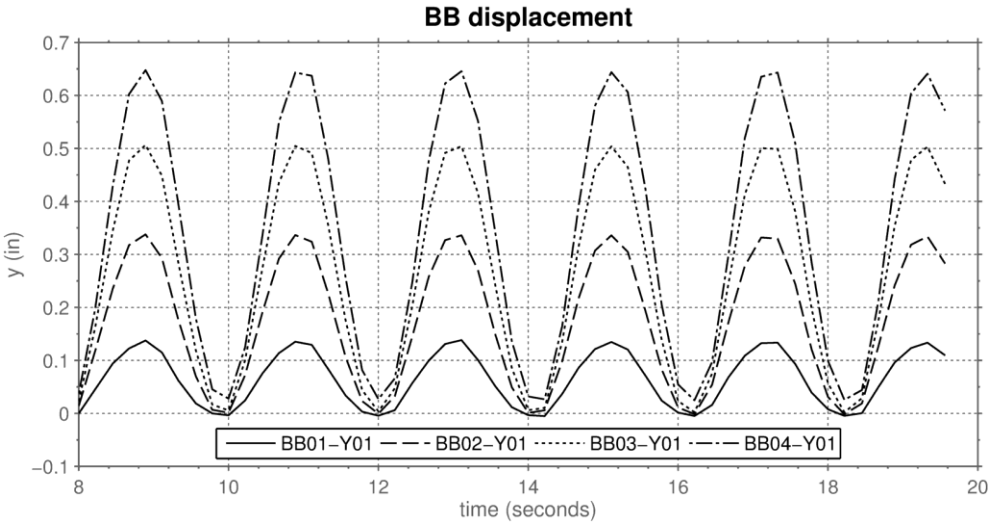

Figure A-50: Bearer Bar Displacement Time History for the REF Test

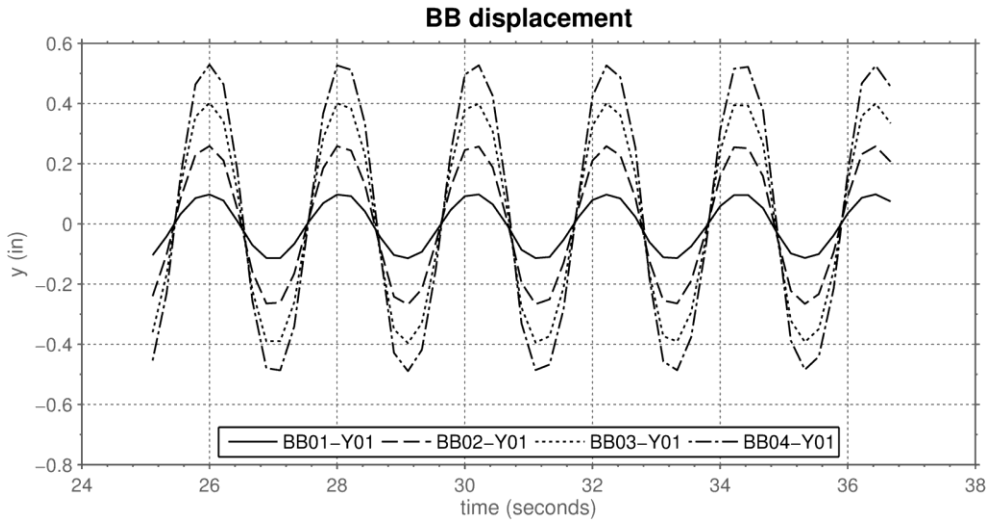

Figure A-51: Bearer Bar Displacement Time History for the PIT01 Test

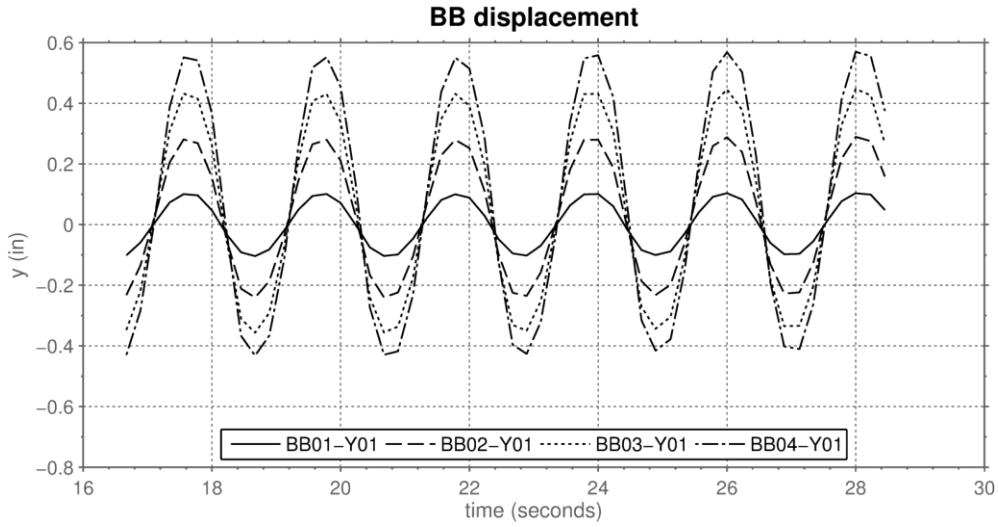

Figure A-52: Bearer Bar Displacement Time History for the PIT02 Test

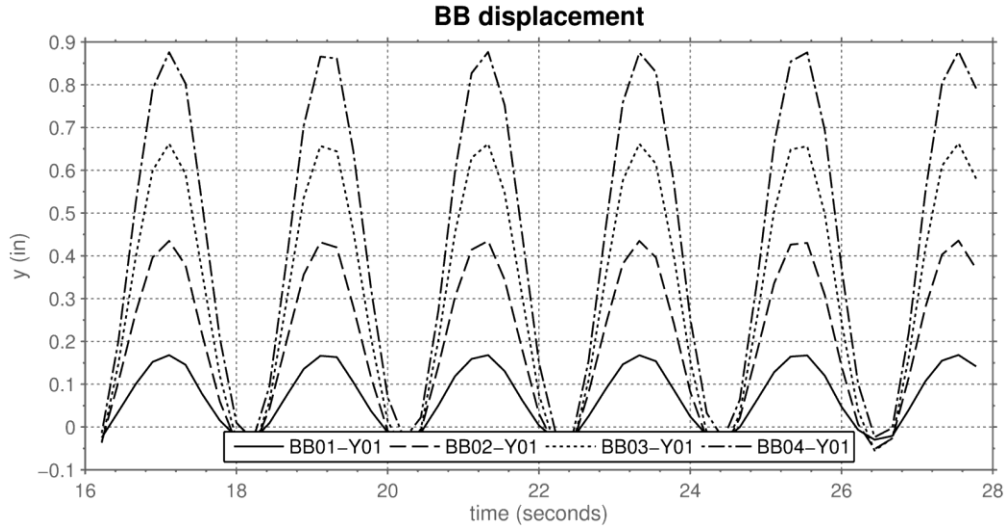

Figure A-53: Bearer Bar Displacement Time History for the ROL Test

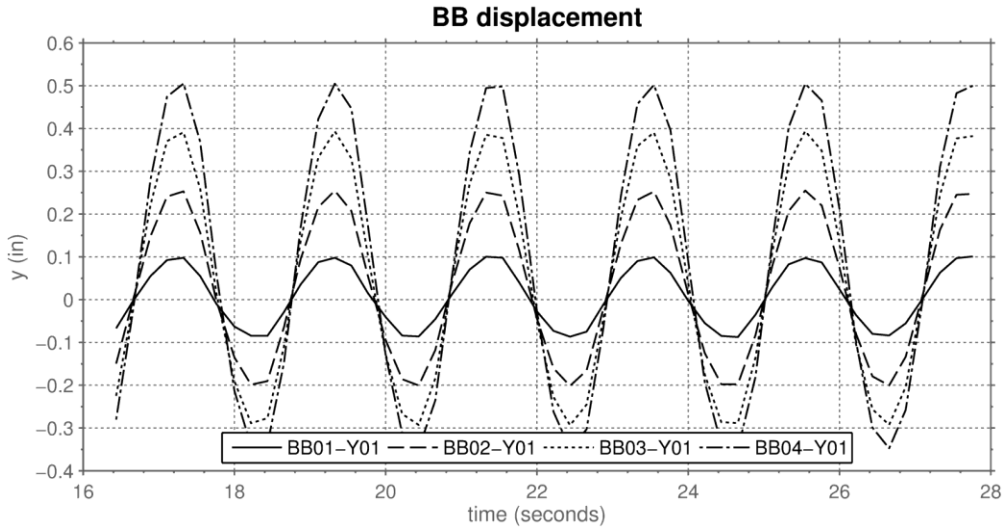

Figure A-54: Bearer Bar Displacement Time History for the REF Test

A.6.5 Rail Stresses

The time history plots for the lateral bending stresses in each rail in the CESURA geometric conditions are presented below. It should be noted that some of the plots have lines which are zero for the entirety of the time period. This is due to the fact that a lead wire has broken and the gage is malfunctioning. This should not be interpreted as a zero stress value, but rather this value should be disregarded.

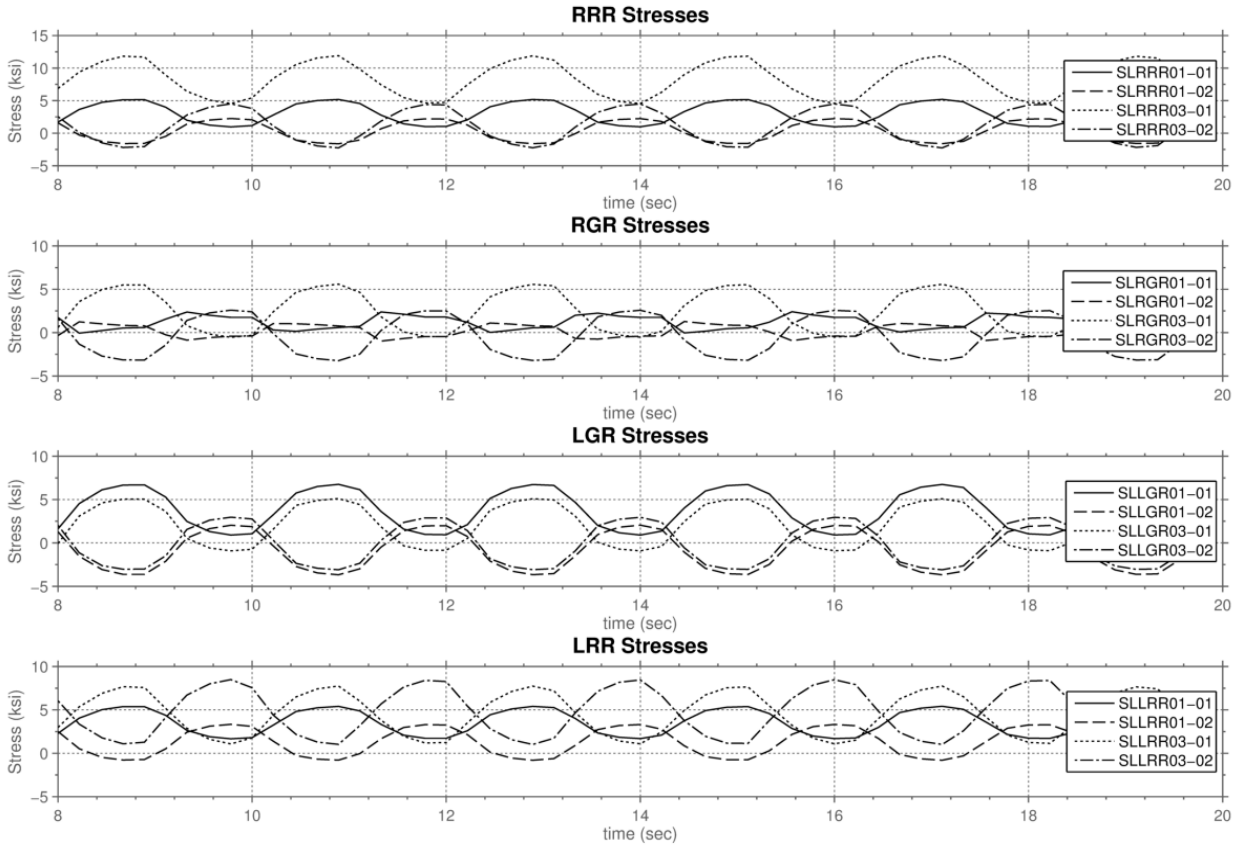

Figure A-55: Rail Stress Time History for the REF Test

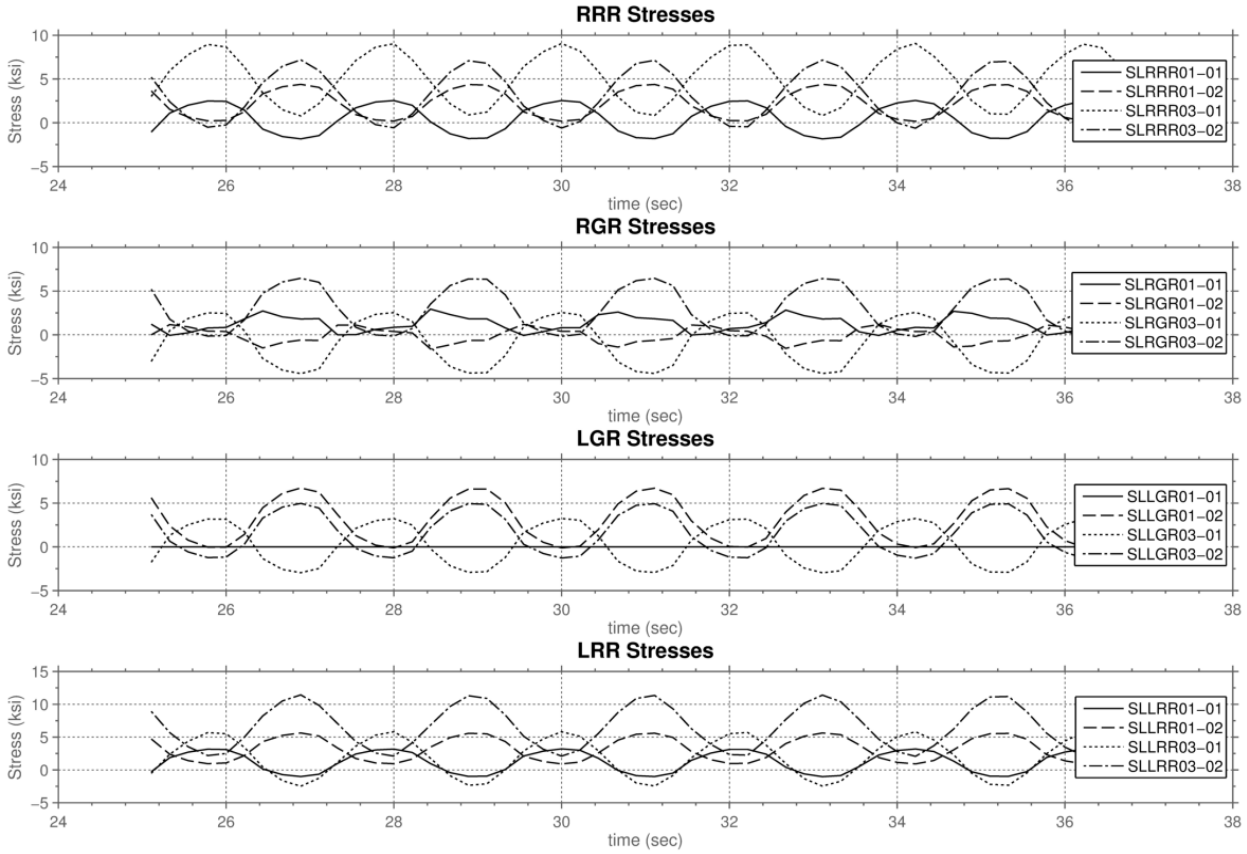

Figure A-56: Rail Stress Time History for the PIT01 Test (Disregard gage SL LGR01-01)

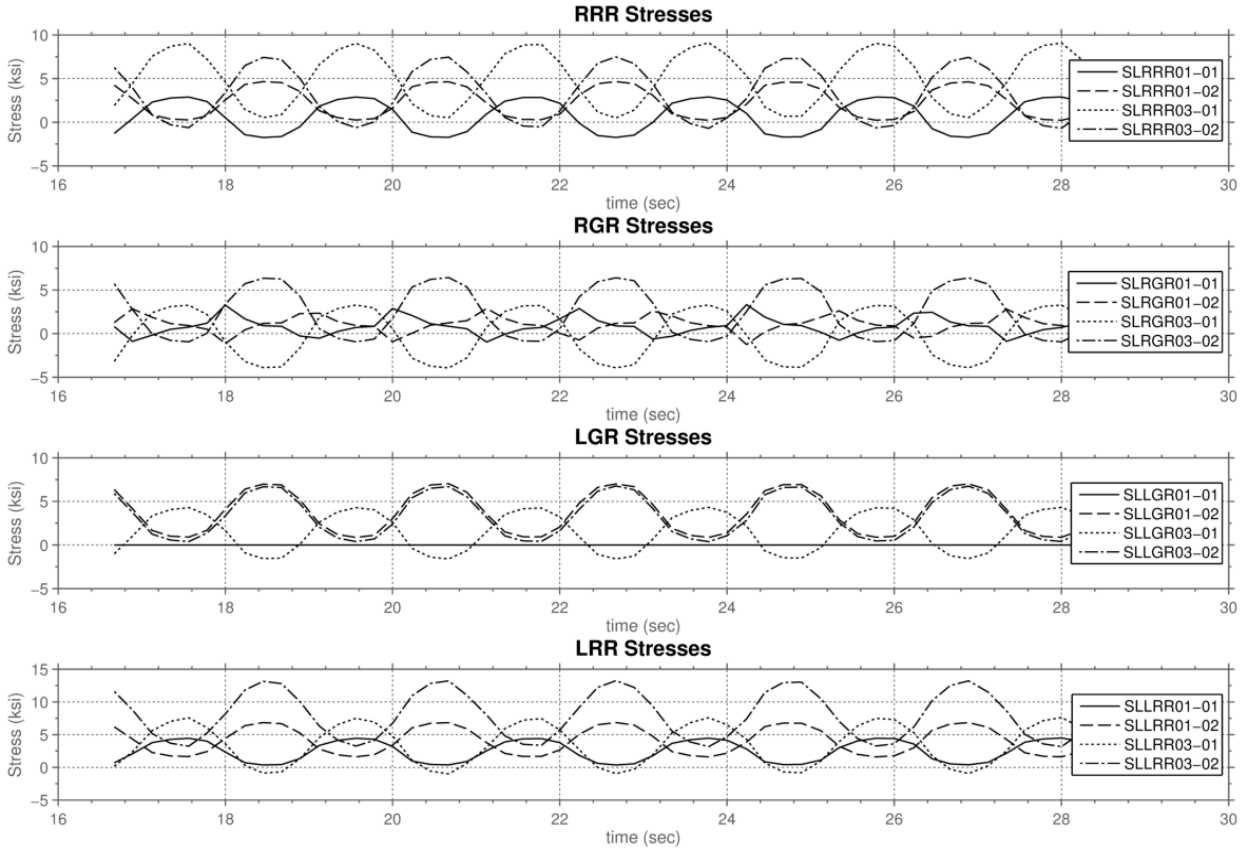

Figure A-57: Rail Stress Time History for the PIT02 Test (Disregard gage SL LGR01-01)

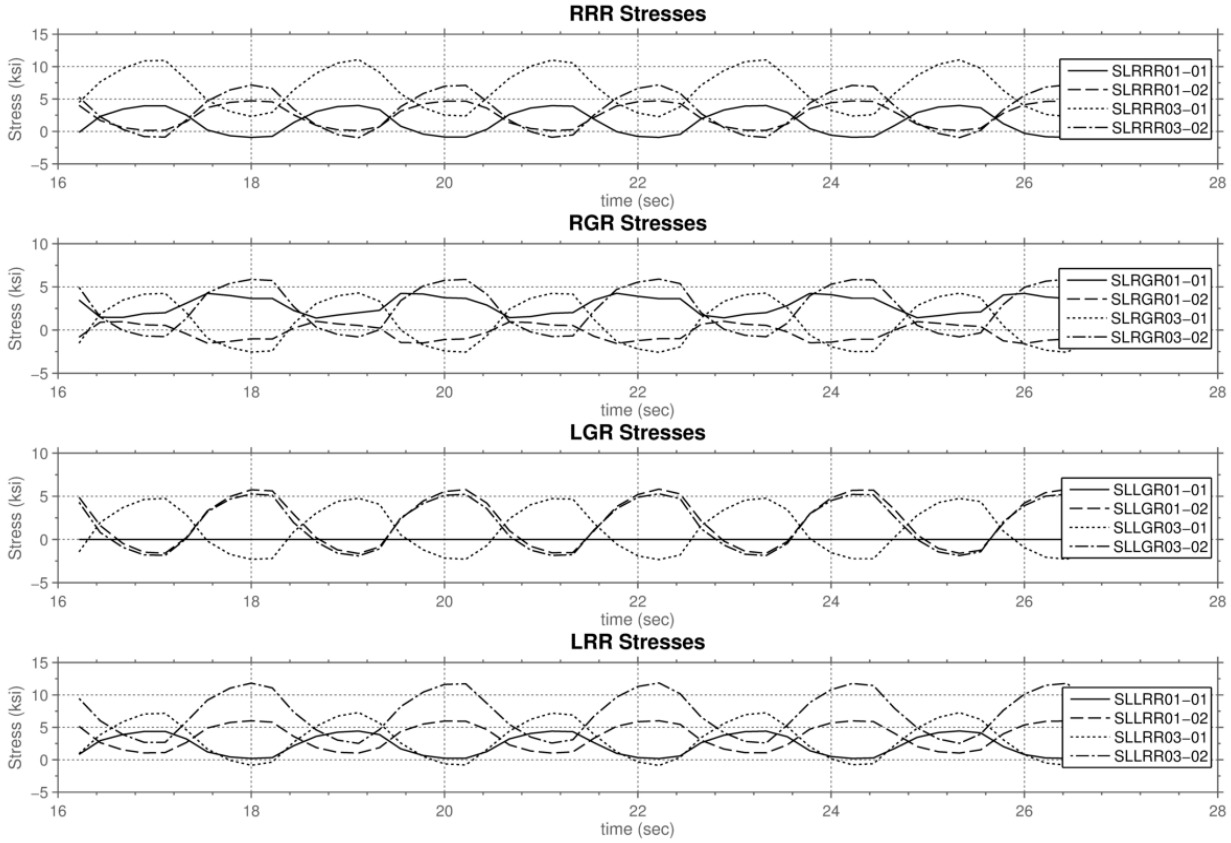

Figure A-58: Rail Stress Time History for the ROL Test (Disregard gage SL LGR01-01)

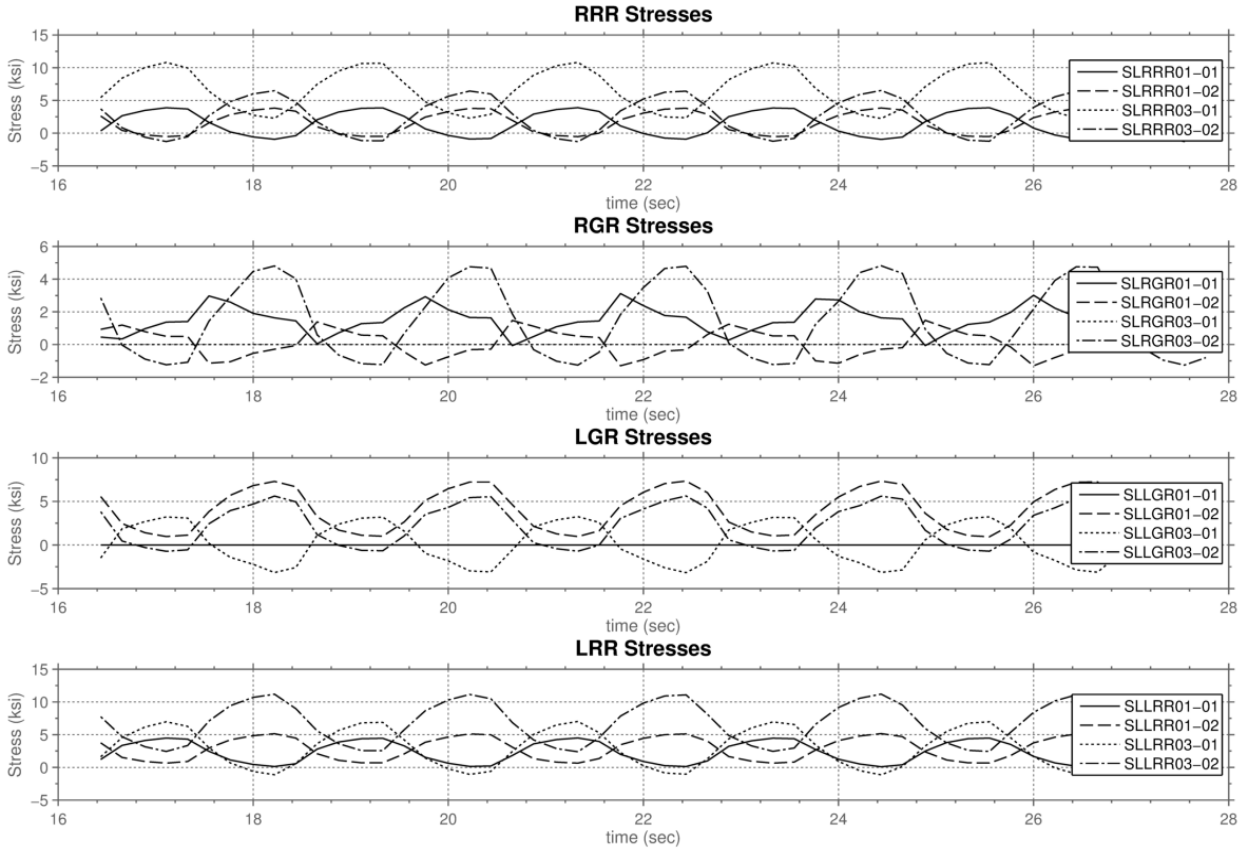

Figure A-59: Rail Stress Time History for the YAW Test (Disregard gages SL RGR03-01 and SL LGR01-01)

Appendix B Detailed Design Drawings

This appendix contains drawings that were created for fabrication of the experimental apparatus and test specimen.

Unless otherwise noted all dimensions are in inches and degrees.

SHEET TOTALS				
ITEM	QUANTITY	MATERIAL	SIZE	ADDITIONAL
(B-2) Beam Assem	1			Quantity: Description:
HSS Beam	1	HSS12x6x3/8	193"	2 14"-Ø1 A36 ROUND
Reinf. Bar	1	$\frac{1}{2}$x4 FLAT BAR	48"	3 $\frac{3}{4}$" A352 BOLT
Conn. Bar	2	$\frac{3}{4}$x5 FLAT BAR	11-1/4"	3 NUT FOR $\frac{3}{4}$" BOLT
(D-1) Sliding Assem	1			Quantity: Description:
Side PL	2	1" PL	10"x17-1/2"	1 14"-Ø1"A36 ROUND
Bot. PL	1	1" PL	10"x8-1/4"	2 $\frac{3}{4}$" A352 BOLT
Top PL	1	$\frac{1}{2}$" PL	10"x6-1/4"	2 NUT FOR $\frac{3}{4}$" BOLT
(D-2) Channels	2	C4x7.2	41-1/2"	
PL Washer	2	$\frac{3}{4}$x2$\frac{1}{2}$ FLAT BAR	8"	
(E-1) Load Assem.	1			Quantity: Description:
Vertical Strut	1	HSS8x8x3/8	24"	4 $\frac{3}{4}$" A352 BOLT
Load Beam	1	HSS8x8x3/8	50-1/2"	4 NUT FOR $\frac{3}{4}$" BOLT
(E-3) End-PL	2	$\frac{3}{4}$" PL	8"x12"	
(P-1) Wall Plate	1			Quantity: Description:
Vertical Plate	1	1" PL	24"x14"	
Conn. Plate	2	1" PL	13"x5"	
(W-1)East-PL	1	1$\frac{1}{2}$" PL	36"x108"	Quantity: Description:
(W-4)Horiz-PL	6	1" PL	5"x5"	
(W-3)Vert-PL	2	1" PL	4"x4"	
(W-2)West-PL	1	1$\frac{1}{2}$" PL	36"x108"	Quantity: Description:
(W-4)Horiz-PL	6	1" PL	5"x5"	
(W-3)Vert-PL	2	1" PL	4"x4"	

SHEET TOTALS				
ITEM	QUANTITY	MATERIAL	SIZE	ADDITIONAL
(S-1) SHORT	4			Quantity: Description:
TOP-PL	4	1" PL	Ø 7"	4 15" A307 THR. ROD
MID-PL	4	1/2" PL	Ø 7 1/2"	4 NUT FOR 1$\frac{1}{2}$" BOLT
L-SHORT	12	L2x2x1/4"	15 "	4 NUT FOR $\frac{1}{2}$" BOLT
BASE-PL	4	1/2" PL	19 "	4 2 " - 1$\frac{1}{2}$" XS PIPE
(S-2) MEDIUM	4			Quantity: Description:
TOP-PL	4	1" PL	Ø 7"	4 15" A307 THR. ROD
MID-PL	4	1/2" PL	Ø 7 1/2"	4 NUT FOR 1$\frac{1}{2}$" BOLT
L-MED	12	L2x2x1/4"	17 3/8"	4 NUT FOR $\frac{1}{2}$" BOLT
BASE-PL	4	1/2" PL	21 "	4 2 " - 1$\frac{1}{2}$" XS PIPE
(S-3) TALL	4			Quantity: Description:
TOP-PL	4	1" PL	Ø 7"	4 15" A307 THR. ROD
MID-PL	4	1/2" PL	Ø 7 1/2"	4 NUT FOR 1$\frac{1}{2}$" BOLT
L-TALL	12	L2x2x1/4"	19 7/8 "	4 NUT FOR $\frac{1}{2}$" BOLT
BASE-PL	4	1/2" PL	23 1/4"	4 2 " - 1$\frac{1}{2}$" XS PIPE

Notes:

University of Washington
Civil and Env. Engineering

REVISIONS			
REV	DESCRIPTION	DATE	APPROVED

Project: CESURA Preliminary
Drawn By: Travis Thonstad
Title: Project Totals
File Name: FrontPage.dwg
Contact: thonstat@u.washington.edu
stanton@u.washington.edu
Sheet: A-1

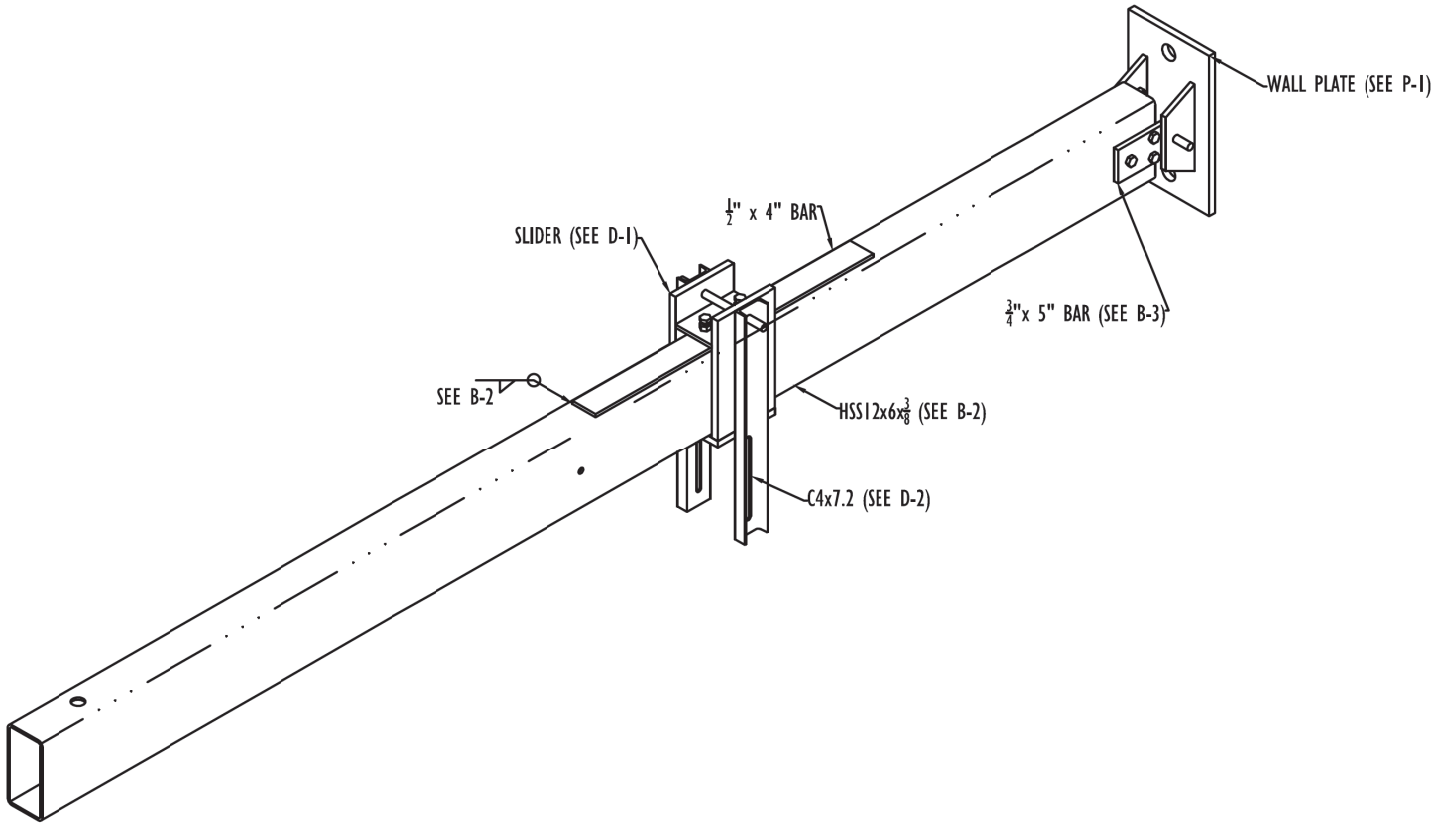

BEAM ASSEMBLY

Notes:

1) All Dimensions given in inches/degrees
2) HSS - A500 Gr. B Steel
3) FLAT BAR - A529 Gr 50 Steel or equivalent
4) All welds to be compatible with base metal
5) Ø 1" Round bar should be able to be passed smoothly through holes when plate is attached with Ø ¾" Bolts

REVISIONS			
REV	DESCRIPTION	DATE	APPROVED

University of Washington
Civil and Env. Engineering

Project: CESURA Prelininary
Drawn By: Travis Thonstad
Title: Beam Assembly
File Name: Beam.dwg
Contact: thonstat@u.washington.edu
stanton@u.washington.edu
Sheet: B-1

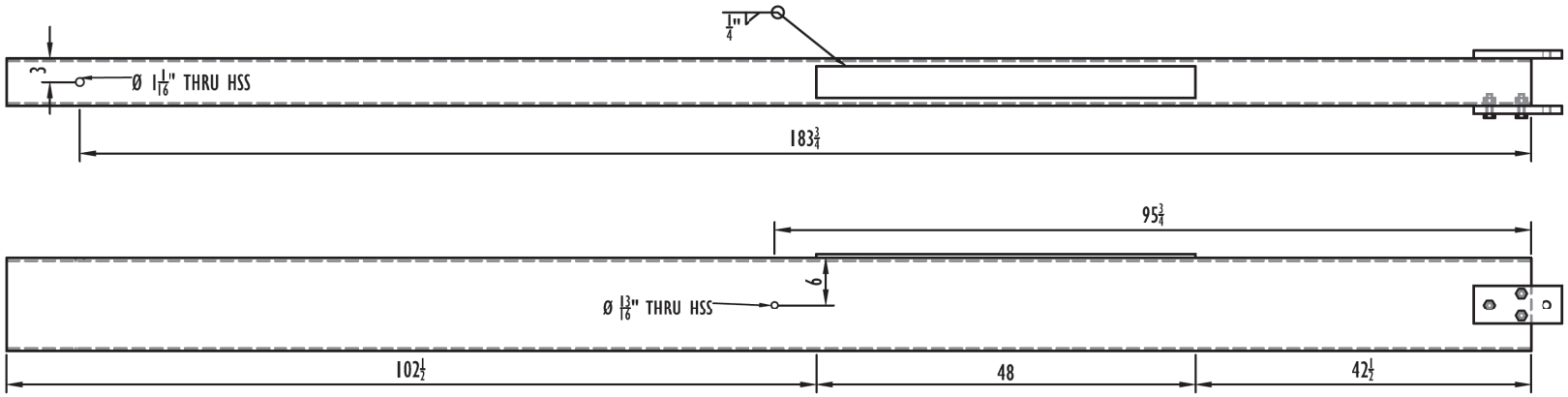

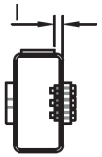

BEAM DETAIL

Notes:

1) All Dimensions given in inches/degrees
2) HSS - A500 Gr. B Steel
3) 3) FLAT BAR - A529 Gr 50 Steel or equivaent
4) All welds to be compatible with base metal
5) Ø 1" Round bar should be able to be passed smoothly through holes when plate is attached with Ø 3/4" Bolts

REVISIONS			
REV	DESCRIPTION	DATE	APPROVED

University of Washington
Civil and Env. Engineering

Project: CESURA Preliminary		Drawn By: Travis Thonstad	
Title: Beam Detail	Contact: thonstat@u.washington.edu		Sheet: B-2
File Name: Beam.dwg	Contact: stanton@u.washington.edu		

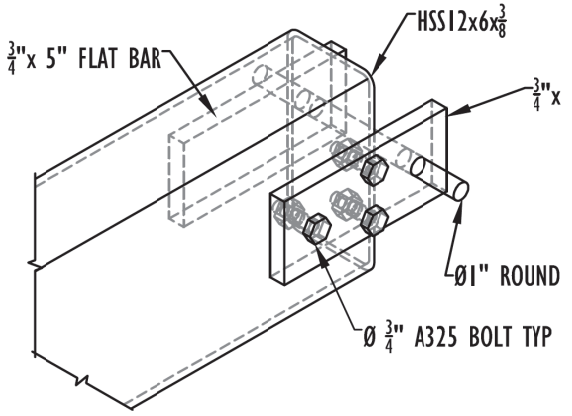

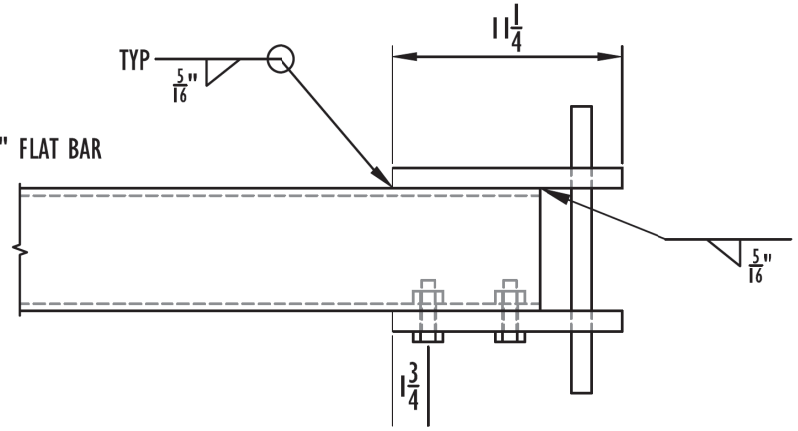

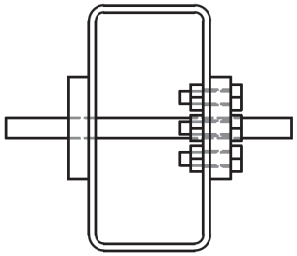

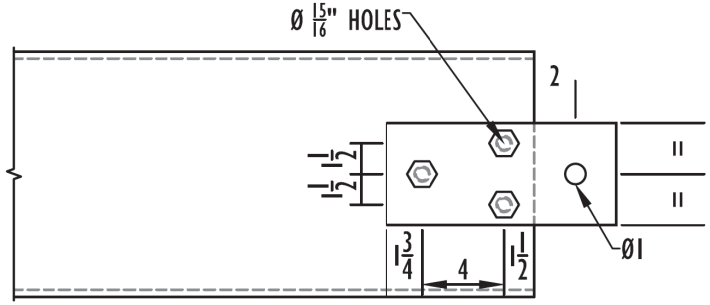

Notes:

1) All Dimensions given in inches/degrees
2) HSS - A500 Gr. B Steel
3) FLAT BAR - A529 Gr 50 Steel or equivalent
4) All welds to be compatible with base metal
5) Ø 1" Round bar should be able to be passed smoothly through holes when plate is attached with Ø 3/4" Bolts

CONNECTION DETAIL

University of Washington
Civil and Env. Engineering

REVISIONS			
REV	DESCRIPTION	DATE	APPROVED

Project: CESURA Preliminary

Drawn By: Travis Thonstad

Title: Connection Detail

File Name: Beam.dwg

Contact: thonstat@u.washington.edu
stanton@u.washington.edu

Sheet: B-3

B - SHEET TOTALS					
ITEM	QUANTITY	MATERIAL	SIZE	ADDITIONAL	
(B-1) Beam Assem	1			Quantity:	Description:
HSS Beam	1	HSS12x6x3/8	193"	2	14"-Ø1 A36 ROUND
Reinf. Bar	1	$\frac{1}{2}$x4 FLAT BAR	48"	3	$\frac{3}{4}$" A352 BOLT
Conn. Bar	2	$\frac{3}{4}$x5 FLAT BAR	11-1/4"	3	NUT FOR $\frac{3}{4}$" BOLT

Notes:

1) All Dimensions given in inches/degrees
2) HSS - A500 Gr. B Steel
3) FLAT BAR - A529 Gr 50 Steel or equivalent
4) All welds to be compatible with base metal
5) Ø 1" Round bar should be able to be passed smoothly through holes when plate is attached with Ø $\frac{3}{4}$" Bolts

University of Washington
Civil and Env. Engineering

REVISIONS			
REV	DESCRIPTION	DATE	APPROVED

Project: CESURA Preliminary

Drawn By: Travis Thonstad

Title: B - Sheet Totals

File Name: LoadBeam.dwg

Contact: thonstat@u.washington.edu
stanton@u.washington.edu

Sheet: B-4

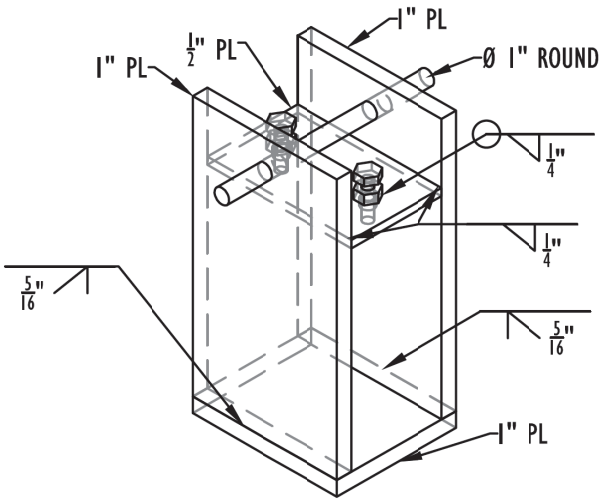

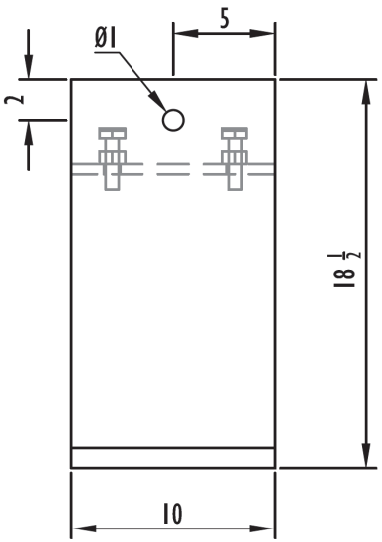

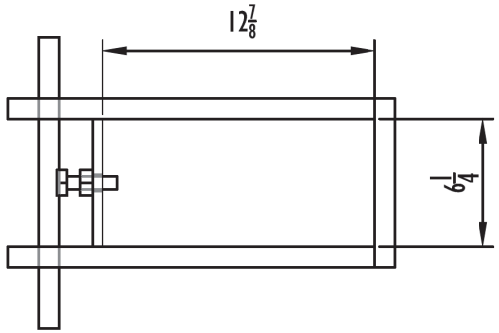

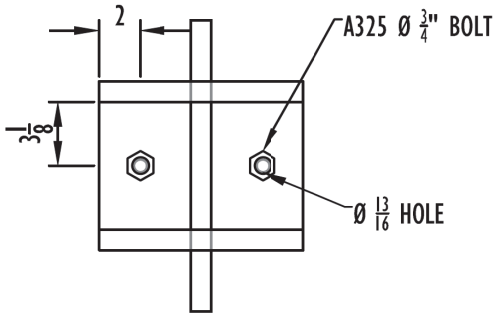

SLIDING ASSEMBLY

Notes:
1) All Dimensions given in inches/degrees
2) A36 Steel
4) All welds to be compatible with base metal
5) Ø 1" ROUND should be able to be passed smoothly through both holes at once
6) Weld nuts to top of PL so that bolts may be threaded through PL

REVISIONS			
REV	DESCRIPTION	DATE	APPROVED

University of Washington
Civil and Env. Engineering

Project: CESURA Preliminary		Drawn By: Travis Thonstad	
Title: Sliding Assembly	Contact: thonstat@u.washington.edu		Sheet: D-1
File Name: Slider.dwg	stanton@u.washington.edu		

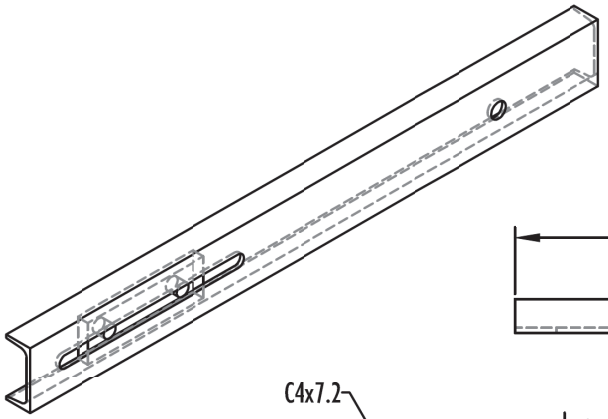

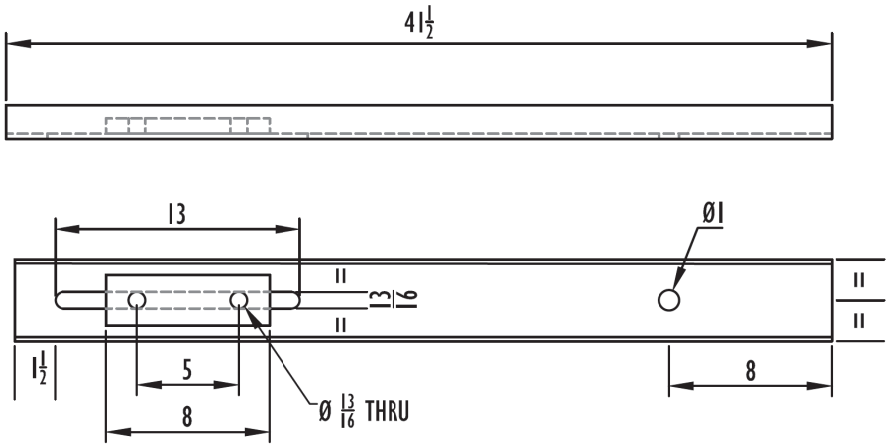

CHANNELS

Notes:
1) All Dimensions given in inches/degrees
2) A36 Steel
4) All welds to be compatible with base metal
5) Ø 1" ROUND should be able to be passed smoothly through both holes at once
6) Weld nuts to top of PL so that bolts may be threaded through PL

REVISIONS			
REV	DESCRIPTION	DATE	APPROVED

University of Washington
Civil and Env. Engineering

Project: CESURA Preliminary		Drawn By: Travis Thonstad	
Title: Sliding Assembly	Contact: thonstat@u.washington.edu		Sheet: D-2
File Name: Slider.dwg	stanton@u.washington.edu		

D - SHEET TOTALS					
ITEM	QUANTITY	MATERIAL	SIZE	ADDITIONAL	
(D-1) Sliding Assem	1			Quantity:	Description:
Side PL	2	1" PL	10"x17-1/2"	1	14"-Ø1"A36 ROUND
Bot. PL	1	1" PL	10"x8-1/4"	2	$\frac{3}{4}$" A352 BOLT
Top PL	1	$\frac{1}{2}$" PL	10"x6-1/4"	2	NUT FOR $\frac{3}{4}$" BOLT
(D-2) Channels	2	C4x7.2	41-1/2"		
PL Washer	2	$\frac{3}{4}$"x2$\frac{1}{2}$"FLAT BAR	8"		

Notes:
1) All Dimensions given in inches/degrees
2) A36 Steel
4) All welds to be compatible with base metal
5) Ø 1" ROUND should be able to be passed smoothly through both holes at once
6) Tack weld nuts onto top of $\frac{1}{2}$" PL so that bolts may be threaded through plate

University of Washington
Civil and Env. Engineering

REVISIONS			
REV	DESCRIPTION	DATE	APPROVED

Project: CESURA Preliminary
Drawn By: Travis Thonstad
Title: D - Sheet Totals
File Name: Slider.dwg
Contact: thonstat@u.washington.edu
stanton@u.washington.edu
Sheet: D-3

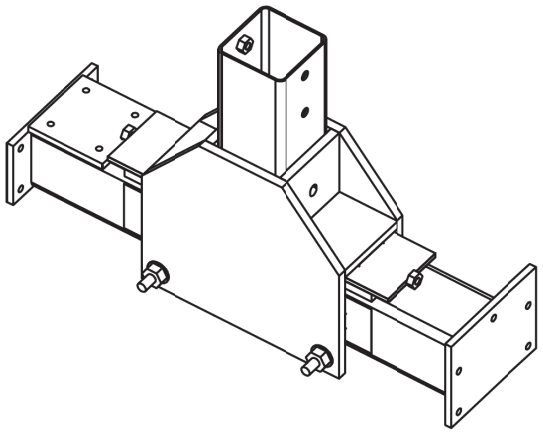

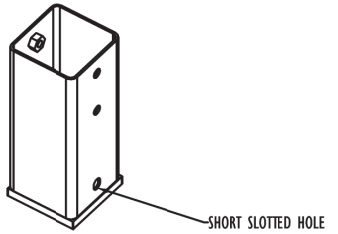

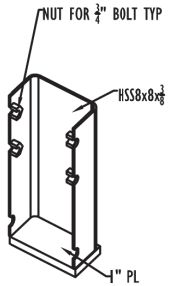

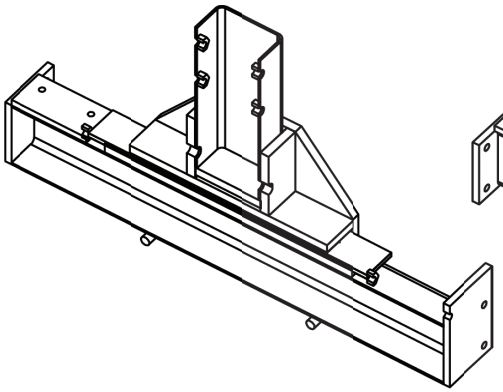

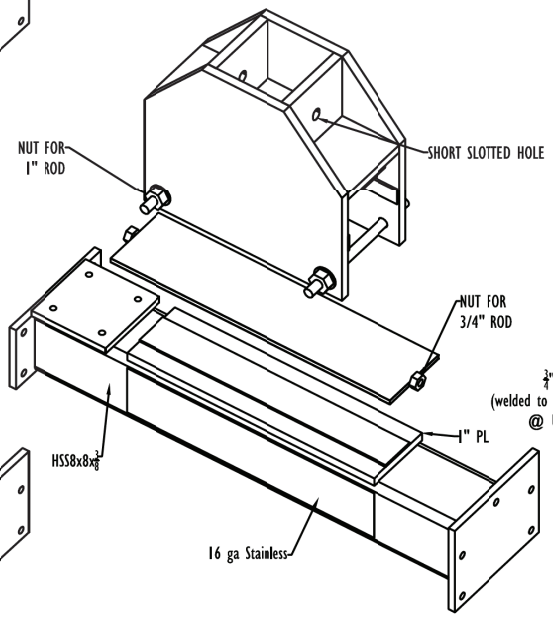

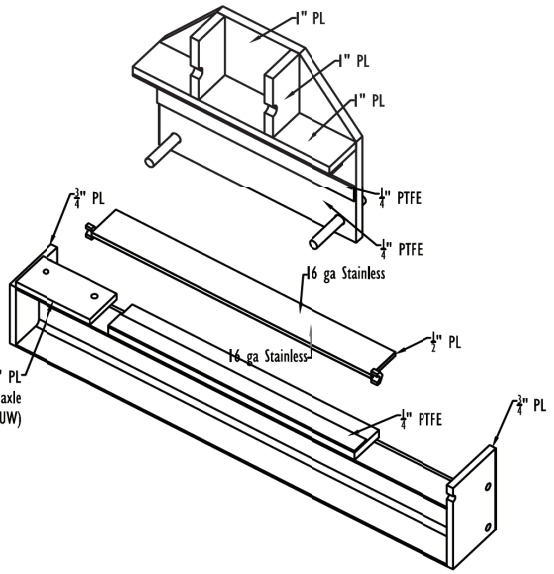

LOADING ASSEMBLY

Notes:

1) All Dimensions given in inches/degrees
2) HSS - A500 Gr. B Steel
3) PL - A36 Steel
4) All welds to be compatible with base metal

REVISIONS			
REV	DESCRIPTION	DATE	APPROVED

Project: CESURA Preliminary

Drawn By: Travis Thonstad

Title: Load Assembly

File Name: LoadBeam.dwg

Contact: thonstat@u.washington.edu
stanton@u.washington.edu

University of Washington
Civil and Env. Engineering

Sheet: E-1

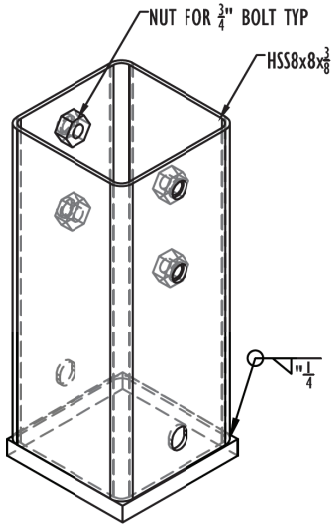

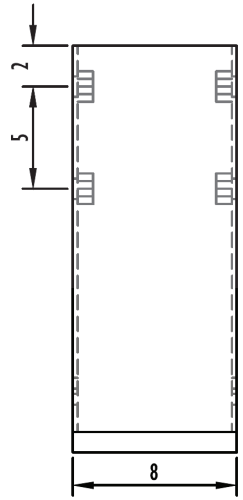

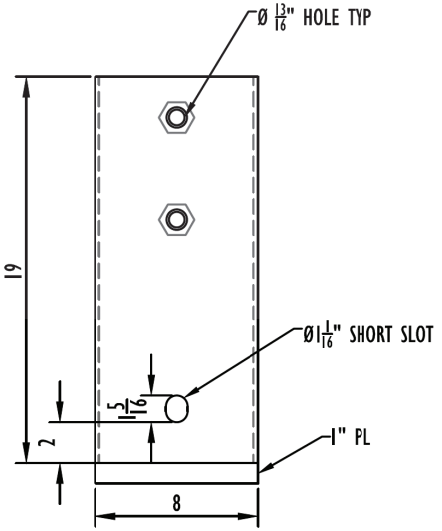

VERTICAL STRUT

Notes:

1) All Dimensions given in inches/degrees
2) HSS - A500 Gr. B Steel
3) PL - A36 Steel
4) All welds to be compatible with base metal

University of Washington
Civil and Env. Engineering

REVISIONS			
REV	DESCRIPTION	DATE	APPROVED

Project: CESURA Preliminary

Drawn By: Travis Thonstad

Title: Vertical Strut

File Name: LoadBeam.dwg

Contact: thonstat@u.washington.edu
stanton@u.washington.edu

Sheet: E-2

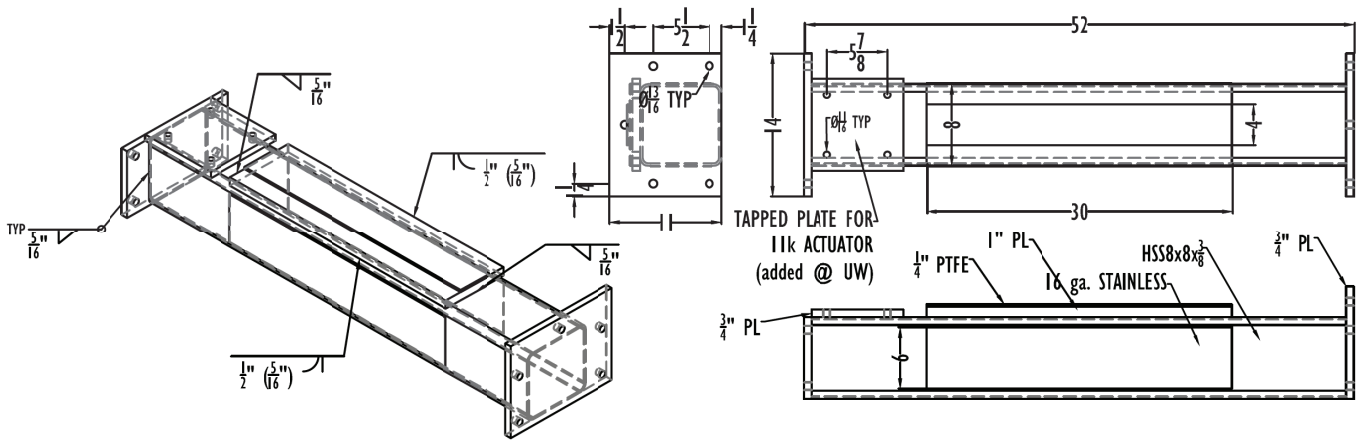

AXLE

Notes:

1) All Dimensions given in inches/degrees
2) HSS - A500 Gr. B Steel
3) PL - A36 Steel
4) All welds to be compatible with base metal

University of Washington
Civil and Env. Engineering

REVISIONS			
REV	DESCRIPTION	DATE	APPROVED

Project: CESURA Preliminary
Drawn By: Travis Thonstad
Title: Axle
File Name: LoadBeam.dwg
Contact: thonstat@u.washington.edu
stanton@u.washington.edu
Sheet: E-3

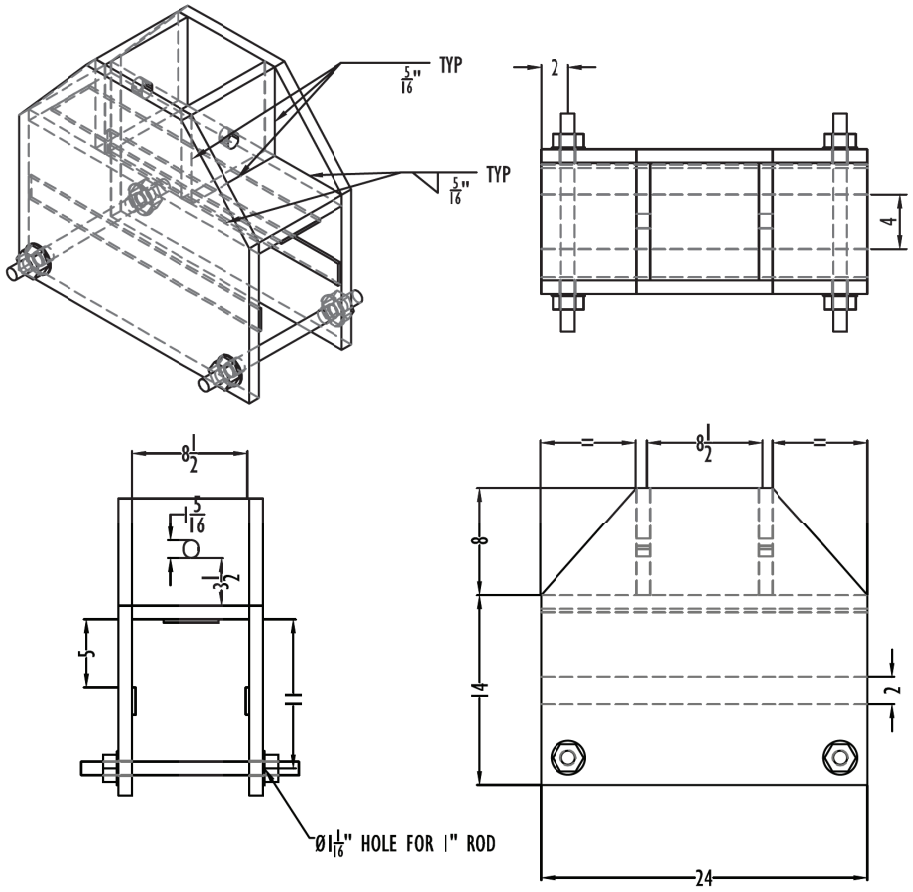

ROCKER

Notes:

1) All Dimensions given in inches/degrees
2) HSS - A500 Gr. B Steel
3) PL - A36 Steel
4) All welds to be compatible with base metal

REVISIONS			
REV	DESCRIPTION	DATE	APPROVED

Project: CESURA Preliminary
Drawn By: Travis Thonstad
Title: Slider
File Name: LoadBeam.dwg
Contact: thonstat@u.washington.edu
stanton@u.washington.edu
Sheet: E-4

University of Washington
Civil and Env. Engineering

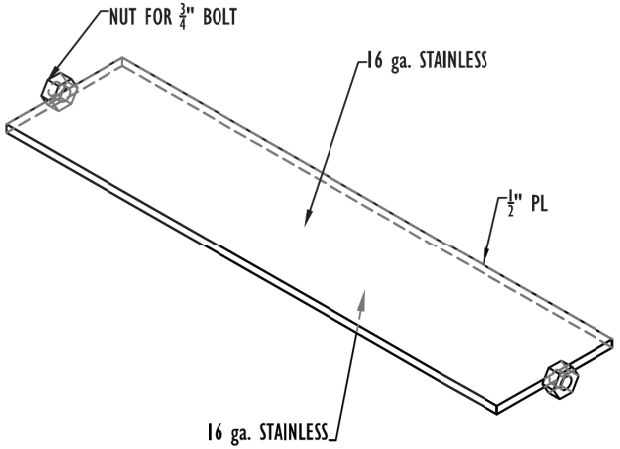

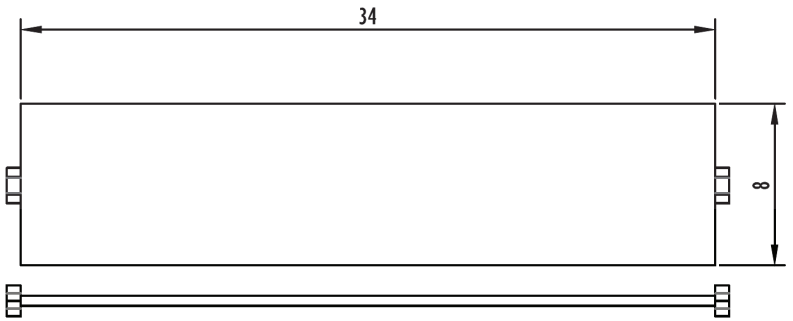

SLIDER

Notes:
1) All Dimensions given in inches/degrees
2) HSS - A500 Gr. B Steel
3) PL - A36 Steel
4) All welds to be compatible with base metal

REVISIONS			
REV	DESCRIPTION	DATE	APPROVED

University of Washington
Civil and Env. Engineering

Project: CESURA Preliminary
Drawn By: Travis Thonstad
Title: Slider
File Name: LoadBeam.dwg
Contact: thonstat@u.washington.edu
stanton@u.washington.edu
Sheet: E-4

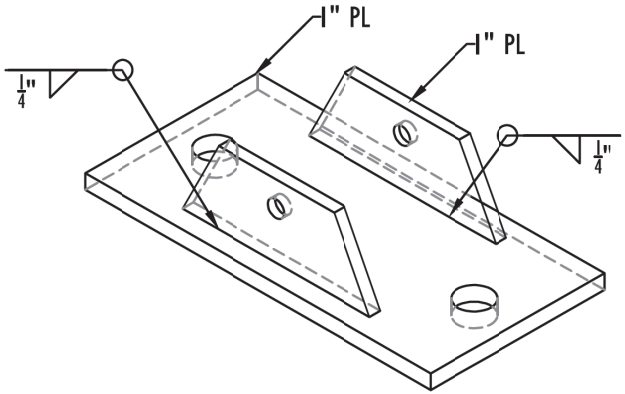

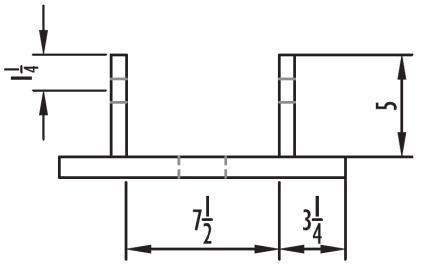

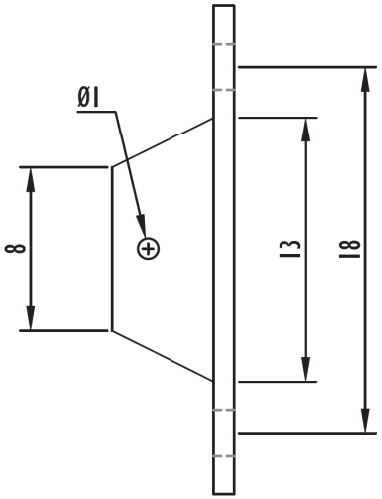

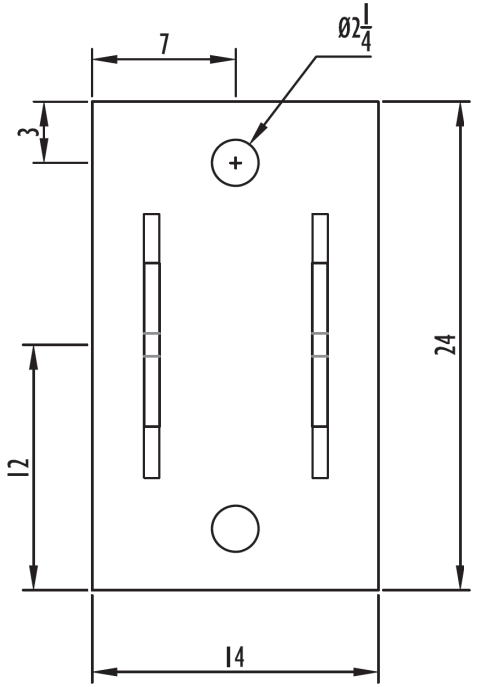

WALL PLATE

Notes:

1) All Dimensions given in inches/degrees
2) PL - A36 Steel
3) All welds to be compatible with base metal
4) Ø1" Round bar should be able to be passed smoothly through holes

REVISIONS			
REV	DESCRIPTION	DATE	APPROVED

Project: CESURA Preliminary
Drawn By: Travis Thonstad
Title: Wall Plate
File Name: WallPlate.dwg
Contact: thonstat@u.washington.edu
stanton@u.washington.edu
Sheet: P-1

University of Washington
Civil and Env. Engineering

P - SHEET TOTALS				
ITEM	QUANTITY	MATERIAL	SIZE	ADDITIONAL
(P-1) Wall Plate	1			Quantity: Description:
Vertical Plate	1	1" PL	24"x14"	
Conn. Plate	2	1" PL	13"x5"	

Notes:

1) All Dimensions given in inches/degrees
2) HSS - A500 Gr. B Steel
3) PL - A36 Steel
4) All welds to be compatible with base metal

University of Washington
Civil and Env. Engineering

REVISIONS			
REV	DESCRIPTION	DATE	APPROVED

Project: CESURA Preliminary

Drawn By: Travis Thonstad

Title: P - Sheet Totals

File Name: WallPlate.dwg

Contact: thonstat@u.washington.edu
stanton@u.washington.edu

Sheet: P-2

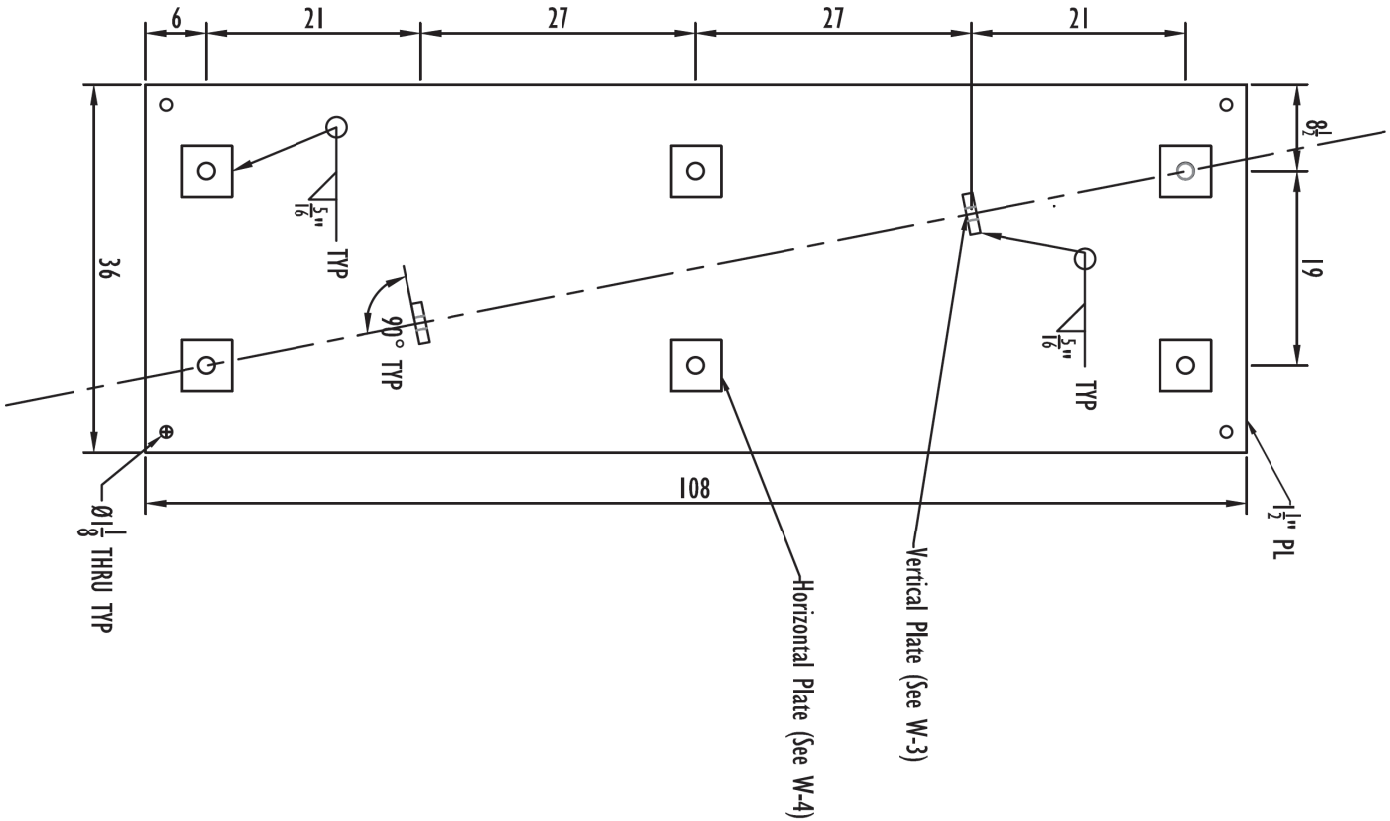

EAST PLATE - BOTTOM

Notes:
1) All Dimensions given in inches/degrees
2) A36 Steel
3) All welds to be compatible with base metal
4) Vertical plates to be welded so that the protruding edge makes a 90° angle with the line shown

REVISIONS			
REV	DESCRIPTION	DATE	APPROVED

University of Washington
Civil and Env. Engineering

Project: CESURA Preliminary		Drawn By: Travis Thonstad	
Title: East Plate - BOT	Contact: thonstat@u.washington.edu stanton@u.washington.edu		Sheet: W-1
File Name: Wing.dwg			

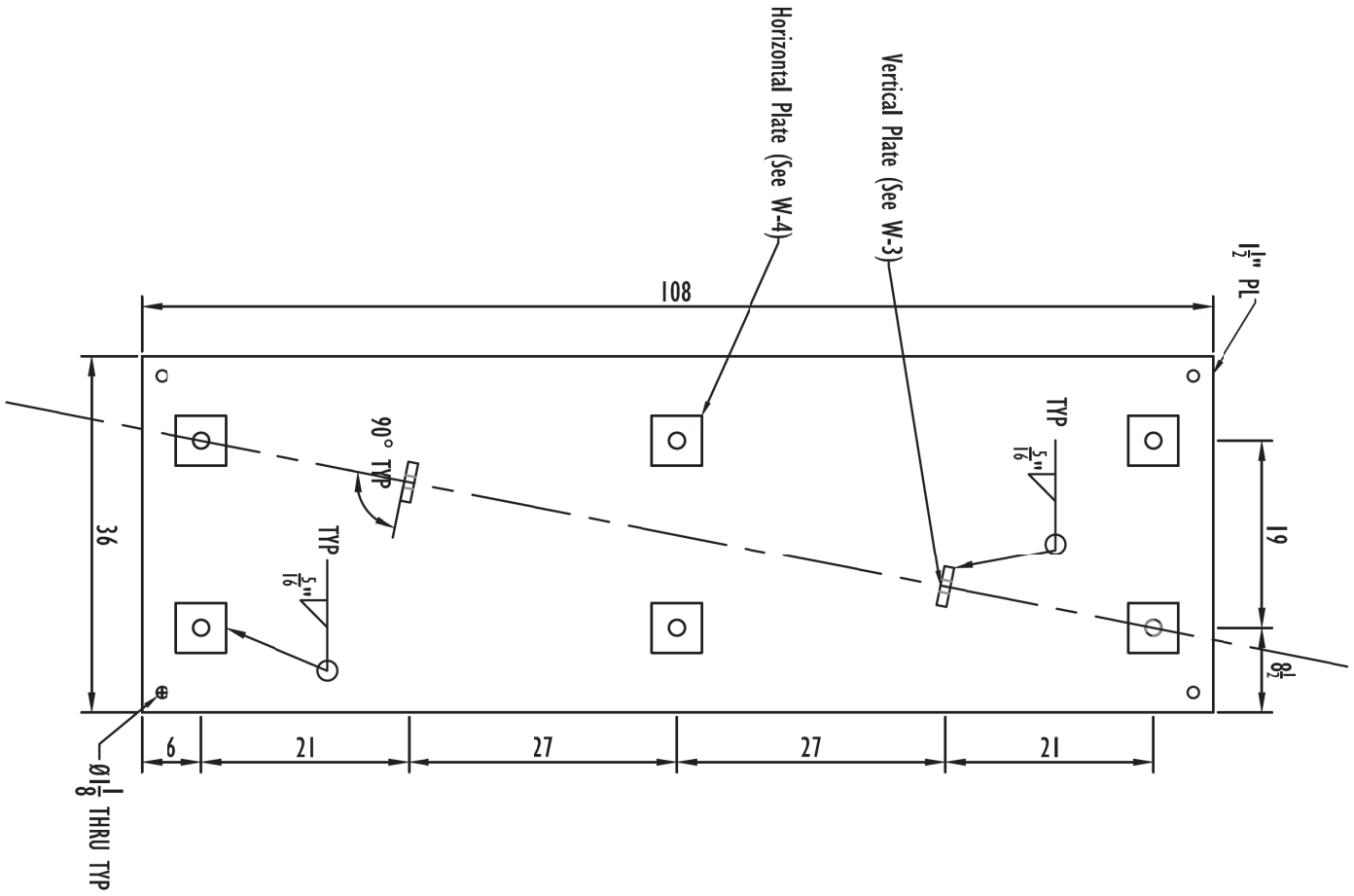

WEST PLATE - BOTTOM

Notes:

1) All Dimensions given in inches/degrees
2) A36 Steel
3) All welds to be compatible with base metal
4) Vertical plates to be welded so that the edge makes a 90° angle with the line shown

REVISIONS			
REV	DESCRIPTION	DATE	APPROVED

University of Washington
Civil and Env. Engineering

Project: CESURA Preliminary
Drawn By: Travis Thonstad
Title: West Plate - BOT
File Name: Wing.dwg
Contact: thonstat@u.washington.edu
stanton@u.washington.edu
Sheet: W-2

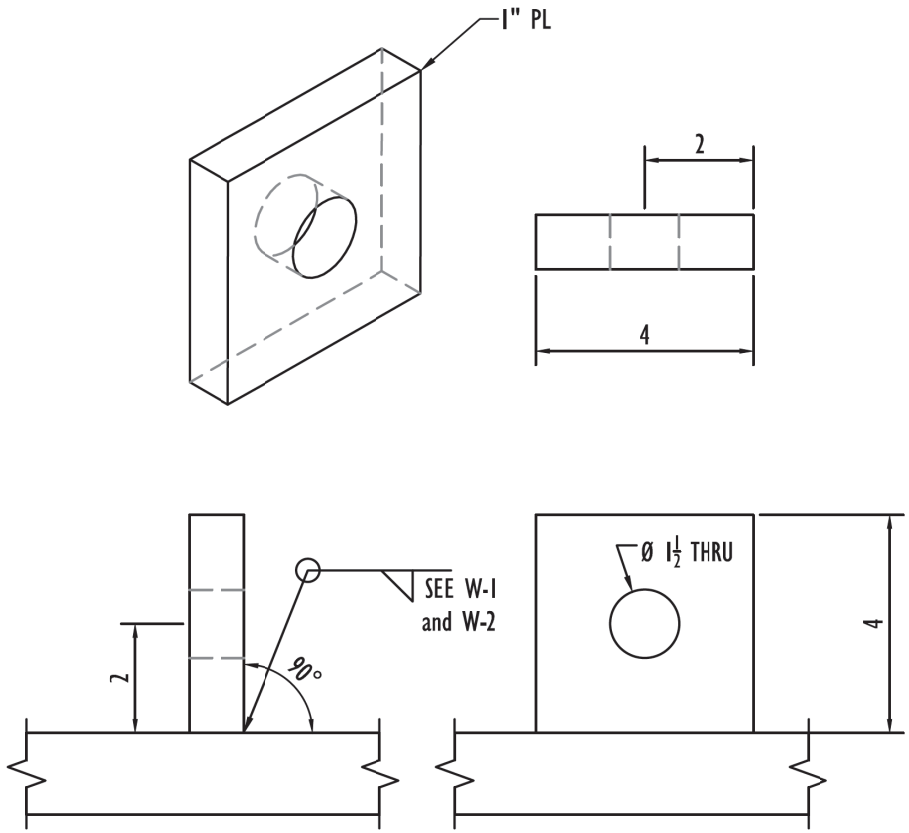

VERTICAL PLATE

Notes:

1) All Dimensions given in inches/degrees
2) A36 Steel
3) All welds to be compatible with base metal

University of Washington
Civil and Env. Engineering

REVISIONS			
REV	DESCRIPTION	DATE	APPROVED

Project: CESURA Preliminary

Drawn By: Travis Thonstad

Title: Vertical Plate

File Name: Wing.dwg

Contact: thonstat@u.washington.edu
stanton@u.washington.edu

Sheet: W-3

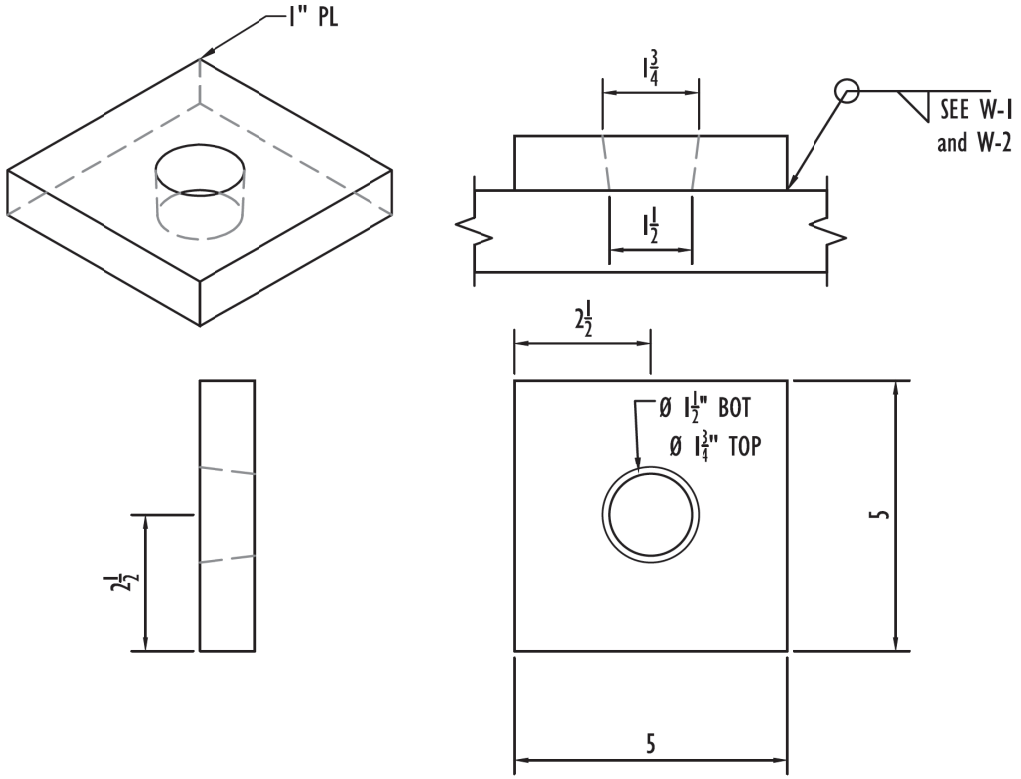

HORIZONTAL PLATE

Notes:

1) All Dimensions given in inches/degrees
2) A36 Steel
3) All welds to be compatible with base metal
4) Tapered hole to be oriented so that larger diameter faces outward

REVISIONS			
REV	DESCRIPTION	DATE	APPROVED

University of Washington
Civil and Env. Engineering

Project: CESURA Prelininary
Drawn By: Travis Thonstad
Title: Horizontal Plate
File Name: Wing.dwg
Contact: thonstat@u.washington.edu
stanton@u.washington.edu
Sheet: W-4

W - SHEET TOTALS				
ITEM	QUANTITY	MATERIAL	SIZE	ADDITIONAL
(W-1)East-PL	1	$1\frac{1}{2}$" PL	36"x108"	
(W-4)Horiz-PL	6	1" PL	5"x5"	
(W-3)Vert-PL	2	1" PL	4"x4"	
(W-2)West-PL	1	$1\frac{1}{2}$" PL	36"x108"	
(W-4)Horiz-PL	6	1" PL	5"x5"	
(W-3)Vert-PL	2	1" PL	4"x4"	

Notes:

1) All Dimensions given in inches/degrees
2) A36 Steel
3) All welds to be compatible with base metal
4) East and West Plates are to fabricated so that the two are mirror images of one another

University of Washington
Civil and Env. Engineering

REVISIONS			
REV	DESCRIPTION	DATE	APPROVED

Project: CESURA Preliminary

Drawn By: Travis Thonstad

Title: W - Sheet Totals

File Name: Wing.dwg

Contact: thonstat@u.washington.edu
stanton@u.washington.edu

Sheet: W-5

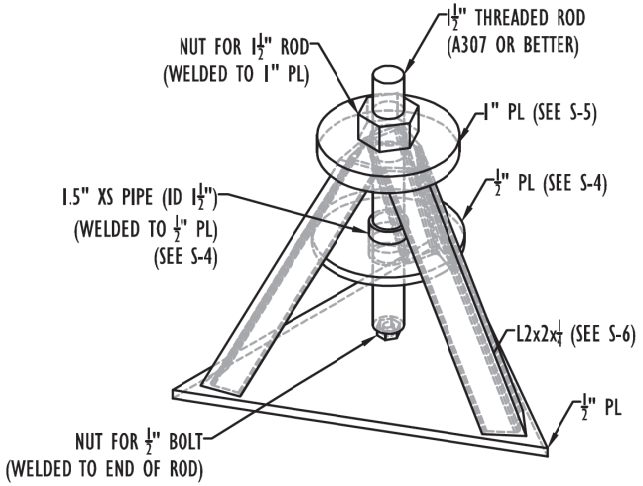

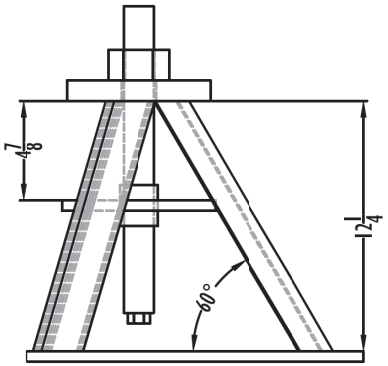

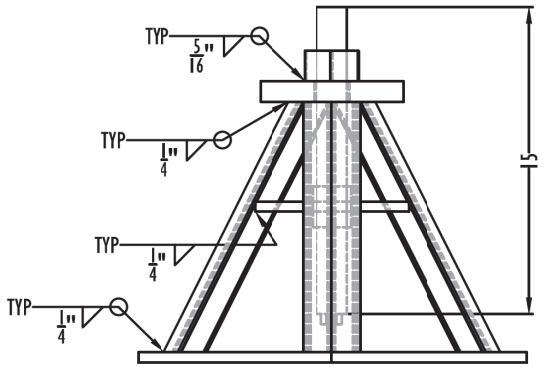

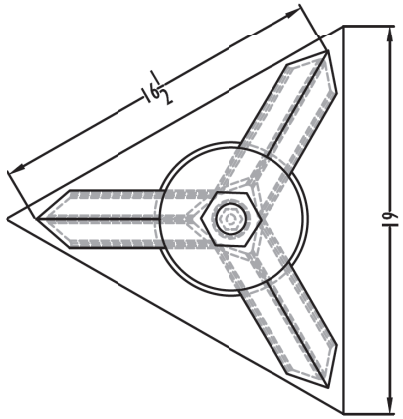

SHORT

Notes:

1) All Dimensions given ir inches/degrees
2) A36 Steel
3) All welds to be compatible with base metal
4) Nut to be welded so that the threaded rod runs freely through
5) See S-7 for final quanities

REVISIONS			
REV	DESCRIPTION	DATE	APPROVED
A	Modified mid plate and incl bot nut	05-19-2012	

University of Washington
Civil and Env. Engineering

Project:	CESURA Preliminary	Drawn By:	Travis Thonstad
Title:	Jack Stand Short	Contact:	thonstat@u.washington.edu
File Name:	JackStand.dwg		stanton@u.washington.edu
		Sheet:	S-1

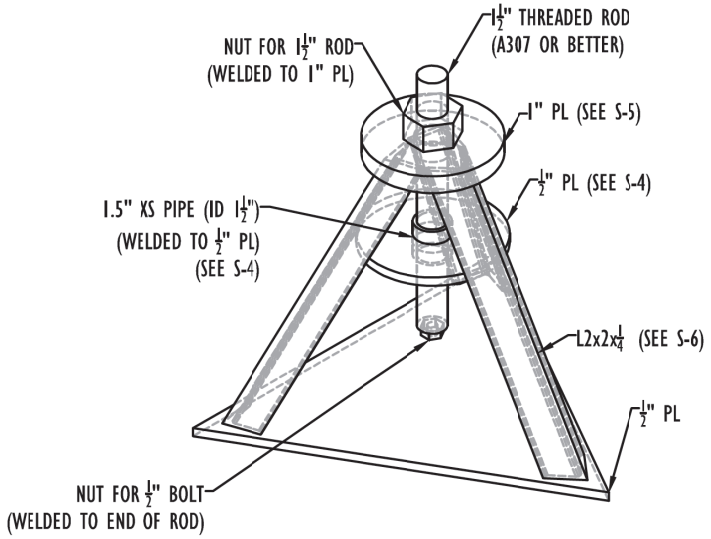

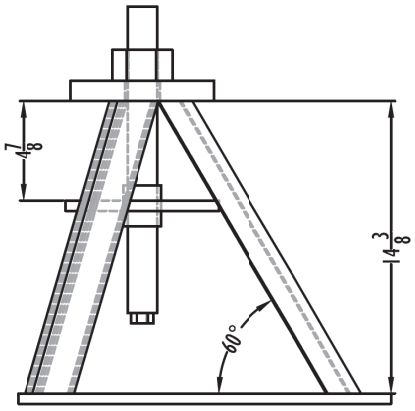

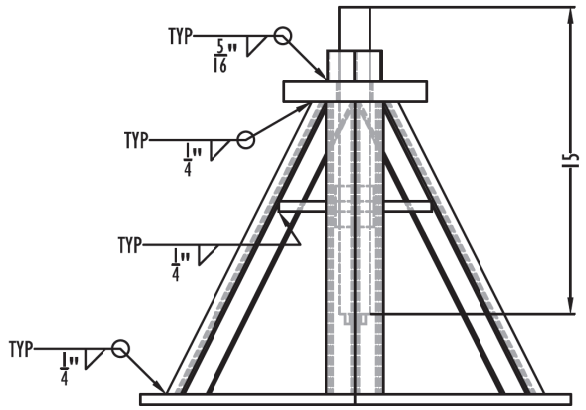

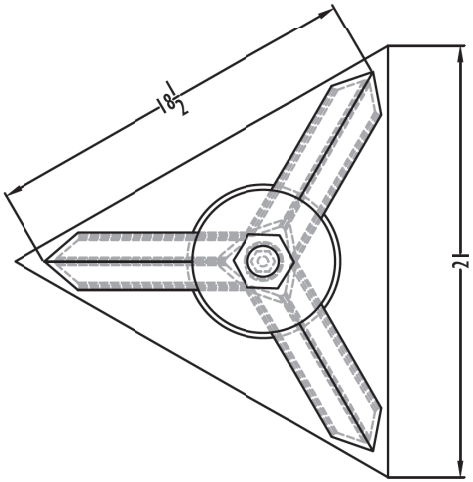

MEDIUM

Notes:

1) All Dimensions given ir inches/degrees
2) A36 Steel
3) All welds to be compatible with base metal
4) Nut to be welded so that the threaded rod runs freely through
5) See S-7 for final quantities

REVISIONS			
REV	DESCRIPTION	DATE	APPROVED
A	Modified mid plate and incl bot nut	05-19-2012	

Project: CESURA Preliminary

Drawn By: Travis Thonstad

Title: Jack Stand Medium

File Name: JackStand.dwg

Contact: thonstat@u.washington.edu
stanton@u.washington.edu

University of Washington
Civil and Env. Engineering

Sheet: S-2

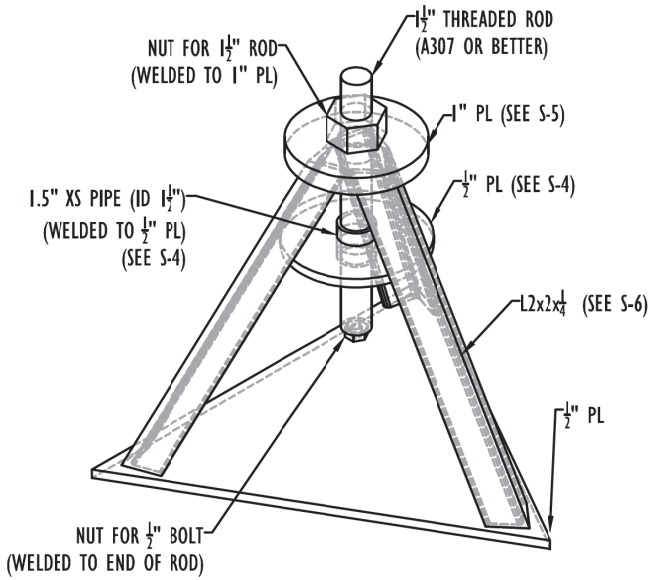

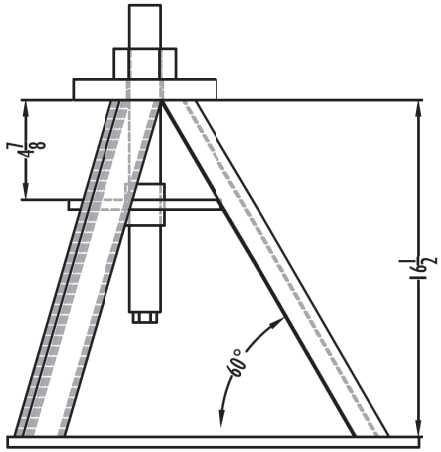

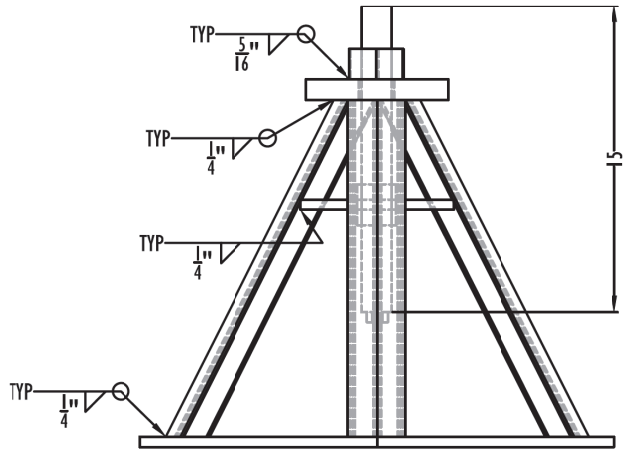

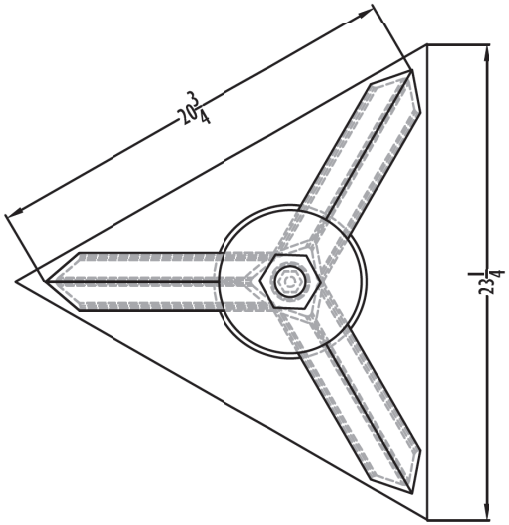

TALL

Notes:

1) All Dimensions given ir inches/degrees
2) A36 Steel
3) All welds to be compatible with base metal
4) Nut to be welded so that the threaded rod runs freely through
5) See S-7 for final quantities

REVISIONS			
REV	DESCRIPTION	DATE	APPROVED
A	Modified mid plate and incl bot nut	05-19-2012	

Project:	CESURA Preliminary	Drawn By:	Travis Thonstad
Title:	Jack Stand Tall	Contact:	thonstat@u.washington.edu stanton@u.washington.edu
File Name:	JackStand.dwg	Sheet:	S-3

University of Washington
Civil and Env. Engineering

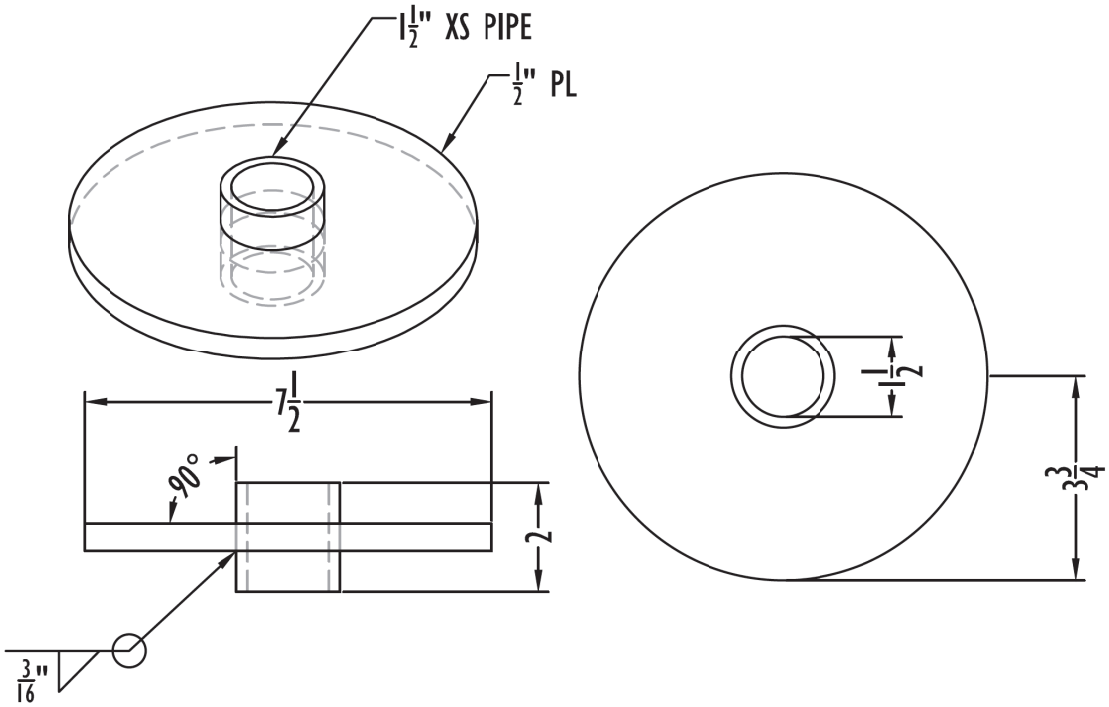

MIDDLE-PLATE

University of Washington
Civil and Env. Engineering

REVISIONS			
REV	DESCRIPTION	DATE	APPROVED
A	Modified mid plate and incl bot nut	05-09-2012	

Notes:
1) All Dimensions given in inches/degrees
2) A36 Steel

Project:	CESURA Preliminary	Drawn By:	Travis Thonstad
Title:	Middle-Plate Detail	Contact:	thonstat@u.washington.edu
File Name:	JackStand.dwg		stanton@u.washington.edu
		Sheet:	S-4

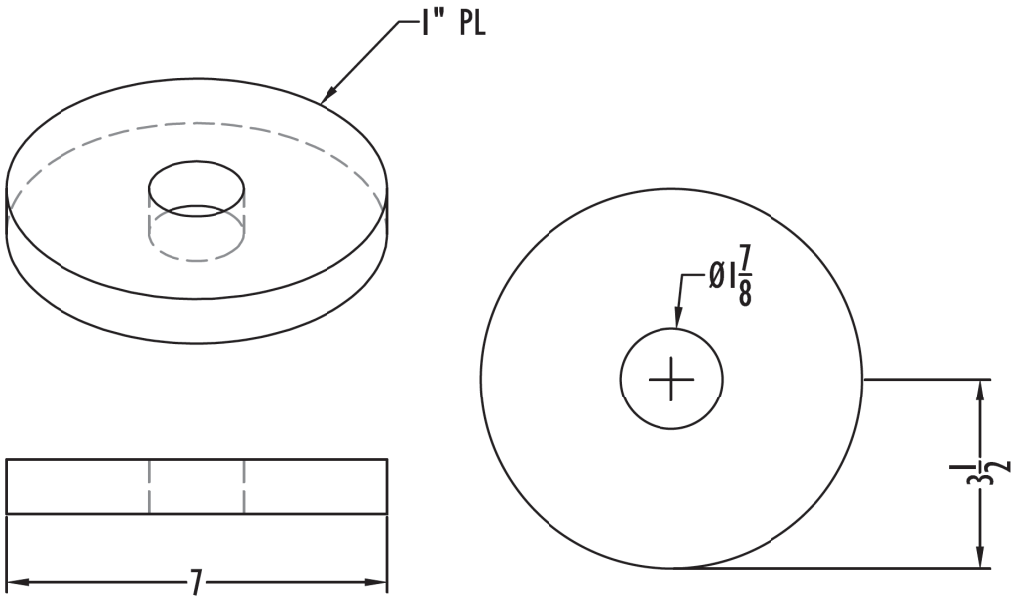

TOP-PLATE

University of Washington
Civil and Env. Engineering

REVISIONS			
REV	DESCRIPTION	DATE	APPROVED
A	Modified mid plate and incl bot nut	05-09-2012	

Notes:
1) All Dimensions given in inches/degrees
2) A36 Steel

Project:	CESURA Preliminary	Drawn By:	Travis Thonstad
Title:	Top-Plate Detail	Contact:	thonstat@u.washington.edu stanton@u.washington.edu
File Name:	JackStand.dwg	Sheet:	S-5

SHORT

MEDIUM

TALL

University of Washington
Civil and Env. Engineering

Project: CESURA Preliminary
Drawn By: Travis Thonstad
Title: Angle Details
Contact: thonstat@u.washington.edu
stanton@u.washington.edu
File Name: JackStand.dwg
Sheet: S-6

Notes:
1) All Dimensions given in inches/degrees
2) A36 Steel

REVISIONS			
REV	DESCRIPTION	DATE	APPROVED
A	Modified mid plate and incl bot nut	05-09-2012	

S - SHEET TOTALS					
ITEM	QUANTITY	MATERIAL	SIZE	ADDITIONAL	
SHORT	4			QTY:	DESCRIPTION:
TOP-PL	4	1" PL	Ø 7"	4	15" A307 THR. ROD
MID-PL	4	1/2" PL	Ø 7 1/2"	4	NUT FOR $1\frac{1}{2}$" BOLT
L-SHORT	12	L2x2x1/4"	15 "	4	NUT FOR $\frac{1}{2}$" BOLT
BASE-PL	4	1/2" PL	19 "	4	2 " - $1\frac{1}{2}$" XS PIPE
MEDIUM	4			4	15" A307 THR. ROD
TOP-PL	4	1" PL	Ø 7"	4	NUT FOR $1\frac{1}{2}$" BOLT
MID-PL	4	1/2" PL	Ø 7 1/2"	4	NUT FOR $\frac{1}{2}$" BOLT
L-MED	12	L2x2x1/4"	17 3/8"	4	2 " - $1\frac{1}{2}$" XS PIPE
BASE-PL	4	1/2" PL	21 "		
TALL	4			4	15" A307 THR. ROD
TOP-PL	4	1" PL	Ø 7"	4	NUT FOR $1\frac{1}{2}$" BOLT
MID-PL	4	1/2" PL	Ø 7 1/2"	4	NUT FOR $\frac{1}{2}$" BOLT
L-TALL	12	L2x2x1/4"	19 7/8 "	4	2 " - $1\frac{1}{2}$" XS PIPE
BASE-PL	4	1/2" PL	23 1/4"		

Notes:

1) All Dimensions given ir inches/degrees
2) A36 Steel
3) All welds to be compatible with base metal
4) Nut to be welded so that the threaded rod runs freely through

University of Washington
Civil and Env. Engineering

REVISIONS			
REV	DESCRIPTION	DATE	APPROVED
A	Modified mid plate and incl bot nut	05-19-2012	

Project: CESURA Preliminary

Drawn By: Travis Thonstad

Title: Final Quantities

File Name: JackStand.dwg

Contact: thonstat@u.washington.edu
stanton@u.washington.edu

Sheet: S-7

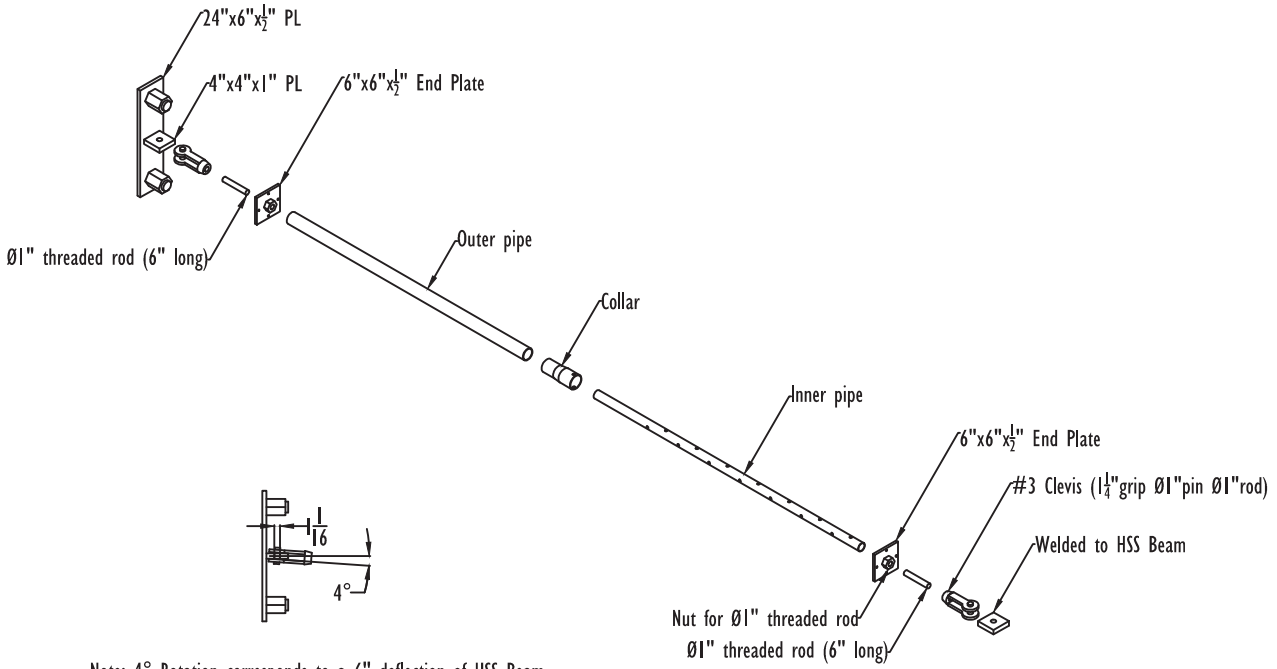

Note: 4° Rotation corresponds to a 6" deflection of HSS Beam

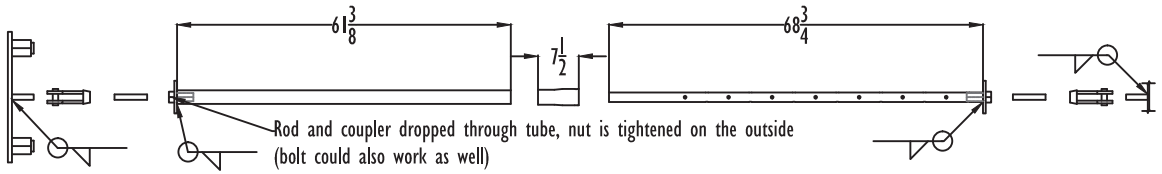

Notes:

BRACE - DETAIL

University of Washington
Civil and Env. Engineering

REVISIONS				Project: CESURA Preliminary	Drawn By: Travis Thonstad	
REV	DESCRIPTION	DATE	APPROVED	Title: BRACE DETAIL	Contact: thonstat@u.washington.edu stanton@u.washington.edu	Sheet: NB-2
				File Name: CESURA3D(5-20).dwg		

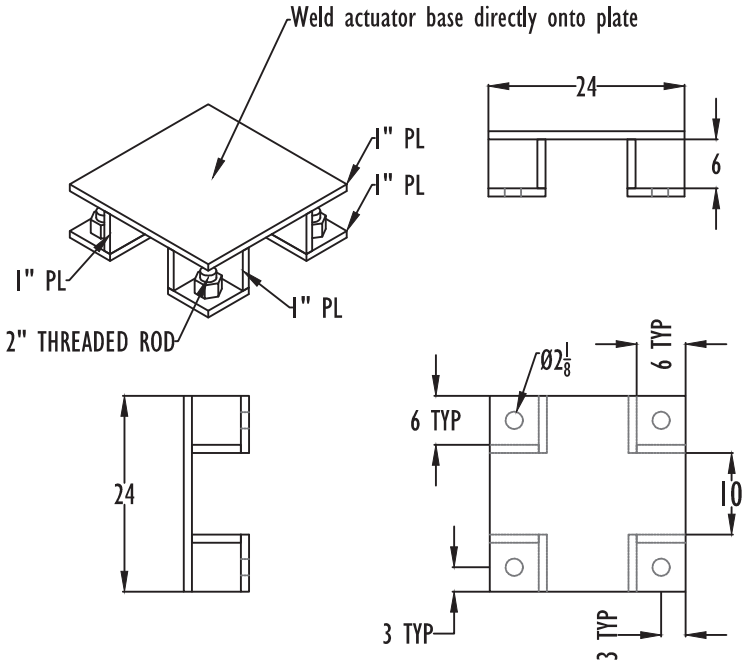

ACTUATOR STAND OFF

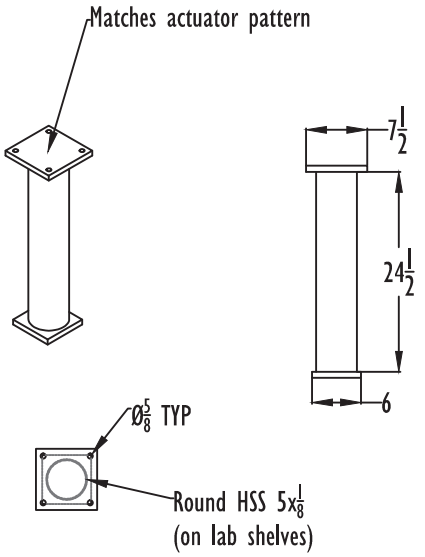

ACTUATOR BASE

HORIZONTAL ACTUATOR ASSEMBLY

Notes:

REVISIONS			
REV	DESCRIPTION	DATE	APPROVED

Project: CESURA Preliminary

Drawn By: Travis Thonstad

Title: H. ACTUATOR ASSEM

File Name: NB_SHEETS.dwg

Contact: thonstat@u.washington.edu
stanton@u.washington.edu

University of Washington
Civil and Env. Engineering

Sheet: NB-3

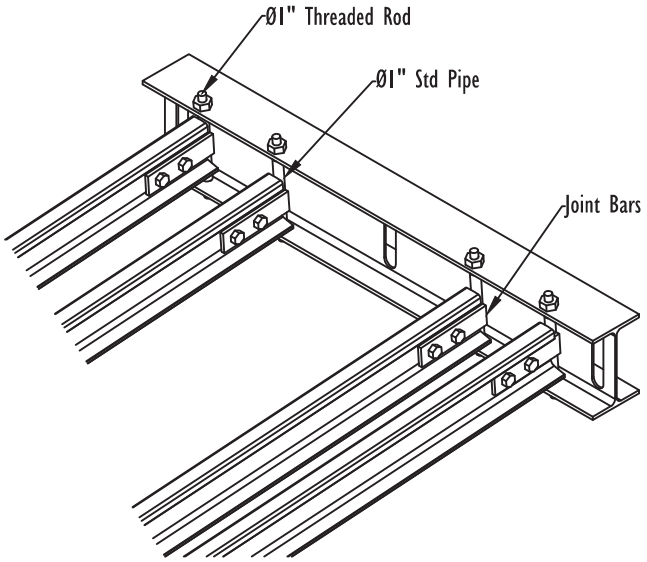

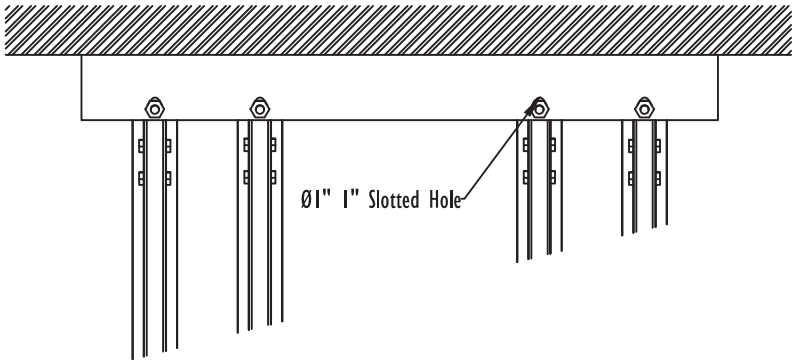

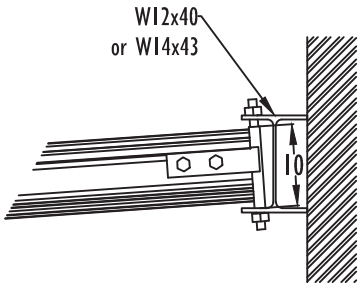

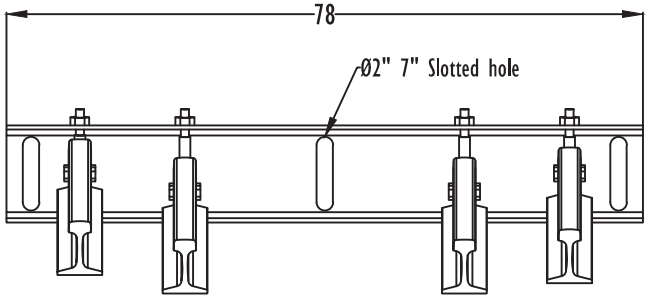

RAIL END PLATE

Notes:

University of Washington
Civil and Env. Engineering

REVISIONS			
REV	DESCRIPTION	DATE	APPROVED

Project: CESURA Preliminary
Drawn By: Travis Thonstad
Title: RAIL END PLATE
File Name: NB_SHEETS.dwg
Contact: thonstat@u.washington.edu
stanton@u.washington.edu
Sheet: NB-4

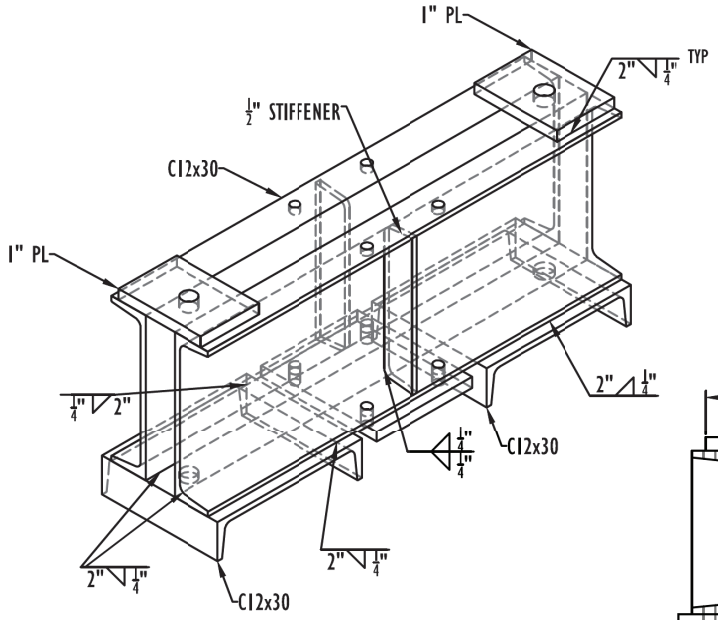

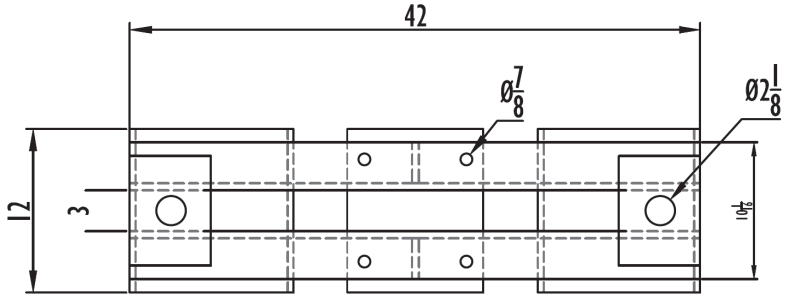

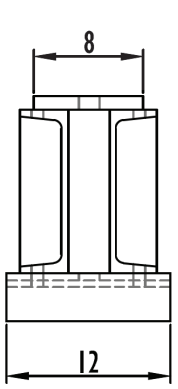

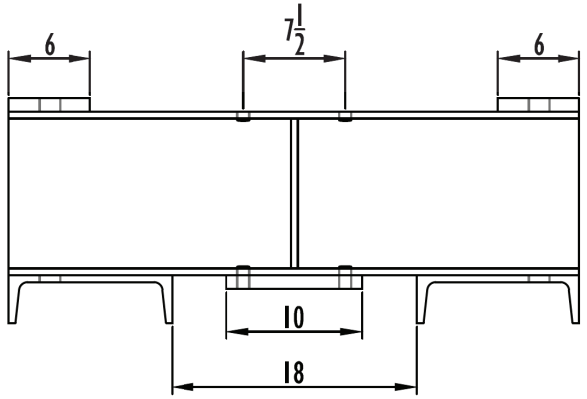

Notes:

ACTUATOR ASSEMBLY

University of Washington
Civil and Env. Engineering

REVISIONS			
REV	DESCRIPTION	DATE	APPROVED

Project:	CESURA Prelininary	Drawn By:	Travis Thonstad
Title:	Actuator Assembly	Contact:	thonstat@u.washington.edu
File Name:	M_SHEETS.dwg		stanton@u.washington.edu
		Sheet:	N-1

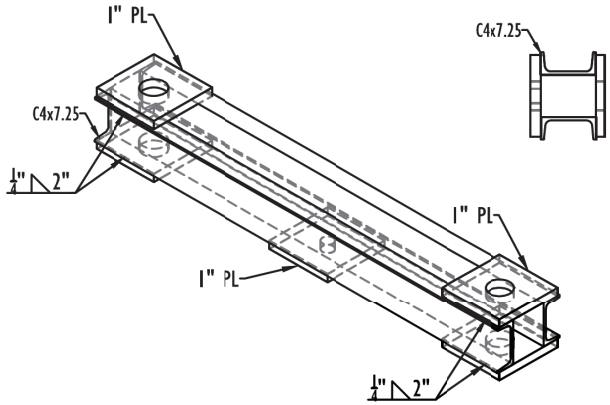

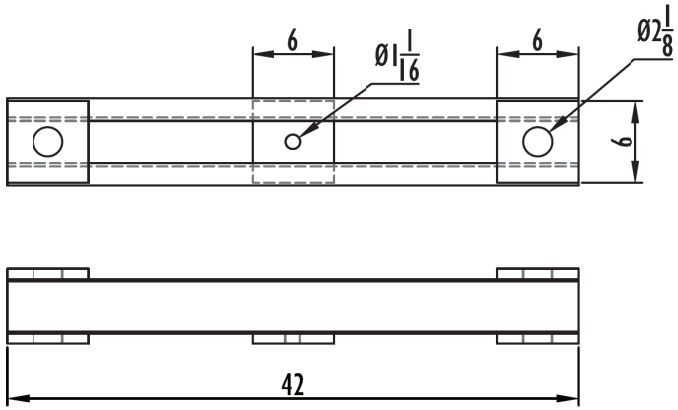

Notes:

TRANSFER BEAM

University of Washington
Civil and Env. Engineering

REVISIONS				Project: CESURA Preliminary	Drawn By: Travis Thonstad	
REV	DESCRIPTION	DATE	APPROVED	Title: Transfer Beam	Contact: thonstat@u.washington.edu stanton@u.washington.edu	Sheet: N-2
				File Name: M_SHEETS.dwg		

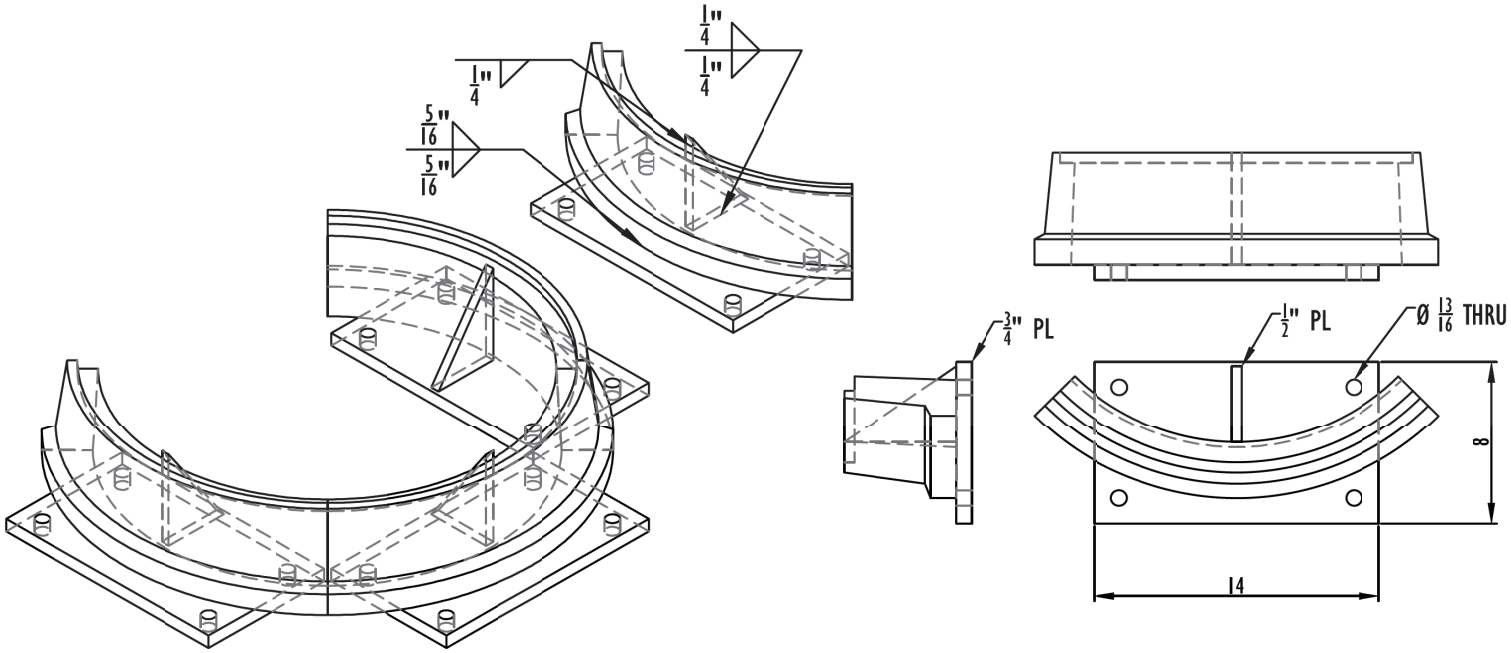

Notes:

WHEEL

University of Washington
Civil and Env. Engineering

REVISIONS				Project: CESURA Preliminary	Drawn By: Travis Thonstad	
REV	DESCRIPTION	DATE	APPROVED	Title: Wheel	Contact: thonstat@u.washington.edu stanton@u.washington.edu	Sheet: N-3
				File Name: M_SHEETS.dwg		

M SHEET TOTALS				
ITEM	QUANTITY	MATERIAL	SIZE	ADDITIONAL
(M-1) MISC STEEL				
PART M-1	1	1" PL	8"x6""	
PART M-2	2	1" PL	12"x10"	
PART M-3	2	$\frac{1}{2}$" PL	11"x3"	Note: 3" FLAT BAR OK
(M-2) MISC. STEEL				
PART M-4	8	1" PL	6"x6"	
PART M-5	15	$1\frac{1}{2}$" PL	6"x6"	
PART M-6	2	1" PL	6"x6"	
PART M-7	4	C4x7.2	42"	
(M-3) MISC STEEL				
PART M-8	4	$\frac{1}{2}$" PL	5.5"x3.75""	
PART M-9	4	$\frac{3}{4}$" PL	14"x8"	
PART M-10	1	$\frac{3}{4}$" PL	9"x9"	
(M-4) SW PLATE	1	$\frac{1}{2}$" PL	48"x44"	
(M-5) SE PLATE	1	$\frac{1}{2}$" PL	48"x44"	
(M-6) N PLATE	2	$\frac{1}{2}$" PL	48"x44"	

Notes:

1) A36 Steel
2) All holes to be flame cut

University of Washington
Civil and Env. Engineering

REVISIONS			
REV	DESCRIPTION	DATE	APPROVED

Project: CESURA Preliminary

Drawn By: Travis Thonstad

Title: M Sheet Totals

File Name: M_SHEETS.dwg

Contact: thonstat@u.washington.edu
stanton@u.washington.edu

Sheet: M-0

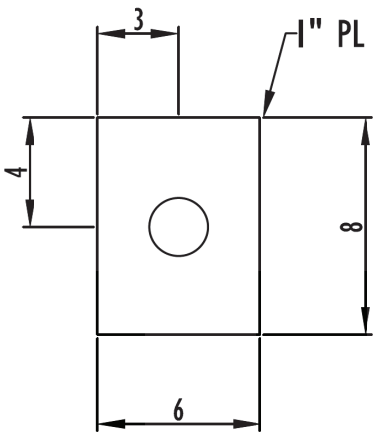

PART M-1

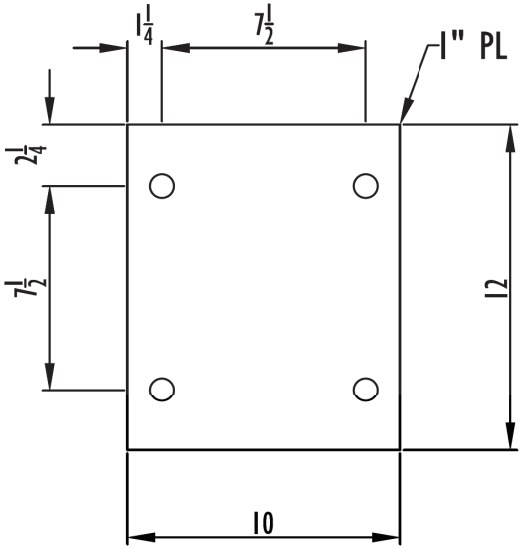

PART M-2

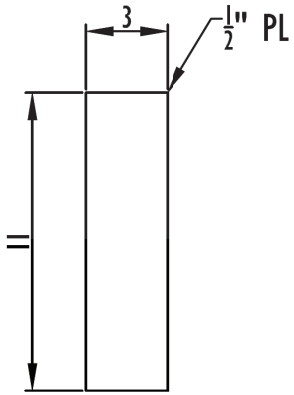

PART M-3

Notes:

1) A36 Steel
2) All holes to be flame cut

MISC. STEEL

University of Washington
Civil and Env. Engineering

REVISIONS				Project: CESURA Preliminary	Drawn By: Travis Thonstad	
REV	DESCRIPTION	DATE	APPROVED	Title: MISC STEEL 01	Contact: thonstat@u.washington.edu stanton@u.washington.edu	Sheet: M-1
				File Name: M_SHEETS.dwg		

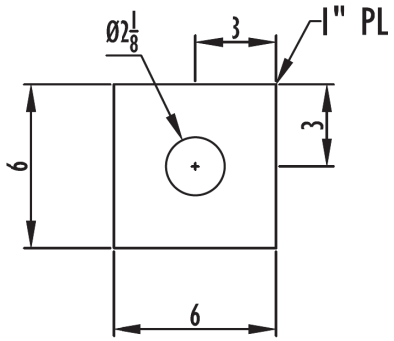

PART M-4

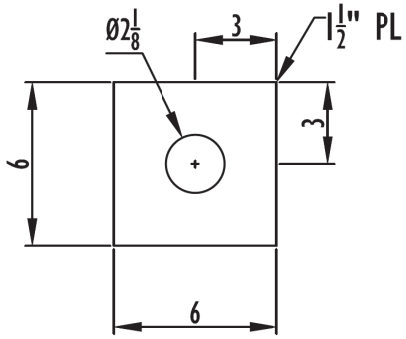

PART M-5

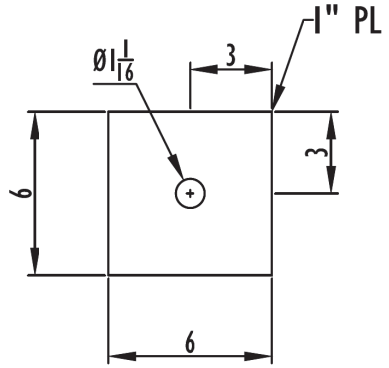

PART M-6

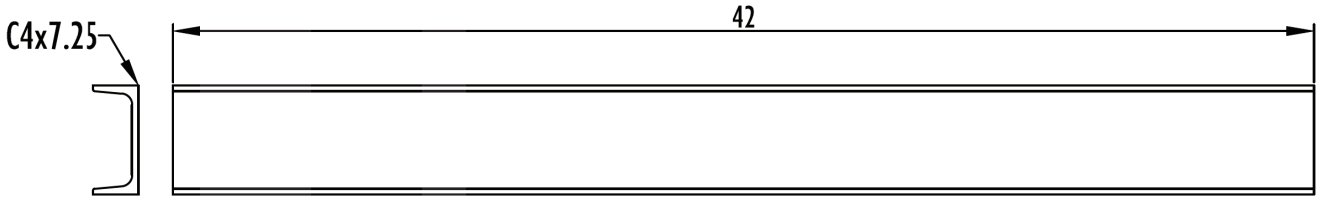

PART M-7

Notes:

1) A36 Steel
2) All holes to be flame cut

MISC. STEEL

University of Washington
Civil and Env. Engineering

REVISIONS				Project: CESURA Preliminary	Drawn By: Travis Thonstad	
REV	DESCRIPTION	DATE	APPROVED	Title: MISC STEEL 02	Contact: thonstat@u.washington.edu	Sheet: M-2
				File Name: M_SHEETS.dwg	stanton@u.washington.edu	

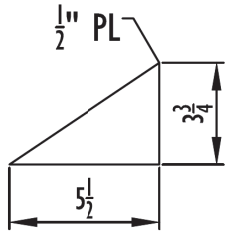

PART M-8

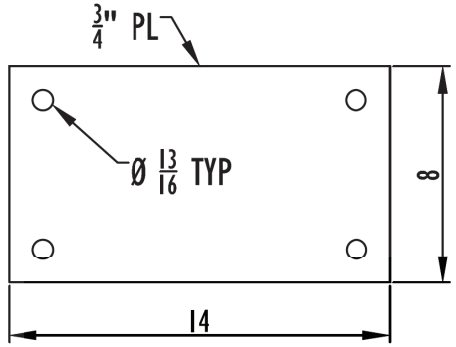

PART M-9

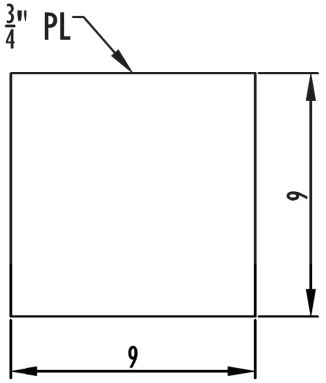

PART M-10

Notes:

1) A36 Steel
2) All holes to be flame cut

MISC. STEEL

University of Washington
Civil and Env. Engineering

REVISIONS					
REV	DESCRIPTION	DATE	APPROVED		

Project:	CESURA Preliminary	Drawn By:	Travis Thonstad
Title:	MISC STEEL 03	Contact:	thonstat@u.washington.edu
File Name:	M_SHEETS.dwg		stanton@u.washington.edu

Sheet: M-2

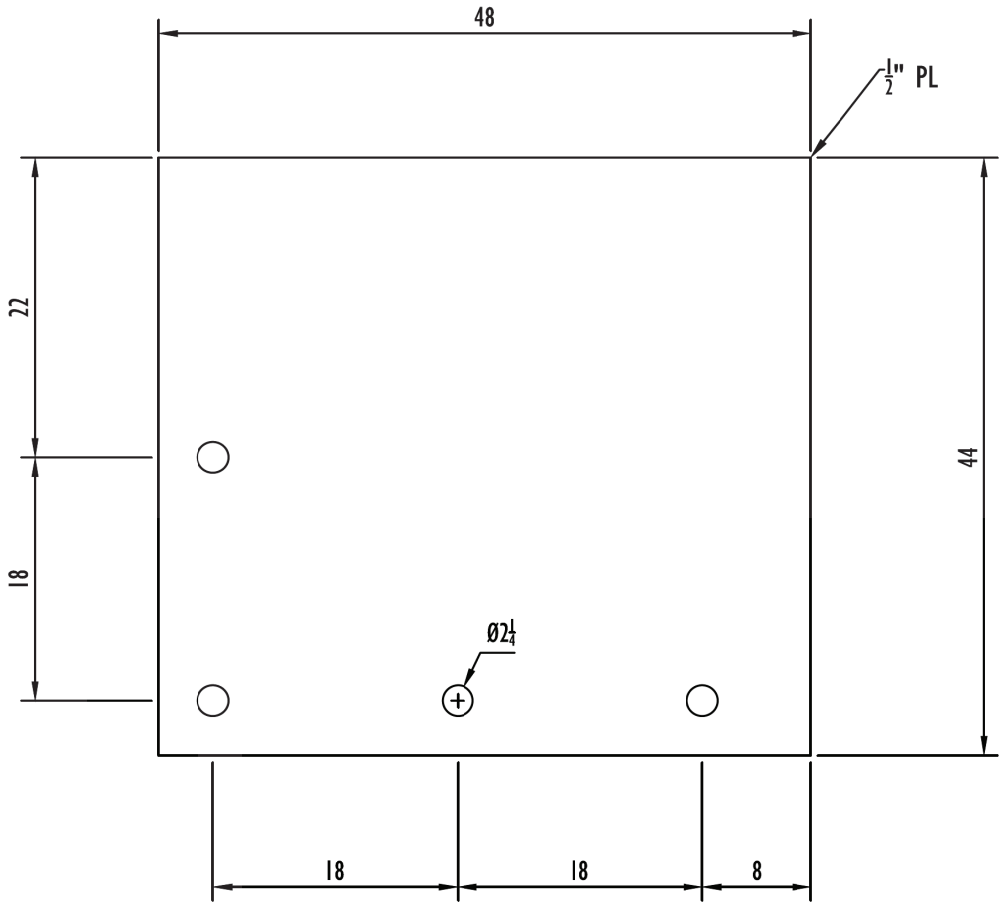

SouthEast PLATE

Notes:

1) A36 Steel
2) All holes to be flame cut

University of Washington
Civil and Env. Engineering

REVISIONS			
REV	DESCRIPTION	DATE	APPROVED

Project: CESURA Preliminary
Drawn By: Travis Thonstad
Title: SE PL
File Name: M_SHEETS.dwg
Contact: thonstat@u.washington.edu
stanton@u.washington.edu
Sheet: M-3

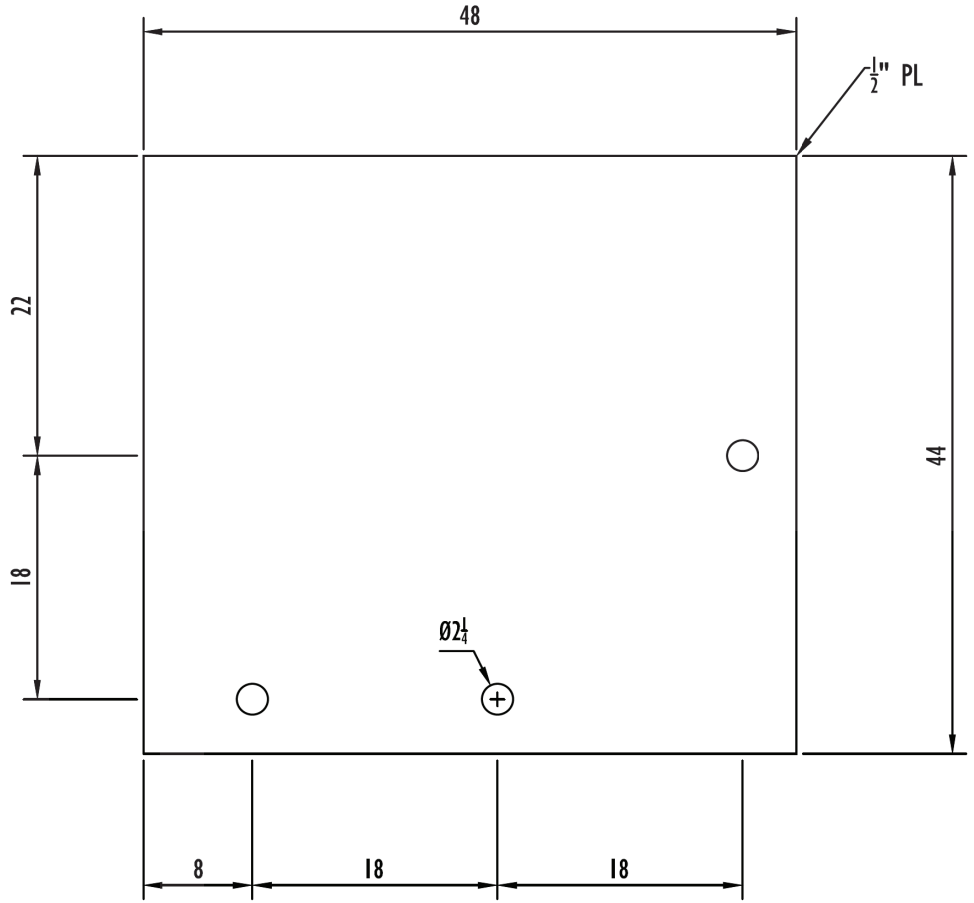

Notes:

1) A36 Steel
2) All holes to be flame cut

SouthWest PLATE

University of Washington
Civil and Env. Engineering

REVISIONS				Project: CESURA Preliminary	Drawn By: Travis Thonstad	
REV	DESCRIPTION	DATE	APPROVED	Title: SW PL	Contact: thonstat@u.washington.edu stanton@u.washington.edu	Sheet: M-4
				File Name: M_SHEETS.dwg		

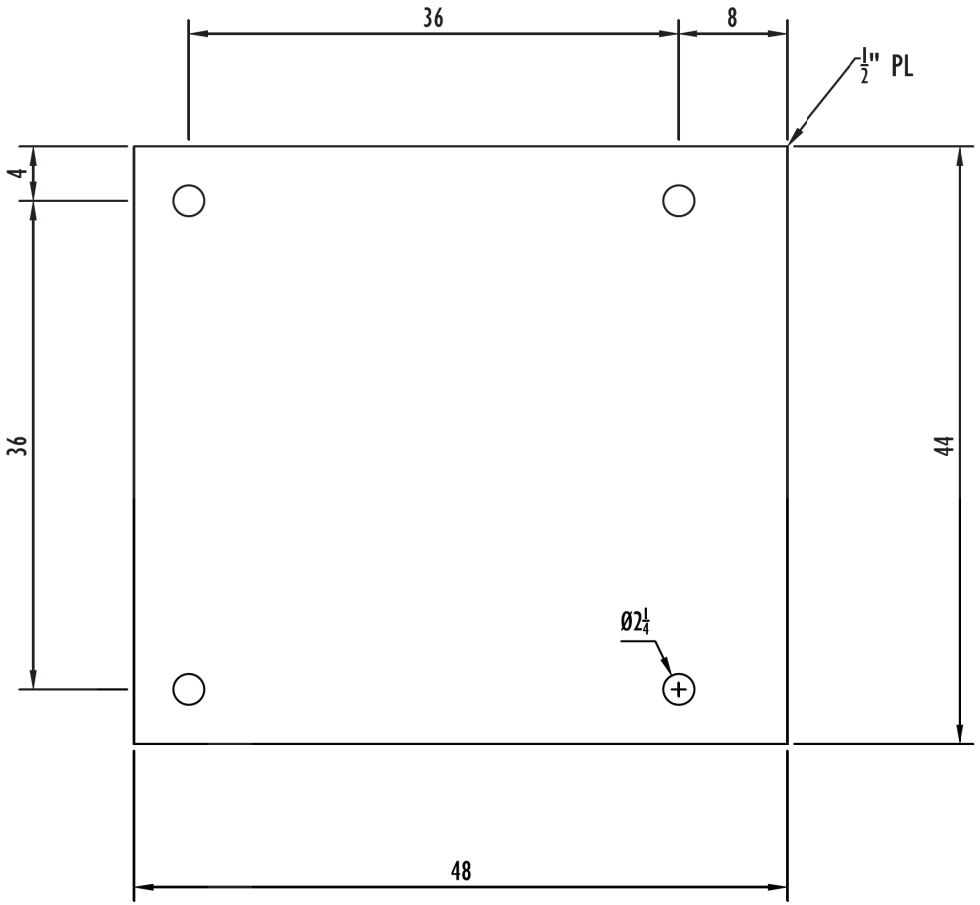

North PLATES

Notes:

1) A36 Steel
2) All holes to be flame cut

University of Washington
Civil and Env. Engineering

REVISIONS			
REV	DESCRIPTION	DATE	APPROVED

Project: CESURA Preliminary
Drawn By: Travis Thonstad
Title: N PL's
File Name: M_SHEETS.dwg
Contact: thonstat@u.washington.edu
stanton@u.washington.edu
Sheet: M-5

Appendix C Final Report Submitted to Parsons Brinckerhoff

This appendix contains the final report that was submitted to Parsons Brinckerhoff on January 7th, 2013. It contains supplemental information and summaries of the testing procedure, the experimental design, and the conclusions of the laboratory experiment. Much of the data presented is repeated in this report. The appendices that are referenced contain information and figures that were previously presented in this document and are not repeated.

LABORATORY TESTING OF THE CESURA RAIL TRACK SYSTEM

Preliminary Report

Prepared for

Parsons Brinkerhoff, Inc.

by

By Prof. John Stanton and Travis Thonstad

Dept. of Civil Engineering,

University of Washington,
Seattle, WA 98195
Dec 2012.

1 Introduction

1.1 Background

Sound Transit is in the process of extending a light rail system to cross the I-90 floating bridge over Lake Washington between Seattle and Bellevue. The bridge consists of a floating span, approximately one mile long, and a transition span at each end. Each transition span connects the floating span to the fixed bridge at the land end. The transition spans are pin-connected so that they can rotate in response to changes in the lake water level. Those rotations are small enough that they have no consequences for road traffic, but that is not the case for a rail system because the rails must rotate at the hinges in the bridge deck. The rails must remain elastic under these rotations, which implies the need for flexibility, but they must also be supported sufficiently rigidly to carry the light rail vehicle traveling at its design speed of 55 mph. The need for the track to be simultaneously rigid and flexible appears to create conflicting requirements.

The CESURA concept (**C**urved **E**lement **Su**pported **Ra**il) was developed to resolve the apparent conflict. It is shown in Figure 1-1.

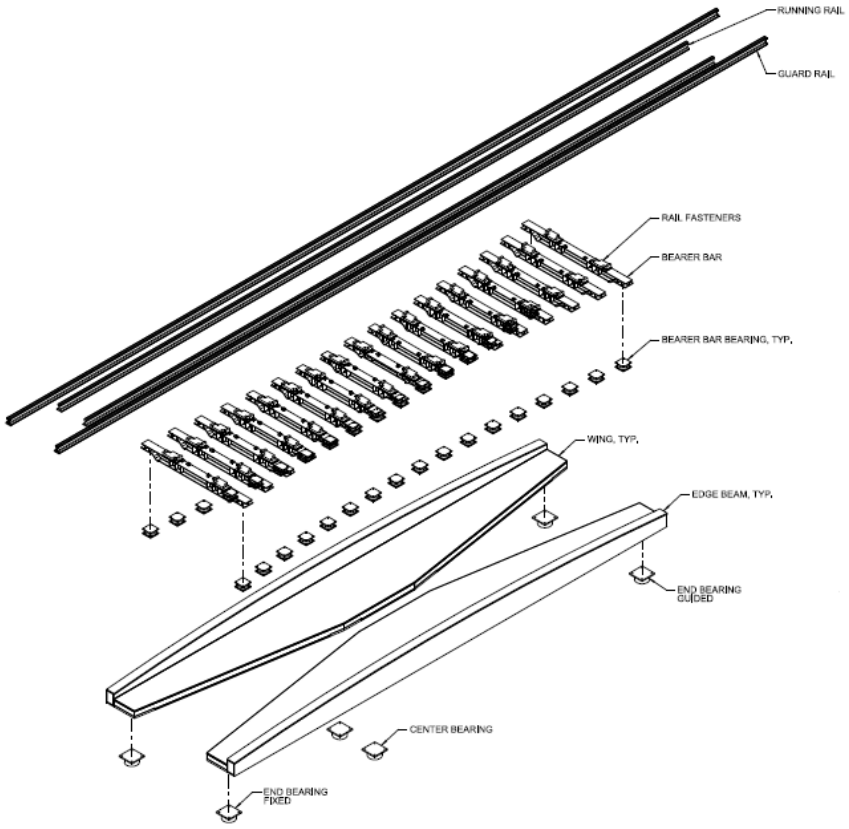

Figure 1-1. Prototype CESURA system

The CESURA system acts like a pin-ended beam that spans over the hinge point between the transition and fixed span or the transition and floating span. The main elements of the system are:

- The two longitudinal box girders, or wings.
- The transverse bearer bars. The serve a purpose similar to that of ties in a conventional track, but they are supported on the wings by bearings that allow rotation and limited translation.
- The rails, which rest on the bearer bars and are secured to them.

The bearings on each wing are set out on a horizontal circular curve, so the bearer bars are all of different lengths; those at the ends are the longest. The wings are supported from below on the transition and fixed or floating spans, so that they move vertically with the transition span in response to lake level changes. However, the wings are supported eccentrically to their longitudinal axes so that, in addition to vertical movement, they undergo rigid body twisting about their longitudinal axes. As the wings twist, the bearer bars move vertically through different distances, and the rails bend in the vertical plane. By suitable choice of the horizontal curve on which the bearings lie, and the location of the supports for the wings, the vertical curvature of the rails can be made to provide a smooth curved transition between the transition and fixed or floating span, while the rails are fully supported along the length of the CESURA track bridge. The length of the track bridge is chosen to ensure that this bending causes stresses that are tolerable.

While the primary purpose of the CESURA track bridge system is to accommodate pitch rotations of the transition span, other displacements also occur. Roll of the floating bridge may occur, for example due to the weight of the light rail vehicle (LRV) entering or exiting (the tracks are located on the extreme edge of the bridge) or due to wave action. Yaw of the transition span, and hence of the track bridge, may also occur due to transverse wind forces on the floating bridge and the corresponding movements. These movements must also be accommodated by the CESURA track bridge system.

Parsons Brinkerhoff (PB) has been engaged to design the system for the I-90 track bridge. Because the system was developed only recently, it has never been built. The University of Washington was engaged to conduct component tests. Further testing of a complete system at the TTCI (Transportation Technology Center, Inc.) facility in Pueblo, Colorado is planned for 2013.

This document constitutes the preliminary report on the component testing conducted at the University of Washington.

1.2 Scope

The scope of the component testing was developed in consultation with PB. The goal was to ensure that the geometry of the system worked as intended, and to study any difficulties with design, fabrication or assembly.

The complete system at full scale is too large to fit in the laboratory, so a choice had to be made between testing the complete assembly at reduced scale or part of the system at full scale. The latter choice was made, largely because of the difficulty of obtaining reduced scale components such as rails

and bearings. Other considerations included cost and the fact that fabrication tolerances do not scale proportionately.

The system that was built and tested represented approximately one quarter of the track bridge, and consisted of four bearer bars with the associated rails and supporting elements.

2 Test Setup and Test Matrix

2.1 Test Setup

The test setup is shown in Figure 2-1.

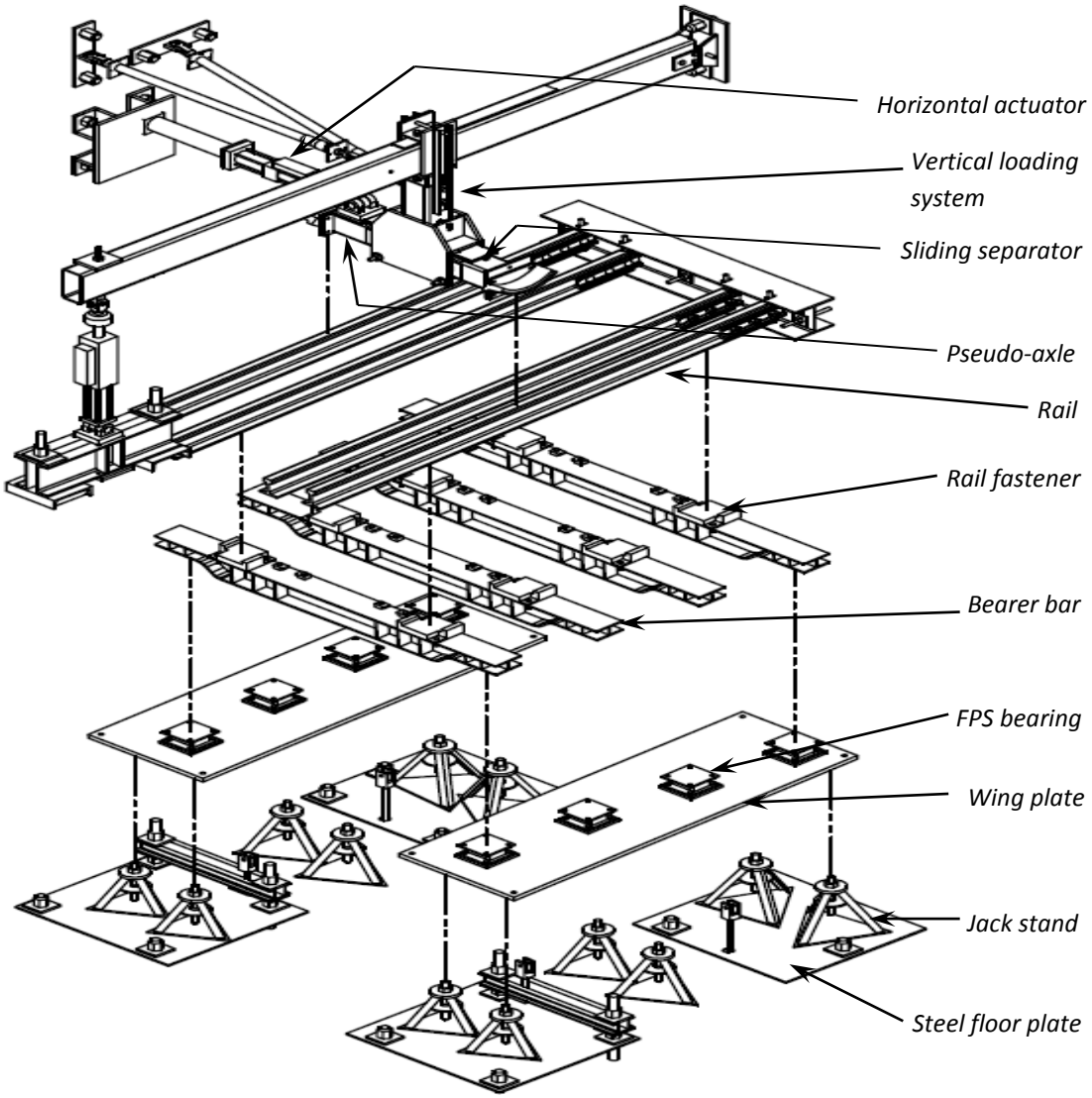

Figure 2-1. Test setup.

The principal components are:

- ***Steel floor plates***, bolted to the laboratory strong floor, to which the assembly could be attached to prevent movement.

- ***Jack stands*** with screw-jack type vertical movement capability. Six stands support each wing plate and allow vertical adjustment so the wing plate can be moved in vertical displacement and rotation about either horizontal axis.
- ***Wing plates***. The two wing plates were made from heavy (1.5" thick) steel plate rather than box sections in the interests of simplicity and economy.
- ***Bearings***. Eight Friction Pendulum bearings were supplied by Earthquake Protection Systems. The geometry of the FPS bearing was originally designed to provide seismic isolation properties. Here the bearings were used to provide transverse displacements and rotations about an axis parallel to the rails. Their spherical geometry would normally allow displacement and rotation in the other two horizontal degrees of freedom, but in this case an internal guide limited those two movements to small values. The bearings contained an uplift restriction device as well.
- ***Bearer bars***. These were made from rolled steel WF8x31 sections. At the ends, the section height was reduced to minimize the vertical distance between the rails and wings. This was achieved by locally cutting off the bottom flange and part of the web, and welding on a curved plate.
- ***Rails and fasteners***. The running rails were attached to the bearer bars using ATP-SW24V Resilient Direct Fixation fasteners. These were intended to provide an inwards cant of 0.025 radians, but were delivered with no cant, so special tapered HDPE shims had to be fabricated and placed under the fasteners. The guard rails were attached using Pandrol e-clip fasteners driven into Pandrol weld-on shoulders attached to loose plates which were bolted to the top flange of the bearer bar. They have no cant, and use a different type of clip, which is welded, rather than bolted, to the fastener.
- ***A "pseudo-axle"***. This component served the purpose of spreading the load from the vertical loading column out to the rails. Use of a real axle from a Light Rail Vehicle was considered, but was rejected because it was heavy and because attaching other components would be difficult. The pseudo-axle consisted of an 8x8x0.375 hollow section with welded end plates. To the end plates were welded sections of the steel "tire" from a LRV, in order to achieve the correct contact geometry between the loading system and the rails.
- ***Vertical loading system***. This consisted of an overhead beam with a hinged connection to the strong wall, a 22-kip vertical actuator which pulled down on the end of the beam, and a vertical loading column that delivered downwards vertical load from the loading beam to the pseudo-axle.
- ***Horizontal actuator***. An 11 kip capacity servo-controlled actuator was bolted to the pseudo-axle in order to provide horizontal loading. It reacted against the east wing of the strong wall and could supply tension or compression.
- ***Sliding separator***. A sliding interface was provided at the bottom of the loading column between it and the pseudo-axle. It was necessary because the vertical loading system was braced laterally to prevent lateral buckling, and so was quite stiff against lateral displacements. In the absence of a sliding separator, much of any horizontal load would have been resisted by the vertical load apparatus, rather than by the rail system, thereby frustrating the purpose of the test. The sliding separator was made from a steel plate with stainless steel sheet welded on

both top and bottom surfaces, and it had a greased PTFE strip above and below. This assembly provided two separate sliding interfaces, which allowed the friction coefficient to be measured in a separate test and then used to correct the load delivered to the rails. To determine the friction coefficient, vertical load was applied (perpendicular to the PTFE surfaces) and the plate with stainless steel surfaces was pulled transversely by a hydraulic jack.

2.2 Instrumentation

Extensive instrumentation was applied.

Load cells measured:

- Load in the 22 kip vertical actuator.
- Load in the 11 kip horizontal actuator.
- Load in the jack used in the PTFE friction tests.
- Load in the jack used in the horizontal load tests.

Potentiometers and LVDTs measured

- Transverse displacements of the bearer bars.
- Vertical deflection of the bearer bars at mid-span.
- Multiple vertical displacements at the ends of the bearer bars (thereby allowing measurement of both vertical deflection and rotation).
- Vertical and horizontal displacements (ideally very small) of the wing plates.
- The orientation of the loading column and vertical loading assembly.

String potentiometers measured

- Global quantities such as movements of the vertical loading system. These were used only for verification of the rig performance, and not for measuring specimen response.

High-sensitivity, two-axis inclinometers measured

- The rotations of the ends of the bearer bars.
- The orientations of the wing plates.

Electrical resistance strain gages measured

- Strains in the flanges of the bearer bars.
- Strains in the rails. These gages existed primarily in the region between Bearer Bars 2 and 3, and were located so as to permit computation of both vertical and transverse bending.

Strain rosettes were used to read

- The strain field in the webs of the bearer bars at the change in depth.

Direct Measurements Inc. (DMI) will supply the instrumentation for the tests at TTCI. They supplied some instrumentation to be used on the UW test assembly to permit comparison of the two sets of values. The sensors included:

- Optical strain gages. These were applied sparingly to the rails. While these gages have some attractive features (such as lack of long term drift) reading them proved problematic. For example, they have to be read by a special camera, and only one was available. In addition the sampling frequency was slow at 1 Hz, which corresponds to two readings per cycle in the horizontal tests.
- Inclinometers. These were US Digital T7 networked absolute single axis instruments, and were attached on three orthogonal faces of an aluminum bracket bolted to the friction pendulum bearing below bearer bar3. The benefit of such a system would be the vertical clearance and the potential to house the instruments against weather, which may prove to be important given the minimum operating temperature of 14°F. The specified sensitivity was less than that of the UW sensors. Again, some difficulties were experienced with reading them satisfactorily due to software limitations.
- LVDTs mounted in an X-pattern in a special frame were attached to the west bearing of bearer bar 3, with the goal of determining its horizontal displacement and rotation about the longitudinal (parallel to the rail). However, the top and bottom components of the bearing move vertically relative to each other as they translate horizontally. Thus three separate motions (transverse and vertical displacements, and rotation) induce displacement in the two LVDTs. Unique identification of those three motions from two sensors is therefore not possible without a third piece of data. In this case, the vertical displacement across the bearing was known from the UW vertical potentiometers measuring the bearer bar motions, but without that data, the X-frame LVDT readings would have had little value.

In all, approximately 150 channels of data were recorded. The number varied slightly from one test to another.

2.3 Test Matrix

The test program is summarized in Table 2-1.

Table 2-1. Test program

Date	Test	Description	Slope (%)	Rotn. (deg)		Yaw (in)	Load control
				Left	Right		
10/6	FRK03	PTFE Friction test	0%	0	0	0	NA
10/8 10/9	STF01-03	Horizontal stiffness tests	0%	0	0	0	NA
10/19 10/23	REF01-02	Reference condition tests	4%	0	0	0	Force
10/27-10/30	PIT01	Pitch 01 test	4%	-3	+3	0	Force
11/2	PIT02	Pitch 02 test	4%	+3	-3	0	Disp
11/6-11/7	ROL01	Roll Test	4%	- 3	-3	0	Disp
11/10-11/11	FRK04-06	PTFE Friction test	4%	0	0	0	NA
11/11-11/12	STF04-06	No Guard rail test	4%	0	0	0	NA
11/14	REF03	Reference condition test	4%	0	0	0	Disp
11/15	YAW01	Yaw Test	4%	0	0	1	Disp

Notes.

1. *Friction test 01 and 02 were pilot tests, and are not reported here.*
2. *Horizontal stiffness tests 01, 02 and 03 were essentially duplicates. They were conducted because of a minor rig malfunction in the first two.*
3. *Test REF01 was conducted with the vertical loading rig half way between Bearer Bars 2 and 3. In all other tests, including REF02, the loading rig was directly over Bearer Bar 3.*
4. *In the pitch and roll tests, positive rotation was counter-clockwise when the observer faced the strong wall.*
5. *Test REF03 was conducted because the DMI instrumentation had become available and the test was used to generate companion values of UW and DMI measurements.*
6. *Friction tests 04 and 05 were duplicates (to account for an instrument malfunction), and were conducted just prior to re-greasing the sliding separator. Test FRK06 was conducted just after re-greasing the sliding separator.*

The PTFE friction tests were conducted to determine the friction coefficient of the PTFE sliding surface. This value was used subsequently to compute the horizontal load on the rails from the measured horizontal load.

The horizontal stiffness tests were conducted under monotonic transverse load applied to Bearer Bar 4, while the pseudo-axle was located directly over Bearer Bar 4. Under these circumstances, most of the vertical load was expected to be carried by Bearer Bar 4, so the resistance would be expected from the bearings beneath Bearer Bar 4 plus any resistance from the frame action of the rails and bearer bars. The latter depends on the moments about the vertical axis developed at the rail fasteners, and they are unknown. They are subject to uncertainty because the clamping force between the rail and fastener base is provided by an elastic clip, and the deformation of that clip depends on the displacement that it undergoes. Particularly with the welded clip fasteners on the guard rails, the clip deformation is likely to vary from one fastener to another.

In the reference condition test, the wings had no pitch, roll or yaw. However, they were configured with a 4% slope, which is the reference condition in the track bridge. The rails sloped upwards towards the wall. In these tests, as in those for the Pitch, Roll and Yaw tests, 10 cycles of repeated vertical load (i.e. 0, Max Load, 0, Max load, etc.) was applied first. Then the full vertical load of 28 kips was applied to the axle and held constant, and the cycles of horizontal load were applied.

In the pitch tests, the jack stands under the wings were adjusted to achieve 3 degrees up (PITCH01) or down (PITCH02), plus the associated twisting motion of the wings. The jack stands were placed so that the diagonal between the opposing corner stands of the group of six was the axis of rotation of the wing when it underwent pitch motions. Thus the two corner jack stands were kept unchanged, and the other four were lowered. One of the other corner stands was then adjusted until the correct pitch was reached, then the remaining three were raised to be snug under the wing. After the combined horizontal and vertical cases had been completed, cycles of vertical load alone were applied to investigate the effects of the vertical cycling when the system was initially offset from the true bearing center.

In the roll tests, the jack stands under one wing were left unchanged, while the other set was adjusted so that both the pitch and twist were the same. This adjustment involved both a vertical translation and a transverse (to the orientation of the rails) rotation. Similar to the pitch adjustments, the diagonal stands were set at the proper elevation, set to match the inner elevations of the pseudo wings. The remaining four stands were lowered, and one of the corner stands was used to adjust the wing to the correct slope and rotation. The remaining three were then raised to be snug under the wing.

A second set of horizontal stiffness tests was conducted on the same configuration as for the REF test, except that the guard rails were disengaged by undoing both the rail clips and fastener bolts. The purpose of the test was to determine the contribution of the guard rails to the total resistance of the system. Because the guard rail clips were stiffer and stronger than those on the running rails, it seemed likely that the guard rails would provide more frame action than would the running rails.

In the yaw tests, the wings remained in the reference condition, however the intermediate plates between the wing plate and the bearing plates on the east side of the test assembly were moved longitudinally through 1” away from the wall. The rails were unfastened from the bearer bars in order to achieve this configuration. The same loading as was used for the REF, PIT and ROL tests was applied. The pseudo-axle was maintained perpendicular to the rails, so, in this case, the wheel segment on the east side was located 1” from the mid-point between Bearer Bars 2 and 3.

The vertical load was applied using force control in all the tests except STF01-03 and FRK03. Those tests were conducted at the beginning of the program when experience with the rig was being developed, and displacement control was used in the interest of safety. (Under force control, the actuator can jump suddenly to full displacement if any resisting element fails.)

3 Lessons Learned During Design and Construction

During design and construction of the test rig and specimen a record was maintained of the lessons learned. These have already been reported separately, and some design and construction sequences have been implemented, but the lessons learned are repeated here in the interests of completeness.

1. ***Ease of assembly and tolerances.*** Overall, the accuracy with which the fabricated components were made was insufficient to allow the system to be assembled within the desired global tolerances. The bearer bars were the source of the majority of the problems even though they were fabricated within conventional tolerance for structural steel. In the lab, many of the bolt holes were reamed out 1/16" over specified size (i.e. bolt diameter plus 1/8" instead of bolt diameter + 1/16") to provide more adjustment.
2. ***Aligning the bearings correctly*** would be easier if each bearing had some alignment device (e.g. a pin) in the center of the bottom plate, which would fit into a matching hole in the wing box. (Alternatively, the stud and hole could be switched). This would allow the correct x and y locations to be maintained while the rotation about the z-axis was adjusted to fit.
3. ***Bearing transportation plates***. The bottom flange in the shallow section of the bearer bar appeared not to be parallel to the top flange. This caused the beam to be effectively cambered, and caused a problem with placing the bearer bars and bearings. To prevent unwanted bearing movements during assembly, the transportation plates need to be kept in place while the bearings are located. Those plates lock the bearing against all motions, including rotation. That means that the bearer bar and bearing cannot be fixed in place, because the underside of the bearer bar is not parallel to the wing plate. The solution used in the lab was to loosen the bolts between bearer bar and bearing just enough to accommodate the relative rotation but not enough to allow relative movement of the two in plan.
4. ***Bearer bar fabrication tolerances***. The as-built bearer bar dimensions varied slightly from the specified values, so that the accuracy of location of the bearer bars and bearings could be no better than +/- 1/8". This could be accommodated in the lab, but, in the prototype, if holes for the bearing bolts are drilled in the wing-box before installation, there may be alignment problems, especially if the wings experience any welding distortion or placement issues. The welded section at the end of the bearer bar, which is intended to keep the profile low, is largely responsible for the in accuracies in fabrication.
5. There are doubts about the ***hold-down force induced by the welded rail clips***. The spring clips are quite stiff (20 mm (0.787 in) bar in torsion), so any difference in vertical elevation of the clip retainer from its intended position will affect the deformation, and thus the force, in the spring clip. Such height differences appear probable and depend on welding sequence, etc ., of the clip plate to the supporting plate.
6. ***FPS bearings***. Are these the right bearing types to use? Will they bind up when asked to undergo pure rotation, when vertical load is applied simultaneously? Do they really need to have a vertical hold-down capacity?
7. ***Guard rail hold***-down system. The clip-holders used in the lab are welded to the supports, and the clip is hammered in after welding. Several potential problems are perceived:

a. Once welded, the only way of adjusting the fixture is to burn it off and start again, unless it is first welded to a loose plate which is later bolted down with oversize holes.
b. Access to the area to be welded is not easy, which makes a high quality weld more difficult to ensure.
c. If any weld metal obstructs the clip-hole, it will have to be cleared out to allow the clip to be inserted.
d. The weld on the clip-holder is highly asymmetric (it is small where the force is high and large where the force is small). This makes no sense from the viewpoint of stiffness and strength.
e. The welder found that, despite efforts to hold down the clip restrainer, it lifted up 1/32" to 1/16" during welding. This vertical out-of true has consequences for the hold-down spring force, especially because the clip itself is quite stiff. (See 3 above).

Cant on the running rail fixtures. The fixtures received in the lab had no cant, whereas they were expected to be canted at 1:40. This was corrected by inserting tapered (HDPE) shims custom designed and fabricated at short notice because the commercial supplier had none in stock.

4 Observed Response

In operation, the CESURA system worked very much as expected.

Under vertical load, the forces were transferred from the tires to the rails, into the bearer bars, bearings and wings. No unexpected sounds were heard. The response appeared to be similar in all configurations (Ref, Pitch, etc.). This finding is very satisfactory, in view of the fact that the imposed motions were larger than those to be expected in the prototype. No damage was observed. The tires did not ride up on the rails.

Under horizontal loading, the monotonic load-deflection relationship in the horizontal stiffness tests was trilinear. The first two segments resembled closely the bilinear relationship predicted by the bearing manufacturer. The third segment consisted of an abrupt stiffening, at a displacement of approximately 1.5 in, and was attributed to the rails making contact with the sides of the fasteners and thereby experiencing larger moments at their intersections with the bearer bars.

Under cyclic horizontal load, accompanied by constant vertical load, the horizontal load-deflection relationship was hysteretic. When the horizontal load was reduced to zero, significant transverse displacement remained. Cycling the vertical load did almost nothing to return the system to zero displacement. Prior to the next loading, the system was re-centered using a chain hoist. The hysteresis was attributed to a combination of internal friction in the bearings and frame action resistance from the rail-bearer bar system.

5 Measured Response

5.1 Rig Friction

Four friction tests were carried out during the testing. The slider was re-greased before FRK03, REF02, PIT02, and STF04. Friction measurements were taken just before re-greasing and just after. A typical plot of friction coefficient vs. data point number is shown in Figure 5-1. The friction coefficient was computed from the instantaneous horizontal and vertical loads. The data point number is approximately proportional to displacement. The plot shows an initial rising segment while the rig was deforming elastically and sliding had not yet started. This is followed by a spike in friction, which is interpreted as the breakaway friction value, then a plateau of approximately constant friction during sliding. At the end of the test the computed friction drops to zero because the horizontal load was released before releasing the vertical load. The friction coefficient in the sliding region was obtained using a least squares fit. The average friction over the four tests was 0.0138 (i.e. 1.38%) with coefficient of variation of 4%. Because this measured value is necessarily the average of the two surfaces, but during the primary tests slip would occur at only one surface (presumably the one with the lower friction coefficient), this value is an upper bound to the friction occurring during the primary tests. However, the very low coefficient of variation across the four tests suggests that the friction changed little over time, regardless of wear, re-greasing, etc. It is therefore believed that the friction was very nearly the same on both surfaces. In the primary tests, the resistance to horizontal load due to the PTFE was taken as 0.0138 * 28 kips = 390 lbs. This is about 10% of the peak horizontal load.

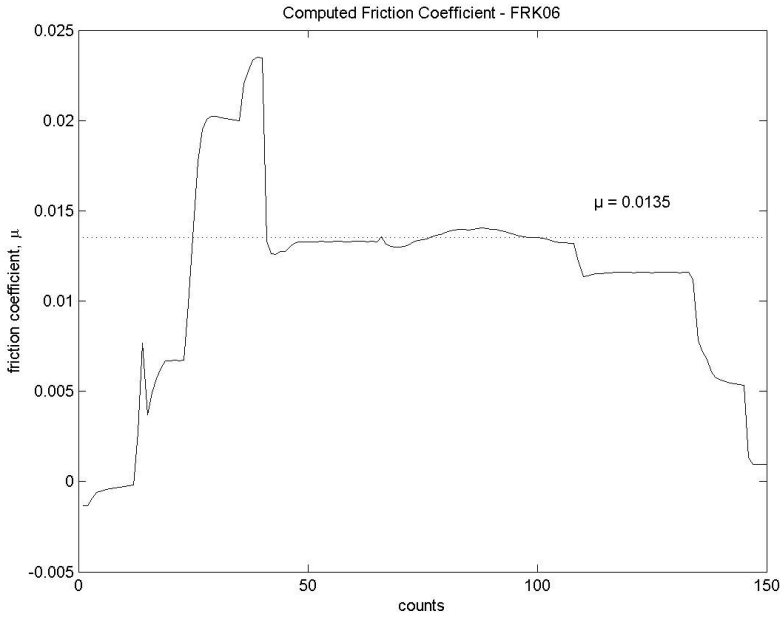

Figure 5-1. PTFE friction test FRK06

5.2 Response to Vertical Load

5.2.1 Rail Response

The rail response to vertical load is typified by the bending stress. That was obtained from the strain gage at mid-width of the rail on the bottom surface of the bottom flange. The gage was located half way between Bearer Bars 2 and 3. In the Reference test, the vertical load was applied directly over the gage (i.e. half way between Bearer Bars 2 and 3). In all the other tests, the load was applied directly over Bearer Bar 3. This was deemed to be a more critical configuration, since it caused higher stresses in the bearer bar and higher lateral deflections at BB04.

Rail stress for the Reference Test is plotted against time in Figure 5-2. During the test, the load was raised to approximately 50% of its full value of 28 kips, then it was cycled at 0.5 Hz between peak load and approximately 10% of peak load.

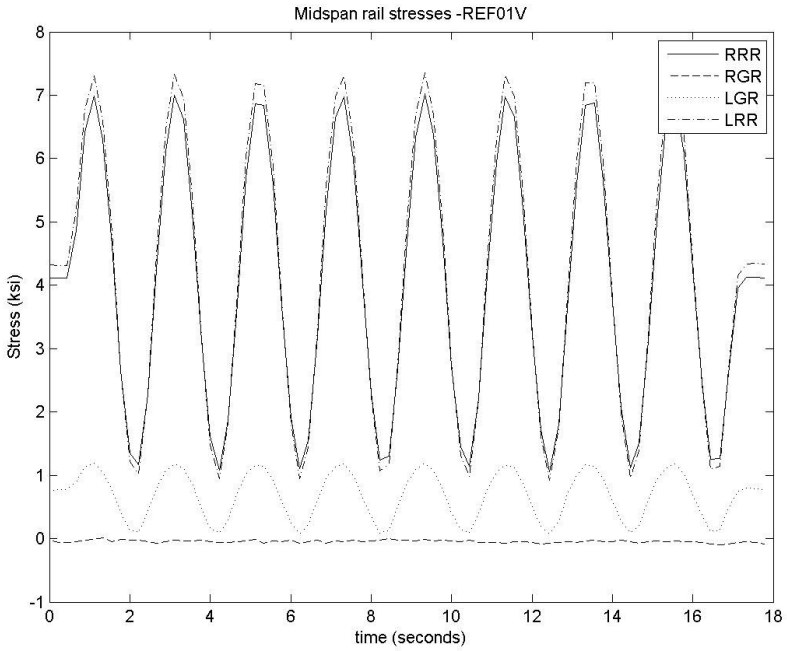

Figure 5-2. Rail bending stress vs time. Reference test, vertical load.

The stresses in the two running rails are almost identical, with a peak of about 7 ksi. The guard rails were not loaded directly, and picked up stress only through vertical frame action through the bearer bars. Unfortunately the gage on the Right Guard Rail (gage RGR) malfunctioned, but the one on the Left Guard Rail showed a stress of approximately 1 ksi. The peak stress in the prototype will differ from that measured here because the full CESURA system is highly indeterminate and because the loading is not all concentrated at a single point.

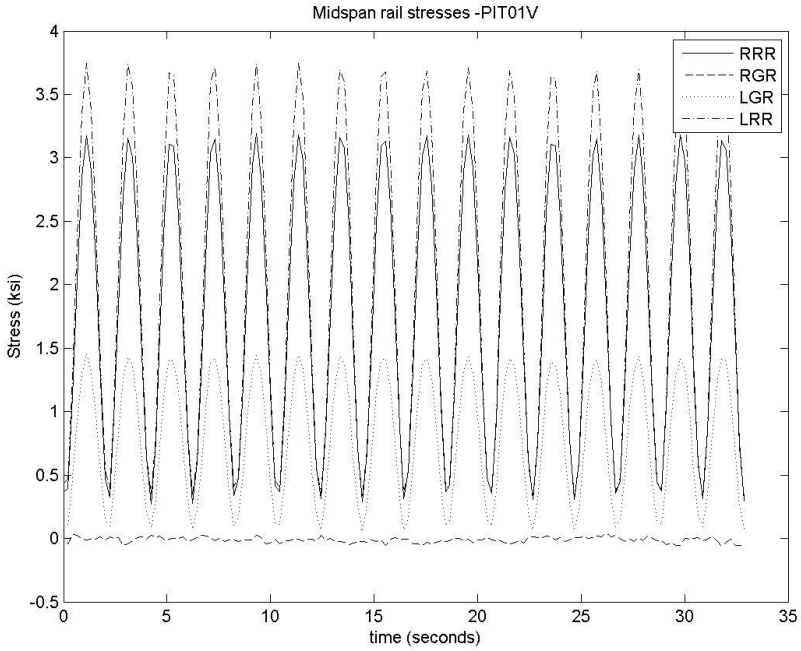

Figure 5-3. Rail bending stress vs time. Test PIT01V, vertical load.

Rail stresses for test PIT01V are shown in Figure 5-3. In this test the load was applied directly over Bearer Bar 3, but the stress is obtained from the gage mid-way between Bearer Bars 2 and 3. The stress is therefore smaller (at approximately 3.5 ksi) than that found in the REF test (7 ksi). The stresses in the two Running Rails differed slightly. It should also be noted that the REF01V test was conducted while the system was at the bearings neutral position while the PIT01V test was conducted with an initial lateral offset to investigate the bearings re-centering capabilities under cycling vertical loads. This initial offset may contribute to the small difference in rail stresses between the right and left running rail.

The stresses depend on the relative rigidities of the rails and bearer bars. For the reference test, the stresses can be shown theoretically to be bounded by 3.8 ksi (assuming rigid bearer bars) and 11.5 ksi (assuming rigid rails). The measured results (7 ksi) therefore lie approximately in the middle of the theoretical range. This finding lends credibility to the measured values. Because in the prototype each bearer bar has a slightly different length, the rigidity with which each one supports the rails is different, and this feature complicates the analysis slightly.

5.2.2 Bearer Bar Response

The bearer bar response is characterized by the mid-span deflection, the end rotation and the shear stress in the web. The latter was monitored using strain rosettes at the change in section.

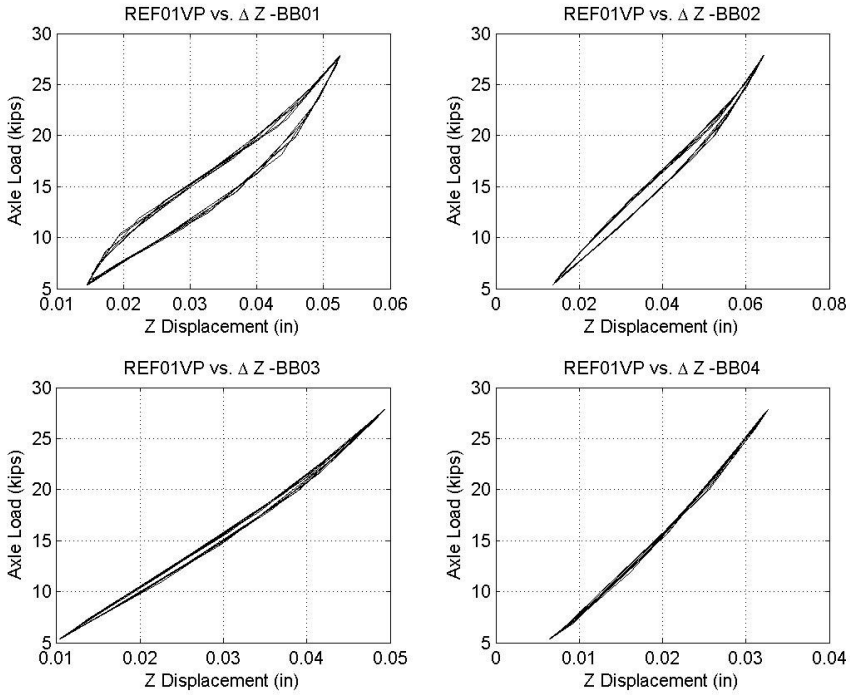

Figure 5-4. test REF01. Vertical load vs mid-span deflection of bearer bars.

Figure 5-4 shows the load vs. mid-span deflection of all four bearer bars in the reference test. The load was located half way between Bearer Bars 2 and 3, so the loading was nominally symmetric. The critical response quantity is the change in deflection during loading and unloading, since a small initial deflection exists from earlier phases of the loading. As might be expected, the displacement response is higher in the interior than at the exterior bearer bars. However, it is not quite symmetric, with the peak occurring at Bearer Bar 2. Bearer Bar 4 is the longest, and therefore the most flexible, so it might expected deflect more than Bearer Bar 1, but the opposite is in fact true. Similarly Bearer Bar 2 deflects more than Bearer Bar 3, despite the latter's greater length. The reason for the slightly asymmetric deflection pattern is not known.

The deflections with other load configurations showed similar trends, except that they were more concentrated near the Bearer Bar 4 end of the rails, because the loading was applied over Bearer Bar 3, rather than half way between Bearer Bars 2 and 3.

A calculation of the deflection of a single bearer bar under the full load provides a check on the measured magnitudes. The dimensions of Bearer Bar 3 are used here, so the span is 98.6", the loads are applied at an assumed spacing of gage plus 1" (to allow for the true point of contact between tire and rail), or 57.5", and the bearer bar is taken as prismatic, with the properties of a W 8 x 31. The total load of 28 kips then causes a mid-span deflection of 0.10". This may be compared with the total measured deflection of all four bearer bars (0.18"). The total deflection is used because the total load is shared between all four bearer bars. The measured value is larger, as it should be, because the bearer bars contain a reduced section and are therefore more flexible than the idealized prismatic beam.

Furthermore, the measured deflection values were taken between the bearer bar and the floor, so they include components of deflection due to bending of the wing members and vertical movement within the bearing. (The geometry of the FPS bearing mechanism is such that rotation also causes vertical displacement.)

In test PIT02 the total deflection was 0.26” rather than the 0.18” observed in the REF test. Again the deflections were concentrated towards Bearer Bar 4. This finding suggests that Bearer Bar 4 may have been more flexible than the others, despite its shorter length. This issue merits further investigation.

In conclusion, the total measured deflection is consistent with expectations, but the distribution of deflections among the bearer bars is not.

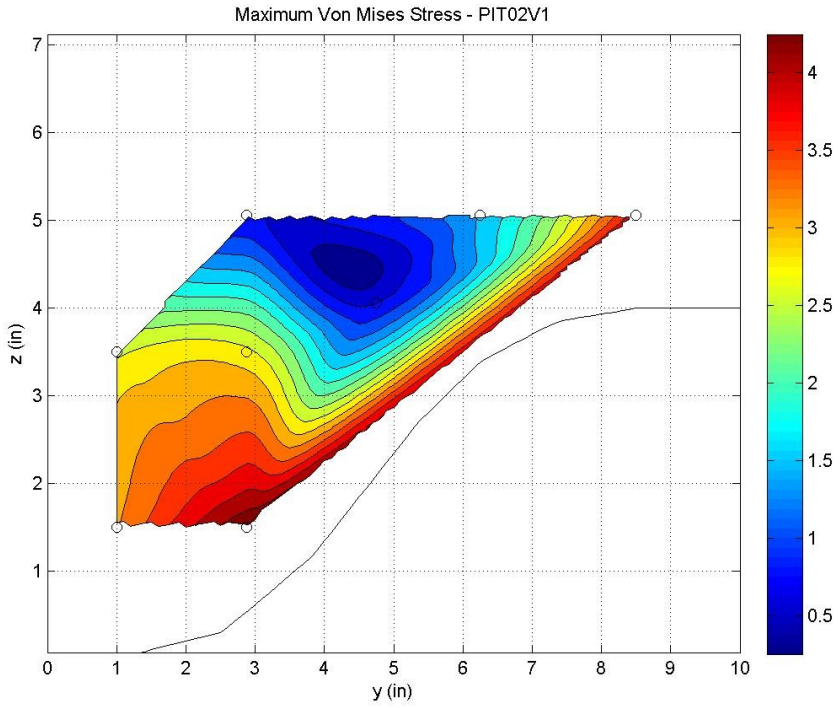

Figure 5-5. Bearer Bar 3. Distribution of von Mises stress at maximum load.

The web of Bearer Bar 3 was heavily instrumented with strain rosettes with the goal of providing a measured data set with which to compare values obtained from FEA. The region where the depth change occurs was targeted as the one of greatest interest. In the full depth section of the bearer bar, the web area is 8” x 0.285” = 2.28 in^2. If the full 28 kip load is carried by Bearer Bar 3, the shear force is 14 kips and the average shear stress is 6.14 ksi. In the reduced section, the depth is 4”, so the predicted average stress is 12.28 ksi.

The maximum von Mises stresses, computed from the measured shear strains, are shown in Figure 5-5 for test PIT02V1. They are plotted as a contour plot. For pure shear, the von Mises stress is √3, or 1.732, times the shear stress.

The strains are not consistent with expectations of both distribution and magnitude. The distribution differs from the classical one for shear in that the measured strains are smallest at mid-depth and largest near the bottom of the section. The magnitude is different because the peak measured von Mises stress in the variable depth region (4.5 ksi) is less than the calculated value for the full-depth region (1.732*6.14 = 10.6 ksi). The implication is that the load from the rails is being distributed quite widely among the bearer bars.

The unexpected distribution of shear stress may be affected by both the overall geometry associated with the change in depth, and by the presence of a relief hold in the web to permit the butt weld in the bottom flange. However, a detailed FE analysis of the region is recommended. If the relief hole raises the stress, it could be mitigated by moving the butt weld closer to mid-span, in a region away from the change in depth.

To investigate the anomaly in magnitude, the shear force in the end of each bearer bar was computed form the measured strain at mid-span. The strain was used to compute the moment at mid-span, then the shear at the end was computed using equilibrium and the assumption that the bearer bar was simply supported. It was also assumed that the guard rails imposed no vertical forces on the bearer bars. The dimensions of each bearer bar were different, and were accounted for in the calculations. The resulting shear forces were 2.4, 0.34, 1.4 and 7.0 kips in bearer bars 01 through 04. These values imply a total load of 22.2 kip, which differs from the true value of 28 kips. The distribution of load among the bearer bars is also unexpected. First, the load in Bearer Bar 3 was expected to be the largest since the load was applied directly to it, but that was not the case. Second, the loads were distributed quite widely across all four bearer bars.

The distribution of forces among the bearer bars, computed from measured quantities, merits more detailed study and this will be undertaken before submitting the final report. However, the evidence from the bearer bar shears, combined with the evidence from the rail stresses, suggests that the distribution of forces in the bearer bars is more even than might be expected from the structural properties of the members. This behavior could be explained qualitatively by the existence of the elastomer in the running rail fasteners, and the lack of elastomer in the guard rail fasteners. The guard rails would then connect all the bearer bars together quite rigidly, causing non-zero vertical forces in the fasteners but leading to more uniform end shears in the bearer bars. At the same time the running rails would transfer their loads to the bearer bars through an axially flexible element (the elastomer layer, plus the HDPE), which would make the distribution of load from them to the bearer bars more uniform. Both effects would lead to a more uniform load distribution.

5.3 Lateral Stiffness under Monotonic Loading

5.3.1 System and Bearing response

The lateral stiffness of the system was measured under monotonic load by applying transverse load to the end of Bearer Bar 4. The full 28 kip load was applied simultaneously over Bearer Bar 4. The stiffness test was conducted six times during the program. The load-displacement curve from test STF03 is shown in Figure 5-6 and shows all of the trends seen in the other tests.

Figure 5-6 shows the load versus deflection history of STF03 which was conducted in the neutral condition, without the 4% slope.

Initially, the system is very stiff and hardly moves until the load reaches about 1 kip. There follows a region of essentially linear stiffness while the system displaces to approximately 1.5", at which point the stiffness increases by a factor of 4 or more.

In Lateral stiffness test STF03: Load vs displacement at Bearer Bar 4.Figure 5-6, the y-intercept of the initial slope corresponds to F/W = 1.35 kips/28 kips = 4.5 %, which can be interpreted as the internal friction in the bearing, which is within the bearing manufacturer's range for the response of the bearings alone.

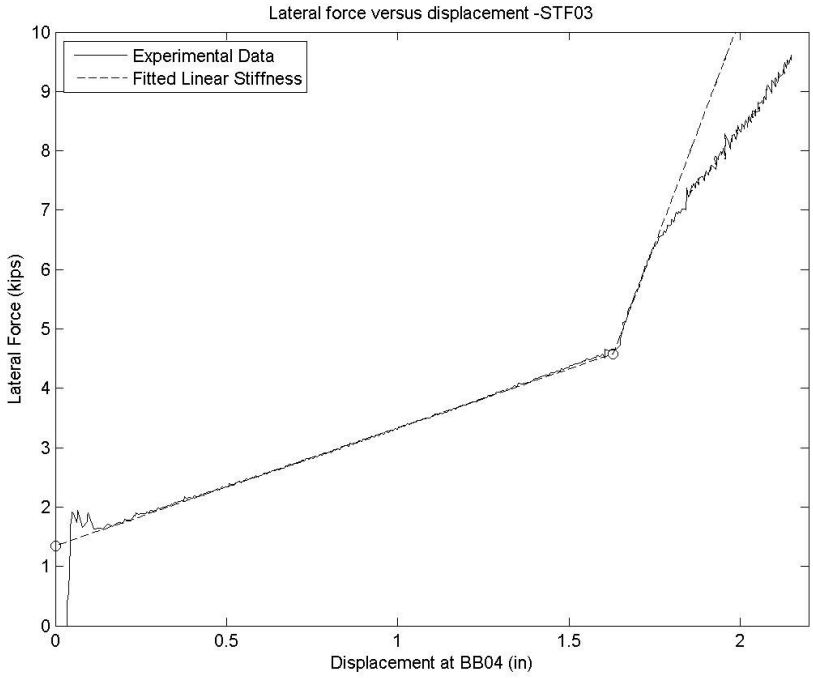

Figure 5-6. Lateral stiffness test STF03: Load vs displacement at Bearer Bar 4.

The behavior may be compared with the behavior predicted by the bearing manufacturer. Prior to the start of sliding, the bearing is essentially rigid. It then has a secondary stiffness that is linear, with a value of *W/L*, where *L* is the effective length of the pendulum and *W* is the vertical load. For these bearings, the manufacturer specifies geometry that leads to *L* = 20.5 in. For a vertical load of 28 kips, the expected stiffness is 28^{k}/20.5" = 1.37 kips/inch. The average load during each test lay in the range 27.0 to 28.0 kips. Thus the theoretical stiffness with which the measured one should be compared is 1.32 to 1.37 k/in).

The measured system stiffnesses are given in Table 5-1. The measured stiffnesses are all greater than the theoretical bearing stiffness, which suggests that other components were providing additional

stiffness. The frame action provided by the rails and bearer bars is the most likely source of additional stiffness.

The system stiffness decreased slightly with each successive test. Since the geometry of the bearings did not change, that decrease must be associated with the rails and bearer bars. It is possible that the connections loosened slightly due to cyclic deformations, leading to a slight loss in stiffness. It should be noted that tests STF04, STF05, and STF06 were conducted after the guard rails were disengaged.

In test STF04 the average vertical load was 27.8 kips, so the horizontal stiffness of the bearing was 1.36 k/in, and the running rails must have provided the remaining 0.5 k/in to give the total of 1.86 k/in. The curve is very close to linear between displacements of 0.2 and 1.6 in., which suggests that the running rail connections to the bearer bars were behaving elastically in that range.

Table 5-1. Measured transverse stiffness

Test	Stiffness (k/in)	Displacement Δ_2
STF01	2.20	> 0.65
STF02	2.15	1.61
STF03	1.99	1.52
STF04[1]	1.92	> 1.75
STF05[1]	1.86	1.68
STF06[1]	1.85	1.56

Notes:

1. *These tests were conducted without guard rails.*

The increase in stiffness at about 1.6” displacement suggests that, at that displacement, contact is made between two components that subsequently provide additional stiffness. In some of the tests the increase in stiffness was not seen, most likely because the displacement did not reach the necessary value. It was seen in test STF05, so it cannot have been caused by the guard rails alone because they were absent in that test. The running rail fasteners were quite sophisticated devices. The rail rests in a shallow, close-fitting recess so that only a small rotation about a vertical axis brings the edge of the rail flange in contact with the edge of the recess. Contact between the rail and the edge of the recess would explain the sudden change in stiffness. Two components were present that might have caused the additional stiffness to be elastic. First, the base of the fastener consisted of two steel plates, separated by a layer of rubber approximately 0.5” thick. The purpose of the rubber layer is to provide acoustic isolation, but it might also permit some elastic rotation of one plate relative to the other about the vertical axis (perpendicular to the plane of the plates.) Second, an HDPE shim separated the fastener from the bearer bar, and this could have provided elastic stiffness for relative rotation of the two components, through a mechanism similar to the rubber layer embedded in the fastener.

5.3.2 Rail Response

The contribution to horizontal resistance of the frame system consisting of bearer bars and rails can be further investigated through the transverse forces and deformations in the rails. These can be deduced from the readings of the strain gages on the edges of the bottom flanges of the rails.

Two pairs of strain gages were attached to the bottom flange of each rail between Bearer Bars 2 and 3. Each pair gave the strain gradient across the bottom flange at the location, from which the lateral moment could be computed. The pairs of gages were separated by 17". The change in moment over that length was then used to obtain the lateral shear force in the rail.

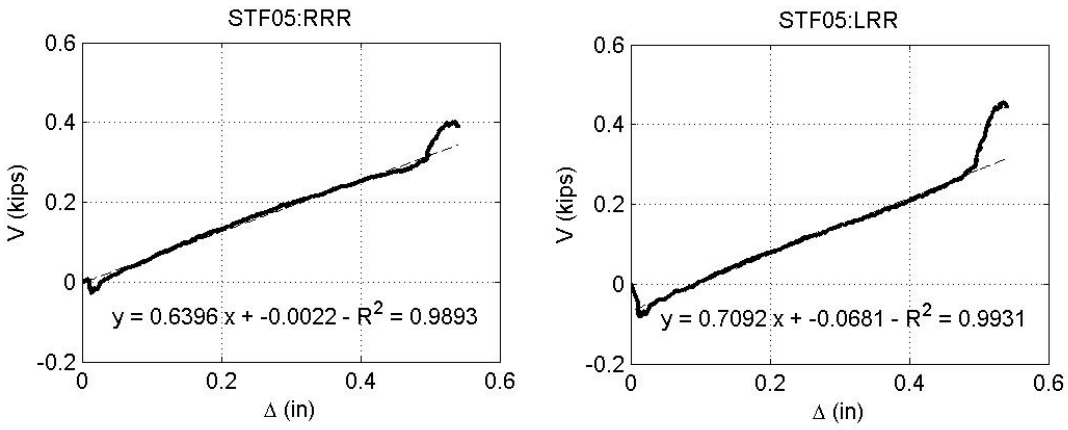

Figure 5-7. Test STF05. Rail lateral shear force vs displacement.

The shear force vs. displacement plot from lateral stiffness test STF05 is shown in Figure 5-7. The force is the shear force in the rail between Bearer Bars 2 and 3, and the displacement is the relative horizontal displacement between those two bearer bars. This is 28% of the total displacement at Bearer Bar 4, since the rails moved almost as rigid bodies, rotating about the pins at the wall end.

Computing the shear force requires taking the difference between gage readings twice – once across the flange and again along the 17" length of the rail. Differencing any data, especially experimental data, increases the relative error in the quantity. Thus the values of the shear forces computed here should be regarded as indicative rather than precise.

For the running rails, the plots of shear force vs. displacement are approximately straight lines with a constant positive stiffness. That indicates approximately linear behavior, which is consistent with the overall load-displacement behavior shown in Figure 5-6. Both running rails exhibit a small drop in load initially, and that same behavior was also seen in other stiffness test results. The cause is unknown.

The guard rail plots (not shown here) show patterns that are difficult to explain. They are highly nonlinear, the plots for the two rails are different, and suggest slip in the connection. Similar patterns of guard rail behavior were seen in tests STF02 and STF03. In tests STF04 thru STF06, in which the guard rails were disconnected, the guard rail responses were negligible, as expected.

Figure 5-6 showed a marked increase in stiffness for the whole system near the maximum displacement during test STF03, and that was tentatively attributed to frame action, which implies shear forces in the rails. Figure 5-7 also shows a similar increase in stiffness for the rail near the maximum displacement during test STF05. This suggests that the running rails fasteners were locking up near the maximum displacement used in the test, after which the stiffness of the running rails, and that of the whole system, increased.

Strain gages were applied to the rails only between Bearer Bars 2 and 3, so no information is available about shear forces between Bearer Bars 3 and 4. Ideally, lateral strain gages would have been applied to the rails in every bay. This was not possible here, because all the available slots in the data acquisition system were already being used, but it should be borne in mind for future applications, such as the testing at TTCI.

5.4 Response to Combined Vertical and Horizontal Load

In the tests that formed the main part of the program, the pseudo-axle was placed either between Bearer Bars 2 and 3 (REF test) or over Bearer Bar 3 (all other tests) and the full vertical load of 28 kips was applied. Cyclic horizontal load was then applied to the pseudo-axle up to a maximum of 4 kips.

In about half the cases, the loads were applied using displacement control for safety reasons. Thus the peak positive and negative loads are not exactly the same, and the peak loads in different tests are also not identical. The peak-to-peak force range averaged 7 kips, and was never less than 5.6 or more than 7.5 kips.

5.4.1 Load-Displacement response

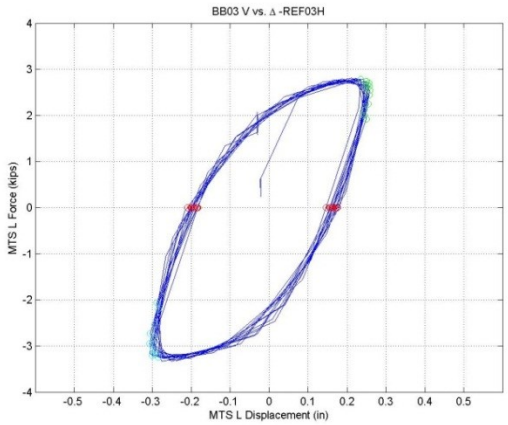

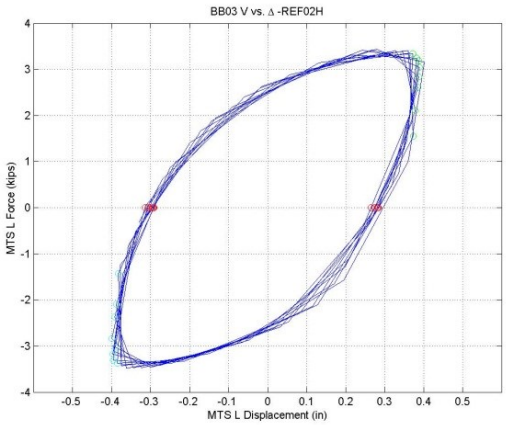

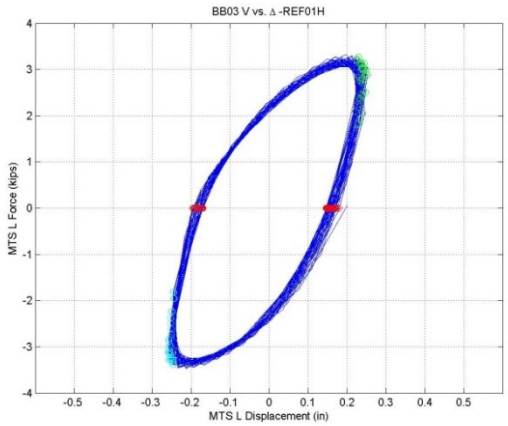

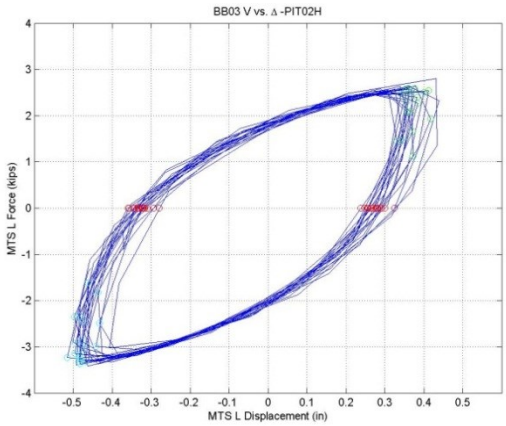

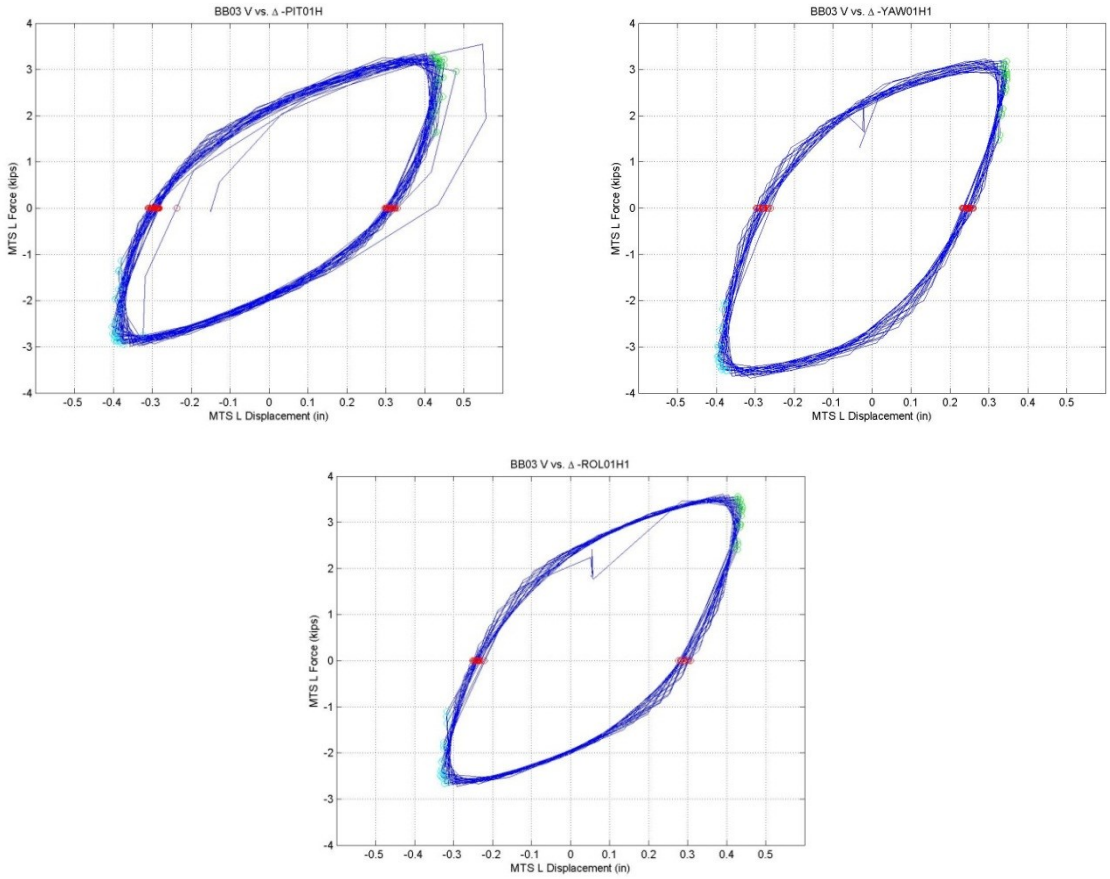

Figure 5-8. Horizontal force vs displacement curves.

Figure 5-8 shows the horizontal force vs. displacement curves for three reference tests, two roll tests, two pitch tests and the yaw test. The results share some common characteristics.

- All the curves are hysteretic.
- The initial stiffness after a reversal point is on the order of 80 to 100 kips/in. This is the same order of magnitude as the initial stiffness observed in the horizontal stiffness tests.
- The stiffness degrades gradually and smoothly. This suggests that several bearings contributed to the resistance, and that they started sliding at different times.
- The equivalent viscous damping lies between 30% and 40% in all cases. The Energy Dissipated per Cycle (EDC) is closely related, and can be used to compute an average dissipative force throughout the cycle. That force was typically on the order of 1.5 kips. If it was supplied by the friction in the FPS bearings alone, it implies a friction coefficient of μ = 1.5/28 = 0.5, or 5%. Because other evidence suggests that some energy was dissipated in the rail fasteners, the FPS bearing friction was probably less than 5%. The FPS specifications call for friction of 8% +/- 6%. Thus a value slightly less than 5% is plausible.
- When the force dropped to zero, a significant residual displacement remained. It was characterized by the “Normalized Cross-Over Displacement” (NCOD). It is defined as

$$NCOD = \frac{\left(\Delta_0^+ - \Delta_0^-\right)}{\left(\Delta_{max} - \Delta_{min}\right)}$$

where

Δ_0^+ and Δ_0^- are the displacements at zero force in the positive and negative directions,

and Δ_{max} and Δ_{min} are the peak displacements in the positive and negative directions.

The NCOD is a measure of the residual displacement as a fraction of the peak displacement. An NCOD of zero indicates an elastic system that re-centers completely, while NCOD = 1.0 indicates a perfectly plastic system in which the residual displacement is equal to the peak displacement.

In these tests the NCOD values lay in the range 0.70 - 0.80. This confirms the visual observation that the system failed to re-center.

After applying the combined loading in the pitch test and two of the reference tests, an additional set of ten cycles of vertical load was applied with the intention of determining whether it would improve the re-centering of the system. It made almost no difference. In the most extreme case (PIT02) the residual displacement decreased by 0.016 in, i.e. by 4%. In most cases it decreased by less than 2%.

A friction pendulum bearing will not re-center naturally under arbitrary loading. If it is displaced laterally and then released, it will move towards the center but will come to rest a distance of approximately $L\mu$ from the origin, where L is the effective pendulum length and μ is the friction coefficient. If μ is taken here as 5% and L = 20.5”, and no other forces act on the system, the bearings should be expected to come to rest approximately 1” from the origin. The behavior seen in the combined loading tests is consistent with this characteristic.

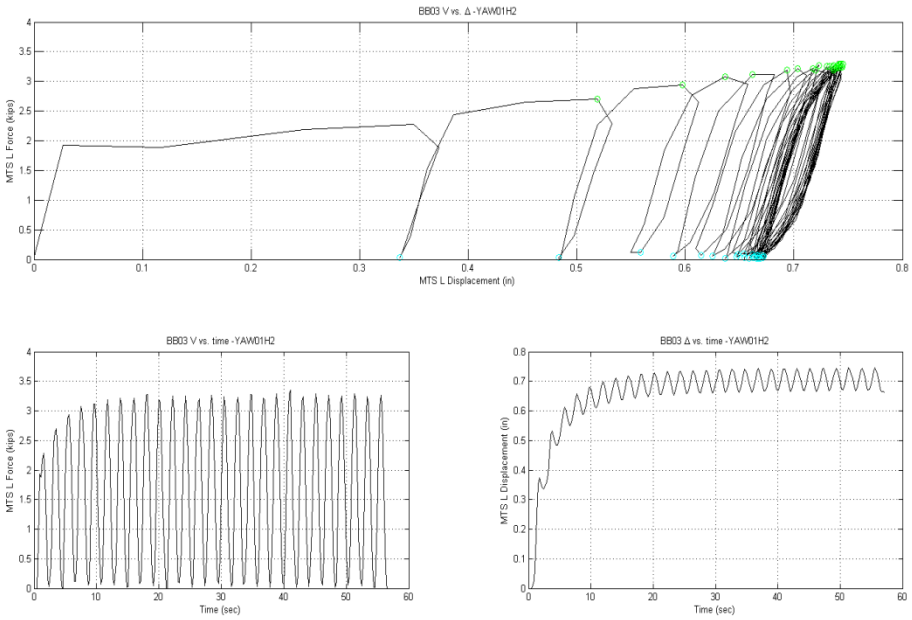

Figure 5-9. Load vs Displacement during one-way ratcheting test

After completing the formal test program, an additional loading was applied. With the rig in the yaw configuration, repeated load (cycle of zero to P and back to zero) was applied one direction with the goal of investigating any displacement "ratcheting" that might occur. The results are shown in Figure 5-9. The peak load in each cycle did not reach the maximum value of 3.25 kips until approximately cycle 6, because of constraints on the way that it was applied. However, the test showed that the displacement of the system does stabilize, after which any further load cycles retrace the load-displacement path of the previous cycles.

The envelope to the force-displacement curve is approximately bilinear, and the stiffness of the second segment is approximately 2.1 kip/inch. This is consistent with the values found in the horizontal stiffness tests. The results also show that the system shows that the residual displacement at zero load is approximately 90% of the peak displacement.

5.4.2 Rail Deformations and stresses

Figure 5-10 shows the lateral force displacement response of the rails during the combined loading in test PIT01, PIT02 and REF02.

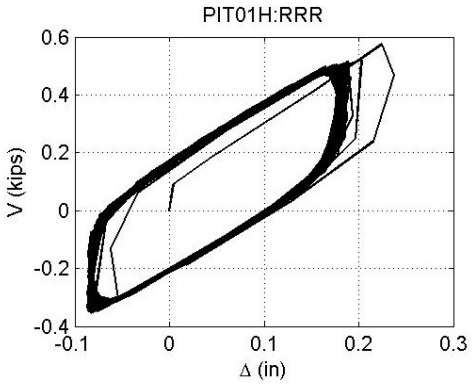
PIT01H:RRR
V (kips)
Δ (in)

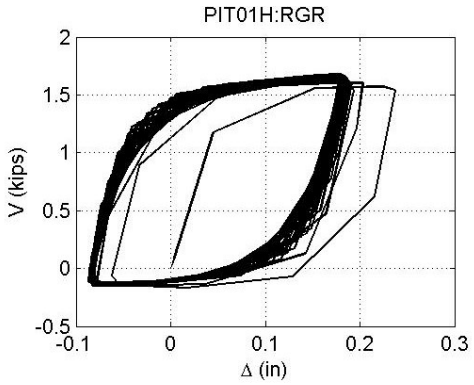
PIT01H:RGR
V (kips)
Δ (in)

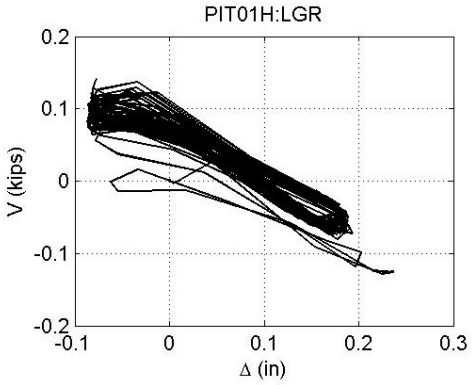
PIT01H:LGR
V (kips)
Δ (in)

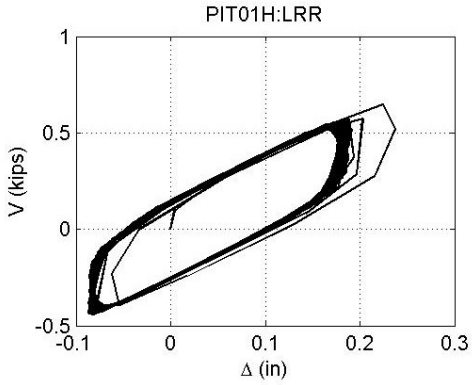
PIT01H:LRR
V (kips)
Δ (in)

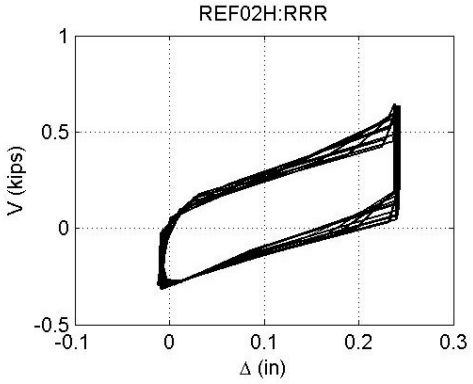
REF02H:RRR
V (kips)
Δ (in)

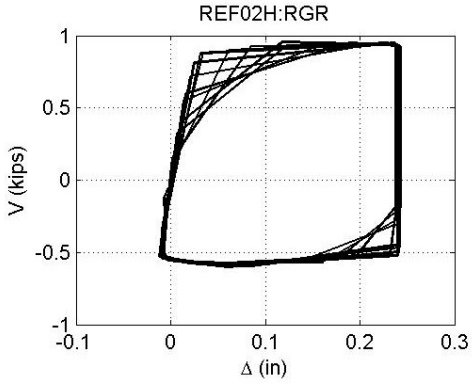
REF02H:RGR
V (kips)
Δ (in)

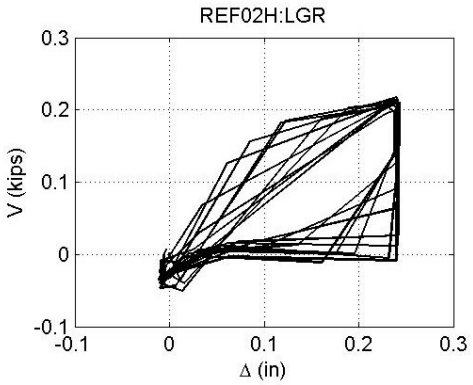
REF02H:LGR
V (kips)
Δ (in)

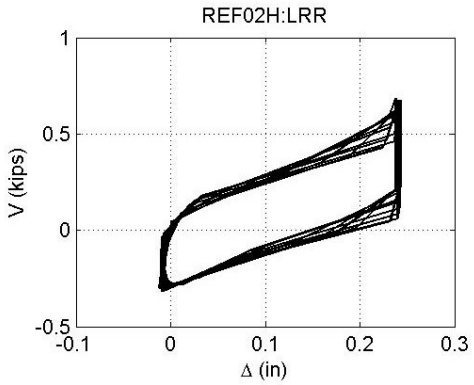
REF02H:LRR
V (kips)
Δ (in)

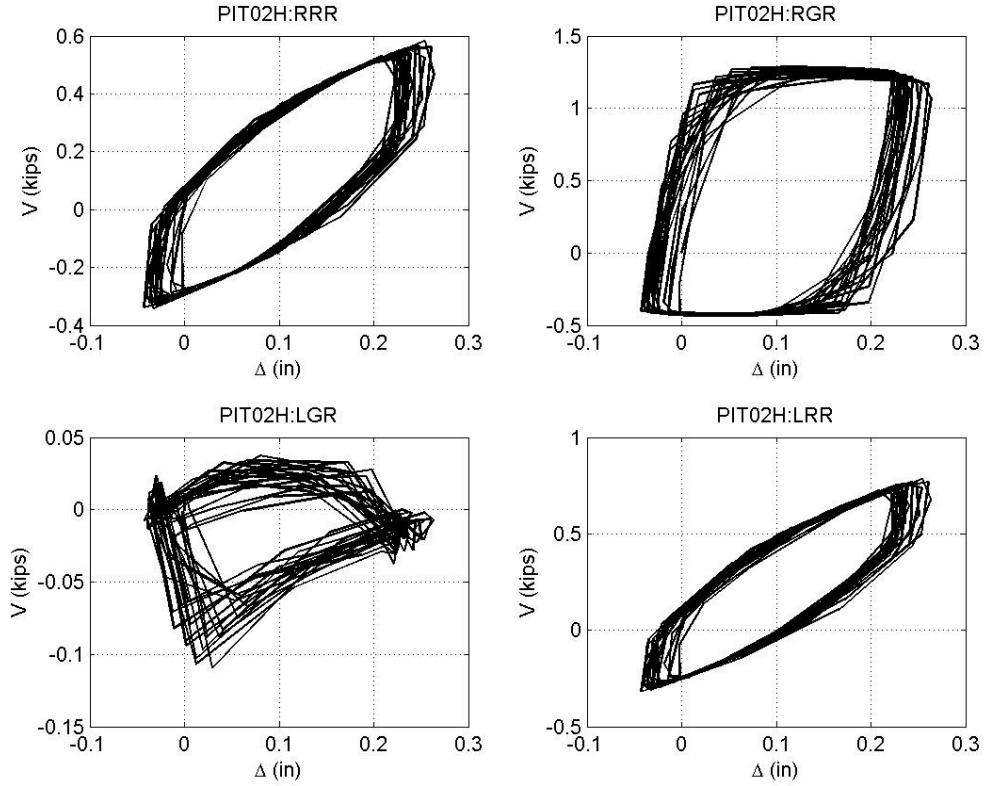

Figure 5-10. Lateral shear force in rail vs relative displacement between Bearer Bars 2 and 3.

The response of the left guard rail (LGR plot) should be disregarded because one of the strain gages was not working properly. The right guard rail plot suggests behavior that is close to rigid-plastic, as might be expected from a bolted connection that slips after enough moment has been applied to it. By contrast, the two running rail plots suggest a system that is basically elastic with some friction in it. The values suggest that the elastic flexibility is provided by the fasteners. If the fasteners were rigid, the lateral stiffness would be that of the rail alone, or $12EI/L^3$ = 155 k/in. The stiffness of the elastic part of the measured curve is approximately 2.5 /in. The connections must be the cause of the additional flexibility. The elastomeric layer in the fasteners provides a physical mechanism that would cause this behavior.

6 Analysis and Discussion of Findings

6.1 System behavior

The system behaved much as expected, and revealed no major unanticipated shortcomings.

6.1.1 Observed

Under vertical load, the force between the bearer bars and bearings was always compressive. This is desirable because it reduces the possibility of fatigue damage caused by intermittent loss and re-gaining of contact, with the corresponding impacts.

Under transverse load, the system did not re-center. This is partly an inherent characteristic of the bearings used and partly the result of inelastic behavior (i.e. friction and slip) in the connections between the rails and bearer bars. These two resisting mechanisms act in parallel.

6.1.2 Implications for Prototype Track Bridge

The global geometry of the test specimen differed from that of the prototype track bridge, so the test results need to be interpreted in the light of the geometric differences.

For vertical load effects, the rails in the prototype bridge are continuous over a greater length (approximately 42 ft) than the rails in the lab tests (approximately 10 ft.) Therefore the compressive contact between rail and bearer bar observed in the lab tests may not hold true in the prototype. This should be checked using FE analysis. The properties of the two sets of fasteners appear to have an important influence in the distribution of load to the different bearer bars, and the possibility of uplift. Their properties should be accounted for in any numerical model.

For transverse load effects, the most significant difference between the test and prototype configurations lies in the fact that the rails in the test specimen were able to displace essentially in rigid body rotation, whereas the rails in the prototype are fixed at each end against lateral displacement and must deform into a curved shape. This rail bending provides an additional re-centering mechanism, if the rails remain elastic. More detailed evaluation of the test results is desirable to determine better the extent of the elastic and frictional mechanisms that promote or inhibit re-centering. Those mechanisms are governed by the behavior of the local connections. If those behaviors can be better defined, they should be incorporated into an FE model of the prototype bridge to determine its global behavior.

7 Summary and Conclusions

7.1 Summary

Laboratory tests were conducted to investigate the characteristics of the CESURA system, which is to be used to build a track bridge for Sound Transit's light rail system over the I-90 floating bridge. The track bridge will be installed at each of the articulation points at the ends of the transition spans between the floating and fixed sections of the bridge. A track bridge is needed there to accommodate the concentrated rotations that would otherwise occur in the rails.

The test specimen represented approximately one quarter of the track bridge, at full scale. The bearings and bearer bars were supplied by the manufacturers who will fabricate them for the prototype. The test rig was designed to be adjustable so that the specimen could be changed to match a wide range of possible configurations, including pitch, roll and yaw.

Vertical load tests were conducted using 10, or in later tests 20, cycles of load from zero to full load (28 kips axle load). Combined loading tests were conducted using a fixed vertical load (28 kips) and cyclic horizontal load (up to +/-4 kips, to simulate wind loads).

7.2 Conclusions

The following conclusions were drawn:

1. The CESURA system consists of many precision parts which must be assembled accurately. Assembly difficulties experienced in the lab can and should be addressed by developing a robust fabrication sequence. The bearing attachment system should be detailed so that the bearings can be replaced easily.
2. The rails were shimmed to avoid stresses in the rails and bearer bars due to lack-of-fit. Even in the controlled conditions of the laboratory, the process was quite time-consuming. In the field, where all the components may be moving due to movements of the floating bridge in addition to thermal changes, successful shimming could be particularly difficult.
3. The vertical load tests showed that, in the test specimen, the contact forces at the rail fasteners were always compressive. This behavior is desirable. Whether it also holds true in the prototype depends on the relative stiffnesses of the rails, bearer bars and rail fasteners. That should be carefully checked using numerical modeling, which should include an allowance for both the properties of the rail fasteners and slight inaccuracies in fabrication.
4. The Direct Fixation fasteners used for the running rails contained an elastomeric layer for acoustic isolation. They were also set on HDPE shims to achieve the desired rail cant. Those two polymeric layers provided some vertical flexibility between the rails and bearer bars. If the same fastening system is used in the prototype, it will reduce the potential for tension in the fasteners and uplift at the FPS bearings compared to the values that would occur in the absence of the polymeric layers. It will also reduce the load applied to each bearer bar and the associated bearer bar deflection. All three of the results appear to be desirable. A potential drawback of the more flexible supports is that the rail stresses may increase.

5. The rail and bearer bar system is statically indeterminate, so the distribution of the vertical load among those components depends strongly on the relative stiffnesses. In the lab, the wing elements were represented by stiff plates that were supported at close spacing by relatively rigid jack-stands. The flexibility of the real wing section in the prototype should be included in the investigation of the distribution of vertical loads and the associated local forces.
6. The extent of re-centering under horizontal load needs to be evaluated for the prototype geometry, using component data from the tests. Some features promote re-centering (rail stiffness, bearing geometry, etc.) while others inhibit it (bearing friction, friction in the rail fasteners, etc.) The relative magnitudes of the forces in these mechanisms should be evaluated in detail to estimate the net effect on re-centering. The connections between the guard rail and the bearer bars should be chosen so that either they are rigid or can rotate freely so that the rails have no effect on re-centering or contribute positively to it. A connection that slips after reaching a load less than the full applied load will inhibit re-centering.
7. The FPS bearings were able to provide the required displacements and rotations.
8. The bending stresses in the rails under vertical load are never greater than 7 ksi.
9. The von Mises stresses in the webs of the bearer bars at the change in section are never greater than 4.5 ksi.

7.3 Recommendations

The following tentative recommendations are offered. It is likely that they will require slight modification, and that others will be added, as the data from the testing are analyzed more fully.

1. The lateral re-centering properties of the system should be investigated using FE analysis. The contributions from the rail lateral bending (not present in the lab configuration) and the properties of the rail fasteners should be included. If PTFE sliders are to be used, with the goal of permitting longitudinal movement of the rails, their properties should also be included.
2. If the properties of the FPS bearings are found to dominate the re-centering, two strategies for improvement appear possible and both should be considered. The bearing's effective pendulum length and internal friction coefficient both affect the degree to which re-centering will occur. A reduction in either would improve the re-centering. However, reducing the effective length of the pendulum would increase the vertical displacement for a given horizontal displacement, and this change might have unintended consequences for other components. Reducing the internal friction, if that is possible, might be preferable.
3. Instrumentation in future tests, such as those planned at TTCI, needs to be planned carefully. Experience from these component tests should be used in that planning. Examples include the need for strain gages on the rails in a number of "bays", instrumentation to detect the distribution of loads to the bearer bars, improvements to DMI's proposed LVDT array for measuring bearing displacements and rotations, clarification on the way that the optical strain gages are intended to be read (if they will indeed be used), selection of sensors suitable for the magnitudes of response expected, etc.

4. The stress field in the web of the bearer bars at the variable depth region should be analyzed. The fact that the measured stresses were highly anomalous, and the presence of a relief hole in what appears to be a critical location, both suggest the need for closer study.
5. The fabrication sequence should be planned to facilitate the fitting and assembly of components, and component tolerances should be planned to achieve the desired accuracy in the complete assembly. Shimming of the rails should be conducted under controlled conditions.